



HAL
open science

Etude numérique des micromécanismes de l'endommagement ductile dans des microstructures hétérogènes

Victor Trejo Navas

► **To cite this version:**

Victor Trejo Navas. Etude numérique des micromécanismes de l'endommagement ductile dans des microstructures hétérogènes. Science des matériaux [cond-mat.mtrl-sci]. Université Paris sciences et lettres, 2018. Français. NNT: 2018PSLEM066 . tel-02493152

HAL Id: tel-02493152

<https://pastel.hal.science/tel-02493152>

Submitted on 27 Feb 2020

HAL is a multi-disciplinary open access archive for the deposit and dissemination of scientific research documents, whether they are published or not. The documents may come from teaching and research institutions in France or abroad, or from public or private research centers.

L'archive ouverte pluridisciplinaire **HAL**, est destinée au dépôt et à la diffusion de documents scientifiques de niveau recherche, publiés ou non, émanant des établissements d'enseignement et de recherche français ou étrangers, des laboratoires publics ou privés.

THÈSE DE DOCTORAT

de l'Université de recherche Paris Sciences et Lettres
PSL Research University

Préparée à MINES ParisTech

A numerical study of the micromechanisms of ductile damage in heterogeneous microstructures

Etude numérique des micromécanismes de l'endommagement ductile dans des microstructures hétérogènes

École doctorale n°364
Sciences Fondamentales et Appliquées

Spécialité Mécanique Numérique et Matériaux

COMPOSITION DU JURY :

Mme Anne-Marie Habraken
Université de Liège, Présidente du jury

M Julien Yvonnet
Université Paris-Est, Rapporteur

M Meinhard Kuna
TU Bergakademie Freiberg, Rapporteur

Mme Sabine Rolland
Université Grenoble Alpes, Examineur

M Thilo Morgeneyer
Paris Sciences et Lettres, Examineur

M Marc Bernacki
Paris Sciences et Lettres, Examineur

M Pierre-Olivier Bouchard
Paris Sciences et Lettres, Examineur

Soutenue par
Victor Manuel TREJO NAVAS
le 20 12 2018

Dirigée par **Pierre-Olivier Bouchard**
et par **Marc Bernacki**



Contents

1	Introduction	5
1.1	Objectives and outline	9
1.2	Publications	10
2	Bibliographic review and methodology	13
2.1	Bibliographic review	14
2.1.1	Numerical modeling of ductile damage at the macroscale	14
2.1.2	Numerical modeling of ductile damage at the microscale	18
2.1.3	Numerical techniques to model ductile damage at the microscale	21
2.2	Material and methodology	28
2.2.1	Nodular cast iron	28
2.2.2	General methodology	30
2.2.3	Studied specimens	37
2.2.4	Microstructure immersion	39
2.2.5	Mechanical behavior	39
2.2.6	Boundary conditions	41
2.2.7	Closing comments	41

3	A comparative study of image segmentation methods for micromechanical simulations of ductile damage	45
3.1	Introduction	46
3.2	Methodology	47
3.2.1	Image segmentation	47
3.2.2	Observables	56
3.3	Results	57
3.3.1	Mesh sensitivity analysis	57
3.3.2	Model cross comparison	66
3.3.3	Comparison of segmentation methods	69
3.3.4	Uncertainty quantification	78
3.4	Conclusions and perspectives	80
4	An examination of microscopic precoalescence strain measures in ductile cast iron through micromechanical simulations based on 3D imaging	83
4.1	Introduction	84
4.2	Observables	84
4.3	Comparison of DVC and FE strain measures	87
4.3.1	90° specimen	87
4.3.2	45° specimen	91
4.4	Strain field evolution	95
4.4.1	Discussion	95
4.5	Effect of probe size on FE strain measures	103
4.5.1	Mesh sensitivity analysis	103
4.5.2	Probe size sensitivity analysis	106

4.6	Conclusions	111
5	Void growth and coalescence in a three-dimensional non-periodic void cluster	115
5.1	Introduction	116
5.2	Methodology	118
5.2.1	Methodology for the study of void and/or inclusion clusters	118
5.2.2	Parametric study	119
5.3	Results	121
5.3.1	Results for the case with $d_1 = 1$ and $d_2 = 1$	121
5.3.2	Effect of d_2	124
5.3.3	Effect of d_1	129
5.3.4	Global results and discussion	132
5.3.5	Effect of hardening	134
5.4	Conclusions	135
6	Towards a micromechanical coalescence model in nodular cast iron	140
6.1	Introduction	141
6.2	Results and analysis	142
6.2.1	Comparison with laminography images	142
6.2.2	Strain evolution in the intervoid ligament	144
6.2.3	Precoalescence strain as coalescence criterion	148
6.2.4	Precoalescence strain in the stress space	149
6.2.5	Uncoupled damage parameters as coalescence indicators	152
6.2.6	Intervoid distance as coalescence criterion	154

6.2.7	A simple probabilistic approach	161
6.3	Discussion	166
6.4	Conclusions and perspectives	167
7	Conclusions and perspectives	171
7.1	Conclusions	171
7.2	Perspectives	173
A	Strain profiles	177

Chapter 1

Introduction

Contents

1.1	Objectives and outline	9
1.2	Publications	10

The problem of fracture is of practical interest in a wide range of engineering applications such as transport, aerospace, nuclear, civil structures, medical implants and microelectronics. It is indeed challenging to think of a process or application in which the structural integrity or lifetime expectancy of solid components are not of prime importance. Of course, not all solid components are meant to withstand mechanical loadings. In the process of design of a plastic toothbrush, for example, its mechanical resistance might not be the first priority in the mind of an engineer. He might however worry about thermo-mechanical fatigue of the injection mold used to create it. Even when fracture is not the main concern in the final use of an object, it is often an important concern during processing.

Structure-property relationships are at the core of the problem of fracture. Processing history and microstructure play an essential role in the final properties of a piece. Fracture is thus an active research field for materials science and engineering. Although it has been studied for decades and seen many and considerable advances, many open questions remain. To put it more broadly, it is desirable to improve the ability to predict fracture for existing and new materials.

Fracture is a complex problem. It is very material-specific. It can occur differently in static or dynamic conditions. The fracture properties of a material are also temperature-dependent. Cyclic loadings result in particular fracture processes known as fatigue. If fracture occurs after a small amount of plastic deformation, it is denoted brittle fracture. If, on the contrary, it is preceded by considerable plastic deformation, it is denoted ductile fracture. The present work restricts its focus to ductile fracture of metallic materials. More specifically, most of the results concern the ductile fracture of nodular cast iron. The methodology and numerical developments, however, can be extended to other heterogeneous materials made of 3 phases (matrix, particles and voids).

This work, carried out at the Center for Material Forming - MINES ParisTech (Cemef - MINES ParisTech) is part of the ANR COMINSIDE project, which constitutes a collaboration with the Centre des Matériaux (MINES ParisTech) and the Laboratoire de Mécanique et Technologie Cachan (LMT Cachan - Ecole Normale Supérieure Paris-Saclay). The global objective corresponds to the meaning of the COMINSIDE acronym, to contribute to the understanding, observation, modeling and simulation of ductile damage mechanisms. The interaction between strain and damage mechanisms at the micrometer scale is of particular interest.

To introduce ductile damage, a metallic tensile specimen is evoked. Initially, the material deforms elastically until the plastic threshold is reached. Then, during plastic deformation, work hardening takes place and the stress in the specimen continues to increase. Eventually, a decrease in the stress will be observed despite work hardening. The responsible mechanism for the subsequent loss of load-bearing capacity is ductile damage and it competes with work hardening. The softening effect of ductile damage increases with deformation and finally

leads to fracture of the specimen. This simple description concerns the macroscale.

At the microscale, the evoked specimen presents an initial population of inclusions dispersed in the metallic matrix. These inclusions induce local heterogeneities that will trigger ductile damage mechanisms at the microscale. When the specimen is sufficiently deformed, after entering the plastic range, an initial population of voids nucleate either by particle fracture or decohesion of the matrix-particle interface. If the specimen is deformed further, these nucleated voids will grow through plastic deformation of the matrix. Eventually, after significant growth, interactions between different voids will arise. With these interactions voids will unite or coalesce through different possible mechanisms. The result of this process is the initiation and propagation of macroscopic cracks which will lead to specimen failure. These are the micromechanisms of ductile damage and the object of study of this work: void nucleation, growth and coalescence.

Simple evidence of the micromechanisms of ductile damage can be obtained from the observation of a fracture surface. Fracture surfaces for Al0.2Fe, Al0.8Fe, Al1.2Mn [1] are shown in Figure 1.1. Dimples of different sizes are observed. These dimpled surfaces are characteristic of ductile fracture. Non-destructive three-dimensional imaging techniques have enabled the evolution of the micromechanisms to be observed during *in-situ* mechanical tests. An example of this type of observation is shown in Figure 1.2 for a plate-like specimen of 2139 Al-Cu alloy in naturally aged T3 condition [2, 3]. These observations provide a fully three-dimensional description of crack initiation and propagation in the plate-like specimen.

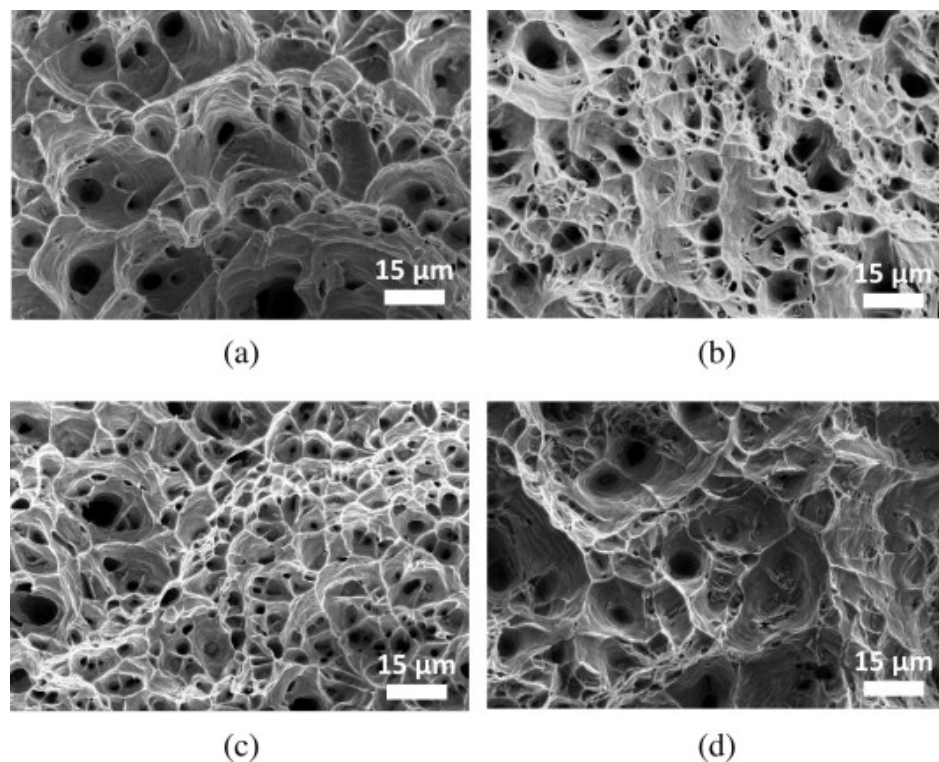


Figure 1.1: Fracture surfaces for (a) Al0.2Fe, (b) Al0.8Fe, (c) Al1.2Mn, and (d) AlMgSi. Figure reproduced from [1].

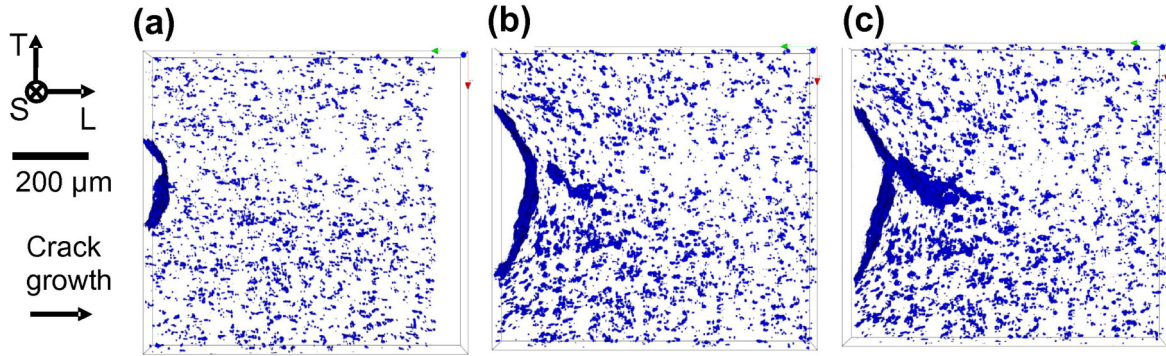


Figure 1.2: Three-dimensional view of ductile crack initiation and propagation in a plate-like specimen of 2139 Al-Cu alloy in naturally aged T3 condition. The voids are represented in blue. Figure reproduced from [3].

This is a simple and general description of ductile damage. The real process is complex and depends on the material and loading conditions. A material may contain particles of different natures, shapes and sizes, as well as different populations of voids. Other microstructural phenomena related to the crystallographic structure can also play a role and interact with the micromechanisms of ductile damage. The thermomechanical history of the material must not be neglected.

To model this complex process at the macroscopic scale, methods of different natures have been proposed. Fracture criteria with uncoupled damage indicators constitute a simple approach. In this approach, a function of the stress state is integrated over the strain path and fracture is considered to occur when the integral reaches a given threshold. This approach is easy to implement, it can be carried out entirely as postprocessing since the impact of damage on the material behavior is neglected. This points at a shortcoming of this approach: it is appropriate only when softening due to damage is negligible.

Coupled approaches can provide more accurate predictions since they take into account softening. These models can be phenomenological or based on micromechanics. Phenomenological approaches often require modifications to provide accurate predictions in different situations, such as different loading conditions. The nature of models inspired by the micromechanics of ductile damage should provide more universal predictions. However, since they are derived from very idealized situations, they present similar shortcomings and phenomenological extensions are very common. With these extensions, new parameters are introduced and parameter identification becomes more complex. Two additional challenges are handling multi-axial and non-proportional loadings [4, 5].

These shortcomings and challenges explain the motivation to explore the micromechanisms of ductile damage. Indeed, modeling the microstructure could provide more accurate predictions. However, modeling the microscopic scale in the whole geometry of interest is unfeasible due to the computational resources it would require. Many numerical studies have

been dedicated to the study of ductile damage at the microscale through different approaches and numerical techniques such as finite elements (FE) [6], cellular automaton [7] or fast Fourier transform [8]. Most studies resort to simplified or idealized configurations such as periodic microstructures in unit-cell approaches. Modeling microstructural evolutions inducing severe topological changes such as nucleation and coalescence is a challenging task in three-dimensional configurations.

This is the context in which the COMINSIDE project started. The numerical developments previously carried out during the COMINSIDE project made it possible to robustly model ductile damage at the microscale from void nucleation to coalescence and up to large plastic strains. This numerical framework allowed for reasonable computational costs, which made fully three-dimensional simulations of complex Representative Volume Elements (RVE) possible. This numerical framework was then integrated in a numerical-experimental framework [9, 10] that combines Synchrotron Radiation Computed Laminography, Digital Volume Correlation and FE simulations. This framework allows FE simulations to be carried out with immersed microstructures and realistic boundary conditions and constitutes the main methodology of this work and will be described in detail in Chapter 2.

1.1 Objectives and outline

The current PhD thesis started in the COMINSIDE project in a stage of further improvement of the framework and exploitation. The global objective of this work is to contribute to the understanding of the micromechanisms of ductile damage through numerical simulations with immersed microstructures and realistic boundary conditions in heterogeneous microstructures. The contributions made to the COMINSIDE project are documented in this manuscript.

- Chapter 2 provides the state of the art of ductile damage and fracture modeling at different scales and a detailed description of the experimental-numerical framework.
- Since this is a recent framework, not all of the related uncertainties are known. Microstructure immersion is an important part of the methodology and it requires a procedure known as image segmentation. Chapter 3 constitutes an exploration of the uncertainties caused by image segmentation and a quantification of the impact of these uncertainties on the final mechanical observables.
- Once the order of magnitude of the implied uncertainties is known, global and local strain measures are compared with experimental measurements to validate the results of the FE simulations in Chapter 4.
- Chapter 5 constitutes a parenthesis in terms of methodology. In an effort to clarify the

observed coalescence mechanisms in nodular cast iron, a purely numerical parametric study of a three voids cluster is carried out with a proposed *ad-hoc* approach.

- The main experimental-numerical methodology is exploited in Chapter 6 in an attempt to establish a new coalescence criterion.
- The conclusions and perspectives are discussed in Chapter 7.

1.2 Publications

Articles in peer-reviewed international journals

As lead author

- V. M. Trejo Navas, M. Bernacki, P.-O. Bouchard, Void growth and coalescence in a three-dimensional non-periodic void cluster, *International Journal of Solids and Structures*, 139 (2018):65-78.
- V. M. Trejo Navas, A. Buljac, F. Hild, T. Morgeneyer, L. Helfen, M. Bernacki, P.-O. Bouchard, A comparative study of image segmentation methods for micromechanical simulations of ductile damage, *Computational Materials Science*, 159 (2019): 43-65.
- V. M. Trejo Navas, A. Buljac, F. Hild, T. Morgeneyer, M. Bernacki, P.-O. Bouchard, An examination of microscopic precoalescence strain measures in ductile cast iron through micromechanical simulations based on 3D imaging, *in progress*.
- V. M. Trejo Navas, A. Buljac, F. Hild, T. Morgeneyer, M. Bernacki, P.-O. Bouchard, Towards a micromechanical coalescence model in nodular cast iron, *in progress*.

As co-author

- A. Buljac, V. M. Trejo Navas, F. Hild, T. Morgeneyer, M. Bernacki, P.-O. Bouchard, On the calibration of elastoplastic parameters at the microscale via X-ray microtomography and digital volume correlation for the simulation of ductile damage, *European Journal of Mechanics-A/Solids* 72 (2018):287-297.
- M. Shakoor, V. M. Trejo Navas, D. Pino Muñoz, M. Bernacki, P.-O. Bouchard, Computational methods for ductile fracture modeling at the microscale, *Archives of Computational Methods in Engineering* (2018):1-40.

Participation in international conferences

As presenting author

- V. M. Trejo Navas, M. Shakoор, M. Bernacki and P.-O. Bouchard, Ductile fracture – Influence of heterogeneous microstructure on nucleation, growth and coalescence mechanisms, *Conference on Numerical Methods in Industrial Forming Processes (NUMIFORM)*. Troyes (France), July 4-7, 2016.
- V. M. Trejo Navas, M. Shakoор, A. Buljac, F. Hild, T. Morgeneуer, M. Bernacki, P.-O. Bouchard, A micromechanical study of ductile damage with a laminography-digital volume correlation- finite element framework, *14th International Conference on Fracture (ICF 14)*. Rhodes (Greece), June 18-23, 2017.
- V. M. Trejo Navas, M. Shakoор, A. Buljac, F. Hild, T. Morgeneуer, M. Bernacki, P.-O. Bouchard, A micromechanical study of void nucleation mechanisms in aluminum alloys, *6th European Conference on Computational Mechanics (ECCM 6)*. Glasgow (United Kingdom), June 11-15, 2018.
- V. M. Trejo Navas, M. Shakoор, A. Buljac, F. Hild, T. Morgeneуer, M. Bernacki, P.-O. Bouchard, Microscopic strain calculations at the onset of coalescence in nodular cast iron, *22nd European Conference on Fracture (ECF22)*. Belgrade (Serbia), August 26-31, 2018.

As co-author

- P.-O. Bouchard, M. Shakoор, V. M. Trejo Navas, M. Bernacki, Numerical modeling of failure mechanisms in complex heterogeneous microstructures, *21st European Conference on Fracture (ECF21)*. Catania (Italy), June 20-24, 2016.
- P.-O. Bouchard, V. M. Trejo Navas, M. Shakoор, M. Bernacki, T. Morgeneуer, A. Buljac, F. Hild, Numerical modeling of ductile fracture at the microscale combined with x-ray laminography and digital volume correlation, *20th International ESAFORM Conference on Material Forming (ESAFORM 2017)*. Dublin (Ireland), April 26-28, 2017.
- P.-O. Bouchard, M. Shakoор, V. M. Trejo Navas, M. Bernacki, Numerical modeling of ductile fracture mechanisms in complex heterogeneous microstructures (**plenary session**), *Fifth International Conference on Computational Modeling of Fracture and Failure of Materials and Structures (CFRAC 2017)*. Nantes (France), June 14-16, 2017.
- P.-O. Bouchard, M. Shakoор, V. M. Trejo Navas, M. Bernacki, A parametric analysis of void coalescence mechanisms based on 3D finite element microscale computations, *XIV*

International Conference on Computational Plasticity (COMPLAS 2017). Barcelona (Spain), September 5-7, 2017.

- A. Buljac, M. Shakoov, V. M. Trejo Navas, M. Bernacki, P.-O. Bouchard, A. Bouterf, L. Helfen, F. Hild, T.F. Morgeneyer, J. Neggers, S. Roux, On the integration of measured data in numerical simulations at the microscale, *IDICs conference*, Barcelona (Spain), November, 2017.
- P.-O. Bouchard, V. M. Trejo Navas, M. Shakoov and M. Bernacki, Numerical modeling of nucleation mechanisms for 3D heterogeneous microstructures (**keynote presentation**), *13th World Congress in Computational Mechanics (WCCM2018)*. New York (USA), July 22-27, 2018.
- P.-O. Bouchard, V. M. Trejo Navas, M. Shakoov, A. Buljac, M. Bernacki, T. Morgeneyer, F. Hild, Analysis of local strain in nodular graphite cast iron at the onset of coalescence by means of 3D numerical modeling combined with X-Ray laminography and digital volume correlation, *13th World Congress in Computational Mechanics (WCCM2018)*. New York (USA), July 22-27, 2018.
- P.-O. Bouchard, V. M. Trejo Navas, M. Shakoov, T. Morgeneyer, A. Buljac, L. Helfen, F. Hild and M. Bernacki, Recent advances in the finite element modelling of ductile fracture at mesoscale (**plenary session**), *17th International Conference on Metal Forming*. Toyohashi (Japan), September 16-19 September, 2018.

Participation in national conferences

As presenting author

- V. M. Trejo Navas, M. Shakoov, M. Bernacki and P.-O. Bouchard, Influence of heterogeneous microstructure on the micromechanisms of ductile fracture, *CSMA 2017 - 13ème colloque national en calcul des structures*. Giens (France), May, 2017.
- V. M. Trejo Navas, M. Shakoov, M. Bernacki and P.-O. Bouchard, A study of the effect of microstructural heterogeneities on ductile damage, *3es Journées Matériaux Numériques*. Tours (France), Janvier 31 - Fevrier 2, 2017.

Chapter 2

Bibliographic review and methodology

Contents

2.1	Bibliographic review	14
2.1.1	Numerical modeling of ductile damage at the macroscale	14
2.1.2	Numerical modeling of ductile damage at the microscale	18
2.1.3	Numerical techniques to model ductile damage at the microscale . . .	21
2.2	Material and methodology	28
2.2.1	Nodular cast iron	28
2.2.2	General methodology	30
2.2.3	Studied specimens	37
2.2.4	Microstructure immersion	39
2.2.5	Mechanical behavior	39
2.2.6	Boundary conditions	41
2.2.7	Closing comments	41

2.1 Bibliographic review

Modeling ductile damage at the macroscale can be split in two main approaches: uncoupled fracture criteria and coupled damage models. Within each approach, criteria and models can have either physical bases or phenomenological ones. The purpose of this section is not to provide an exhaustive review of damage models and failure criteria, but to give useful information of the most common approaches for a better understanding of the work that will be discussed in the rest of the manuscript.

2.1.1 Numerical modeling of ductile damage at the macroscale

Uncoupled fracture criteria

Uncoupled approaches were briefly commented upon in Chapter 1. In this approach, the ductile damage process is summarized in a single damage parameter (or damage indicator) D that is calculated as the integral of a function of the stress state along the strain path [4]:

$$D = \int f(\boldsymbol{\sigma}) d\bar{\varepsilon}_p, \quad (2.1)$$

where $\boldsymbol{\sigma}$ is the stress tensor and $\bar{\varepsilon}_p$ the equivalent plastic strain. Generally these uncoupled models or fracture criteria are expressed in terms of functions of the three invariants of the stress tensor. Namely, they are expressed in terms of the stress triaxiality ratio T , the von Mises equivalent stress σ_{eq} and the Lode parameter L :

$$T = \frac{\sigma_1 + \sigma_2 + \sigma_3}{3\sigma_{eq}}, \quad (2.2)$$

$$L = \frac{2\sigma_2 - \sigma_1 - \sigma_3}{\sigma_1 - \sigma_3}, \quad (2.3)$$

where σ_i is the i^{th} principal stress and $\sigma_1 > \sigma_2 > \sigma_3$.

The uncoupled damage parameter D does not affect the material behavior, i.e., no damage-induced softening affects the load-bearing capacity of the material. This means that it can be calculated simply during postprocessing.

Some fracture criteria are based on micromechanical considerations. The Rice-Tracey fracture criteria, for instance, is based on a void growth model derived for a spherical void in a

perfectly plastic material under hydrostatic stress [11]. This analysis revealed the exponential influence of the stress triaxiality ratio for predominantly hydrostatic conditions. Using this void growth model as fracture criterion amounts to considering that fracture occurs when a critical void fraction is reached.

Other fracture criteria are phenomenological. This is the case of the Bai-Wierzbicki fracture criterion [12]. At this point, it was well established that, just as the Rice-Tracey fracture criterion predicts, the fracture strain decreases as the stress triaxiality ratio increases. Recent experimental results showed considerably different degrees of ductility for mechanical tests at low triaxiality levels. Bai and Wierzbicki designed their fracture criterion to explain these differences by introducing dependency from the third invariant of the stress tensor through the Lode angle.

Many other phenomenological or micromechanics-based fracture criteria have been proposed [13–18].

Continuum damage mechanics

From the macroscopic point of view, damage can be introduced through an internal variable D that represents the stage of the material in the irreversible fracture process: a value of $D = 0$ corresponds to a sound material and $D = 1$ to a completely damaged material. This phenomenological approach does not consider the micromechanisms of ductile damage. It was initially proposed by Kachanov in his study of creep [19] with the introduction of the effective stress $\bar{\sigma}$:

$$\bar{\sigma} = \frac{\sigma}{1 - D}. \quad (2.4)$$

The constitutive equations may be used without modification by substituting the stress by the effective stress and adopting the hypothesis of strain equivalence. This hypothesis assumes the strain associated to a given damaged state with the applied stress is equivalent to the strain associated with the corresponding undamaged state with the corresponding effective stress.

Continuum damage mechanics constitute a thermodynamically sound framework for ductile damage. The evolution of D is derived from a potential and it may never decrease. Different models have been proposed in this framework such as the Rousselier model [20, 21] and the Lemaitre model [22]. Since the Lemaitre model is arguably the most extensively adopted one, a brief explanation is presented in this section.

The energy density release rate Y can be derived from the state potential and expressed

as follows [23]:

$$Y = \frac{\sigma_{eq}^2}{2E(1-D)^2} \left[\frac{2}{3}(1+\nu) + 3(1-2\nu) \left(\frac{-p}{\sigma_{eq}} \right)^2 \right], \quad (2.5)$$

where E is the Young modulus, ν the Poisson ratio, and p is the pressure, defined as:

$$p = -\frac{\sigma_1 + \sigma_2 + \sigma_3}{3}. \quad (2.6)$$

The following expression was proposed for the damage dissipative potential F_D by Lemaitre [22]:

$$F_D = \frac{S}{(b+1)(1-D)} \left(\frac{Y}{S} \right)^{b+1}, \quad (2.7)$$

where S and b are two material parameters. The damage evolution is obtained with:

$$\dot{D} = \dot{\lambda} \frac{\partial F_D}{\partial Y}. \quad (2.8)$$

where $\dot{\lambda}$ is the plastic multiplier.

The Lemaitre model has been modified to account for plastic anisotropy [24] and to improve its prediction capacity, for example, under compressive charges [25] or for low stress triaxialities [26].

Porous plasticity - the Gurson model

The Gurson model is a widely adopted porous plasticity behavior law derived with an upper bound approach in a spherical model with a concentric void surrounded by a perfectly plastic matrix [27]. The resulting yield surface is:

$$\phi(p, \sigma_{eq}) = \left(\frac{\sigma_{eq}}{\sigma_0} \right)^2 + 2f \cosh \left(-\frac{3}{2} \frac{p}{\sigma_0} \right) - 1 - f^2, \quad (2.9)$$

where σ_{eq} the equivalent stress, σ_0 the flow stress and f the void fraction. Since the Gurson model overestimated the localization strain in a periodic array of voids, Tvergaard [28] added three additional parameters q_1 , q_2 and q_3 to the model:

$$\phi(p, \sigma_{eq}) = \left(\frac{\sigma_{eq}}{\sigma_0}\right)^2 + 2q_1 f \cosh\left(-\frac{3q_2}{2} \frac{p}{\sigma_0}\right) - 1 - q_3 f^2. \quad (2.10)$$

To account for the accelerated void growth at the onset of coalescence, Tvergaard and Needleman [29] introduced an effective porosity f^* in the model:

$$\phi(p, \sigma_{eq}) = \left(\frac{\sigma_{eq}}{\sigma_0}\right)^2 + 2q_1 f^* \cosh\left(-\frac{3q_2}{2} \frac{p}{\sigma_0}\right) - 1 - q_3 f^{*2}. \quad (2.11)$$

The effective porosity f^* is equal to f up to a critical value of f_c and then increases faster to account for coalescence:

$$f^* = \begin{cases} f & \text{if } f < f_c \\ f_c + \frac{f_u - f_c}{f_f - f_c} (f - f_c) & \text{if } f \geq f_c, \end{cases} \quad (2.12)$$

where f_c , f_u^* and f_f are material parameters related to the coalescence mechanisms.

The Gurson model with these two heuristic extensions, the introduction of coefficients to match predictions in a periodic array of voids and the introduction of an effective porosity to account for accelerated void growth at the onset of coalescence, is known as the Gurson-Tvergaard-Needleman (GTN) model and is extensively used. The total rate of increase of the void fraction is usually expressed as a superposition of the effect of void growth and void nucleation [30]:

$$\dot{f}_{total} = \dot{f}_{nucleation} + \dot{f}_{growth}. \quad (2.13)$$

The contribution of void growth to the increase rate of the porosity can be expressed straightforwardly in terms of the void fraction and the increase rate of the equivalent plastic strain $\dot{\epsilon}^P$ if the contribution of elastic strain is neglected:

$$\dot{f}_{growth} = (1 - f) \text{tr}(\dot{\epsilon}^P). \quad (2.14)$$

Chu and Needleman [30] proposed to express the contribution void nucleation with a normal distribution that depends on the equivalent plastic strain $\bar{\epsilon}^P$:

$$\dot{f}_{nucleation} = \frac{\psi}{S\sqrt{2\pi}} e^{-1/2\left(\frac{\bar{\epsilon}^P - \bar{\epsilon}_N}{S}\right)^2} \dot{\epsilon}^{Pl}, \quad (2.15)$$

where S is the standard deviation and ψ is the coefficient used to link the nucleated void volume and the void fraction.

Extensions of the GTN model have been developed in an effort to extend its utility beyond the simplifying hypothesis present in its derivation. A very common heuristic extension consists in introducing hardening in the model by simply calculating the flow stress σ_0 with a hardening law [31]. Gologanu et al. [32] proposed an extension for elliptical voids under axisymmetric loading. To improve the model's prediction ability for shear-dominated loadings, Nahshon and Hutchinson proposed an extension detailed in [33]. Other extensions aim at accounting for void size effect [34], plastic anisotropy [35], micro-inertia [36], presence of particles [37] and kinematic hardening [38]. Most of these extensions introduce additional parameters that need to be identified.

2.1.2 Numerical modeling of ductile damage at the microscale

This section presents a brief and non-exhaustive overview of micromechanical studies. The different approaches are presented in increasing order of complexity in terms of how realistically the microstructure is modeled.

The unit-cell approach [28, 39] has been very important in the development of the local approach to fracture. A great number of studies have been and continue to be carried out with this approach. Typically, in the unit-cell approach, a single inclusion or void is embedded in a unit-cell surrounded by periodic boundary conditions. This greatly simplifies the study of the micromechanisms of ductile damage and allows the effect of many microstructural variables to be assessed. Doing so, however, imposes an important simplifying hypothesis: that the studied microstructure can be represented by a periodic arrangement of microstructural features.

The hypothesis of a periodic microstructure is not always an appropriate approximation. This constitutes a compelling reason to enrich the available tools and methodologies for the study of ductile damage. Within the unit-cell framework, different works have extended the original framework by considering unit-cells with multiple voids/particles. Thomson et al. [40] studied the effect of the orientation of a particle cluster with respect to the main loading direction, on void nucleation and growth. The study was later extended to assess void coalescence [41]. McVeigh et al. [42] studied the onset of the void-sheet mechanism with a unit-cell submitted to shear loading. In plane strain conditions, Tvergaard compared clusters with different numbers of voids, but equal total void volume, and concluded that void clusters grow more rapidly [43]. The role of secondary voids and their spatial distribution on void growth and coalescence was assessed by Tekoglu [44] and by Khan and Bhasin [45]. Tekoglu found that the stress at the onset of coalescence decreases when the secondary porosity volume increases.

A second group of studies has investigated non-uniform distributions of voids without recurring to the unit-cell approach. Ohno and Hutchinson [46] studied the effect of void clustering on plastic flow localization by modeling a band of non-uniformly distributed voids between two bands of homogeneous material. Horstemeyer et al. [47] quantified coalescence effects based on temperature for different arrangements of voids. Bandstra and Koss [48] investigated void-sheet coalescence with a computational model of two voids for stress state and proposed a critical local strain value for the onset of void-sheet coalescence based on the nucleation strain for secondary particles. Bandstra et al. [49] examined the deformation localization behavior with void arrays based on experimentally observed microstructures. Tvergaard and Needleman [50] assessed the effect of two populations of second-phase particles on crack growth and observed that crack growth resistance decreases for random arrays of particles. Bandstra and Koss [51] assessed the sensitivity of void growth and coalescence to intervoid spacing. Shakoor et al. [52] compared uniform and random arrangements of voids to investigate the resulting difference in ductility and showed that coalescence occurs faster for random arrangements of voids compared to periodic distributions. This makes some of the results obtained with the unit-cell approach questionable.

A third group of works has focused on modeling realistic microstructures based on experimental images. Sun et al. [53] modeled an actual microstructure based on scanning electron microscope (SEM) image, under plane stress conditions. Vanderesse et al. [54] meshed a volumetric image obtained by X-ray microtomography and carried out FE simulations. Padilla et al. [55] carried out FE simulations of a microstructure obtained via X-ray microtomography in order to assess the evolution of damage in a single lap shear joint. Buljac et al. [9] used synchrotron 3D imaging to immerse microstructures and carry out FE analyses with realistic boundary conditions [10] obtained via digital volume correlation (DVC) and in-situ laminography tests.

Coalescence modeling

The Rice-Tracey or the Gurson void growth model could be used to predict void coalescence. Coalescence through void impingement would occur when the void diameter equals the distance between the center of the two voids. Basing a coalescence criterion on a critical void fraction or void growth ratio and using a void growth model seems natural, however, this critical value depends strongly on the stress state [56]. This fact can be illustrated by considering two different stress states: a hydrostatic stress and pure shear. Under hydrostatic stress, considerable void growth will precede coalescence, while under pure shear, voids will rotate and extend in the shear direction until coalescence without any void growth. Moreover, for a periodic microstructure, a fracture strain can be derived with this methodology. This leads, however, to unrealistically high fracture strains and critical void growth ratio [57]. Both, the Rice-Tracey and the Gurson void growth model overestimate ductility. For this reason, smaller values of critical void growth ratios were then proposed by different authors [29, 58].

In a periodic microstructure, the void growth stage is followed by strain localization in the intervoid ligament which accelerates coalescence. The beginning of this localization stage is usually referred to as the onset of coalescence. Void growth models are thus insufficient to predict void coalescence and final material failure. The work of Brown and Embury [59] and of Thomason [60] are early efforts to take into account this localization strain.

Although the treatment of coalescence in the GTN model (see Equation 2.12) is common given the popularity of the model, it is a simple approach that has seen little evolution from its creation. The Thomason model is also widespread and has benefited from several extensions. Thomason also developed a three-dimensional version [61]. This version of the Thomason model resulted from the analysis via upper-bound methods of a three-dimensional and periodic array of square-prismatic voids. A layer of these voids is limited by two rigid regions. The Thomason model can be summarized as a threshold condition on the stress normal to the planar region containing the void arrangement:

$$\sigma^T(\chi, \omega) = \sigma_0 (1 - \chi^2) \left[\alpha \left(\frac{\chi^{-1} - 1}{\omega} + \beta \sqrt{\chi^{-1}} \right) \right], \quad (2.16)$$

where σ^T is the threshold stress, σ_0 is the equivalent stress of the perfectly plastic matrix material, α is equal to 0.1, and β is equal to 1.2. The threshold stress is a function of the void geometry, represented by the void aspect ratio ω and of the void spacing, represented by the ratio χ of void radius and void spacing.

Since the original Thomason model included no evolution laws for χ and ω , it was capable of predicting the onset of coalescence only and could not be used afterward. Evolution laws for these two parameters have been proposed by other authors [62, 63] extending the usefulness of the model. The Thomason model has also been extended through unit-cell calculations to account for strain hardening in the matrix by making α and β functions of the hardening parameters [64]. No coalescence is predicted by the Thomason model for penny-shaped cracks, i.e., for very small values of the void aspect ratio. Extensions have been proposed to overcome this drawback [65]. Micro-inertia has been accounted for in the extension proposed by Molinari et al. [66]. The original model and its extensions are valid only for tensile loadings. Efforts to generalize the model to other loading conditions were carried out by Torki et al. [67] and Tekoglu et al. [68] for combined tension and shear. Since the derivation of the Thomason model relies on periodicity, its application to complex heterogeneous microstructures is not straightforward and its validity for realistic topologies is not clear.

2.1.3 Numerical techniques to model ductile damage at the microscale

This section offers a brief overview of four numerical approaches to model ductile fracture at the microscale and is inspired from [69]. These approaches have the potential to improve on the limitations of the macroscopic approach. There are, however, general challenges that must be overcome. The large strains associated to ductile damage and the topological changes that occur in the microstructure are at the origin of these challenges.

Element erosion

In the element erosion or element deletion method, a damage indicator is used. When the value of the damage indicator is beyond a given threshold in an element of a finite element (FE) mesh, this element is eliminated from the mesh [70]. The damage indicator may be the strain itself. The behavior of the elements may or may not be coupled with the evolution of the damage indicator, i.e., softening may or may not be considered.

This method allows multiple cracks to be inserted dynamically during the FE simulation. Its main advantages are its low computational cost and ease of implementation. The obtained results are, however, very sensitive to mesh size and element shape [71]. Mass loss is also an important concern. Despite its shortcomings, recent applications can be found in the literature. For example, Perzynski et al. [72] used the technique to model ductile fracture in a dual phase steel with two-dimensional (Figure 2.1) and three-dimensional simulations.

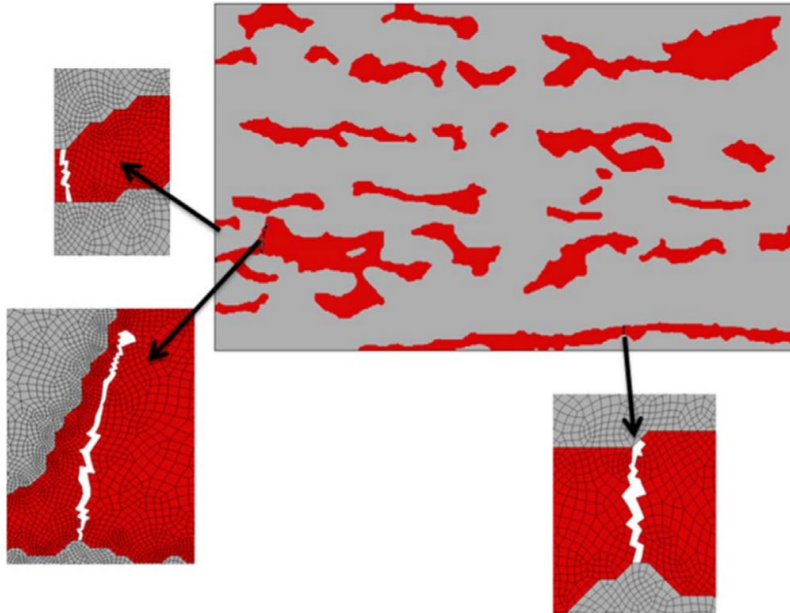


Figure 2.1: FE mesh of a dual phase microstructure after element deletion. Figure reproduced from [72].

More recent methods have been defined in order to eliminate the shortcomings related to

the element erosion method.

Enriched finite element methods

In order to model discontinuities without element erosion or remeshing, a family of enriched FE methods have been developed and have been documented by different authors [73–75]. The most popular of these methods is the eXtended Finite Element Method (X-FEM) [76], which is based on the partition of unity concept [77]. The Generalized Finite Element Method (GFEM) is another relevant enriched method [78]. Initially, in GFEM, all the nodes in the discretization were enriched; later, local enrichment was adopted. The distinction between X-FEM and GFEM has become less clear as the methods have evolved [75]. A very attractive feature of these methods is the fact that discontinuities might be modeled independently of the mesh, i.e., conformity is not required. Most of the applications of enriched FE methods have been dedicated to brittle fracture. This subsection discusses some of the works that have dealt with ductile fracture.

Strong discontinuities such as cracks and holes can be modeled with enriched FE methods. The material/void interface is captured thanks to a discontinuous enrichment, typically using the Heaviside function as enrichment function [76]. To capture the stress singularity in the near crack tip region, an additional enrichment is necessary [79]. The latter requires careful choice of the enrichment function, and knowledge of the analytic solution. These enrichment techniques are usually implemented locally and not in the whole FE mesh. This constitutes the basis of X-FEM.

The basic methodology has been extended to account for arbitrary branched and intersecting cracks in two-dimensional cases [80]. The X-FEM methodology has also been extended to 3D by enriching the elements near the crack front with the radial and angular behavior of the 2D asymptotic crack tip displacement field. Analogous development have been made with the GFEM [81]. Further flexibility in the description of the crack geometry was introduced by coupling the Level-Set (LS) method [82] to the X-FEM: the zero isovalue of a signed distance function gives the position of the crack surface, and its intersection with a second and almost orthogonal signed distance function describes the crack front [83].

When the X-FEM is used to model a strong discontinuity, the crack is embedded within some FE elements, that will distort significantly due to the displacement jump. The X-FEM can also be used to define a stress/strain jump with a continuous displacement. This is relevant for the modeling of inclusions in ductile fracture simulations. In the elements containing the matrix-inclusion interface, i.e., the weak discontinuity, the absolute value of an LS function can be used as enrichment function [84]. More sophisticated approaches for modeling inclusions with the X-FEM have been developed more recently [85].

Enriched FE methods provide the capability of modeling weak and strong discontinuities, i.e., interfaces between two material phases [84] and void-material interfaces [76], as well as stress singularities [79]. These methods can handle branching and intersecting cracks [80], non planar cracks [83] and complex 2D and 3D geometries [86]. These features are relevant for the study of ductile damage.

Yet, most of the literature is dedicated to brittle fracture. Even in works in which ductile materials are the object of study [87], the focus is on the calculation of stress intensity factors and large deformations are not pursued. These methods were conceived precisely to avoid remeshing, which might be necessary if the considerable deformation associated to ductile fracture is to be accounted for, even with an enriched FE formulation.

The practical application of enriched FE formulations is less straightforward than the implementation of its basic techniques; limitations and additional complications arise. Their implementation can be burdensome depending on the structure of the FE code due to the variable number of degrees of freedom that comes with local enrichment [88].

Traditional Gauss quadrature is not adequate for enriched elements. There are different strategies to tackle this problem, but the most common one is subpartitioning of enriched elements, with higher order integration for crack tip elements [76].

In the first X-FEM implementations, topological enrichment was used for the crack tip enrichment, i.e., only those nodes whose support contained the crack tip were enriched. This resulted in a deteriorated order of convergence. To solve this issue, a geometric enrichment was proposed where enrichment is added for all nodes within a distance to the crack tip [89]. Although this improves the convergence rate, the conditioning is deteriorated and the problem size increases [90].

Ill-conditioning can also arise if an element is cut by an interface such that one of the resulting subvolumes is comparatively very small with respect to the other. To alleviate the conditioning problems associated to XFEM, ad hoc preconditioners have been proposed [91].

An additional obstacle to the application of enriched FE methods to ductile fracture problems is related to their application beyond elastic problems. Even though bimaterial interfaces or void-material interfaces can be handled transparently independently of the behavior of the material, crack tip enrichment functions depend on material behavior. Although some developments have been made for elasto-plastic materials [92], their application remains restricted to confined plasticity, and enriching crack tip elements for more advanced material laws remains a considerable challenge.

These drawbacks of X-FEM might deter from its application to ductile fracture problems. Indeed, the number of works that employ it to study ductile fracture is very small with respect to brittle fracture. It should nevertheless not be discarded as it can be applied to model the

fracture of brittle components in ductile materials' microstructures. For instance, the failure of ductile dual phase steels has been studied at the microscale by applying the X-FEM to the brittle martensitic phase [72, 93, 94]. As shown in Figure 2.2, interesting results can be obtained using this approach.

Void nucleation by fracture of brittle components within ductile materials' microstructures can hence be modeled using X-FEM. Enriched FE methods are nevertheless not yet applicable to model the growth of these cracks into large voids.

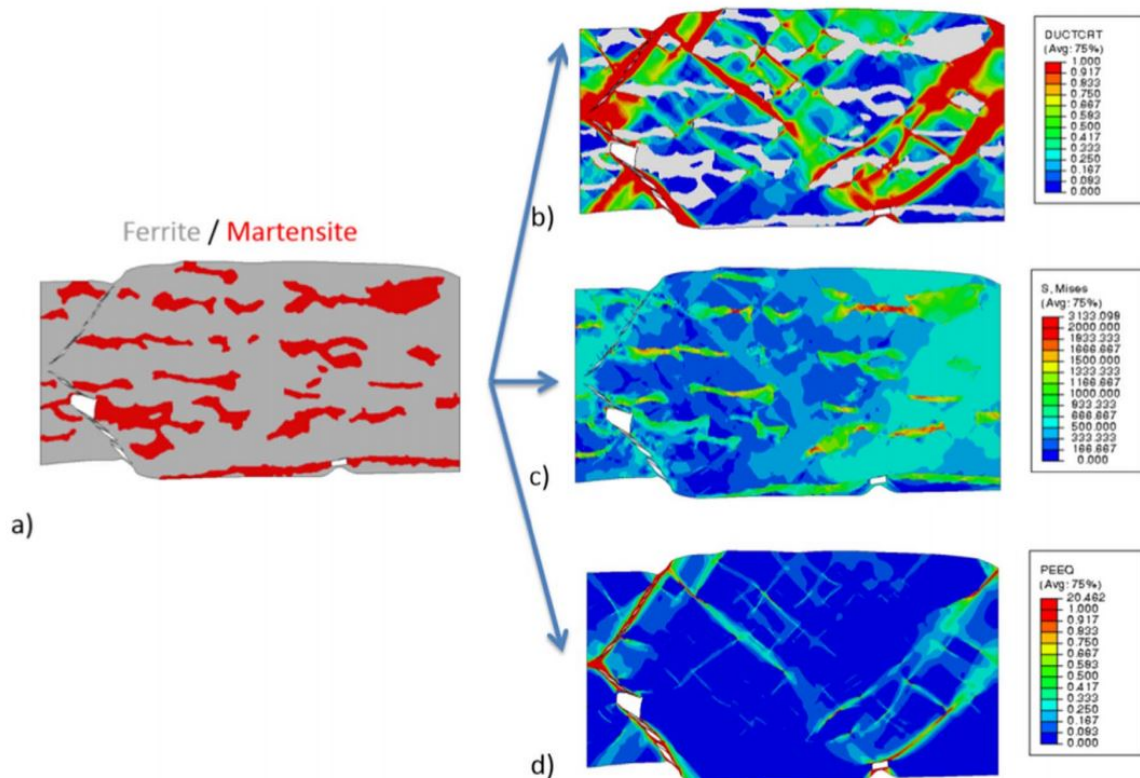


Figure 2.2: Micromechanical simulation of a 2D dual phase steel microstructure showing the ductile fracture of the ferrite phase modeled using element deletion and the brittle failure of the martensite phase modeled using X-FEM. (a) Microstructure with ferrite in gray and martensite in red. (b) Damage variable in ferrite phase. (c) Von Mises stress field. (d) Equivalent plastic strain field. Figure reproduced from [72].

Phase-field method

The phase-field method is based on the notion of diffuse interface proposed by Cahn and Hilliard [95]. In the phase-field method, damage is described with a bulk variable ϕ that takes values from 0 to 1. When $\phi = 0$, the material is completely undamaged and when $\phi = 1$, the material has lost all of its load-bearing capacity. Mathematically, this method consists in the minimization of a potential energy, from which the evolution of the phase-field variable ϕ is derived. A defining feature of the phase-field method is the presence of a characteristic length scale l_c . Discontinuities in the interfaces are smeared out along this characteristic

length. This makes interface-capturing easier to handle, which is an attractive feature of the method. Its ease of implementation is another advantage.

Most of the applications of the method to fracture problems have been dedicated to brittle fracture [96,97]. In a simple application for brittle materials, the minimization functional can be expressed as the superposition of the elastic potential energy and the fracture energy. Since loss of load-bearing capacity occurs only in tension, the elastic potential can be decomposed into a tensile and a compressive component. Minimization of the potential through the Clausius-Duhem inequality results in the means to update the stress state and the phase-field variable. Care must be taken to enforce the irreversibility of the process, i.e., to avoid a decrease of ϕ [98].

Although no variational theory that describes the full complexity of ductile damage has been proposed, some extensions have been put forward [99]. A necessary ingredient for the study of ductile damage with the phase-field approach is the inclusion of the plastic energy in the minimization functional. An inadequate formulation of the plastic energy term can lead to wrong predictions of the onset of damage [100]. This is one difficulty associated to the application of the phase-field method to ductile fracture. Another difficulty is the formulation of a comprehensive functional that takes into account failure mechanisms of ductile damage such as particle fracture and debonding of the matrix-inclusion interface. The method does have the potential to combine different physics into an unified framework. An example is given by the work of Shanthraj et al. [101], who modeled a highly anisotropic polycrystalline metallic material and observed damage nucleate at a triple junction.

Recently, the phase-field method with a voxel-based approach has been successfully used to model the brittle fracture of real concrete heterogeneous microstructures with realistic boundary conditions coming from DVC [102]. The employed framework is able to model crack propagation in the particle-matrix interface [103, 104].

Mesh modification

This section presents a brief bibliographic review of approaches based on mesh modification to model the micromechanisms of ductile damage. The term mesh modification is used here to denote global or local remeshing or global or local adaptive mesh refinement. Only automatic mesh modification methodologies that require no human intervention are considered here. Although challenging, mesh modification approaches are appropriate for modeling ductile damage at the microscale since they are capable of avoiding element inversion [105] associated to large strains, and of dealing with the topological changes of the microstructure.

Mesh adaption consists in locally scaling mesh size with a factor based on an approximation error such as the well known ZZ estimator [106]. The ZZ estimator is an estimation of

the error of the FE solution of a given variable by comparison with a reconstructed higher order approximation of the same variable. A possible technique for the reconstruction of this higher order approximation is the Superconvergent Patch Recovery technique [106,107]. As illustrated by the work of El Khaoulani and Bouchard [108], the use of anisotropic mesh adaption can reduce the mass loss and mesh dependence that results from element deletion. The employed anisotropic mesh adaption strategy used the interpolation error of a damage variable and its gradient [109]. Although these techniques are more common in macroscopic ductile damage applications, there is no reason why they could not be used in microscopic modeling.

A form of mesh adaption that has been employed at the microscale is geometry-based mesh adaption. More specifically, in a first order FE scheme, the principal curvatures of geometric boundaries can be used to calculate a geometric error. The principal curvatures can be obtained from the first and second derivatives of the distance functions that describe the geometry [52,110]. If this methodology is used to model cracks, a minimum mesh size needs to be prescribed in the crack tip region to limit refinement since one of the principal curvatures is guaranteed to be infinite [111]. Isotropic and anisotropic mesh adaption are possible with this methodology.

Mesh adaption techniques are attractive to model microstructures with inclusions and voids since the computational cost can be considerably reduced with respect to a uniform mesh. One important aspect that demands consideration is the treatment of the interfaces. Mesh adaption techniques do not handle interfaces as naturally as the enriched FE methods. Distance functions have been used to describe interfaces [110,111]. The zero isovalue of the distance function indicates the position of the interface. In the general case, elements will be crossed by the interface. To deal with this complication, the most common approach is to use a mixing or transition law in these elements to attribute them values of the mechanical properties. An additional complication is volume conservation, which is more critical in large strains. If acceptable volume conservation is to be achieved, the mesh must be refined severely at interfaces.

These complications can be avoided if the FE mesh is conform to the interfaces. An early example is the work of Antretter and Fischer [112], who modeled a two-phase composite at the microscale. Their two-dimensional model included two brittle inclusions, one of which was initially fragmented. The propagation of this crack onto the matrix followed a predefined path. Arbitrary crack paths require robust mesh modification operations.

Shortly after, a remeshing technique for crack propagation was proposed by Bouchard et al. [113]. The crack was advanced a given length at each load with a stress based crack initiation and propagation criterion. Mid-side nodes were used to represent the stress singularity at the crack tip. Global remeshing of the domain was carried out after each propagation step. A similar approach was followed by Mediavilla et al. [71], who paid special attention to field

transfer. In this methodology, the crack was first inserted in the FE mesh without any opening. An appropriate field operator was then applied to history variables. The crack nodes were finally duplicated and the strain and stress fields were recalculated. The objective of these procedures is to ensure mechanical equilibrium and avoid energy diffusion during crack propagation. An application of this methodology in a compact tension specimen is depicted in Figure 2.3. This work illustrates a general difficulty of mesh modification methodologies: consistent field transfer.

The framework of Mediavilla et al. [71] was extended to 3D by Javani et al. [114]. Cracks are inserted following a non-local damage field. The evolution of the crack geometry is dictated by the damage field at the crack tip. Global frequent remeshing occurs during crack initiation and propagation. An application is shown in Figure 2.4 for a three-dimensional double notched specimen. Feld-Payet et al. [115] proposed a crack path tracking algorithm that extends this methodology to arbitrarily branching cracks according to a scalar variable.

The discussed crack propagation approaches so far require global remeshing. This can be very expensive even if mesh adaption is used. In this situation, local mesh refinement would be desirable. A methodology for crack propagation in two-dimensional triangular meshes with local mesh refinement was proposed by Areias et al. [116]. Arbitrary crack propagation is possible thanks to an arbitrary mesh splitting methodology. To achieve this, edge and node splitting is carried out and followed by node repositioning to improve the quality of the modified elements. This approach is also able to handle crack or void coalescence.

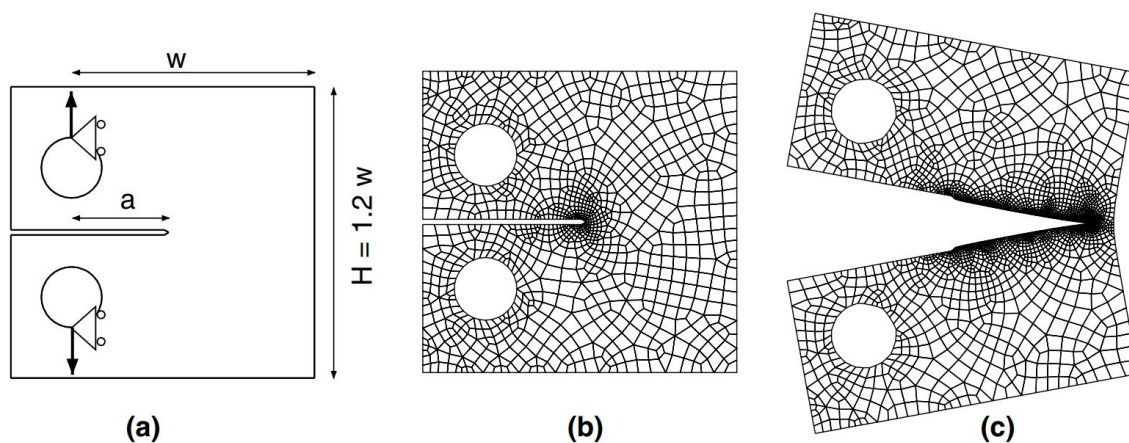


Figure 2.3: Crack propagation in compact tension test. (a) Dimensions and boundary conditions, (b) initial configuration and (c) final configuration. Figure reproduced from [71].

A different way to address the aforementioned drawbacks of the approach proposed by Roux et al. [110, 111] was proposed by Shakoor et al. [52]. This approach consists in local remeshing operations able to dynamically construct explicit interfaces in a monolithic framework. Mixing laws are thus avoided and volume conservation dramatically improved. Two-dimensional void coalescence and micro-cracking of inclusions were modeled with this framework. Further developments later allowed three-dimensional simulations to be carried

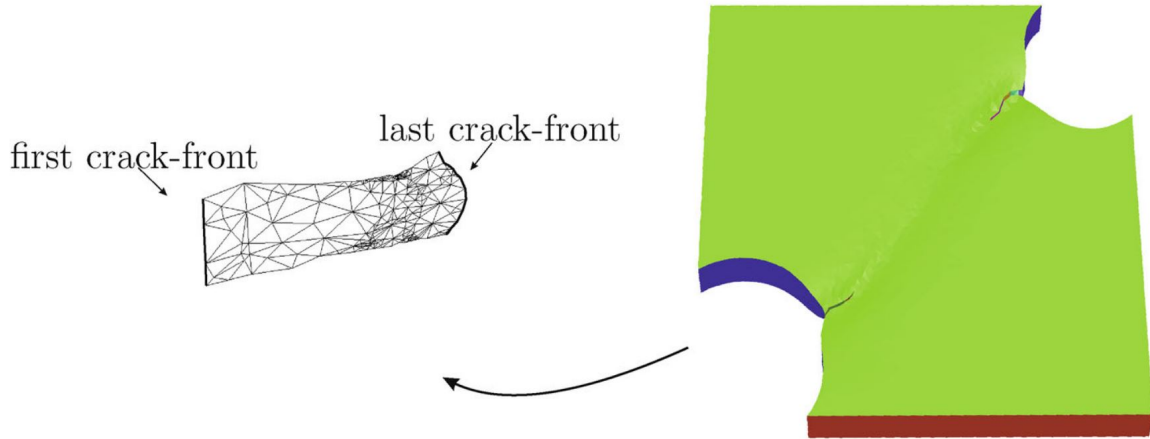


Figure 2.4: Crack surface corresponding to the bottom notch of a double notched specimen. Figure reproduced from [114].

out with particle fragmentation and debonding as well as plasticity driven void growth and coalescence [117]. An example of the capabilities of this framework is shown in Figure 2.5 in a micromechanical simulation of a metal matrix composite with void nucleation by particle debonding and fragmentation, growth and coalescence are taking into account.

Mesh modification techniques are a promising approach for the micromechanical study of ductile damage. The developments in this area have been steadily increasing the capabilities of mesh modification techniques. Most studies are limited to two-dimensional applications, but three-dimensional applications are becoming more common. Linear tetrahedral elements have proved easier to handle than hexahedral elements or higher order elements. The main hindering factor is the difficulty of implementation of these techniques. Although challenging, they are appropriate for managing the large strains and complex topological changes that manifest in the micromechanisms of ductile damage.

2.2 Material and methodology

2.2.1 Nodular cast iron

The main material studied in this work is nodular cast iron or spheroidal graphite. Namely, a commercial nodular graphite cast iron with commercial code EN-GJS-400, is studied. This carbon-rich iron alloy is used in many engineering applications such as gearboxes, crankshafts, pipes and nuclear or transportation casks [118, 119]. It is used in the transport industry for railway wheels [120], for example, and in the energy industry for an important number of wind turbine parts [121]. The capability to predict its failure is thus of practical importance.

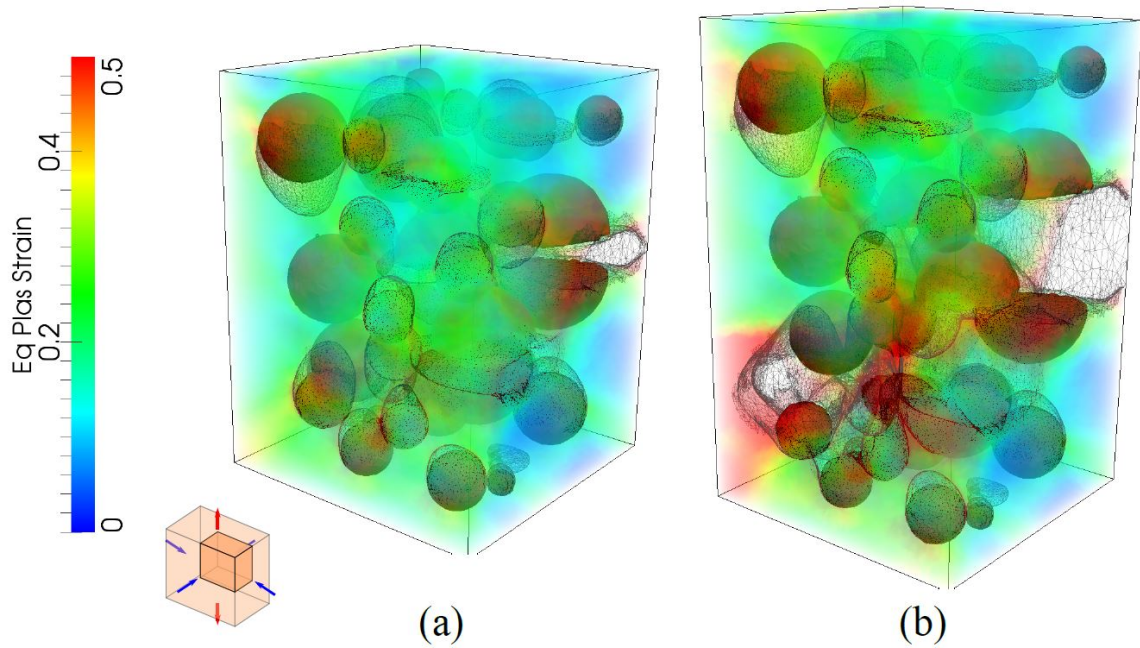


Figure 2.5: Micromechanical simulation of a metal matrix composite with void nucleation by particle debonding and fragmentation, growth and coalescence for an applied tensile strain of (a) 25% and (b) 50%. Figure reproduced from [6].

As opposed to gray cast iron, it is considerably ductile, which is why it is also referred to as ductile cast iron. The reason for its ductility is its microstructure. Instead of lamellar graphite as in classical cast iron, the graphite is present in the form of approximately spherical nodules. This results in increased strength and toughness similar to some grades of steel. The graphite volume fraction varies from 7% to 15% and have a diameter between $10 \mu\text{m}$ and $15 \mu\text{m}$ [119]. Figure 2.6 shows three different types of nodular cast iron: ferritic, ferritic-pearlitic, and pearlitic. Only ferritic cast iron is studied in this work.

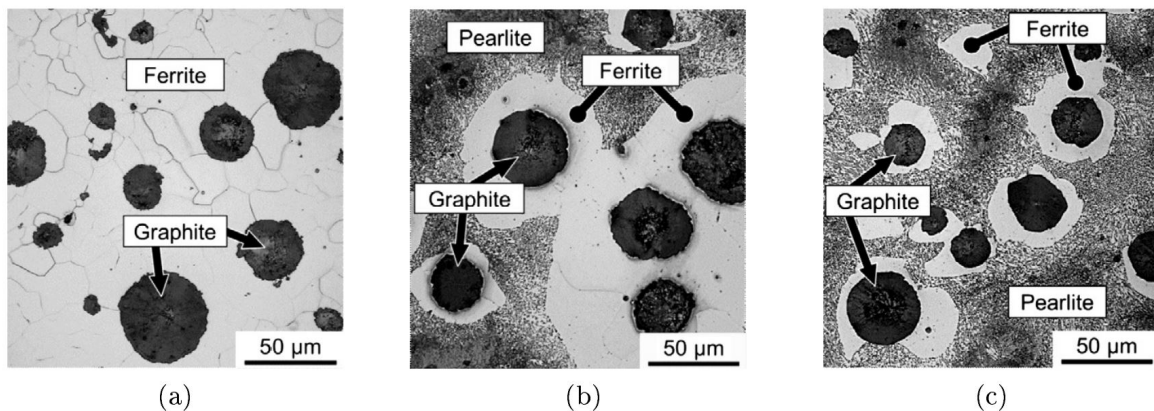


Figure 2.6: Microstructures of different kinds of nodular cast iron. (a) Ferritic microstructure. (b) Ferritic-pearlitic microstructure. (c) Pearlitic microstructure. Figure reproduced from [122].

Under monotonic static loading, debonding of the matrix-nodules interface is observed

as soon as plastic activity starts [123]. Plasticity-driven void growth is observed with further straining. In a ferritic nodular cast iron, the prevailing mechanism of coalescence is internal necking, although local void sheeting events have been identified [123]. A secondary population of voids also intervenes in the coalescence process [123, 124].

Several studies have approached nodular cast iron with unit-cell models [125–132]. In some of these studies, the graphite was modeled as void [125–128]. The conclusions of these studies regarding the effect of stress triaxiality on void shape evolution and growth, coincide with the trends observed for materials with considerably smaller void fraction [133]. This encouraged the use of the GTN model for nodular cast iron, which was often calibrated with the results of the uni-cell calculations.

Uniform and non-uniform void distributions were studied by Zhang et al. [128] with the unit-cell approach. Void size and spacing were found to influence void growth and coalescence. The effect of the graphite on the fracture process has also been assessed. No remarkable difference was observed when deformation was not enough to reach the void coalescence stage [130]. When the unit cells are deformed further, however, a considerable effect of the graphite inclusions on void coalescence is observed [125]. After sufficient deformation, lateral contraction of the voids is hindered by the particles and earlier coalescence results through necking of the matrix.

A few studies have assessed the effect of the secondary voids on the fracture process. Brocks et al. [125] did not find a noticeable effect, while Kuna and Sun [126] observed that coalescence between the primary voids occurred earlier in the presence of secondary voids. After studying side effects due to secondary voids in ductile crack propagation, Hütter et al. [134] highlighted the need for simulations with more realistic microstructures. Scanning Electron Microscope (SEM) observations of the fracture surface of the nodular cast iron studied in this work have confirmed the presence of a population of secondary voids [123].

2.2.2 General methodology

In the framework of the COMINSIDE project, an experimental-numerical framework was recently developed to study ductile fracture at the microscale. It is composed of three key techniques. First, three-dimensional images of specimens under load are acquired *in-situ* via Synchrotron Radiation Computed Laminography (SRCL) [135]. Second, Digital Volume Correlation (DVC) [136] enables kinematic data to be measured from the registration of SRCL images. Last, Finite Element (FE) simulations with advanced meshing/remeshing techniques [117] are carried out on immersed microstructures and realistic boundary conditions extracted from SRCL images via DVC analyses. Details about these three techniques are given in the following sections. This framework will be referred to as SRCL-DVC-FE and constitutes the main methodology of the present work. A simple scheme of the SRCL-DVC-

FE methodology is depicted in Figure 2.7

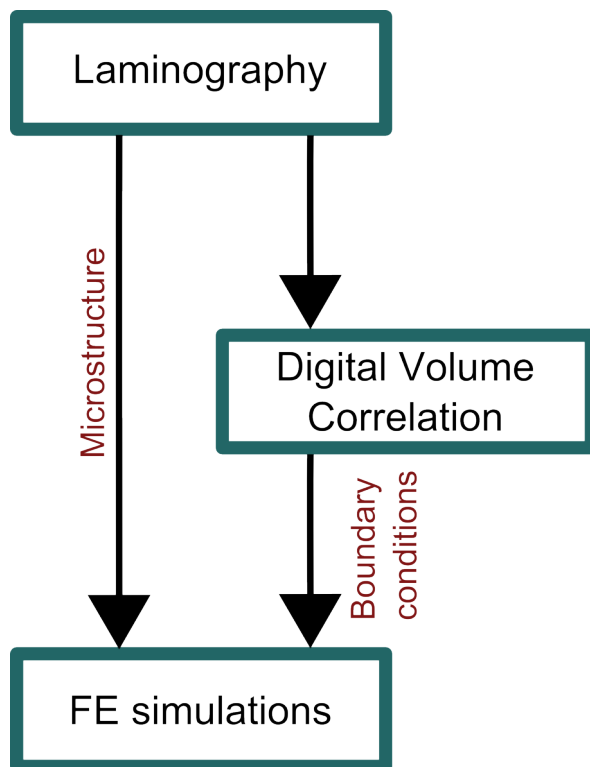


Figure 2.7: A simple scheme of the SRCL-DVC-FE methodology.

Laminography

Laminography is a non-destructive three-dimensional X-ray imaging technique for flat, laterally extended objects [135]. Soon after the discovery of X-ray radiation, medical [137] and non-medical [138] applications soon appeared [139]. During an X-ray computed tomography scan, X-rays are directed from an X-ray source, go through the scanned object and reach an X-ray sensor. Three-dimensional images can be obtained if multiple scans at different angles are performed. To obtain the final three-dimensional image from these scans, a technique called reconstruction is required [140].

The X-ray absorption of a material dictates how easy it is for X-rays to penetrate this material. Metals present high X-ray absorption. For this reason, high energy sources are employed. This also limits the geometries that can be used for observation. Round tensile experiments with a radius of approximately 1 *mm* are usually employed. Laminography allows this limitation to be partially overcome and other stress states to be accessed [3, 141, 142]. Experimental setups for tomography and laminography are schematized in Figure 2.8.

The achievable spatial resolution with tomography and laminography is in the micrometer scale. Although this resolution is lower than the resolution achievable with Scanning Electron Microscopy, it is enough to provide three-dimensional details of the micromechanisms of

ductile damage in combination with in-situ tests.

Very detailed experimental information at the microscale have been made available thanks to three-dimensional non-destructive imaging. Tomography [143,144] and laminography [135, 145] provide unprecedented detail on the evolution of the micromechanisms of ductile damage.

In this work, reconstructed three-dimensional volumes originated during in-situ mechanical tests of nodular cast iron specimens, are used. This data had been obtained at beamline ID16 of the European Synchrotron Radiation Facility (ESRF).

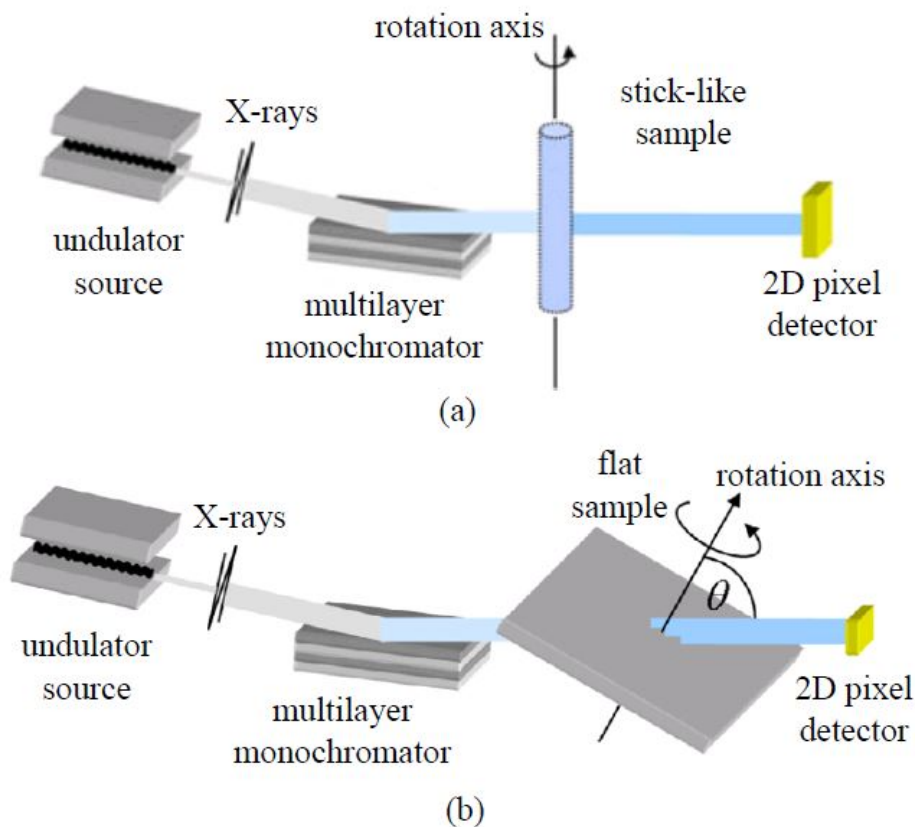


Figure 2.8: Schematic representations of experimental setup for (a) tomography and (b) laminography. Figures reproduced from [136] and [146], respectively.

Digital volume correlation

In Digital Image Correlation (DIC), a succession of two-dimensional images of the surface of a specimen during a mechanical test are used to obtain the kinematic field at the surface through a minimization problem that relates successive images. This is a widely used technique for identification of material properties [147, 148]. Digital Volume Correlation (DVC) constitutes the extension of this technique to 3D [149, 150].

Grayscale images are used in this project. In this type of image, each voxel presents a

gray scale value that positions it in the scale from black to white. If the difference between two grayscale images is calculated, the gray level residuals are obtained. If two images are identical, the gray level residuals will be zero. DVC consists in finding the displacement field $\mathbf{u}(\mathbf{x})$ that minimizes the gray level residuals $\rho(\mathbf{x})$ between the reference configuration f and the deformed configuration g :

$$\rho(\mathbf{x}) = f(\mathbf{x}) - g[\mathbf{x} + \mathbf{u}(\mathbf{x})]. \quad (2.17)$$

In DIC, the surface of the specimen is speckled to enhance contrast and facilitate the residual minimization procedure. This is not possible in the bulk material for DVC. Instead, the natural contrast provided by the microstructural heterogeneities must be used. This has an impact on the spatial resolution of the solution. If the DVC element is too small, the problem becomes ill-defined. This is illustrated by the relationship between element size and strain uncertainty. When the element size decreases, the strain uncertainty increases [142]. A high volume fraction of microstructural heterogeneities, such as in nodular cast iron, favors contrast and convergence of DVC calculations. Other measures may be taken to favor convergence, such as mechanical regularisation in which resulting kinematic fields are required to comply with mechanical admissibility [151]. DVC analyses have been successful in an aluminum alloy with a very low content of inclusions [136].

The first DVC analyses were local in nature [152]. This means that local kinematic fields could be calculated with local information. If the kinematic degrees of freedom are considered to be spatially coupled, the problem becomes a global minimization problem. This is referred to as global DVC [153] and facilitates the minimization procedure by imposing displacement continuity.

In this work, data resulting from global DVC analysis of laminography images, are used. High strain gradients and displacement discontinuities such as that manifest in the micro-mechanisms of ductile damage are challenging for DVC and require special attention. For more details, the reader can refer to the review by Buljac et al. [150].

Finite elements

The finite element method [154, 155] is used here to model ductile damage at the microscale with a monolithic multiphase framework in the CimLib library [156]. The term monolithic refers to the solution of the governing equations with a single mesh and a global framework for all of the present phases. Small deformation theory is used with an additive decomposition of the strain tensor for elasto-plasticity. This section summarizes the used Lagrangian framework.

Governing equations

The governing equations in the mechanical problem are the conservation of momentum and the conservation of mass. The conservation of momentum can be written as:

$$\rho \frac{D\mathbf{v}}{Dt} = \nabla \cdot \boldsymbol{\sigma} + \mathbf{f}, \quad (2.18)$$

where ρ is the density of the material, v the velocity, $\frac{D\mathbf{v}}{Dt}$ its material derivative, $\boldsymbol{\sigma}$ the Cauchy stress tensor and \mathbf{f} the volume forces. Mass conservation can be expressed as:

$$\frac{\partial \rho}{\partial t} + \nabla \cdot (\rho \mathbf{v}) = 0. \quad (2.19)$$

Appropriate boundary conditions on the boundary $\Gamma = \Gamma_v \cup \Gamma_t$ of the domain Ω for the velocity and the stress tensor, must be used:

$$\mathbf{v} = \mathbf{v}_{app} \text{ on } \Gamma_v, \quad (2.20)$$

$$\boldsymbol{\sigma} \mathbf{n} = \mathbf{t}_{app} \text{ on } \Gamma_t, \quad (2.21)$$

where \mathbf{t}_{app} is the traction vector \mathbf{t} on boundary Γ_t .

If inertia is neglected and the deformation can be described as quasi-static, and if volume forces are negligible, the conservation of momentum can be reduced to:

$$\nabla \cdot \boldsymbol{\sigma} = \mathbf{0}. \quad (2.22)$$

The Cauchy stress tensor can be decomposed into its deviatoric and spherical components. After this decomposition, the conservation of momentum can be re-expressed as:

$$\nabla \cdot \mathbf{S} - \nabla p = \mathbf{0}, \quad (2.23)$$

where p is the pressure and \mathbf{S} the deviatoric stress tensor.

It is possible to express the continuity equation explicitly in terms of the pressure by

introducing the bulk modulus χ :

$$\chi = \rho \frac{\partial p}{\partial \rho}. \quad (2.24)$$

In a Lagrangian framework, after dropping the advection term, introducing the bulk modulus, and expressing the divergence of the velocity as the trace of the strain rate tensor $\dot{\boldsymbol{\varepsilon}}$, the mass conservation equation can be expressed as:

$$\text{tr}(\dot{\boldsymbol{\varepsilon}}) + \frac{1}{\chi} \frac{\partial p}{\partial t} = 0. \quad (2.25)$$

Weak formulation

The FE method provides approximate solution of the governing equations. Their weak form can be obtained by multiplying the equations by test functions $v^* \in V$ and $p^* \in P$ where V and P are appropriate functional spaces given by:

$$\begin{cases} V = \{\mathbf{v}, \mathbf{v} \in H^1(\Omega)^d | \mathbf{v} = \mathbf{v}_{app} \text{ on } \Gamma_v\}, \\ V_0 = \{\mathbf{v}, \mathbf{v} \in H^1(\Omega)^d | \mathbf{v} = 0 \text{ on } \Gamma_v\}, \\ P = \{p, p \in L^2(\Omega)\}, \end{cases} \quad (2.26)$$

where d is the space dimension, V the space of kinematically admissible velocity fields and V_0 the space of kinematically admissible velocity fields to zero. Integration over the volume of the domain Ω and the use of the Green formula yields the associated variational problem: find $(v, p) \in (V, P)$ such that $\forall (v^*, p^*) \in (V_0, P)$:

$$\begin{cases} \int_{\Omega} \mathbf{S}(\mathbf{v}) : \dot{\boldsymbol{\varepsilon}} d\Omega - \int_{\Omega} p \cdot \nabla \mathbf{v}^* d\Omega - \int_{\Gamma} \mathbf{t} \cdot \mathbf{v}^* d\Gamma = 0, \\ \int_{\Omega} \left(\text{tr}(\dot{\boldsymbol{\varepsilon}}) + \frac{1}{\chi} \frac{\partial p}{\partial t} \right) p^* d\Omega = 0. \end{cases} \quad (2.27)$$

An implicit Euler scheme is used. The domain Ω is discretized in the following way:

$$\Omega_h = \bigcup_{K \in \mathcal{T}_h(\Omega)} K, \quad (2.28)$$

where Ω_h is a discretization of the domain Ω , $\mathcal{T}_h(\Omega)$ a finite element mesh of the domain Ω , K a simplex of a given mesh size h .

In order to apply the finite element approach, vector spaces of finite dimensions V_h and P_h close to the continuous spaces V and P of infinite dimension, such that the discrete solution $(v_h, p_h) \in (V_h, P_h)$ approximates the solution of the continuous problem $(v, p) \in (V, P)$.

The existence and uniqueness of the solution depends on the choice of the space functions V_h and P_h . In particular, they have to satisfy the Brezzi Babuska stability conditions [157]. The MINI element or bubble element is used [158]. This tetrahedral element provides an approximation of the pressure in P1 space. An enriched P1 space or P1⁺ space is used to approximate the velocity. In the P⁺ space, besides the 4 basis linear functions (in 3D), an extra basis function contributes to the approximation. This additional basis function is equal to one in the center of the element and equal to zero in all of the nodes. This introduces an additional degree of freedom with an additional unknown. The calculation of the introduced unknown can be avoided if static condensation is carried out [159]. The Newton-Raphson method is used to solve the global problem and the return mapping algorithm is used at the element level of the integration of the behavior law [160].

Mesh adaption

A specific body-fitted mesh adaption strategy was developed [52] to mesh heterogeneous microstructures with conform meshes at interfaces. The position of an interface is described by the zero isovalue of a signed distance function ψ . To perform element splitting, the cut-cell method is used [161]. The intersection of the interface with an edge of the mesh is detected when there is a change of sign of the distance function at the nodes connected by the edge. Linear interpolation allows the intersection point to be obtained. In the parallel implementation of this methodology, each process operates independently and the inter-partition boundaries are not modified. In a second step, repartitioning is performed in order to deal with unfitted elements [162].

Since the fitting methodology can produce bad quality elements, a star-connecting optimization process is carried out. Figure 2.9 schematizes some of the operations included in the star-connection procedure. To preserve the internal boundaries, node creation, node deletion and star-reconnection are constrained when faces that carry the interfaces are operated upon. Special care is taken to conserve the volume of the phases present in a patch. A good compromise between volume conservation and element quality is the objective of these considerations [117].

Isotropic or anisotropic [163] mesh adaption may be combined with the interface-fitting procedure [52]. In this work, isotropic adaption with respect to the maximum principal curvature λ_{max} is used. In this case, the isotropic metric \mathbf{M} can be constructed as follows:

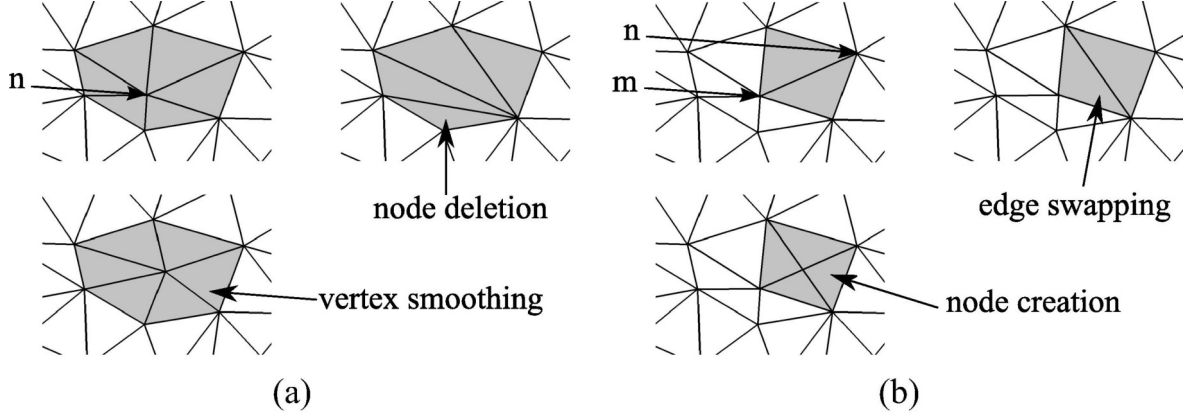


Figure 2.9: Some examples of operations included in the star-connecting procedure. Figure reproduced from [52].

$$\mathbf{M} = \text{diag} \left(\frac{1}{h^2} \right), \quad (2.29)$$

where h is the mesh size. The mesh size can be expressed as a function of the curvature as follows:

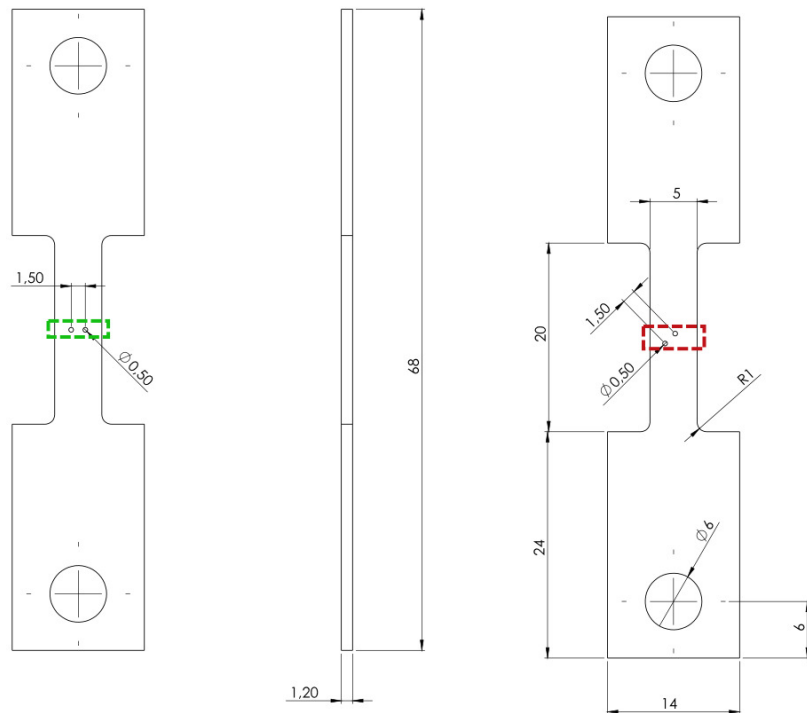
$$h = \max \left(\min \left(\frac{h_c}{\lambda_{max}} + \left(h_{max} - \frac{h_c}{\lambda_{max}} \right) \frac{\phi}{\epsilon_h}, h_{max} \right), h_{min} \right), \quad (2.30)$$

where h_c corresponds to the mesh size that would be imposed if $\lambda_{max} = 1$, h_{min} and h_{max} are the smallest and largest allowed mesh sizes respectively, ϕ the distance function of the interface, and ϵ_h a fixed user-controlled thickness along which the mesh size varies linearly from $\frac{h_c}{\lambda_{max}}$ to h_{max} .

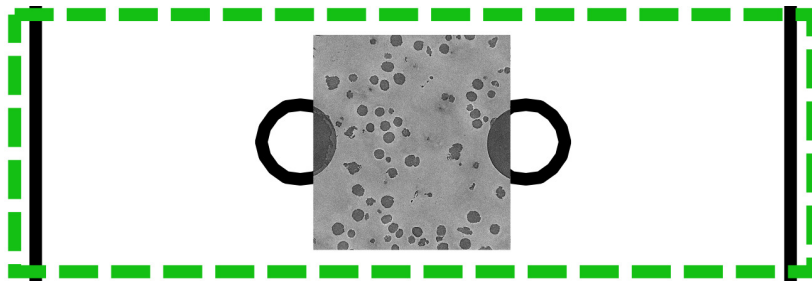
2.2.3 Studied specimens

Nodular cast iron presents a high volume fraction of graphite nodules, which makes it attractive for DVC. DVC relies on contrast of the SRCL images due to microstructural heterogeneities, which is provided by the difference of density between the graphite nodules and the ferritic matrix.

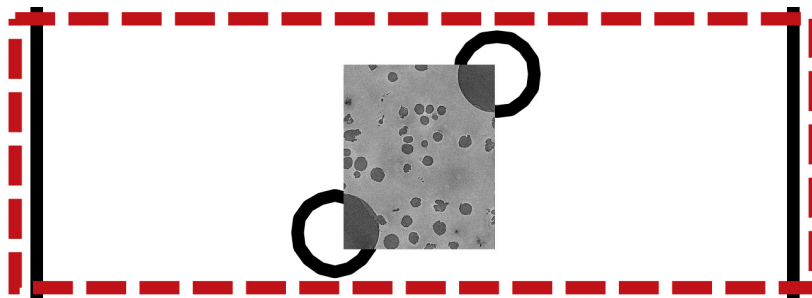
Two different nodular cast iron specimens that were previously studied [123] are considered in this work. Each of them contains two holes with a diameter of $500 \mu\text{m}$ that were machined by Electrical Discharge Machining (EDM). The ligament connecting the centers of these two holes forms an angle of 90° with the loading direction in the first geometry, and 45° in the second geometry. The geometries of the specimens are shown in Figure 2.10



(a)



(b)



(c)

Figure 2.10: (a) Geometry of the two studied specimens and zoom around the scanned zone for the (b) 90° and (c) 45° specimens.

2.2.4 Microstructure immersion

The immersion of the microstructures of the laminography images in the FE mesh comprises the following stages:

- Image processing and segmentation is carried out, i.e., each voxel is assigned a physical phase based on its gray level and possibly other topological information.
- A signed distance function to the interfaces is calculated in the image.
- The distance function is interpolated onto the FE mesh through trilinear interpolation.
- Direct reinitialization of the distance function is carried out [164].
- A FE mesh is generated.

Figure 2.11 illustrates this procedure.

2.2.5 Mechanical behavior

The ferritic matrix is considered to be elastoplastic with Ludwik’s isotropic hardening law:

$$\sigma_{eq} = \sigma_y + K\varepsilon_{pl}^n, \quad (2.31)$$

where σ_{eq} is the von Mises equivalent stress, ε_{pl} the cumulated plastic equivalent strain, σ_y the yield stress, K the hardening modulus and n the hardening exponent. The employed values for the Young’s modulus E , and Poisson’s ratio ν were $E = 210$ GPa, and $\nu = 0.3$. The values for σ_y , K , and n were previously calibrated at the microscale by means of X-ray microtomography, DVC, and FE simulations [165]. The scheme in Figure 2.12 presents the parameter identification methodology in detail. The values obtained through this procedure were $\sigma_y = 245$ MPa, $K = 330$ MPa, and $n = 0.21$.

Since the graphite nodules present very early debonding and have a very low load-bearing capacity [119, 166], they will be considered as voids in the FE simulations. The term ‘void’ will thus be used to refer to the volume corresponding to the nodules and actual voids. This hypothesis has been adopted and validated previously [9] and will be discussed during this work. The void phase is modeled as a compressible Newtonian fluid with viscosity $\eta = 2.1$ MPa s⁻¹. This viscosity value is chosen after a sensitivity analysis to ensure that the stress levels induced in the matrix are negligible. This approach facilitates handling the void phase in the present monolithic framework [110].

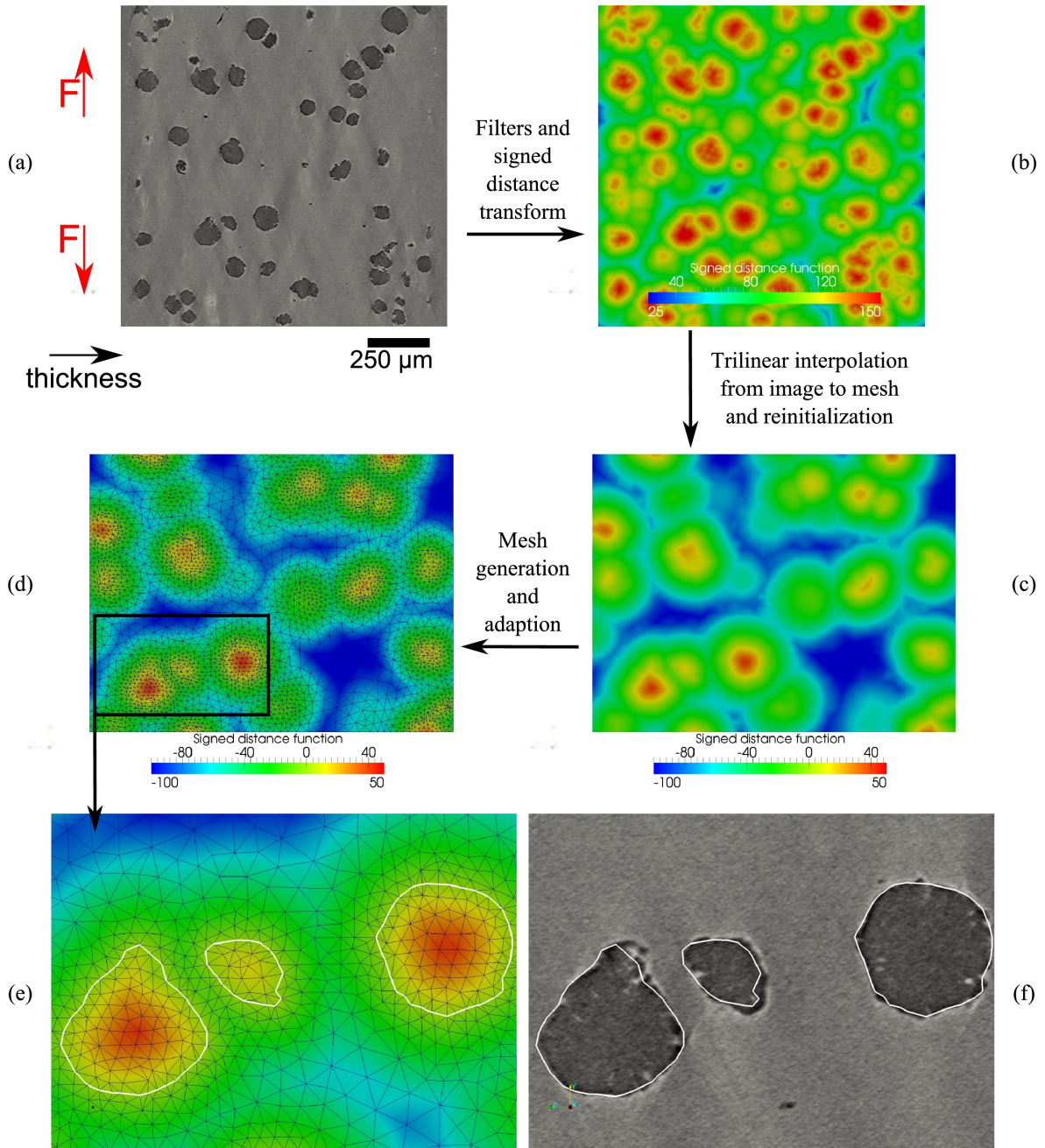


Figure 2.11: Immersion of the microstructure in the FE mesh. (a) Two-dimensional section of laminography image. (b) Signed distance function. (c) Signed distance function after interpolation on the FE mesh. (d) Interface-fitted FE mesh adapted to the local maximum curvature. (e) Zoom on the FE mesh. (f) Comparison between original image and obtained interface in the FE mesh. Figure adapted from [10].

The FE domain is contained in the Region Of Interest (ROI) analyzed via DVC. This is done so to ensure that boundary conditions are available during the whole simulation. The largest domain that provides boundary conditions for all of the available DVC increments, is chosen.

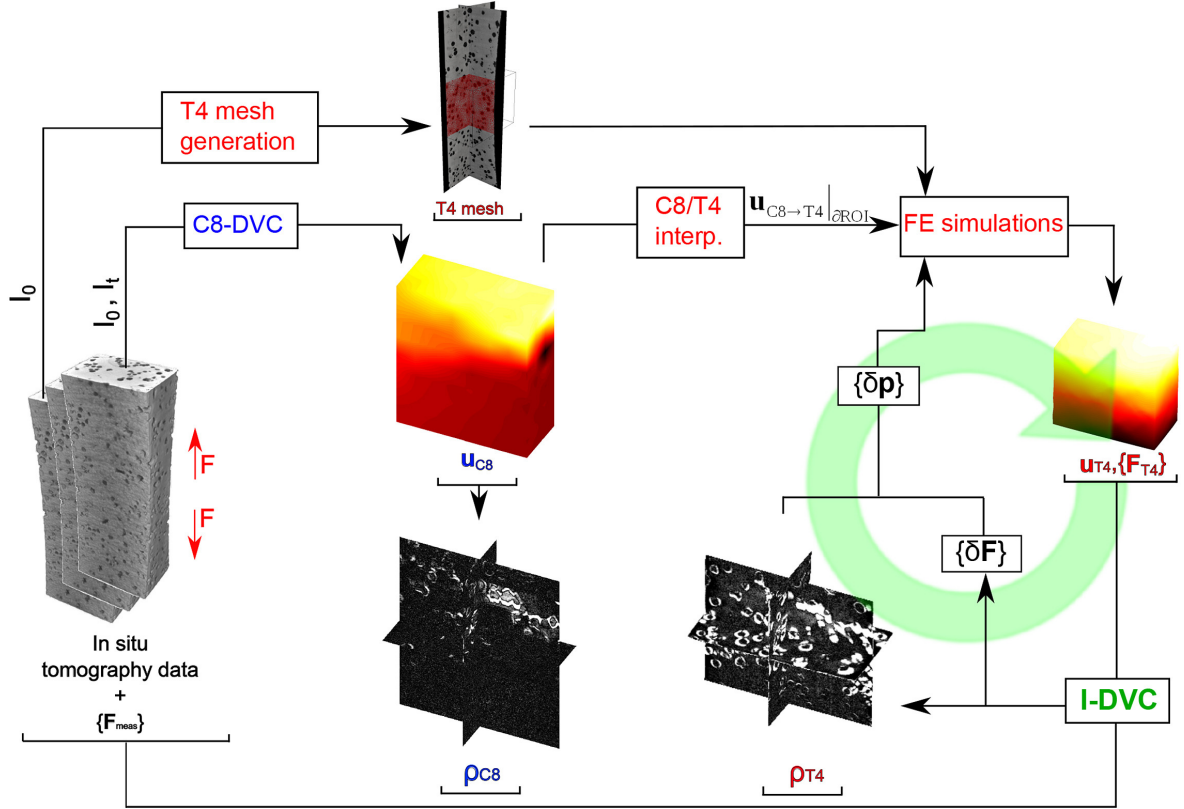


Figure 2.12: Scheme presenting the methodology for parameter identification at the microscale. Global DVC with 8-noded elements is carried out on a series of volumes I_t to obtain kinematic information based on the reference configuration I_0 . The resulting gray level residuals ρ_{C8} and displacements u_{C8} are interpolated on a FE mesh of 4-noded tetrahedra. FE simulations with a set of parameters p are performed. The resulting displacement field u_{T4} and reaction forces F_{T4} are used to compute global equilibrium residuals δF and local gray level residuals ρ_{T4} . Figure adapted from [165].

2.2.6 Boundary conditions

The DVC analysis produces three dimensional displacement fields. These heterogeneous displacement fields are interpolated onto the border of the FE domain and applied as Dirichlet boundary conditions at each loading step [10]. Each loading step constitutes an increment for the FE simulations. A manual testing device is used to apply a displacement via screw rotation. The corresponding screw displacements are summarized in Table 2.1.

2.2.7 Closing comments

In this PhD work, improvements to the SRCL-DVC-FE framework were developed in order to enhance the automatic analysis of void nucleation, growth and coalescence.

Three-dimensional simulations of realistic microstructures are undoubtedly a rich source

Table 2.1: Screw displacement applied to each of the specimens.

Increment	Screw displacement [μm]	
	45° specimen	90° specimen
0	0	0
1	248	186
2	372	248
3	496	289
4	620	330
5	744	372
6	868	413
7	992	454
8	1074	496
9	1136	537
10	1198	578
11	1260	599
12	-	620
13	-	641
14	-	661
15	-	682
16	-	703
17	-	722
18	-	744
19	-	765

of information. This information is not necessarily easy to extract, however. To facilitate this task, the postprocessing capabilities of the CimLib library were extended. One initial limitation was that it was not possible to obtain information of particular microstructural feature such as a single void or particle. The use of a single level-set function per phase and frequent remeshing complicated this task. This first limitation was removed with developments carried out during this PhD work, which made it possible, for example, to follow the evolution of the void volume of a single void or the average equivalent stress in a particle up to the end of the simulation. An additional difficulty came up later when topological changes such as coalescence occurred. A coalescence detection technique was implemented to overcome this difficulty.

Although the framework was already able to handle the evolution of ductile damage from void nucleation to coalescence, a problem was identified when nucleation occurred in multiple particles simultaneously in the same strain increment. The consequence of this problem were non-deterministic results of the simulations. Different nucleation patterns were obtained each time the same simulations was run. The cause of this problem was identified and was related to remeshing after nucleation in parallel computations. The solution of this problem required complete reformulation of the model that manages void nucleation. With this development, deterministic nucleation patterns were obtained.

In the study of void coalescence, additional developments were necessary to evaluate different variables in the intervoid ligaments of each void pair present in the simulations in an automatic and efficient manner. These are used in Chapters 5 and 6.

Since this is a recent framework, it is important to make sure that the possible uncertainties present in all of the stages of the methodology are small enough. The uncertainty associated to image segmentation is analyzed and quantified in Chapter 3. The capabilities of the model are validated in Chapter 4 through a detailed comparison with DVC results for local strain measurements all the way up to coalescence.

Résumé en français

Ce chapitre présente une revue bibliographique et la méthodologie générale suivie dans ce travail.

La revue bibliographique couvre la modélisation numérique de l'endommagement ductile à l'échelle macroscopique et microscopique, ainsi que des techniques numériques permettant de modéliser l'endommagement ductile à l'échelle microscopique.

La modélisation à l'échelle macroscopique de l'endommagement ductile peut être classée en deux catégories principales : les critères de rupture non couplés et les modèles d'endommagement couplés. Les modèles de chaque catégorie peuvent être phénoménologiques ou avoir des bases physiques. Les critères de rupture non couplés négligent l'adoucissement du matériau. Dans cette approche, un paramètre d'endommagement est calculé comme l'intégrale d'une fonction de l'état de contrainte le long du chemin de déformation. La rupture survient lorsque ce paramètre atteint un seuil critique.

Concernant les modèles couplés, deux modèles très populaires ont été présentés et discutés : les modèles de Lemaitre et de Gurson. Le premier est phénoménologique et s'appuie sur des bases thermodynamiques tandis que le second repose sur les micromécanismes d'endommagement ductile. Tous deux ont fait l'objet de plusieurs extensions heuristiques pour améliorer leurs capacités prédictives.

Les approches à l'échelle microscopique ont été présentées par ordre croissant de complexité en termes de modélisation réaliste de la microstructure, en commençant par l'approche « unit-cell » pour terminer par des microstructures réalistes et entièrement tridimensionnelles. Les approches les plus courantes de modélisation de la coalescence à l'échelle microscopique ont été présentées en mettant l'accent sur le modèle de Thomason.

Quatre techniques numériques différentes de modélisation de l'endommagement ductile à l'échelle microscopique ont été décrites et leurs avantages et inconvénients ont été discutés.

Ces techniques sont l'érosion d'éléments, les méthodes d'éléments finis étendus, la méthode de champ de phase et l'approche basée sur l'adaptation de maillage et le remaillage automatique.

La méthodologie principale, développée dans le cadre du projet COMINSIDE, est composée de trois techniques clés. Premièrement, les images tridimensionnelles des spécimens sous charge sont acquises in situ par laminographie sous rayonnement synchrotron (SRCL). Deuxièmement, la corrélation d'images volumiques (DVC) permet de mesurer les données cinématiques à partir de l'enregistrement des images SRCL. Enfin, des simulations par éléments finis (FE) utilisant des techniques avancées de maillage et remaillage sont effectuées sur des microstructures immergées et des conditions limites réalistes extraites d'images SRCL via des analyses DVC. Cette méthodologie a été appliquée principalement à la fonte à graphite sphéroïdal, un alliage de fer riche en carbone utilisé dans plusieurs applications d'ingénierie.

Chapter 3

A comparative study of image segmentation methods for micromechanical simulations of ductile damage

Contents

3.1	Introduction	46
3.2	Methodology	47
3.2.1	Image segmentation	47
3.2.2	Observables	56
3.3	Results	57
3.3.1	Mesh sensitivity analysis	57
3.3.2	Model cross comparison	66
3.3.3	Comparison of segmentation methods	69
3.3.4	Uncertainty quantification	78
3.4	Conclusions and perspectives	80

3.1 Introduction

Micromechanical simulations based on three-dimensional imaging techniques are becoming more common to study the behavior of heterogeneous microstructures [9, 10, 54, 55, 165]. In the context of ductile damage, this route enhances the possibilities for studying the corresponding micromechanisms (*i.e.*, void nucleation, growth, and coalescence). With the coupling of imaging techniques and numerical simulations, new challenges arise. One of them is to define an accurate and efficient technique for image segmentation, namely, determining to which physical phase each of the voxels belongs to. The objective of this chapter is to assess the influence of the image segmentation technique on the results of numerical simulations dedicated to ductile damage. The focus is on the SRCL-DVC-FE methodology and the impact of this segmentation stage on the accuracy of the FE predictions.

Image segmentation is a well established field with a large number of methods adapted to different types of images and applications. These techniques range from medical applications [167] to quantification and analyses of porous microstructures [168]. Segmentation can be as simple as global thresholding [169] or as complex as more recently developed techniques based on machine learning [170, 171].

One application in which the fields of image segmentation and mechanics have converged is the determination of mechanical properties of complex structures or microstructures [9, 10, 165, 172, 173]. This coupling provides an opportunity to better understand the relationship between microstructure and properties. For example, Madra et al. [172] analyzed qualitatively and quantitatively porosity in woven glass fiber reinforced composites via various segmentation methods. Another example is the study of complex metallurgical microstructures through pattern recognition techniques [173].

Although some studies have addressed the relevance of the employed segmentation method [168, 172, 173], the focus was generally restricted to the result of the segmentation step. The present chapter aims at assessing the effect of image segmentation up to its final use in the context of a micromechanical study of ductile damage applied to nodular graphite cast iron. More specifically, this chapter is dedicated to understanding and quantifying the effect of image segmentation on the final mechanical observables of interest (global stress and strain measurements and local strain measurements as well as void fraction and volume). If image segmentation introduces considerable uncertainty on the desired micromechanical quantities, these quantities cannot be used reliably. To the best of the author's knowledge, this work constitutes the first effort of documentation and quantification of this problem.

The measurement uncertainties of DVC applied to laminography data were evaluated for cast iron [174]. The present chapter aims at assessing the uncertainties in the results of the FE simulations in the SRCL-DVC-FE framework that could be expected to originate from the segmentation of SRCL images. The SRCL-DVC-FE framework is a recent methodology and

understanding the uncertainties in the chain of different employed techniques is necessary. Thus, the objective of this chapter is to understand and quantify the influence of image segmentation on the final FE results. This is of prime importance not only for the SRCL-DVC-FE methodology, but for any two-dimensional or three-dimensional numerical studies of immersed microstructures.

The chosen mechanical quantities that result from simulations carried out with the SRCL-DVC-FE framework can be used for calibrating void nucleation, growth or coalescence models. Sensible input is required for these tasks to be successful. For this reason, it is important to assess the magnitude of the uncertainty introduced during image segmentation.

In order to assess the effect of the segmentation procedure in the results of the FE simulations within the SRCL-DVC-FE framework, three different established approaches were chosen (Section 3.2). They had to be able to deal with the measurement noise during image acquisition as well as with artefacts resulting from incomplete sampling of the 3D Fourier domain [175]. An additional criterion for the selection of the segmentation methods was their ability of being automated in the SRCL-DVC-FE chain of techniques, *i.e.*, the desired methods should be able to produce satisfactory results without requiring excessive fine-tuning of their intrinsic parameters. Micromechanical FE simulations are then carried out by immersing each of the segmented images and comparisons are made between the resulting predictions. This analysis has the objective of assessing the effect of image segmentation on the results of FE simulations of immersed microstructures. The comparisons have another practical consequence; the uncertainty introduced during image segmentation of the results of the simulations can be estimated based on these comparisons. The comparative study and the subsequent uncertainty estimation are presented in Section 3.3.

3.2 Methodology

3.2.1 Image segmentation

Before immersing the microstructures in the FE mesh, it is necessary to differentiate the various phases in the 3D SRCL images of the reference configurations. This task is called image segmentation. In this work, the image segmentation is conducted in FIJI [176], a distribution of the ImageJ software [177]. Three different image segmentation procedures were employed. Although each procedure consists of several operations, they will be referred to by the name of the defining method or algorithm. The first method, which is based on thresholding by inspection of the images, will be referred to as **Thresholding**. The second method employs an automatic thresholding procedure, and will be referred to as **Automatic Thresholding**. The third and last method, which is based on machine learning, will be referred to as **Random Forest**.

Other methods such as region-growth segmentation [178], fast marching algorithm and Level-set segmentation [179], were briefly tested. They were not selected since they required excessive user input or calibration, were very time-consuming, or provided unsatisfactory results.

Although entire slices of laminography images are presented, only the volume inside of the so-called reconstruction circle is subsequently used in the simulations. The reason is that information outside of this zone is incomplete [174] and hence not suitable for any quantitative analysis.

Ring artefacts are observed in the laminography images. The origin of these artefacts is related to the characteristic modulated intensity pattern of the cross-section of the beam. These modulations cause the manifestation of ring artefacts after reconstruction [174]. An additional requirement on the chosen segmentation methods is to be capable of dealing with the presence of these artefacts.

Thresholding

Thresholding is a very simple segmentation operation that consists in determining the phase of a voxel based on its gray level, and it is particularly adapted for images where only two phases exist [169]. A unique thresholding by inspection was defined and applied to both specimens and will be illustrated only for the 90° specimen for the sake of brevity. This procedure involves four steps.

The first step consists of a three-dimensional averaging filter, *i.e.*, the gray level in a voxel is replaced with the average gray level in its immediate neighborhood. This operation results in smoother albeit coarser images. A mid-thickness slice of the 90° specimen is shown in Figure 3.1 in its original version (Figure 3.1a) and after applying the 3D-mean filter (Figure 3.1b).

The effect of the increased smoothness on the gray level histogram is illustrated in Figure 3.2. The gray level histogram of the original image is bimodal and presents considerable overlap between the two superimposed distributions. This makes the original image difficult to segment through simple thresholding. Applying the 3D-mean filter has the effect of reducing the spread of each of the superimposed distributions. Choosing a reasonable threshold is thus possible. The chosen value was 120 for both images.

Buljac et al. [123] proposed another methodology for reducing the subjectivity in the choice of the threshold. It consisted in using the strain tensor trace obtained from DVC analyses to obtain void growth during the *in-situ* test, and comparing this history with the void growth obtained via segmentation of the 3D images with different thresholds. The chosen threshold was then the one that better matched the void growth evaluated with the

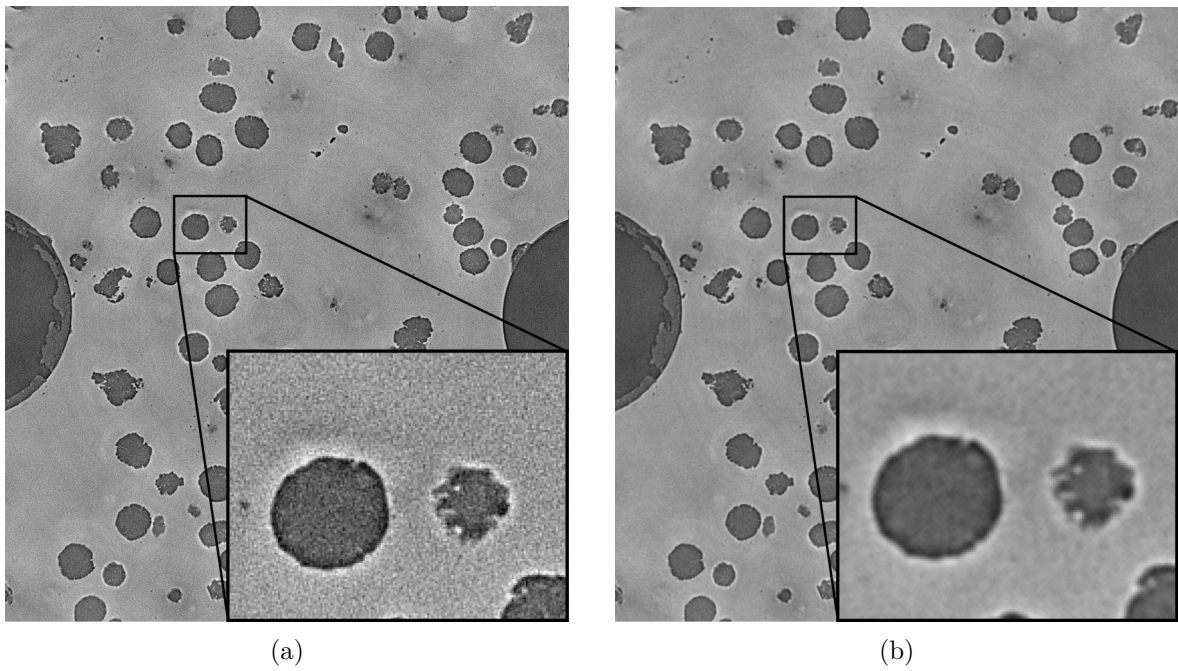


Figure 3.1: (a) Original slice at mid-thickness of the 90° specimen, and (b) after applying the 3D-mean filter.

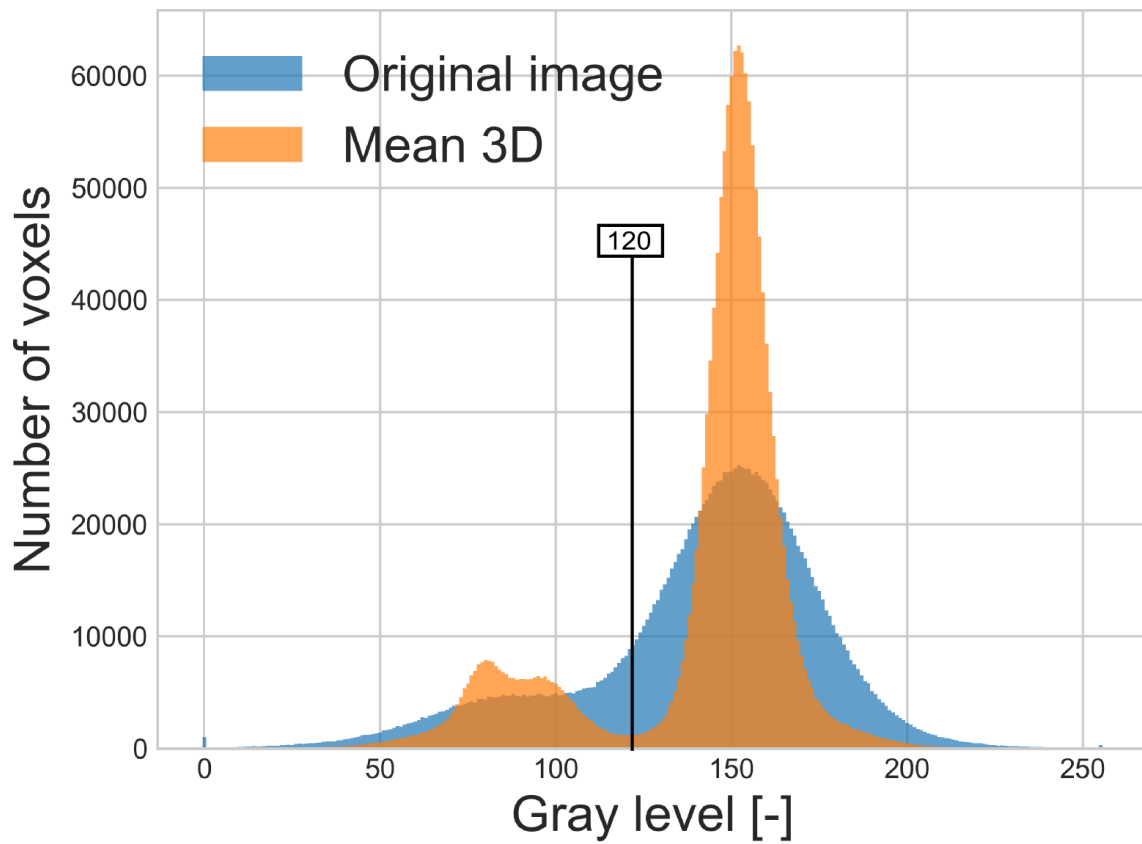


Figure 3.2: Gray level histogram of the original image and after applying the 3D-mean filter.

strain tensor trace (*i.e.*, 115). Although in the current work the threshold was determined by simple inspection of the images and their gray level histogram, it is close to that chosen by Buljac et al. [123].

The result of the thresholding procedure is illustrated in Figure 3.3a. Figure 3.3b shows the final segmented image after applying two additional filters. The first one carries out a fill-hole operation to eliminate white voxels within voids. The second (median) filter is typically used to eliminate salt-and-pepper noise. It is applied to remove isolated black voxels in the matrix (Figure 3.3b).

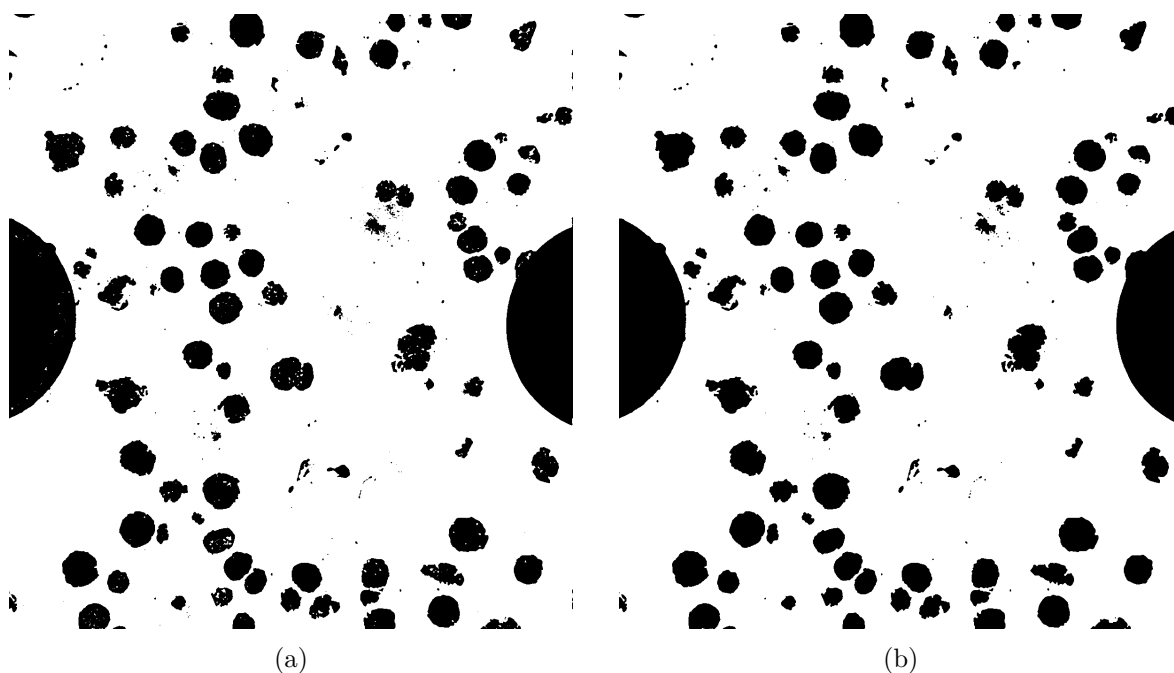


Figure 3.3: Slice at mid-thickness of the 90° specimen after (a) thresholding, and (b) applying the fill-hole and despeckle filters.

Automatic thresholding

A segmentation procedure with an automatic thresholding technique is described in this section. It is carried out in three steps. First, Gaussian blur with standard deviation of 5 voxels is applied to the original image. The automatic thresholding technique is then applied, and finally, a fill-hole operation is performed.

The Gaussian blur accomplishes the same function as the 3D-mean filter applied in the manual thresholding procedure (see Section 3.2.1). The objective of this work is not to carry out a detailed comparison of different segmentation methods under the same condition. The deliberate choice of different preprocessing steps before the segmentation helps emphasizing the effect of the human factor in the entire segmentation procedure.

The automatic thresholding algorithms that are available in FIJI were tested on the mid-thickness slice of the 45° specimen, and the results are summarized in Figure 3.4. The tested techniques are, in order of appearance, the IsoData algorithm [180], Huang’s fuzzy thresholding method [181], the Intermodes method [182], a second implementation of the IsoData algorithm, an iterative version [183] of Li’s Minimum Cross Entropy method [184], a Maximum Entropy method [185], using the mean of the gray levels as a first guess for the threshold value [186], an iterative version of the Minimum Error method [187], the so-called Minimum method with histogram smoothing [182], the moment-preserving method [188], the clustering algorithm [189], the so-called Percentile method, which assumes a given fraction of foreground voxels (0.5 by default) [190], the Maximum Entropy method with Renyi’s entropy [191], the Information Measure method [192], the Triangle method [193], and the automatic multilevel method [194].

The results of the employed automatic thresholding techniques reported in Figure 3.4 were qualitatively examined through comparison with the original image (Figure 3.7c). Similar and satisfactory results were provided by both IsoData methods, Huang’s method, the Intermodes method, Li’s method, the Minimum method, and Otsu’s method. The IsoData algorithm was selected because of its simplicity and applied for segmenting the 3D images of both specimens.

The iterative IsoData algorithm classifies the voxels into two categories with an initial threshold value, and the average gray level of each category is calculated. The average of the latter is then proposed as a new threshold until convergence. The algorithm was applied separately for each slice, *i.e.*, a threshold value was calculated for each individual slice of the volumetric images. This choice was made to be consistent with the Random forest procedure which is too costly to be applied to the whole image.

Random forest procedure

The random forest procedure is based on machine learning [195], and involves two steps, namely, training and classification. After classification, fill-hole and median filters were also applied. During training, a classification model was created. The data used for training were the mid-thickness slice of the specimen, and twenty freehand traces were chosen for each of the two classes (*i.e.*, matrix and voids). The training features were Gaussian blur, Sobel and Hessian filters, difference of Gaussians and membrane projections.

A random forest is a machine learning classification method in which many decision trees vote and the resulting most popular category is retained. A decision tree is a simpler classification model that consists of nodes and branches. The initial node is the root and the terminal nodes are denoted as leafs. Each node, except for leafs, represents a test and each subsequent branch corresponds to the result of a test. The classification ends at the leafs, which contain the label of a class. In this work, the classes are either void or matrix. An

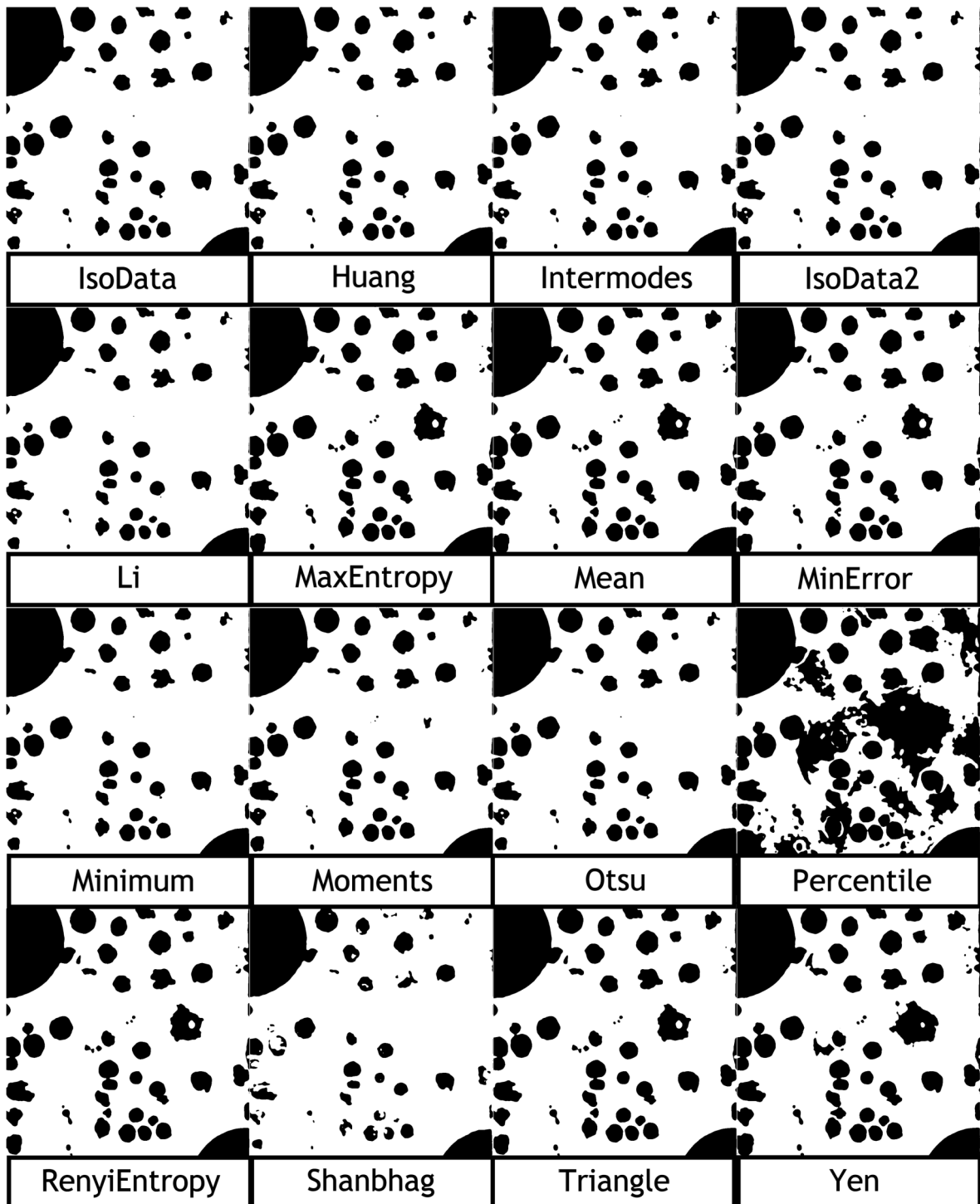


Figure 3.4: Mid-thickness slice of the 45° specimen segmented with different automatic thresholding methods.

example of a possible decision tree for a given voxel is schematized in Figure 3.5. The depicted tree uses two training features, namely, the gray level and the first principal curvature.

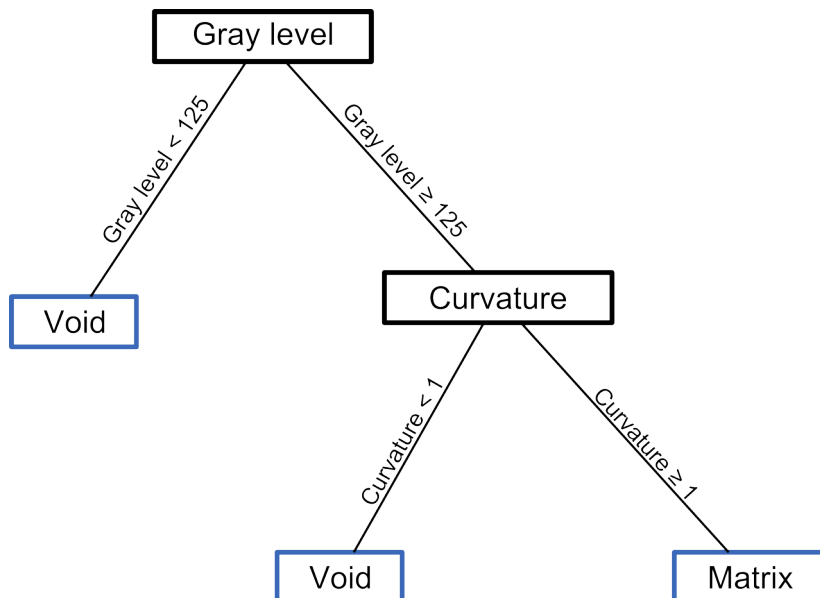
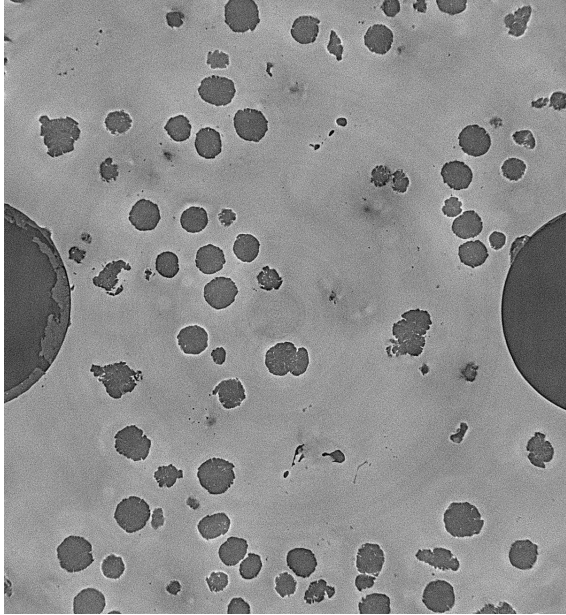


Figure 3.5: Example of a possible decision tree for a voxel with two features (gray level and first principal curvature).

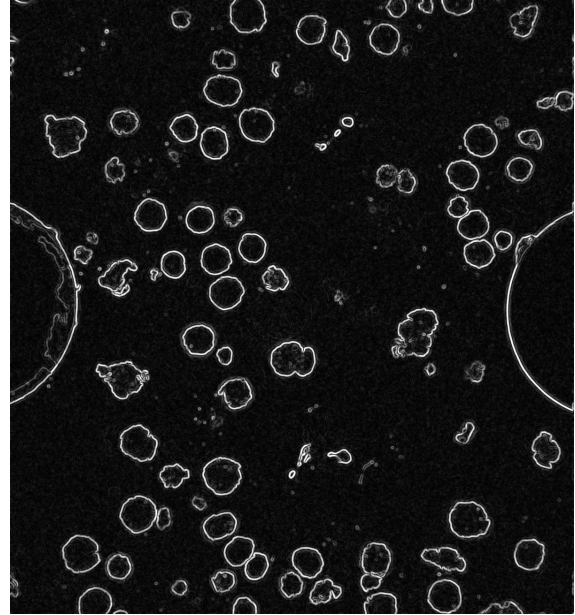
Five Gaussian (blur) filters, with different standard deviations ranging from 1 to 16 voxels, were used. The Sobel filter provides an approximation of the gray level derivative and helps locating interfaces. Information on the curvature of the interfaces is provided by the Hessian filter. The difference of Gaussians filter is useful for blob detection due to laminography artefacts or the nearby presence of voids in the thickness direction. Membrane projections may provide additional information on the location of boundaries. More information on these filters can be found in the documentation of the Weka Trainable Segmentation library [196].

The use of filters and their combinations provide a total of 76 training features. Three of these features are exemplified in Figure 3.6 along with the original image (Figure 3.6a) for the slice at mid-thickness of the 90° specimen. Figure 3.6b shows the result of applying the Sobel filter after Gaussian blur with a standard deviation of 4 voxels. This operation highlights the void/matrix interfaces. Figure 3.6c shows the square difference of the first and second eigenvalues of the Hessian after Gaussian blur with a standard deviation of 16 voxels, *i.e.*, the high curvature zones are determined. Ring-shaped artefacts are brought into evidence with a lesser curvature than the contour of the voids. Membrane projections with the mean of the voxels provides a marginal enhancement of the interfaces and an overall smoothing of the image.

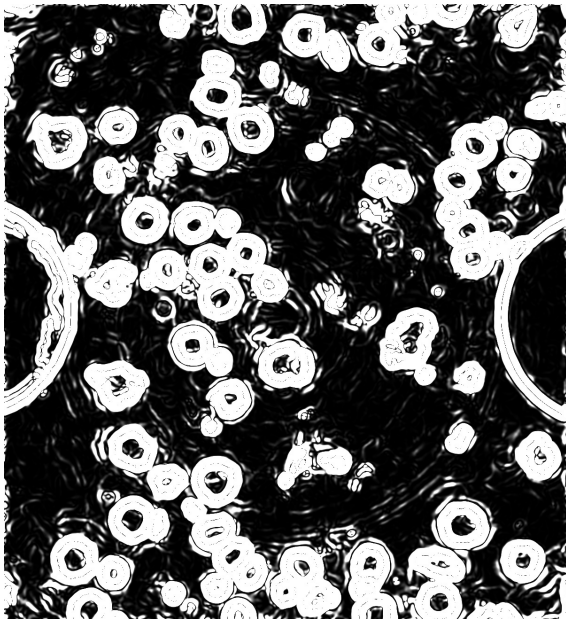
Two features per tree and 200 trees were used in the classification stage. A classifier model for each of the specimen was created. The original and classified images for the slice at mid-thickness of the 90° and 45° specimen are shown in Figure 3.7.



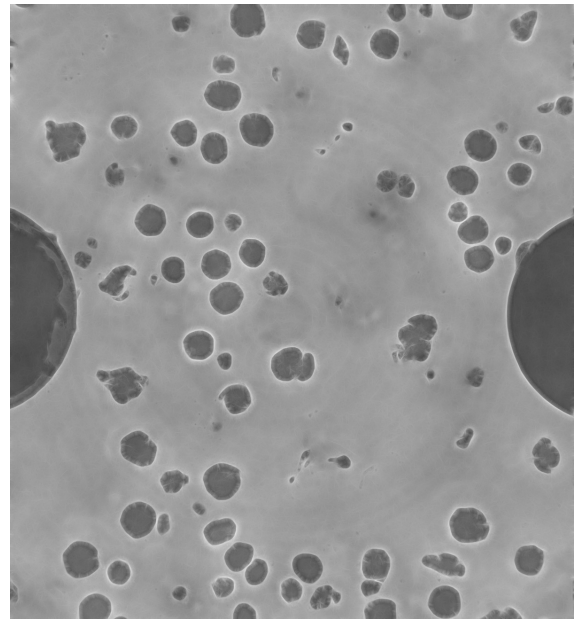
(a) Original image



(b) Sobel filter

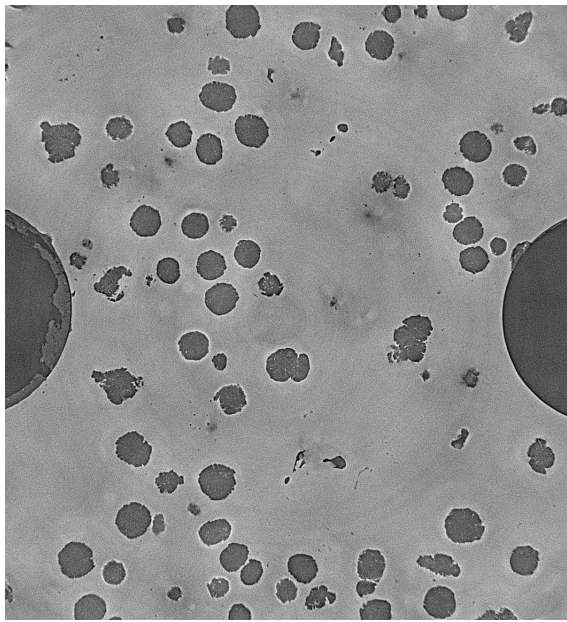


(c) Hessian filter

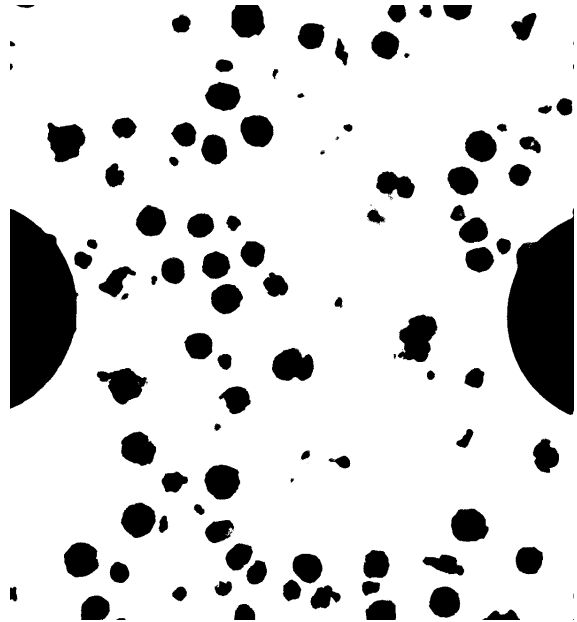


(d) Membrane filter

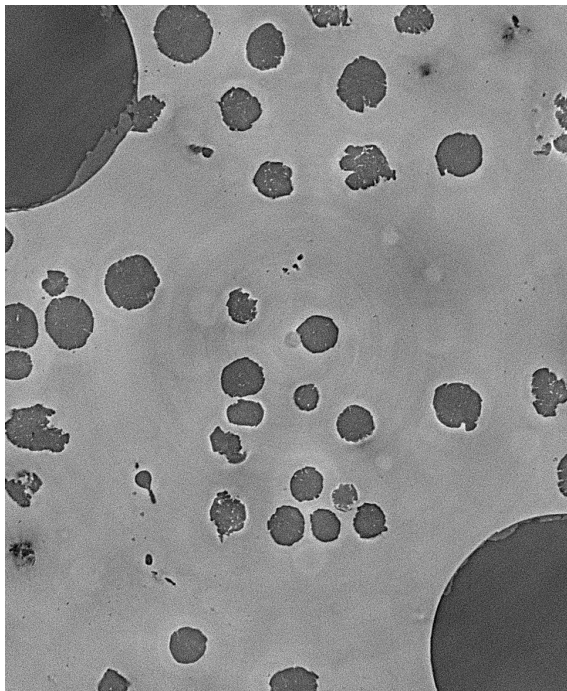
Figure 3.6: Original mid-thickness slice of the 90° specimen, and the result of applying three different filters to the same slice.



(a)



(b)



(c)

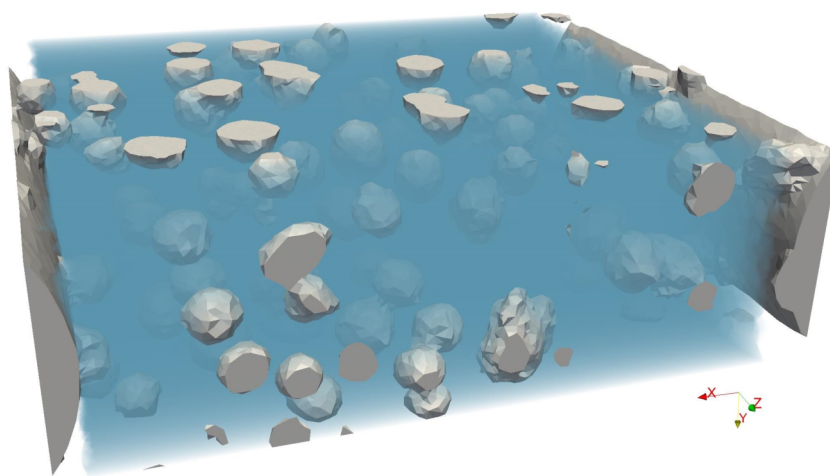


(d)

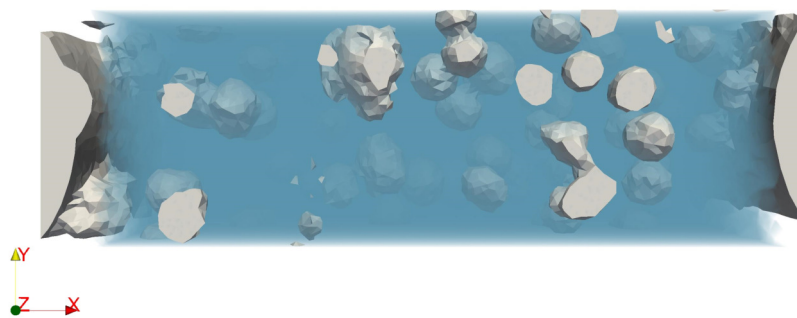
Figure 3.7: Original slice at mid-thickness of the (a) 90° and (c) 45° specimens and the same slice after classification with the random forest procedure. for the (b) 90° and (d) 45° specimens.

3.2.2 Observables

Global and local quantities were considered for each specimen. The global information was calculated in the whole domain for the 45° specimen and in a fraction of the domain for the 90° specimen. The purpose of the latter choice is to exclude the EDM-machined holes from the global calculation since they lie partially inside of the domain for the 90° specimen, and would have led to inaccurate void volume quantification. The domain for the calculation of the global quantities in the 90° specimen is shown in Figure 3.8 as a semi-transparent blue volume. The term global volume will be used to make reference to the whole domain in the case of the 45° specimen simulation, and to the volume depicted in Figure 3.8 for the 90° specimen.



(a)



(b)

Figure 3.8: Two different views of the domain for the 90° specimen simulation. The domain where the global quantities are calculated is shown as a semi-transparent blue volume. Voids are shown in gray.

The global observables are the volume-averaged (or macroscopic) von Mises equivalent strain, the (macroscopic) von Mises equivalent stress, the void volume fraction, and void

growth. The latter is defined as the ratio between the current void volume and the initial void volume.

Additionally, the volume-averaged equivalent strain in two local probes per specimen is assessed. The local probes are displayed as a blue cube (probe 1) and as a red cube (probe 2) in Figure 3.9a for the 90° specimen, and in Figure 3.9b for the 45° specimen. The positions of the probes are exactly the same as those analyzed by Buljac et al. [123]. These volumes enable for the study of void coalescence by ligament failure. The probe volume corresponds, except for probe 2 of the 90° specimen, to that of C8 elements with an edge of 35.04 μm , in DVC calculations. The size of probe 2 of the 90° specimen had to be reduced to 1/16th of the volume of the other probes so that it could fit in the intervoid ligament without being in contact with the voids. The initially cubic shape of the probes corresponds to the DVC elements, and evolves with deformation, *i.e.*, the probed volumes are Lagrangian.

A total of six observables per specimen will be assessed and were chosen in accordance with future work related to experimental-numerical comparisons as well as parameter identification of macroscopic damage laws.

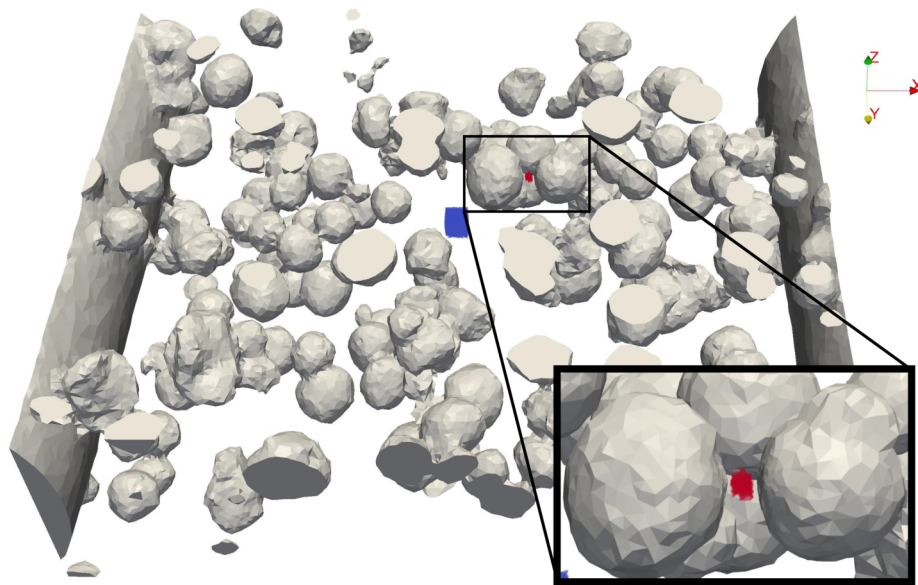
3.3 Results

The results of a mesh sensitivity analysis are first presented for all of the considered observables and both specimens. A comparison of the predictions of the three segmentation procedures is reported in terms of their effect on the observables. Finally, an uncertainty estimation method is proposed.

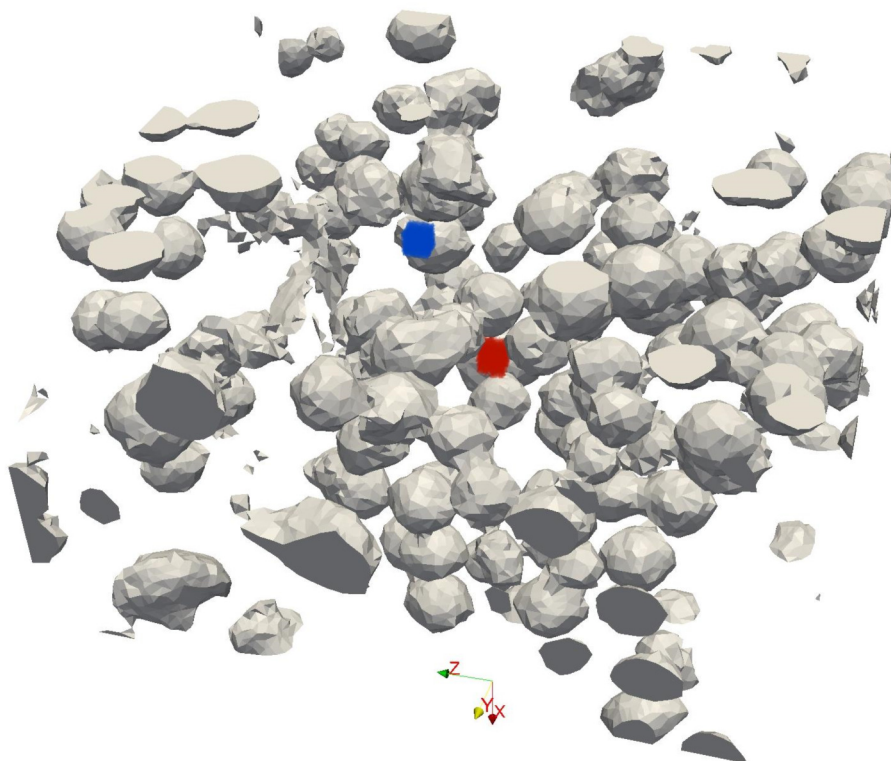
3.3.1 Mesh sensitivity analysis

In addition to the curvature-based mesh adaption described in Section 2.2.2, an additional local refinement was carried out around the probes to ensure mesh-independent local values without significantly increasing the computational cost with further global refinement. The isotropic mesh size h was forced to take the value $h = \frac{h_{min}}{4}$ (see Equation (2.30)) in the probe and its surroundings. This extended locally refined volume was constructed by adding $2h_{min}$ to the distance function that describes the probes. The local refinement is illustrated for probe 1 of the 45° specimen in Figure 3.10.

To simplify the mesh sensitivity analysis, two scaling factors F_1 and F_2 are introduced. The first one, F_1 , multiplies h_c , h_{min} and h_{max} , while the second one, F_2 , multiplies h_c and h_{min} . The values of the original mesh parameters are set to $h_c = 2.5 \times 10^{-3} \mu\text{m}$, $h_{min} = 2.5 \times 10^{-1} \mu\text{m}$, and $h_{max} = 5 \mu\text{m}$. When the scaling factors are introduced, the mesh



(a)



(b)

Figure 3.9: 3D view of the computational domain for the (a) 90° specimen and (b) the 45° specimen. Local probes are shown in blue (probe 1) and red (probe 2). A local zoom displays probe 2 of the 90° specimen.

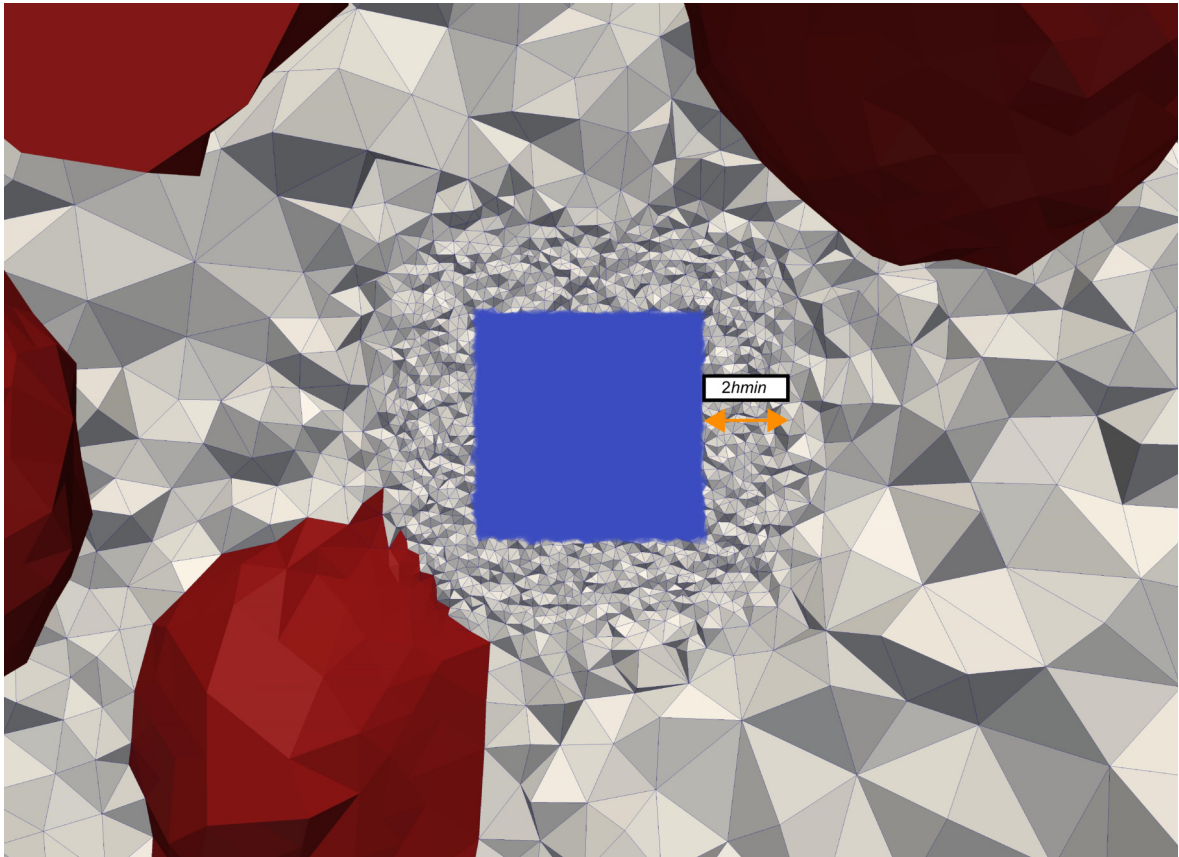


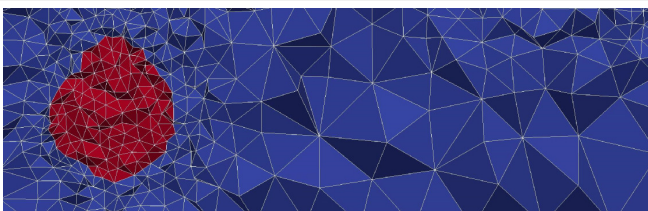
Figure 3.10: Probe 1 (in blue) in the 45° case with the mesh in a 2D slice of the domain showing the local refinement. The extended refined volume around the probe is indicated in orange. The voids are shown in red.

size is calculated as

$$h = F_1 \max \left(\min \left(\frac{h_c F_2}{\lambda_{max}} + \left(h_{max} - \frac{h_c F_2}{\lambda_{max}} \right) \frac{\phi}{\epsilon_h}, h_{max} \right), h_{min} F_2 \right). \quad (3.1)$$

The effect of F_1 is straightforward, namely, modifying F_1 is equivalent to scaling the calculated mesh size h . The effect of F_2 is slightly more subtle. When F_2 decreases, the mesh size close to the interfaces decreases, but the maximum mesh size far away from the interfaces is unchanged. This effect results in an increased mesh size gradient. Table 3.1 summarizes the effect of F_1 and F_2 parameters for the 45° specimen for different combinations.

Table 3.1: Mesh parameters and corresponding number of elements for the 45° specimen. A close-up view of a slice of the mesh is shown for each case. The matrix is shown in blue and voids in red.

Case	F_1	F_2	Number of elements	Mesh
1	4	4	424,806	
2	3	4	749,875	
3	2	4	1,706,833	
4	4	3	753,754	
5	4	2	1,685,267	
6	4	1.5	2,968,499	

Effect of F_1

Simulations were carried out with meshes with three different F_1 values (*i.e.*, $F_1 = 4$, $F_1 = 3$ and $F_1 = 2$). Decreasing F_1 is equivalent to carrying out a global mesh refinement.

90° specimen

In the case of the 90° specimen, the results are shown in Figure 3.11 for the six observables. All observables seem to approach mesh independence as F_1 decreases, *i.e.*, the gap between the results with $F_1 = 2$ and $F_1 = 3$ is smaller than that when $F_1 = 3$ and $F_1 = 4$. The most sensitive variables are the macroscopic equivalent stress (Figure 3.11b) and the void volume fraction (Figure 3.11c). The void volume fraction presents significant differences since the microstructure cannot be described properly by a coarse FE mesh. As the mesh size decreases, the microstructural features are better described. The small decrease of the equivalent strain in probe 2 for the coarsest mesh in the last increment is caused by numerical diffusion of the probe volume during remeshing operations, *i.e.*, this mesh is not fine enough to appropriately handle numerical diffusion.

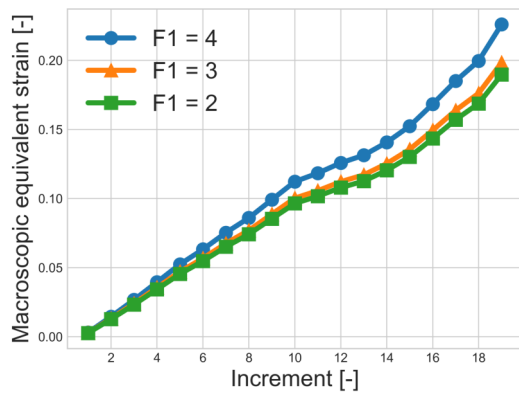
45° specimen

The effect of varying F_1 is shown in Figure 3.12 for the six observables. Contrary to the simulation of the 90° specimen, an unexpected response is found for the 45° specimen when F_1 is varied. The gap between the results with $F_1 = 2$ and $F_1 = 3$ is greater than that between $F_1 = 3$ and $F_1 = 4$.

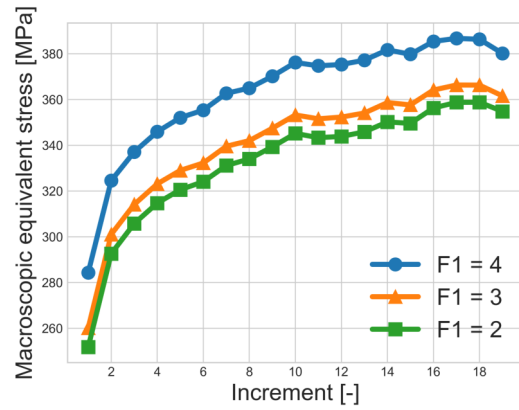
The reason for this trend is that there are microstructural features that the meshes with $F_1 = 3$ and $F_1 = 4$ are too coarse to capture. This explanation is consistent with the trend followed by the void volume fraction (Figure 3.12c) and the macroscopic equivalent stress (Figure 3.12b). When F_1 decreases, the mesh is able to capture smaller voids, as well as the shape of the bigger voids. Hence, the void volume fraction increases, and the loss of load-bearing capacity induces a decrease in the macroscopic equivalent stress.

The equivalent strain in probe 1 barely changes when the mesh size decreases (Figure 3.12e). In probe 2, however, when $F_1 = 2$, the equivalent strain experiences an unexpected and significant decrease (Figure 3.12f).

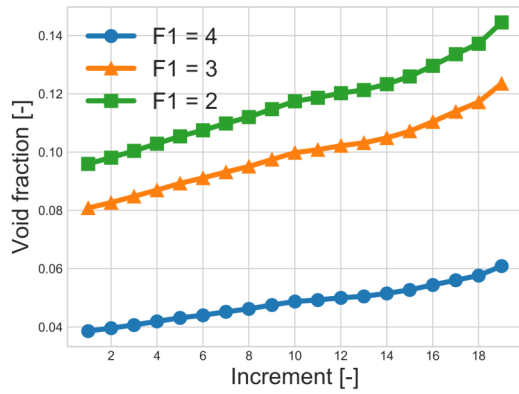
The reason for this effect is that this mesh captures microstructural features that coarser meshes could not, and these features modify the local heterogeneous partition of strain in the vicinity of probe 2. This is illustrated in Figure 3.13 at increment 11 in the slice of the computational domain that contains the center of probe 2 for $F_1 = 4$ (Figure 3.13a)



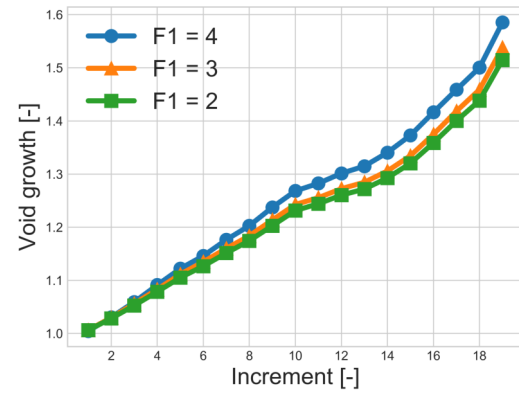
(a)



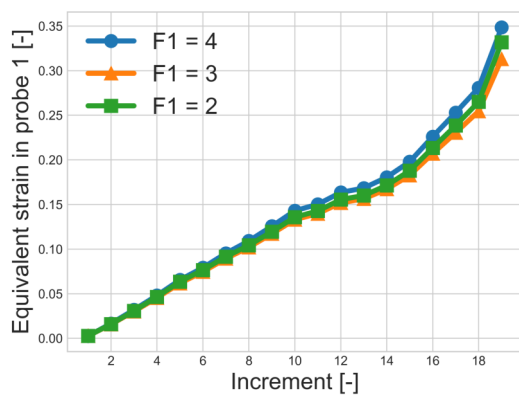
(b)



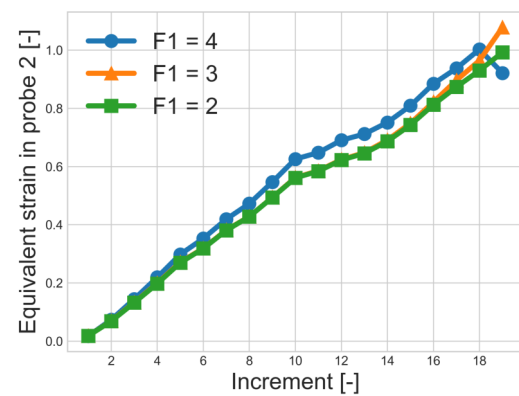
(c)



(d)



(e)



(f)

Figure 3.11: Mesh sensitivity in terms of F_1 for (a) macroscopic equivalent strain, (b) macroscopic equivalent stress, (c) void volume fraction, (d) void growth, and equivalent strain in (e) probe 1 and (f) probe 2 in the 90° specimen.

and $F_1 = 2$ (Figure 3.13b). Although the general strain distribution is similar for both meshes, local differences in topology and strain distribution are observed at different locations including the position of probe 2.

The mesh sensitivity of the void volume fraction in the 90° specimen simulation is too substantial to consider that convergence was achieved. For the 45° simulation, verification of mesh independence is inconclusive because of the unexpected behavior found when F_1 is decreased for the void volume fraction as well as for the strain in probe 2. For these two reasons, it is desirable to extend the mesh verification analysis. However, further refinement of the mesh with a decrease of F_1 is very costly. A different strategy is adopted and described in Section 3.3.1.

Effect of F_2

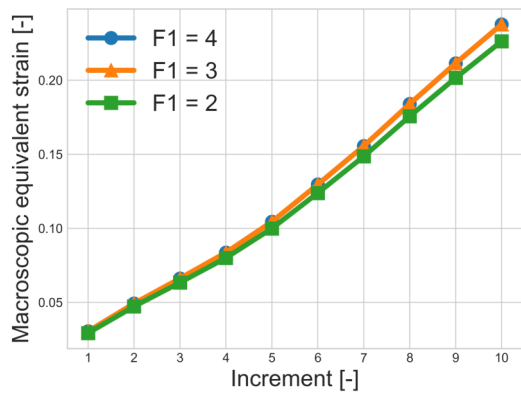
To extend the sensitivity analysis, the effect of varying F_2 is assessed in this section. Decreasing F_2 results in a better description of the interfaces while retaining a fixed mesh size far from them, i.e., this strategy aims at providing a satisfactory description of the geometry while decreasing as much as possible the computational cost. A fixed value of $F_1 = 4$ is used and results for $F_2 = 3$, $F_2 = 2$, and $F_2 = 1.5$ are presented. As a reference to the analysis in Section 3.3.1, the results with $F_1 = 2$ and $F_1 = 4$ are included in the figures as a black solid line.

90° specimen

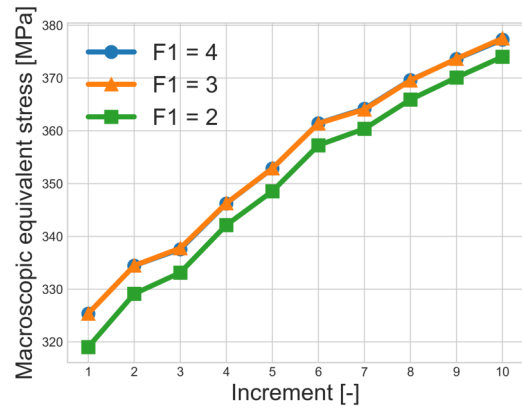
The effect of varying F_2 in the 90° simulation is illustrated for the six observables Figure 3.14. All observables seem to approach mesh convergence as F_2 decreases. The curves with $F_2 = 2$ match very well those when $F_1 = 2$. In general, when F_2 is further decreased to F_1 , the resulting curves stay satisfactorily close to those corresponding to $F_2 = 2$. The void volume fractions remain the most sensitive observable and the variation it undergoes when F_2 decreases from 2 to 1.5 is not negligible.

45° specimen

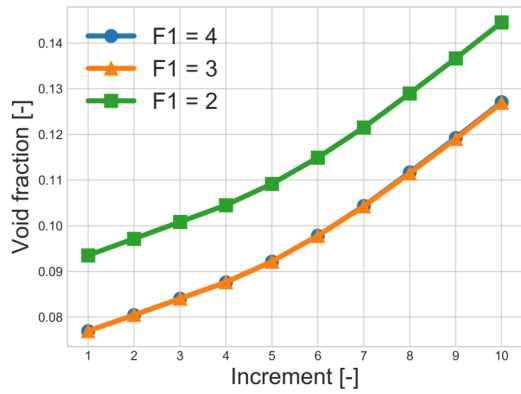
The sensitivity of the observables for the 45° simulation when F_2 is varied is shown in Figure 3.15. For all observables in the 45° simulation, the trend is the same as for the 90° specimen, namely, the gap between two successive curves decreases monotonically as F_2 decreases. In this case too, the curve with $F_2 = 2$ matches very well the reference curve with $F_1 = 2$. The observable most sensitive to the mesh is again the void volume fraction.



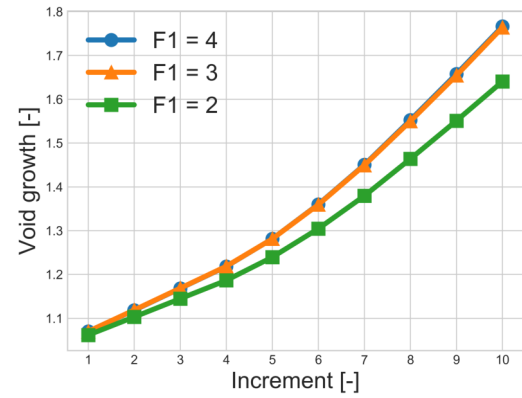
(a)



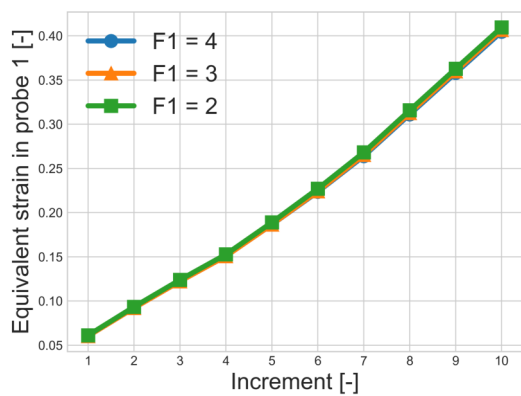
(b)



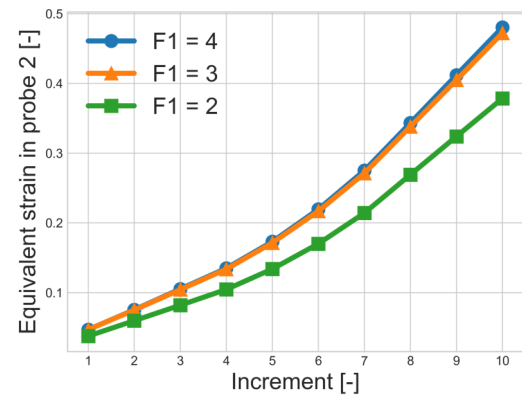
(c)



(d)



(e)



(f)

Figure 3.12: Mesh sensitivity in terms of F_1 for (a) macroscopic equivalent strain, (b) macroscopic equivalent stress, (c) void volume fraction, (d) void growth, and equivalent strain in (e) probe 1 and (f) probe 2 in the 45° specimen.

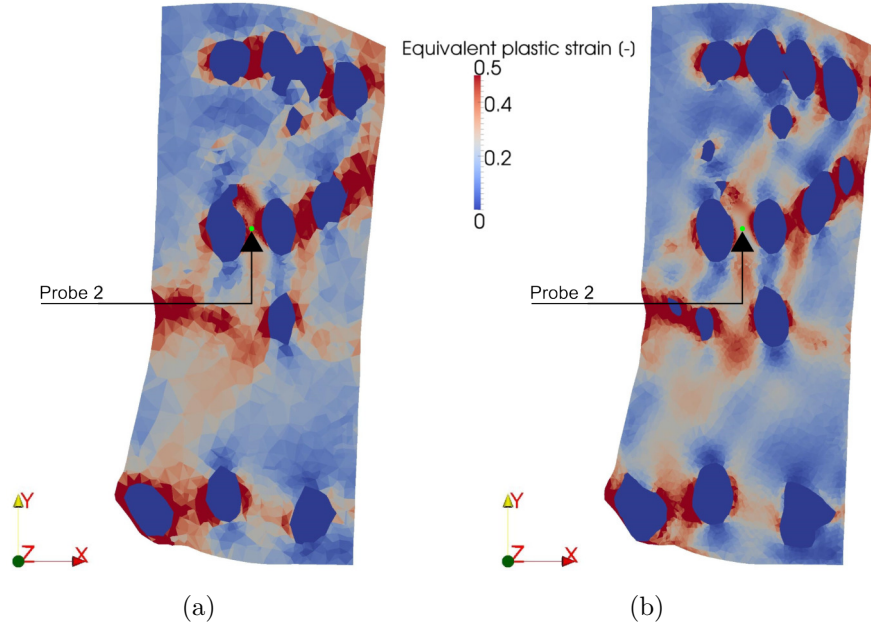


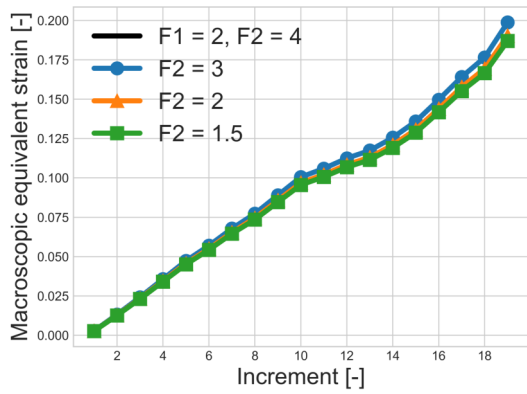
Figure 3.13: Strain distribution at increment 11 in the slice of the computational domain that contains the center of probe 2 for the 45° specimen for (a) $F_1 = 4$ and (b) $F_1 = 2$.

Although the results are satisfactory for most of the observables, given the acceptably small yet non-negligible variations exhibited by the void volume fraction for the simulations of both specimens, further refinement could be considered. The associated computational costs would make further refinement impractical, and more importantly, attention must be paid to the relative order of magnitude of the minimum mesh size with respect to resolution of the laminography images. For example, for the finest employed mesh with $F_1 = 4$ and $F_2 = 1.5$, the resulting minimum allowed mesh size is $1.5 \mu\text{m}$, which is of the same order of magnitude of the laminography resolution with cubic voxels of edge length $1.1 \mu\text{m}$ [9]. The mesh with $F_1 = 4$ and $F_2 = 1.5$ is selected for the remainder of the study.

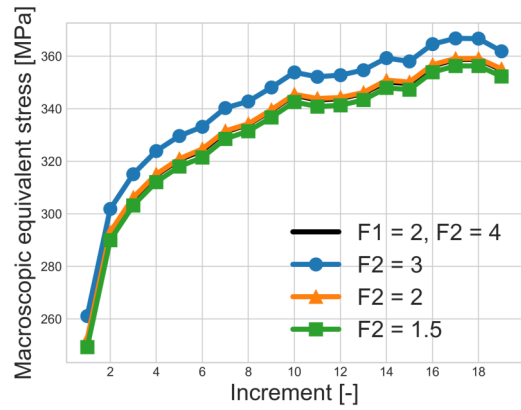
3.3.2 Model cross comparison

For the random forest procedure, a simple training procedure was carried out on a single slice for each specimen. However, the training stage is critical and can be tedious in more complex cases. For this reason, it would be convenient to be able to train a single classifier model in a chosen image and subsequently use the model in other images of similar features. To explore the feasibility of reusing a model in different specimens, a cross comparison is carried out. There are two factors that can play an important role in the comparison, namely, the criterion of the operator who trained the models, and differences between images due to, for example, the variation in beam intensity during laminography acquisitions.

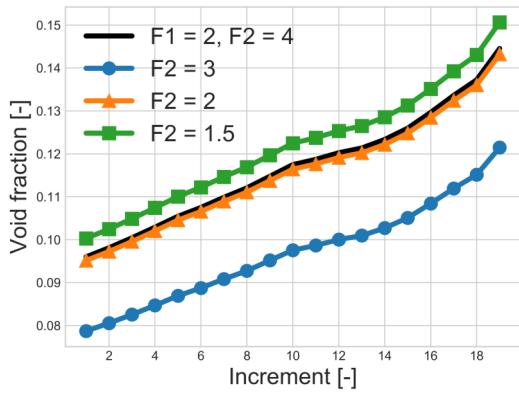
Two simulations were carried out for each specimen, namely, one with the model created for the same specimen, and one with the model created for the other specimen. The results of



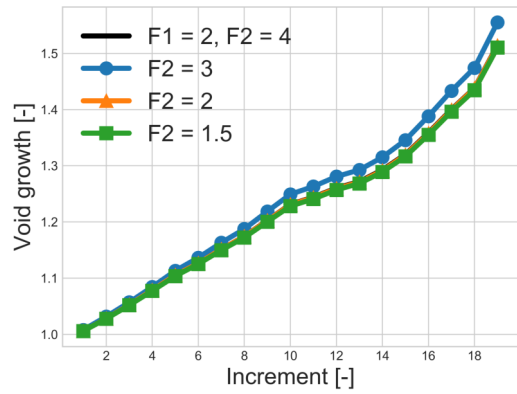
(a)



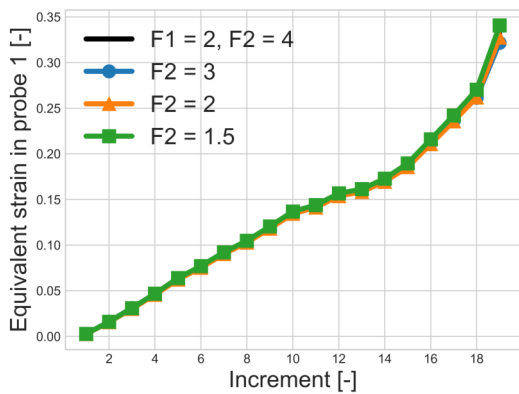
(b)



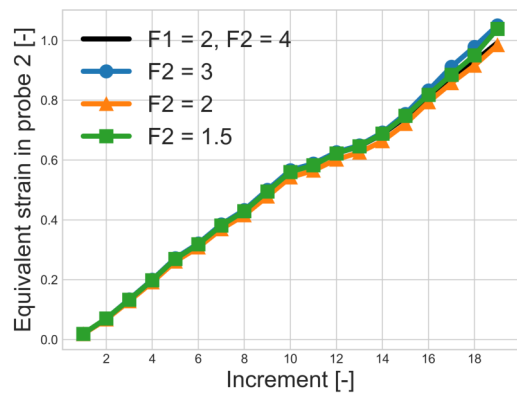
(c)



(d)

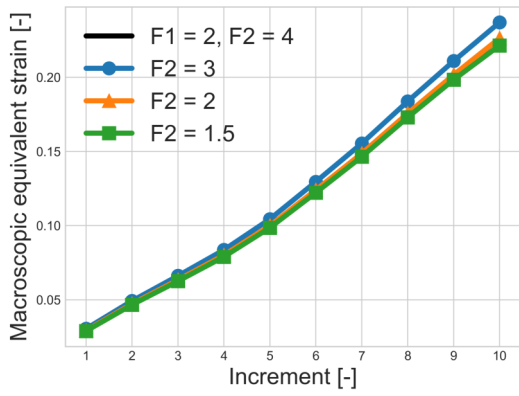


(e)

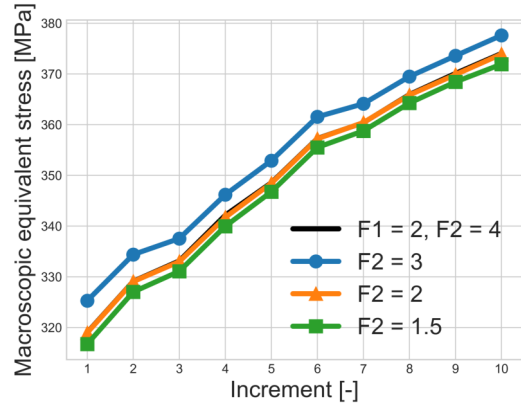


(f)

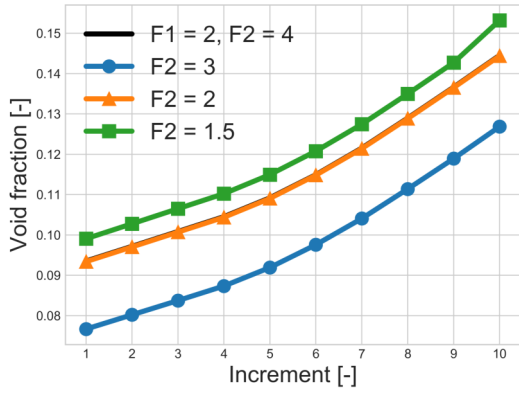
Figure 3.14: Mesh sensitivity in terms of F_2 for (a) macroscopic equivalent strain, (b) macroscopic equivalent stress, (c) void volume fraction, (d) void growth, and equivalent strain in (e) probe 1 and (f) probe 2 in the 90° specimen.



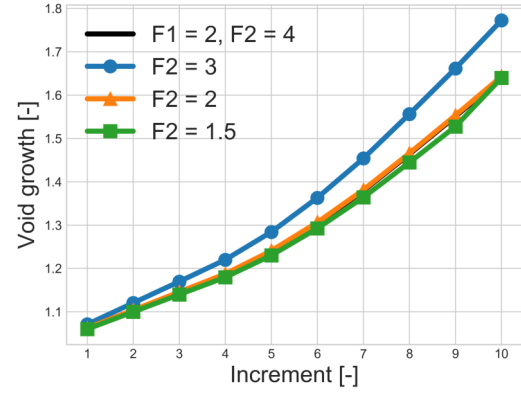
(a)



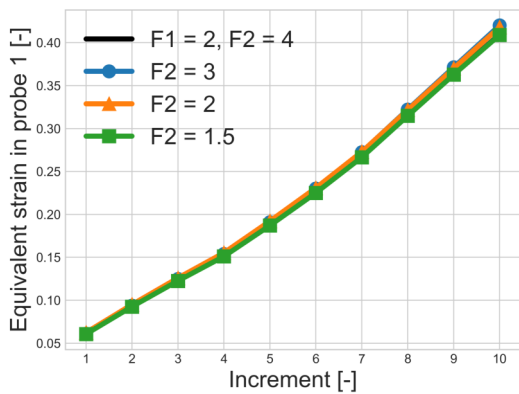
(b)



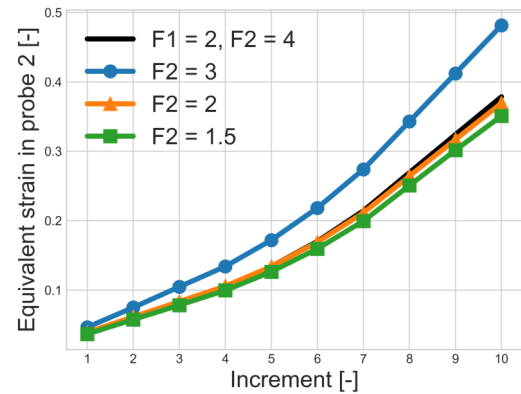
(c)



(d)



(e)



(f)

Figure 3.15: Mesh sensitivity in terms of F_2 for (a) macroscopic equivalent strain, (b) macroscopic equivalent stress, (c) void volume fraction, (d) void growth, and equivalent strain in (e) probe 1 (f) probe 2 in the 45° specimen.

the comparison between each pair of simulations are reported in Figure 3.16 (90° specimen) and Figure 3.17 (45° specimen). Additionally, an absolute difference calculated with respect to the smallest of two compared quantities is reported for each observable.

The comparison for both specimens leads to similar results. The maximum absolute difference for the macroscopic equivalent strain, macroscopic equivalent stress, and for the equivalent strain in probe 1, is of the order of or less than 3×10^{-3} . The void growth has a maximum absolute difference of 1.5×10^{-2} for the 90° specimen and of approximately 3.5×10^{-2} for the 45° specimen. The void volume fraction is less sensitive in terms of absolute differences. A maximum absolute difference of 6.2×10^{-3} was obtained for the 90° case, and 4.2×10^{-3} for the 45° sample.

The equivalent strain in probe 2 exhibits a maximum absolute difference of 9×10^{-3} for the 45° simulation. For the 90° simulation, probe 2 is very sensitive since a maximum absolute difference of approximately 8×10^{-2} is noted. The increased sensitivity of probe 2 in the 90° specimen is due to its size in comparison with the intervoid ligament, which makes it more sensitive to small changes in the surrounding microstructure when different classifier models are used.

Given these results, the re-utilization of a properly trained classifier model for different specimens of the same nature seems feasible. However, care must be exercised when dealing with sensitive variables or with very local information close to the boundaries of the segmented phases.

3.3.3 Comparison of segmentation methods

Numerical simulations were carried out after immersing the segmented images of the microstructures obtained by means of the segmentation procedures. The results of the numerical simulations are compared to assess the effect of the segmentation procedures on the observables described in Section 3.2.2.

First, a qualitative comparison of the images segmented with the three different methods is reported in Figure 3.18 alongside the original slice. The chosen slice is the mid-thickness of the 90° specimen. The three segmented images are similar, albeit with some differences. The image segmented through simple thresholding includes very small voids and some apparent noise. The resulting segmented images from the IsoData and Random forest algorithms are smoothed out in terms of lost features. However, secondary effects are related to filtering out the finest microstructural features and slightly smoothing the interfaces.

From a quantitative point of view, gray level differences can be computed between the original image f and its thresholded (and binarized) copy f_{th} after accounting for global gray

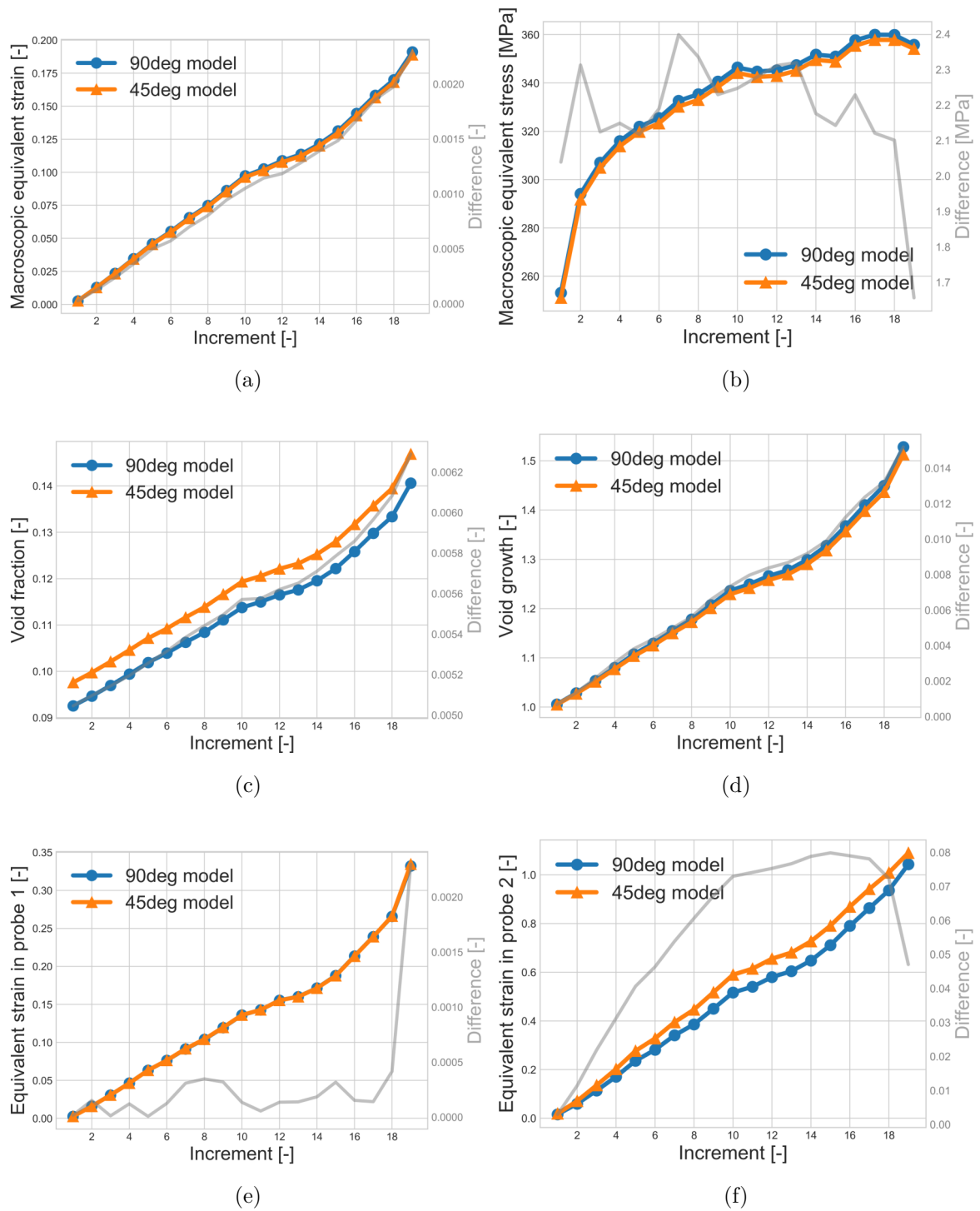


Figure 3.16: (a) Macroscopic equivalent strain and (b) stress, (c) void volume fraction, (d) void growth, and equivalent strain in (e) probe 1 (f) probe 2 for the 90° simulation obtained after segmentation with two different classifier models.

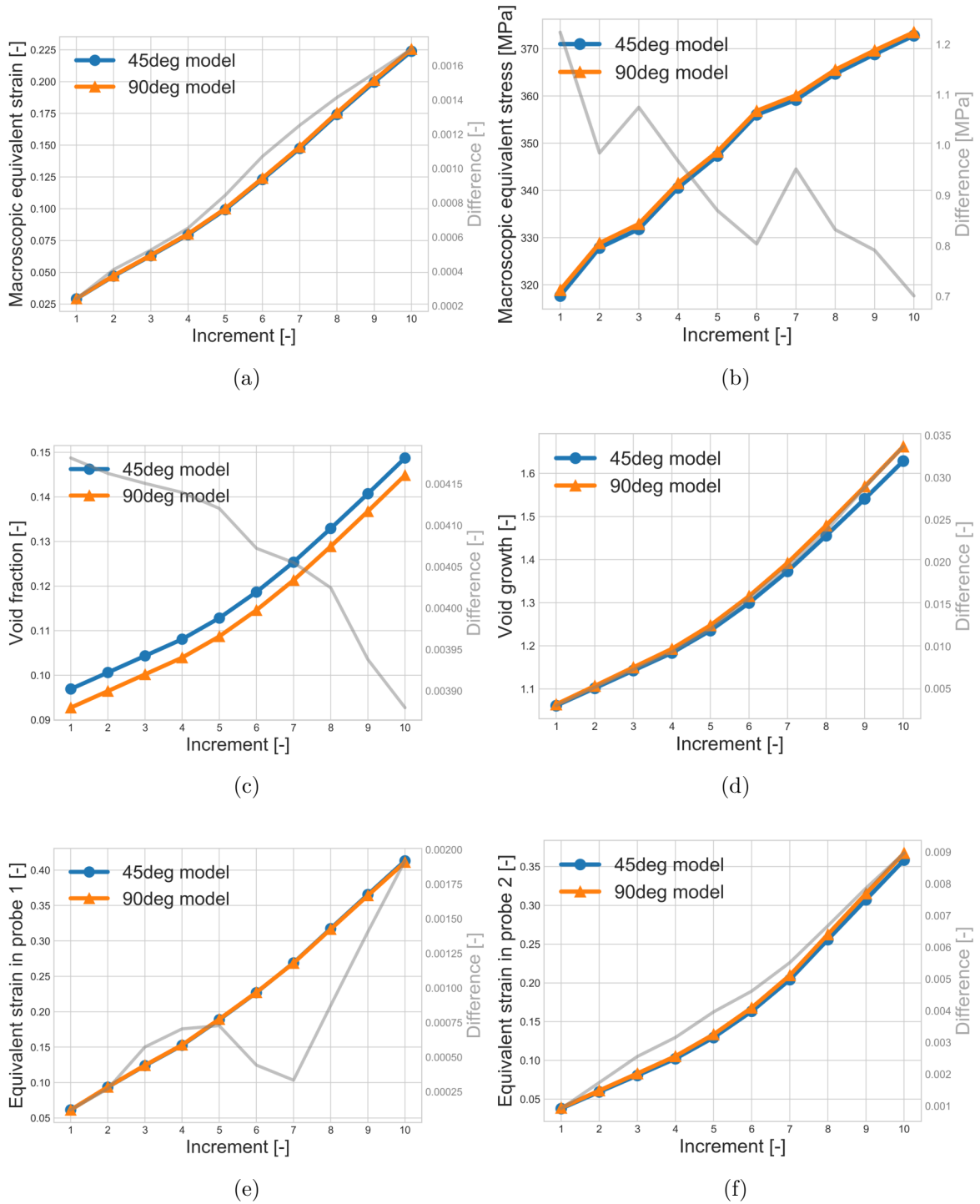
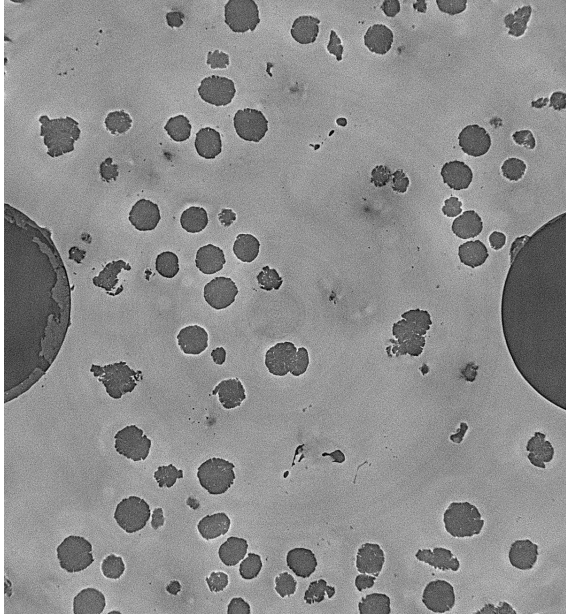
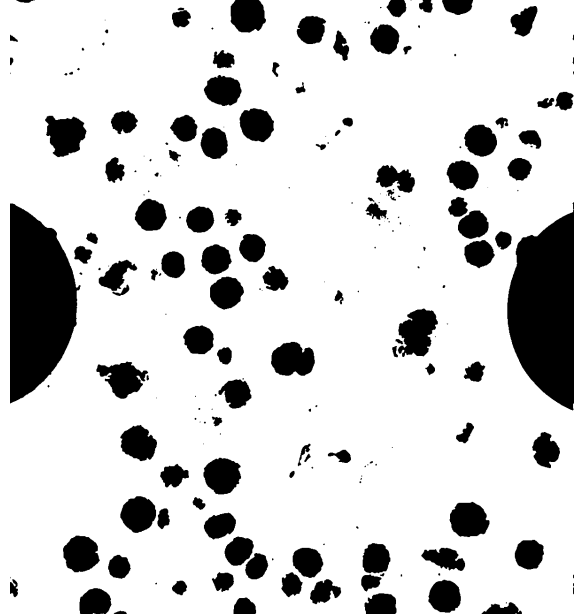


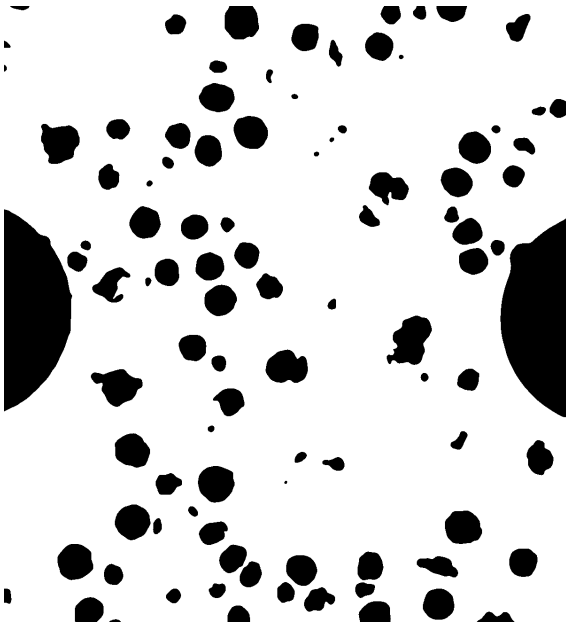
Figure 3.17: (a) Macroscopic equivalent strain and (b) stress, (c) void volume fraction, (d) void growth, and equivalent strain in (e) probe 1 (f) probe 2 for the 45° simulation obtained after segmentation with two different classifier models.



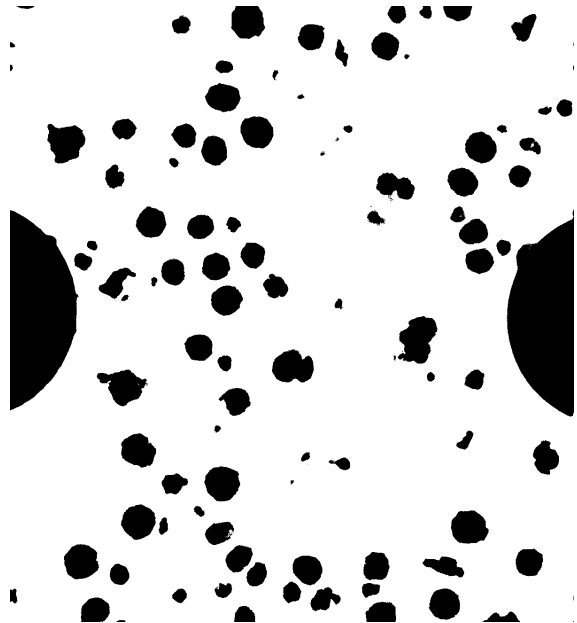
(a) Original image



(b) Thresholding



(c) IsoData



(d) Random forest

Figure 3.18: Original mid-thickness slice of the 90° specimen, and the same slice segmented with three different procedures.

level corrections. In the following, linear corrections are considered

$$g_{th} = a f_{th} + b \quad (3.2)$$

where a and b are obtained by least squares minimization of the sum of squared gray level differences over the region of interest (ROI) so that

$$r(\mathbf{x}) = f(\mathbf{x}) - g_{th}(\mathbf{x}) \quad (3.3)$$

will measure the gray level residuals that are computed for any voxel location \mathbf{x} in the ROI. In Table 3.2, the three different methods are compared for both specimens in terms of their root mean square residuals r_{RMS} . The r_{RMS} values are very similar across the three procedures and both specimens, *i.e.*, the segmented images are of comparable quality irrespective of the segmentation procedure.

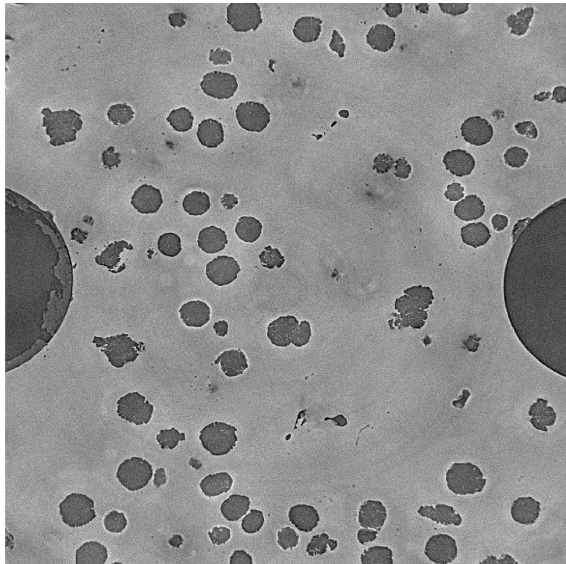
Table 3.2: Comparison of the gray level residuals for the three thresholding methods for the entire ROI in both specimens.

Procedure	a	b	RMS(r)	Specimen
Thresholding	-0.256	151.7	22.3	90°
IsoData	-0.243	151.1	23.5	90°
Random forest	-0.241	150.5	24.1	90°
Thresholding	-0.261	151.7	22.0	45°
IsoData	-0.249	150.9	23.3	45°
Random forest	-0.260	151.3	22.5	45°

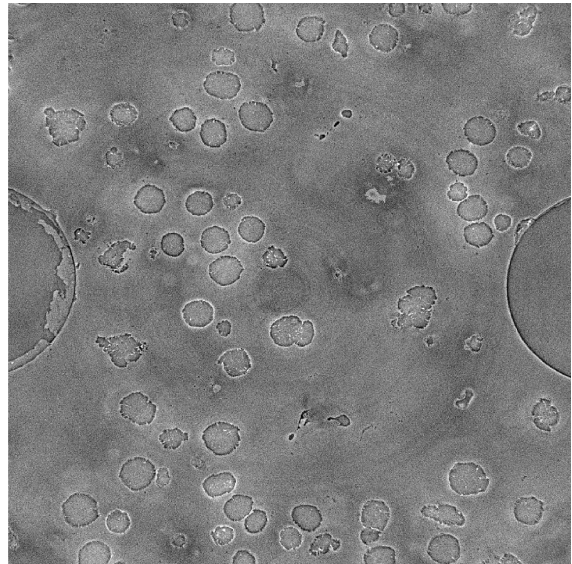
The calculated gray level residuals are shown in Figure 3.19 for the mid-thickness slice of the 90° specimen. The residuals show a very similar behavior in the bulk of the matrix and present more significant differences close to the interfaces.

For the FE simulations, neither the amount of noise left by the thresholding procedure, nor the loss of the smallest microstructural features with the other two procedures are problematic. The minimum allowed FE mesh size, which was based on the resolution of the images (Section 3.3.1), does not capture the remaining noise or the smallest features. The differences that can be perceived by the FE mesh are the non-negligible void shape variations and difference in void volume fraction due to how each method handles partial-volume effects, *i.e.*, how the position of the interfaces is determined.

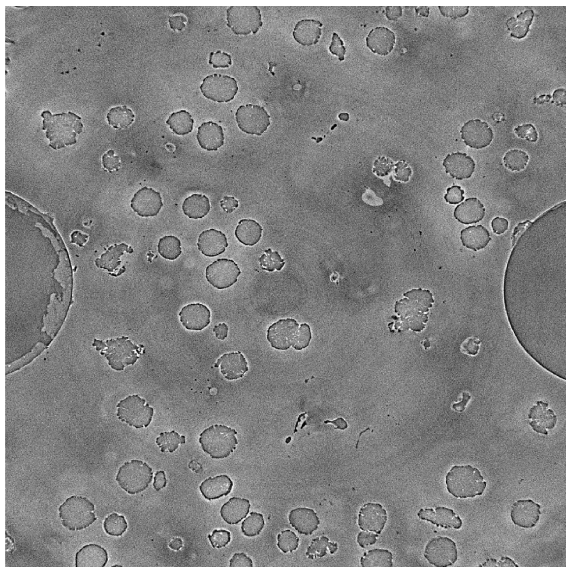
The results for the six observables with the three segmentation procedures are shown in Figure 3.20 for the 90° specimen and in Figure 3.21 for the 45° specimen. The maximum absolute difference is also reported in the figures for all the observables, and it is calculated as the maximum difference between the three results.



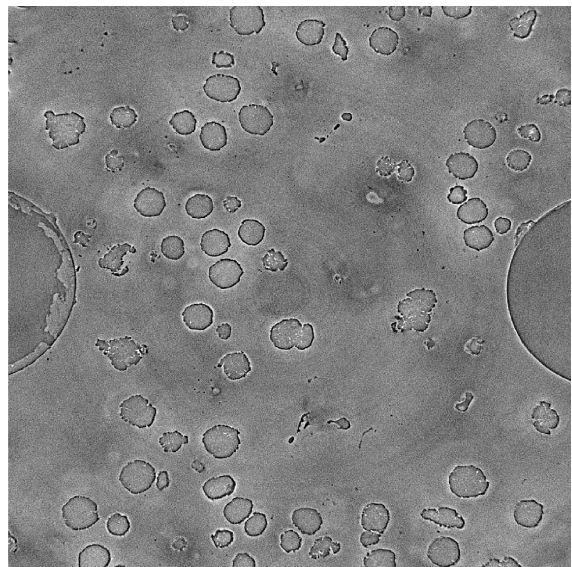
(a) Original image



(b) Thresholding



(c) IsoData



(d) Random forest

Figure 3.19: (a) Original mid-thickness slice of the 90° specimen, and the corresponding gray level residuals for the segmented image with (b) thresholding, (c) IsoData and (d) random forest algorithms.

In the simulation of the 45° specimen, the macroscopic equivalent strain and stress (Figure 3.21) exhibit a very small absolute difference. The maximum difference for the macroscopic equivalent strain is 0.0025, and 1.1 MPa for the macroscopic equivalent stress. For the 90° specimen (Figure 3.20), these variables are slightly higher, but sufficiently small, namely 0.005 and 5.2 MPa for the macroscopic equivalent strain and stress, respectively.

The void growth presents a maximum absolute difference of 0.015 for the 45° specimen (Figure 3.21d), and 0.03 for the 90° specimen (Figure 3.20d). The void volume fraction exhibits higher absolute difference than the void growth for both specimens. In the 45° simulation (Figure 3.21c), the void volume fraction has a maximum absolute difference of 0.005, and 0.014 in the 90° simulation (Figure 3.20d). In the former specimen, the IsoData and Random forest algorithms coincide remarkably, while for the latter specimen, both thresholding methods produce similar results and the void volume fraction predicted with the random forest algorithm is farther away.

The results in the local probes are more sensitive than the macroscopic observables. For both specimens (Figure 3.20e for the 90° specimen and Figure 3.21e for the 45° specimen), the equivalent strain in probe 1 has a lower maximum absolute difference (*i.e.*, 0.013 for the 90° specimen, and 0.007 for the 45° sample) than the equivalent strain in probe 2 (0.085 for the 90° specimen, and 0.014 for the 45° sample). The absolute difference for probe 2 in the 90° simulation is notably high. Since probe 2 of the 90° specimen is smaller and located in a shorter intervoid ligament, it is more sensitive to changes in its neighborhood due to the use of different segmentation procedures. In general, the proximity of a probe to void interfaces is correlated with higher levels of absolute differences. The DVC standard equivalent strain resolutions were estimated to be 0.78% for the 90° configuration and 0.73% for the 45° [123]. The segmentation-related uncertainty is at best equivalent (probe 1 of the 45° specimen) to the DVC uncertainties, but between 2 and 10 times higher for the other magnitudes.

The comparisons carried out herein show that the results of the FE simulations with immersed images stemming from the employed segmentation methods, are sufficiently small so that physical conclusions may be drawn from the results of the simulations and the segmentation procedures are hence considered to be successful. The most sensitive variables to the choice of segmentation method could be identified, namely, the local strain values and the void volume fraction.

In terms of user input, automatic thresholding with the IsoData algorithm is the least demanding methodology since it requires no user intervention. It is followed by simple thresholding by inspection for which the threshold is set from the gray level histogram. The Random forest procedure needs user input for the training of the model, and possibly the choice of parameters and filters if their default values are unsatisfactory. The need for user input may hinder the application of a methodology in an automatic procedure starting at the image acquisition and continuing all the way up to the postprocessing of the FE simulations. How-

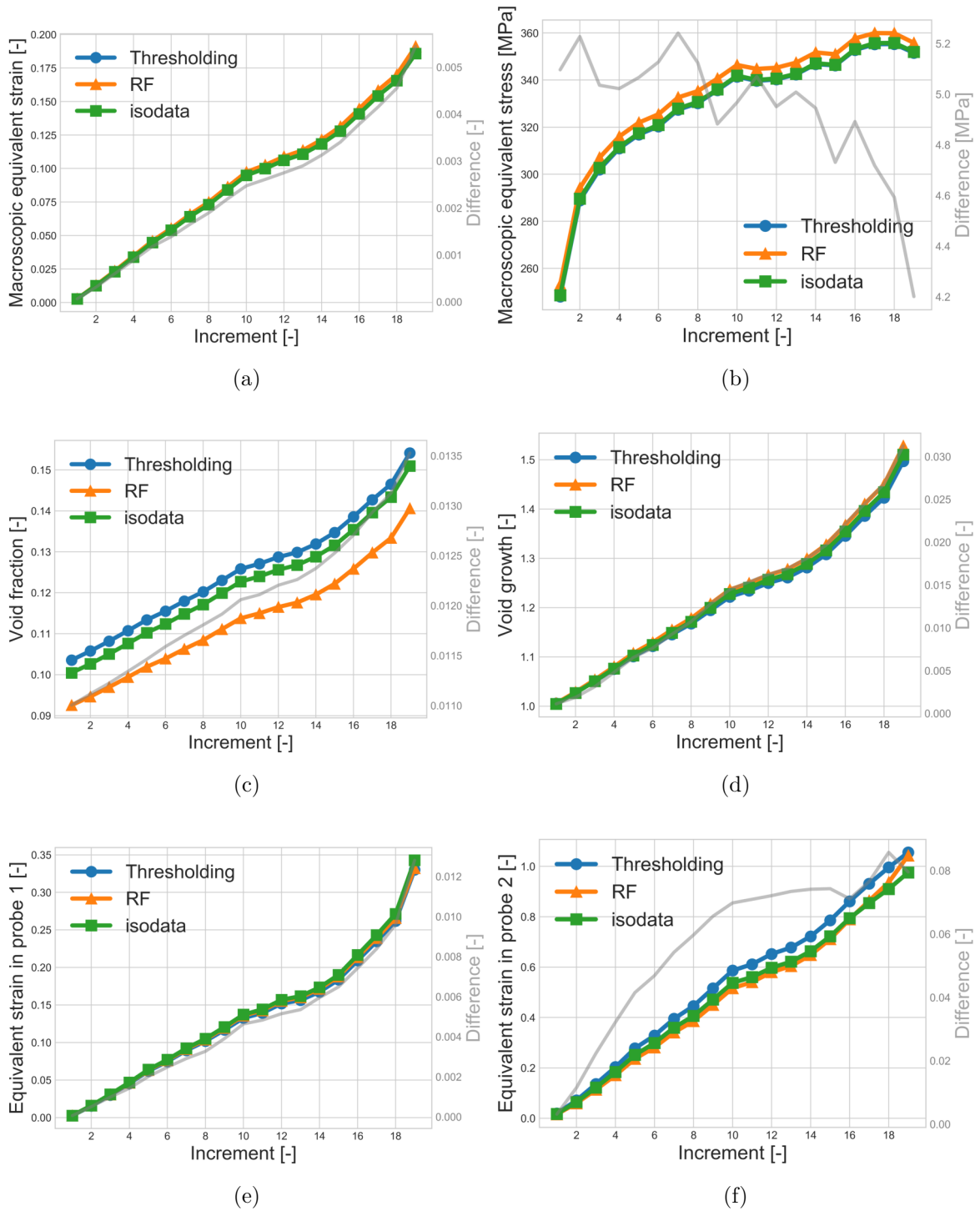


Figure 3.20: (a) Macroscopic equivalent strain and (b) stress, (c) void volume fraction, (d) void growth, and equivalent strain in (e) probe 1 (f) probe 2 for the 90° simulation obtained after segmentation with three different segmentation procedures.

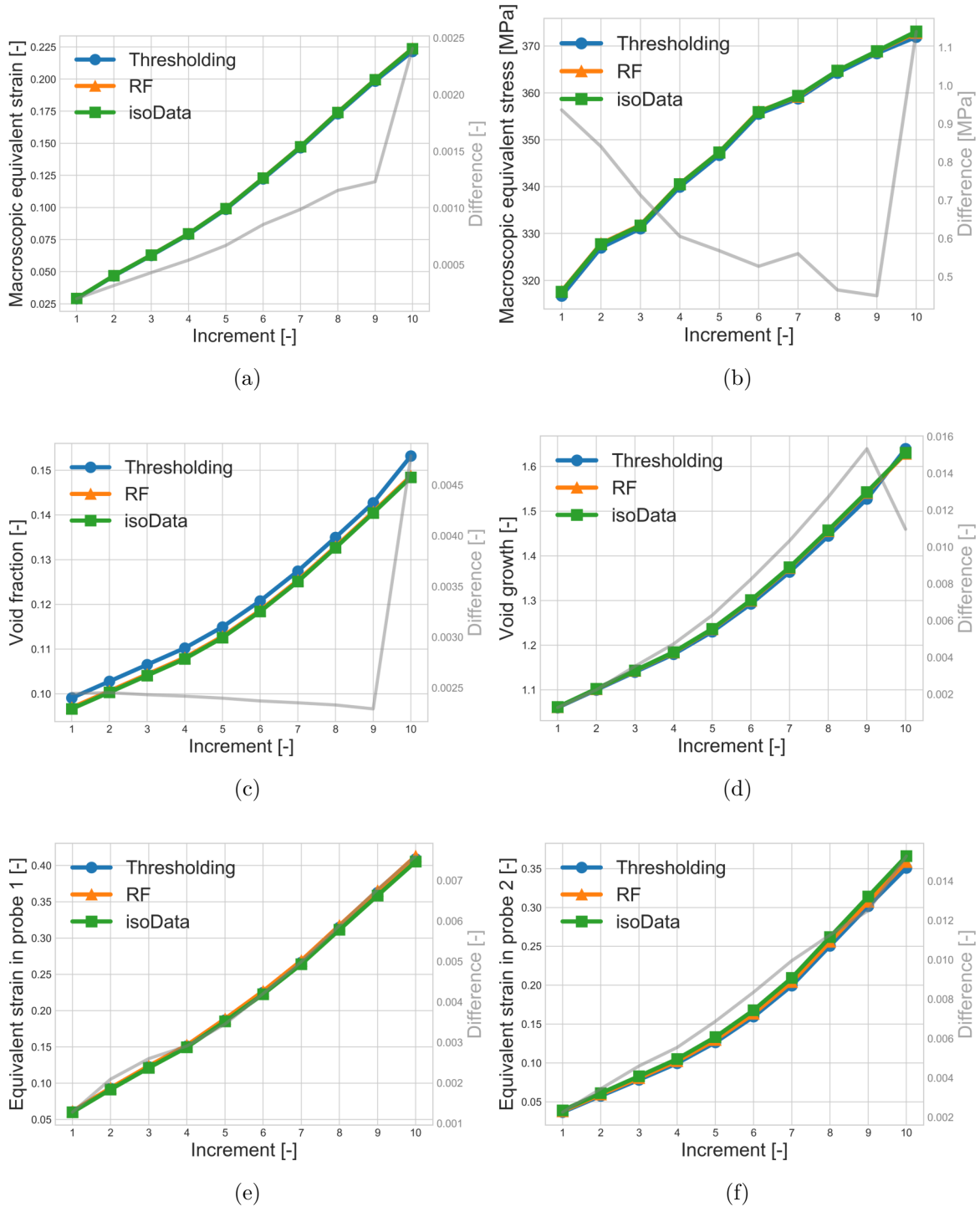


Figure 3.21: (a) Macroscopic equivalent strain and (b) stress, (c) void volume fraction, (d) void growth, and equivalent strain in (e) probe 1 (f) probe 2 for the 45° simulation obtained after segmentation with three different segmentation procedures.

ever, the two latter methodologies may also be incorporated into a fully automated procedure given that the step that requires user input can be carried out once and applied to several cases of similar features.

The manual and automatic thresholding procedures may easily be carried out with limited computing resources. The random forest procedure does require more significant resources in terms of memory and computing time. For this reason, it may be reserved for more complex cases in which thresholding is not viable if the needed computational capacity is not available. More generally, even in cases when thresholding is feasible, it may still be desirable to use the random forest algorithm to provide means for cross-verification.

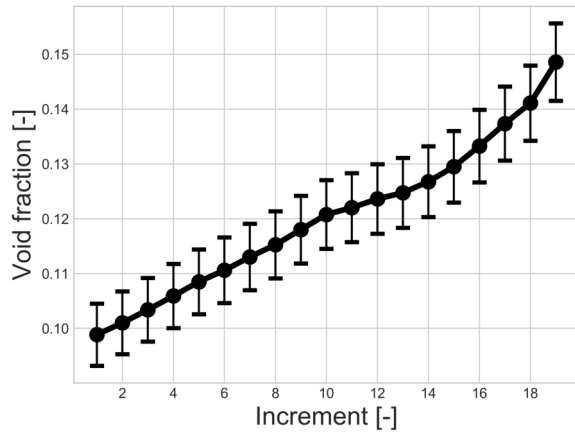
3.3.4 Uncertainty quantification

The comparison of segmentation procedures discussed in Section 3.3.3 is summarized via uncertainty estimations. Three different predictions resulting from the three considered segmentation procedures are available for each observable. To estimate its uncertainty, the average and standard deviation are calculated. This is done separately for each of the observables. The calculated averages and standard deviations are not statistically representative quantities because they are calculated based on only three data sets. They are used here as a concise way of presenting a single measurement and its associated uncertainty. This will be useful when this data is later compared with experimental measurements. The uncertainty estimation was carried out for all of the observables and both samples. The results described in Section 3.3.3 showed that global volume-averaged strain and stress, as well as void growth, are not very sensitive to the choice of the segmentation procedures employed in this chapter. For the sake of brevity, the uncertainty for the most sensitive variables is discussed in this section.

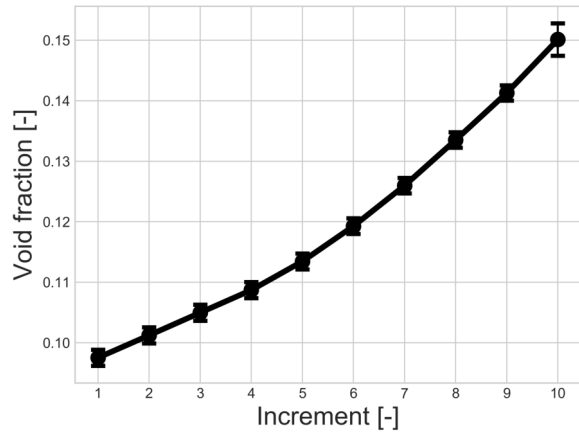
Figure 3.22 shows the change of the average void volume fraction for both specimen, and Figure 3.23, that of the average equivalent strain for the two probes of the 90° simulations. In both figures, the corresponding standard deviation is presented as error bars.

The difference of uncertainties reported for the void volume fraction between the two specimens in Figure 3.22 is noteworthy. This difference exists even though the same segmentation methodologies were applied. Ambiguous determination of the position of interfaces due to partial-volume effects and human factors during data treatment are at the origin of this difference. This observation highlights the importance of dedicating sufficient effort to the image segmentation step and uncertainty estimation when feasible. A disregard of present uncertainties may lead to biased physical conclusions.

Since probe 2 is located in a small intervoid ligament, i.e., it is closer to the void-matrix interface, it presents larger uncertainties than probe 1. For both probes the uncertainty,

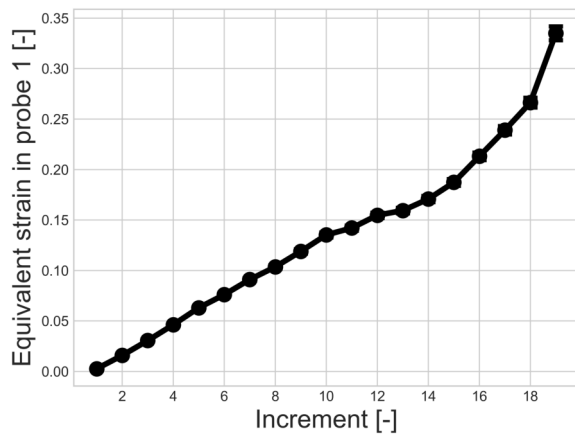


(a) 90° specimen

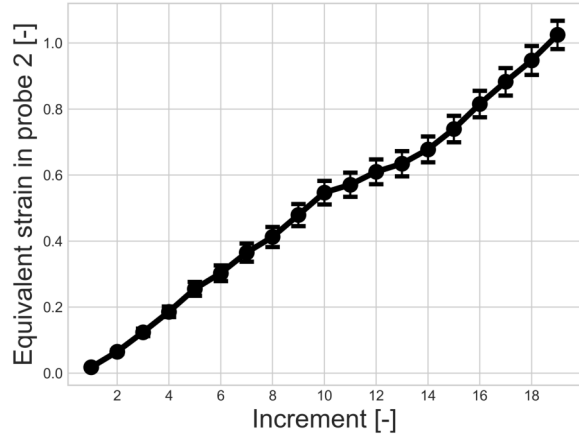


(b) 45° specimen

Figure 3.22: Average of the results of the three segmentation procedures for the void volume fraction with its estimated uncertainty in (a) the 90° simulation, and (b) the 45° simulation.



(a) Probe 1



(b) Probe 2

Figure 3.23: Average of the results of the three segmentation procedures in the 90° simulation for the equivalent strain (a) in probe 1 and (b) probe 2.

depicted in Figure 3.23, increases during the simulation, but remains satisfactorily small.

3.4 Conclusions and perspectives

A comparative study of three segmentation procedures dedicated to the SRCL-DVC-FE methodology was carried out in the context of micromechanical studies of ductile damage. The focus of the conducted analysis was on the effect of image segmentation techniques on the results of FE simulations. Different segmentation procedures were considered, and three were selected and presented in detail. They satisfactorily segmented the three-dimensional images. Six different observables were taken into account for each of the two studied nodular graphite cast iron samples (*i.e.*, macroscopic equivalent strain and stress, void volume fraction and growth, and local equivalent strain in two probes in different intervoid ligaments). To the best of the author's knowledge, this is the first work to document and quantify the effect of image segmentation on the mechanical results of simulations of immersed microstructures. This is relevant for all simulations with immersed microstructures and not only for the SRCL-DVC-FE framework.

The three segmentation procedures were compared in terms of the resulting gray level residuals, of the required computing power and of the required user input. The gray level residuals were very similar for the different procedures. For this reason, the choice of preferred segmentation method depends on the complexity of the problem, the available computing power and the acceptable level of user input. Multiple methods should be employed and compared whenever possible.

First, a mesh sensitivity analysis was conducted to check that the influence of the spatial discretization on the observables was sufficiently small. Care was taken not to use mesh sizes smaller than the order of magnitude of the laminography images resolution. The most sensitive parameters were identified, namely, the local strain values and the void volume fraction, and sufficiently small mesh dependence was reached.

Second, the segmented images were then immersed in an FE mesh and micromechanical calculations with realistic boundary conditions were carried out. The results were compared in terms of the six different observables. A small sensitivity for the macroscopic behavior was found. A maximum relative difference less than 3% was obtained for the macroscopic strain and stress. It is believed that this overall agreement is mainly due to the fact that the (same) measured boundary conditions were prescribed. The void volume fraction and the local strains were the most sensitive variables. The void volume fraction was considerably more sensitive for the 90° specimen (maximum absolute difference of 0.014) than for the 45° specimen (maximum absolute difference of 0.005). The maximum difference in the local strain measures varied from 0.007 to 0.085 and increased with the proximity of the probed volume to the void-matrix interface.

The differences in uncertainty for the void volume fraction across specimens resulted from applying the same segmentation procedures in the same material by the same operator. This highlights the challenges associated with the use of immersed images in FE simulations. They originate from two factors, namely, the ambiguity in the position of the segmented interfaces due to partial-volume effects, and the possible bias introduced by the operator.

An uncertainty quantification based on the comparison of segmentation methods was proposed. Since FE simulations were based on three different segmentation procedures, the uncertainty of an observable was estimated as the standard deviation of the results of the three FE simulations and reported alongside the corresponding average. The estimated uncertainty will be used in the following chapters to compare in detail numerical results with experimental observations for validation purposes.

Résumé en français

Une étude comparative de trois procédures de segmentation dédiées à la méthodologie SRCL-DVC-FE a été réalisée dans le cadre d'études micromécaniques sur l'endommagement ductile. L'analyse menée a porté principalement sur l'effet des techniques de segmentation d'images sur les résultats des simulations par éléments finis. Différentes procédures de segmentation ont été envisagées, et trois ont été sélectionnées et présentées en détail dans ce chapitre pour segmenter de manière satisfaisante les images volumiques.

Six observables différentes ont été prises en compte pour chacun des deux échantillons de fonte à graphite sphéroïdal qui ont été étudiés (c'est-à-dire contrainte et déformation macroscopiques équivalentes, fraction volumique de porosité et croissance, et déformation équivalente locale dans deux capteurs différents dans des ligaments inter-cavités). À la connaissance de l'auteur, il s'agit du premier travail à documenter et à quantifier l'effet de la segmentation d'images sur les résultats mécaniques de simulations de la rupture ductile de microstructures immergées. Ceci est pertinent pour toutes les simulations avec des microstructures immergées et pas seulement pour la méthodologie SRCL-DVC-FE.

Les trois procédures de segmentation ont été comparées en termes de résidus de niveau de gris, de la puissance de calcul requise et du degré requis d'intervention de l'utilisateur l'entrée utilisateur. Les résidus de niveau de gris se sont avérés très similaires pour les différentes procédures. Pour cette raison, le choix de la méthode de segmentation préférée dépend de la complexité du problème, de la puissance de calcul disponible et du niveau acceptable d'intervention de l'utilisateur. Tout d'abord, une analyse de sensibilité au maillage a été réalisée pour vérifier que l'influence de la discrétisation spatiale sur les observables était suffisamment faible. On a pris soin de ne pas utiliser des mailles de taille inférieure à l'ordre de grandeur de la résolution des images de laminographie. Les paramètres les plus sensibles ont été identifiés, à savoir les valeurs de déformation locales et la fraction volumique de

porosité. Une dépendance suffisamment faible au maillage a été observée.

Deuxièmement, les images segmentées ont ensuite été immergées dans un maillage FE et des calculs micromécaniques ont été effectués avec des conditions limites réalistes. Les résultats ont été comparés pour 6 observables différentes. Une faible sensibilité pour le comportement macroscopique a été trouvée. Une différence relative maximale inférieure à 3% a été obtenue pour la déformation et la contrainte macroscopiques. On pense que cet accord général est principalement dû au fait que les conditions limites mesurées ont été prescrites. La fraction volumique de porosité et la déformation dans les capteurs locaux sont les variables les plus sensibles. La fraction volumique de porosité s'est révélée considérablement plus sensible pour l'échantillon à 90° (différence absolue maximale de 0,014) que pour l'échantillon à 45° (différence absolue maximale de 0,005). La différence maximale entre les mesures de déformation locales variaient de 0,007 à 0,085 et augmentaient avec la proximité du capteur vis-à-vis de l'interface matrice-porosité.

Les différences d'incertitude concernant la fraction volumique de porosité entre les échantillons résultent de l'application des mêmes procédures de segmentation dans le même matériau par le même opérateur. Cela met en évidence les défis associés à l'utilisation d'images immergées dans les simulations FE. Ils proviennent de deux facteurs, à savoir l'ambiguïté de la position des interfaces segmentées due aux effets de volume partiel et le biais possible introduit par l'opérateur. Une quantification de l'incertitude basée sur la comparaison des méthodes de segmentation a été proposée. Les simulations FE étant basées sur trois procédures de segmentation différentes, l'incertitude d'une observable a été estimée en tant qu'écart-type des résultats des trois simulations et rapportée avec moyenne correspondante. L'incertitude estimée sera utilisée dans les chapitres suivants pour comparer en détail les résultats numériques aux observations expérimentales pour valider la méthodologie mise en place.

Chapter 4

An examination of microscopic pre-coalescence strain measures in ductile cast iron through micromechanical simulations based on 3D imaging

Contents

4.1	Introduction	84
4.2	Observables	84
4.3	Comparison of DVC and FE strain measures	87
4.3.1	90° specimen	87
4.3.2	45° specimen	91
4.4	Strain field evolution	95
4.4.1	Discussion	95
4.5	Effect of probe size on FE strain measures	103
4.5.1	Mesh sensitivity analysis	103
4.5.2	Probe size sensitivity analysis	106
4.6	Conclusions	111

4.1 Introduction

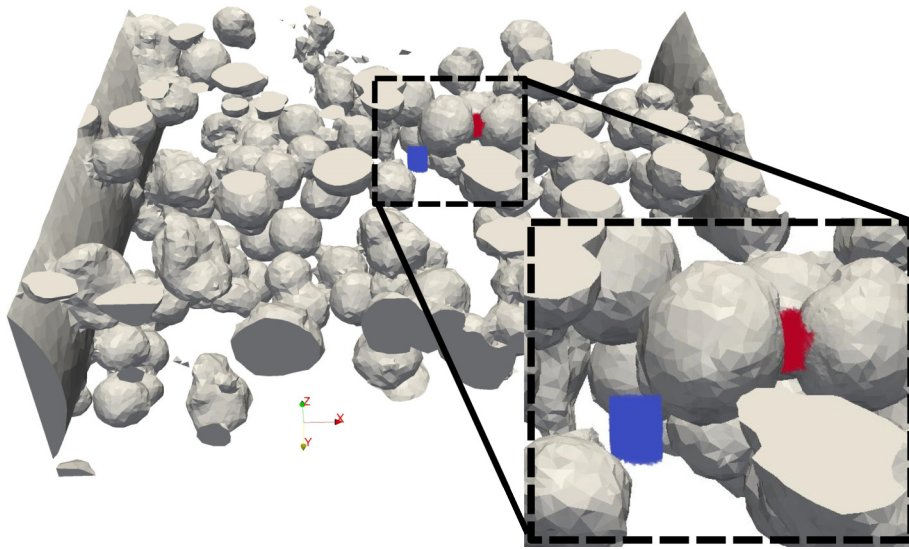
Previous studies have investigated microscopic strain measures in cast iron. Kasvayee et al. [197] carried out a comparison between strain measures predicted by finite element (FE) simulations and local strain measured with digital image correlation (DIC) in nodular cast iron. Salomonsson et al. [198] studied strain localization via 3D finite element simulations of heterogeneous cast iron microstructures and highlighted the three dimensional complexity of the strain field as the possible reason for disagreement between local predictions of strain and digital volume correlation strain measures. Buljac et al. [123] used bulk strain measures obtained with digital volume correlation (DVC) to study void coalescence mechanisms in nodular cast iron.

Critical values of local strain have been investigated as a microscopic coalescence indicator for internal necking [123, 199], void-sheet or shear band formation [48, 123, 199] and fatigue crack formation [200].

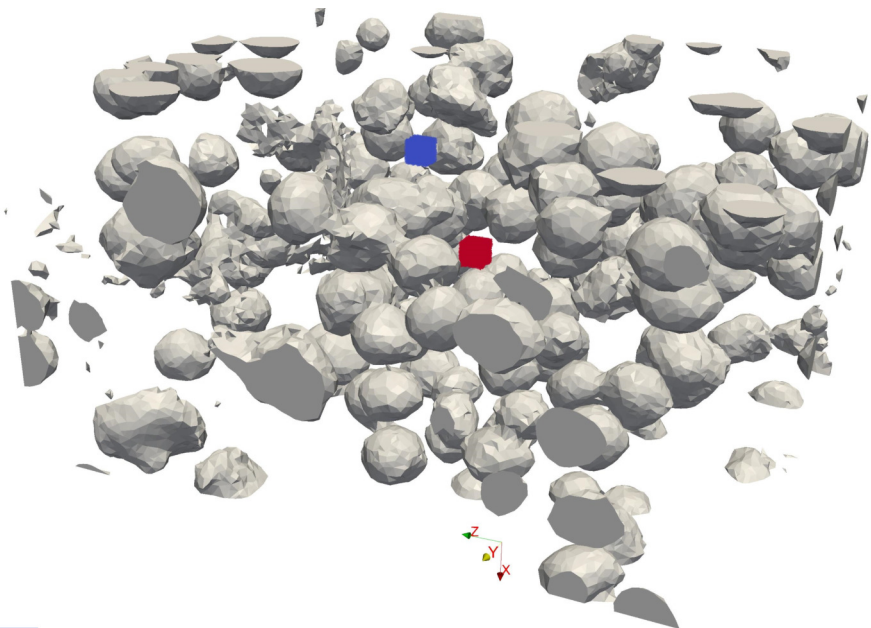
In Chapter 3, the uncertainties associated to image segmentation on mechanical observables were assessed. In this chapter, pre-coalescence strain measurements obtained with the SRCL-DVC-FE framework are compared with DVC strain measurements. The probed zones correspond to the same four probe volumes studied in Chapter 3. This allows the estimated uncertainties to be taken into account in the comparison. The objective is to validate the FE strain measurements. If the validation is satisfactory, the complementarity of the DVC and FE techniques can be exploited in a more complete study of coalescence. A first discussion of strain as a coalescence indicator is presented.

4.2 Observables

The observables assessed in this chapter were already presented in Chapter 3, but are recalled here for the sake of readability. Local strain measures at two different locations as well as a global (or macroscopic) are employed as observables for each specimen. The local strain measures correspond to the accumulated equivalent strain in cubic probes of the size of a DVC element (unless otherwise stated). The shape and size of the probes were chosen in order to facilitate a direct comparison with DVC strain results. The simulated microstructural region is shown in Figure 4.1a and in Figure 4.1b for the 90° and 45° specimens, respectively. Probe 1 (in blue) of each specimen has previously been associated with the void-sheet coalescence mechanism and probe 2 (in red) with internal necking. Two-dimensional slices showing the observed coalescence instances are presented in Figure 4.2 for the 90° specimen and in Figure 4.3 for the 45°.



(a)



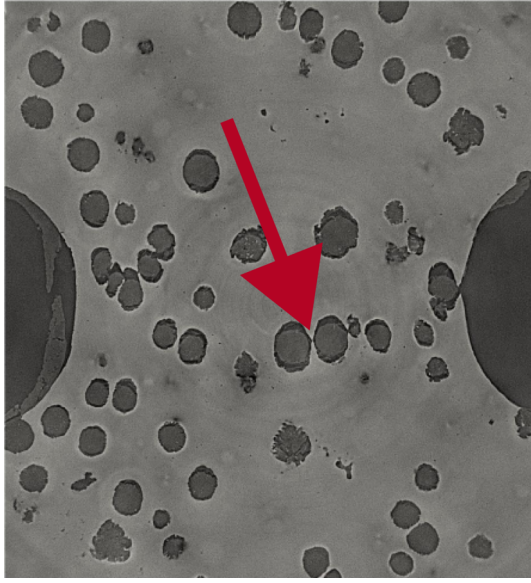
Probe corresponding to observed void-sheet coalescence



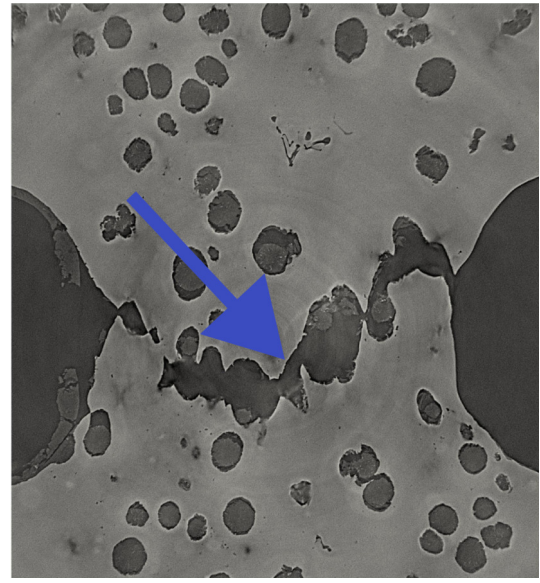
Probe corresponding to observed internal necking coalescence

(b)

Figure 4.1: 3D view of the simulated microstructure for the a) 90° specimen and the b) 45° specimen. Local probe volumes are shown in blue (probe 1) and red (probe 2). A local zoom displays probe of the 90° specimen.

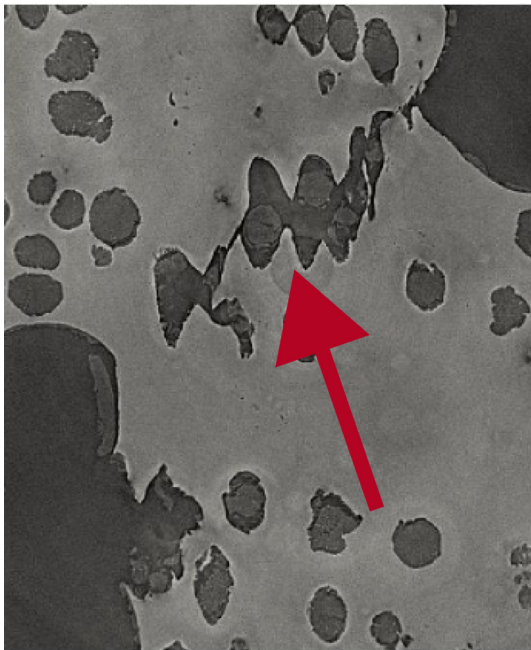


(a)

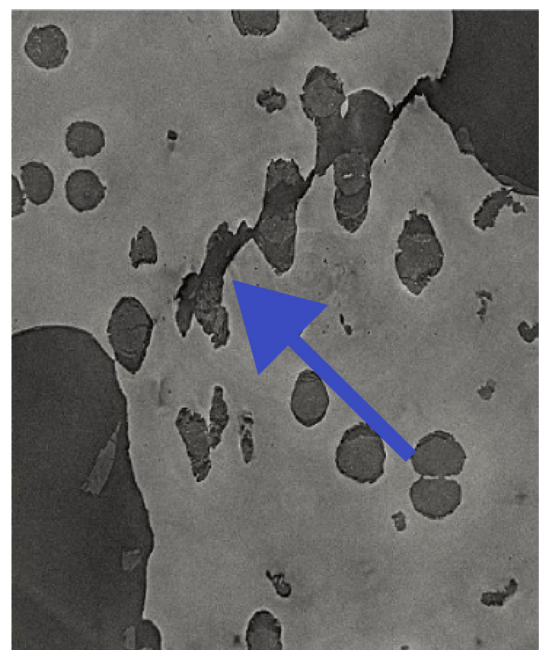


(b)

Figure 4.2: Slices containing the observed coalescence instances for (a) internal necking and (b) void-sheet coalescence in the 90° specimen.



(a)



(b)

Figure 4.3: Slices containing the observed coalescence instances for (a) internal necking and (b) void-sheet coalescence in the 45° specimen.

4.3 Comparison of DVC and FE strain measures

In this section, a comparison of macroscopic and local strain measures obtained from DVC and FE calculations, is presented for the 90° and 45° specimens. The local FE strain measures are calculated in cubic probes with the size of a DVC element in order to be as consistent as possible with the DVC measurements. An estimation of the segmentation-related uncertainty was previously carried out in Chapter 3, and the FE strain measures presented in this section are a result of this procedure. The procedure consisted in carrying out three different FE simulations, each with an immersed microstructure originated from a segmented image with a different segmentation method. Each FE strain measure corresponds thus to the average of these three strain measures and the corresponding standard deviation is reported as the estimated uncertainty.

4.3.1 90° specimen

Figure 4.4 shows the comparison of DVC and FE results in terms of the macroscopic equivalent strain of the 90° specimen along with the absolute difference between the two datasets. A very good agreement is observed up to increment 10. Afterwards the FE simulation overestimates the DVC results with an increasing difference that reaches 2% of strain at the final increment. A good agreement for the macroscopic strain was expected since the FE simulations are driven by displacements obtained by means of DVC.

A comparison of the DVC and FE strain measures in probe 1 of the 90° specimen is presented in Figure 4.5. A remarkably good agreement is observed between the two measures except for the last increment where the DVC strain experiences an accelerated increase that the FE simulation does not manage to capture. Figure 4.5 also presents the contours of the void phase obtained from the FE simulation superimposed with the corresponding slice of the laminography images for three different increments. The approximate position of probe 1 is indicated by a blue square.

DVC and FE strain measures in probe 2 of the 90° specimen are reported in Figure 4.6. Although coalescence occurs at increment 11 by internal necking in the ligament that contains probe 2, the results are reported up to the end of the simulation for the sake of completeness. It is possible to do this with the FE results because the probe deforms with the matrix and during coalescence, it flows out of the disappearing intervoid ligament. The reported strain measure in probe 2 is in this sense no longer associated to the intervoid ligament after increment 11. DVC results are also reported after coalescence since the DVC analysis provides kinematic fields in the whole ROI independently of the phases.

The DVC and FE results in probe 2 present a very good agreement up to increment 16 with an approximately constant strain difference in the order of 0.01. In the following

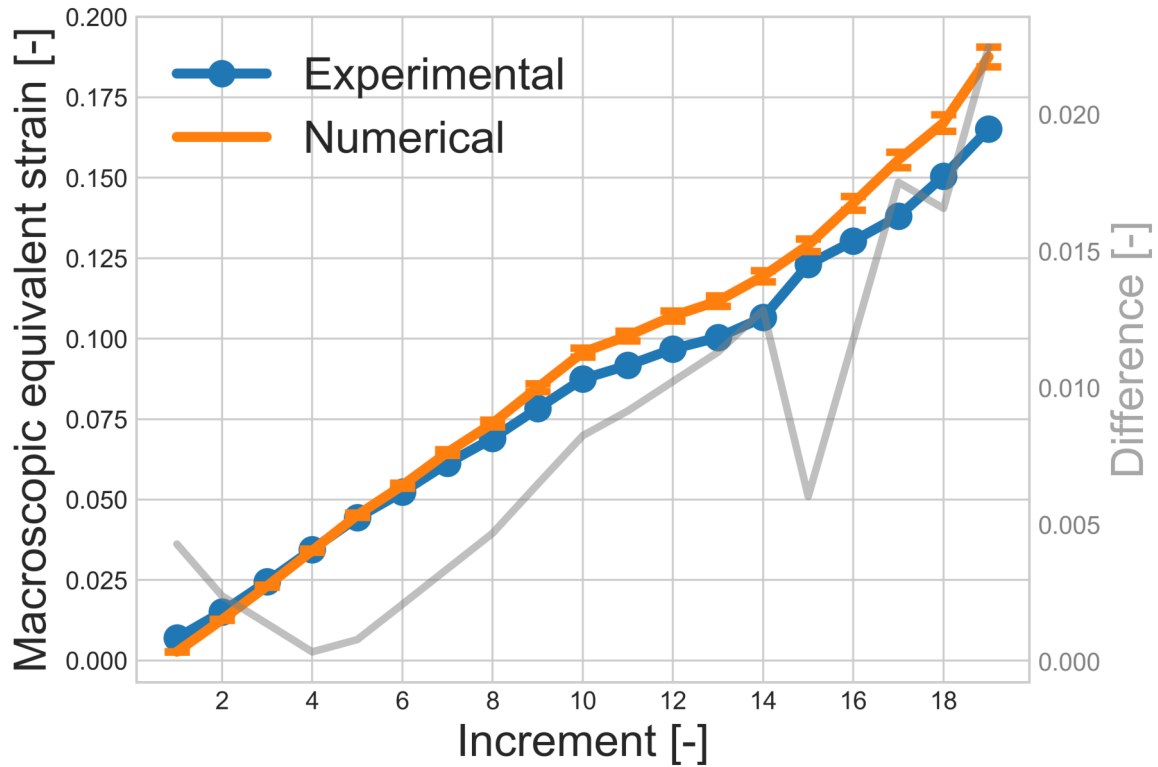


Figure 4.4: Comparison of DVC and FE macroscopic equivalent strain measures for the 90° specimen. The absolute difference is reported as a gray line.

increments and up to the end of the simulation, the DVC values increase at a much higher rate than the FE values. A final and maximum strain difference of 0.20 is obtained.

In the 90° specimen simulation, the magnitude of the reported segmentation-related uncertainty for the macroscopic strain and the strain in probe 1, is negligible with respect to the magnitude of the difference between the DVC and FE measures [201]. However, for the strain in probe 2, the uncertainty increases considerably during the simulation and is in the same order of magnitude as the strain. The reason for this difference between probe 1 and probe 2 is that the intervoid ligament in which probe 2 is located is not big enough to accommodate the whole DVC probe. This makes the results in probe 2 very sensitive to the position of the void-matrix interface.

As evidenced in Figures 4.5 and 4.6, void growth and shape evolution are generally described satisfactorily. There are, however, some minor discrepancies in the position of the interfaces between the FE simulations and the laminography images. In some instances, void growth is underestimated and in others, overestimated. The magnitude of these discrepancies increases during the simulation.

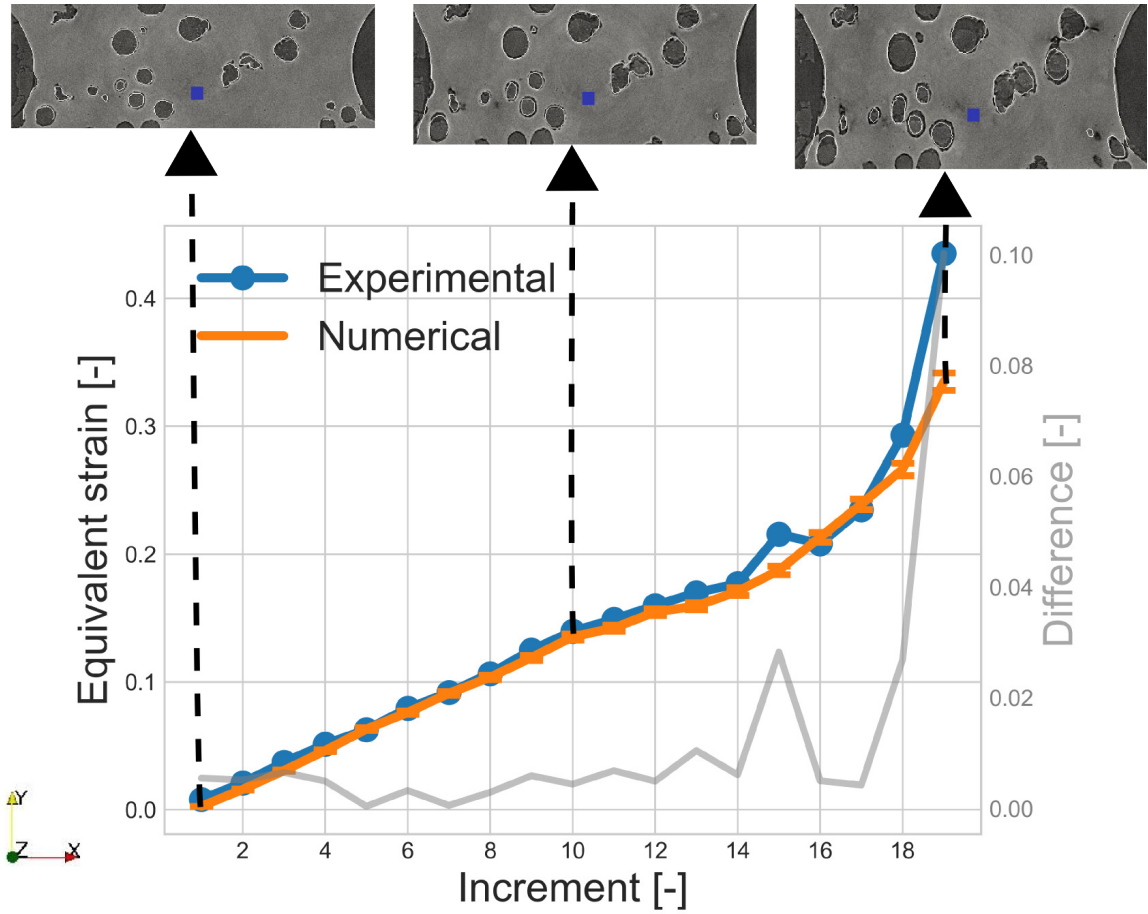


Figure 4.5: Comparison of DVC and FE equivalent strain measures in probe 1 of the 90° specimen. For 3 different increments, a slice of the original image is superimposed with the interface according to the FE simulation. The approximate position of the probe 1 is marked with a blue square. The absolute difference is reported as a gray line.

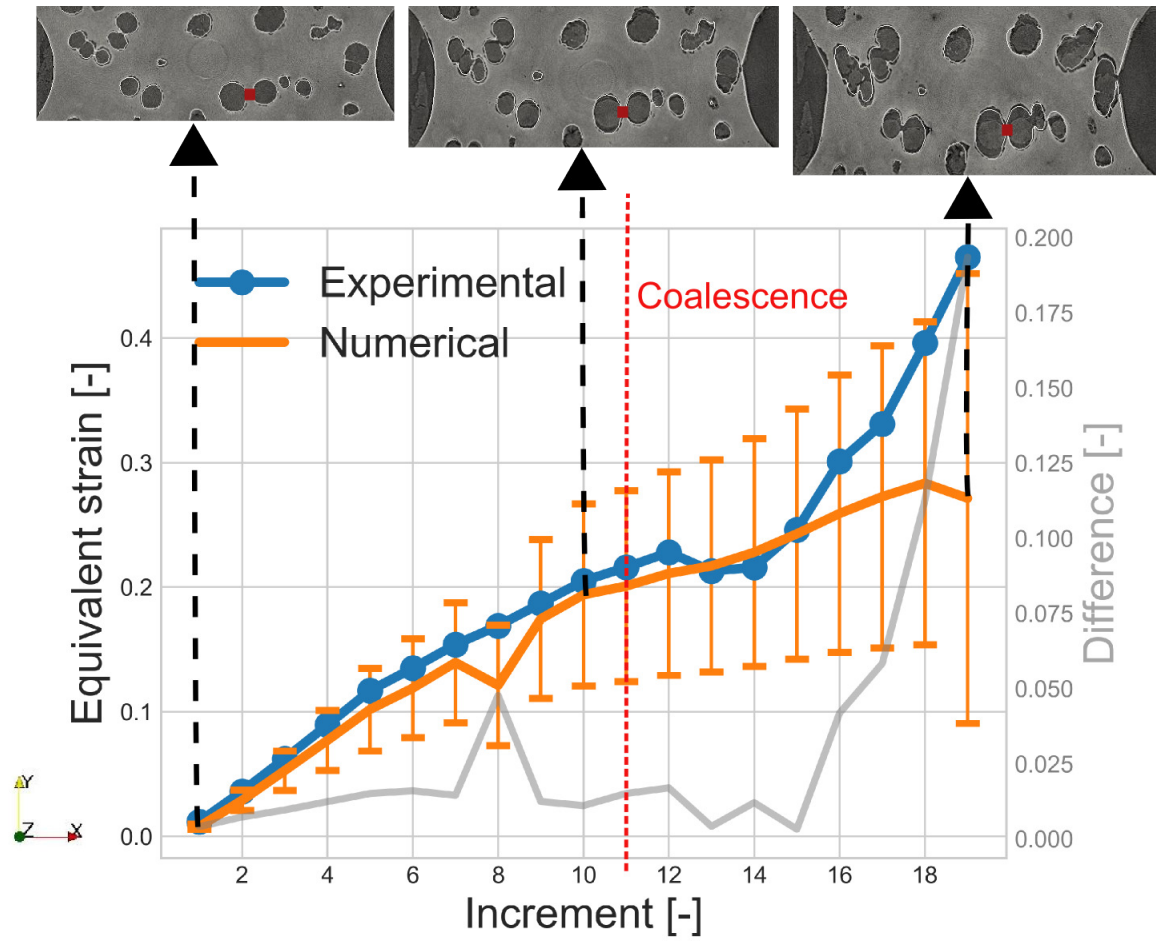


Figure 4.6: Comparison of DVC and FE equivalent strain measures in probe 1 of the 90° specimen. For 3 different increments, a slice of the original image is superimposed with the interface according to the FE simulation. The approximate position of the probe 2 is marked with a red square. The absolute difference is reported as a gray line.

4.3.2 45° specimen

In the case of the 45° specimen (Figure 4.7), the FE macroscopic equivalent strain overestimates slightly the DVC value for the first two increments. Then the two values coincide remarkably well up to increment 7 where the DVC strain values start to show an accelerated increase that is not well reproduced by the FE simulation. At the end of the simulation, a maximum strain difference of 0.04 is registered.

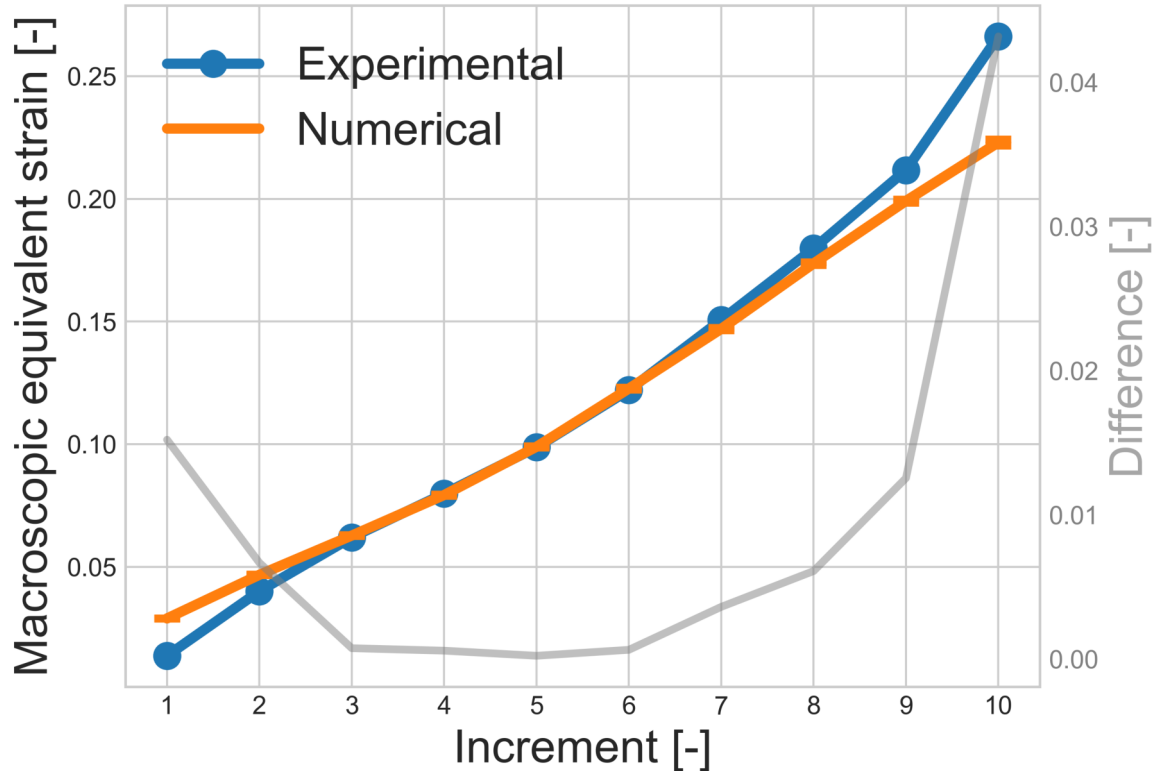


Figure 4.7: Comparison of DVC and FE macroscopic equivalent strain measures for the 45° specimen. The absolute difference is reported as a gray line.

Although the FE simulation of the 45° specimen reproduces well the rate of increase of strain at the local probes, it significantly overestimates the DVC strain values for probe 1 (Figure 4.8) and underestimates the DVC strain values for probe 2 (Figure 4.9). Similarly to the macroscopic equivalent strain, the DVC measured values at the probe volumes show an accelerated increase towards the end of in-situ test, that is not reproduced by the FE simulation. A maximum strain difference of 0.08 is observed for probe 1, and of 0.10 for probe 2.

In contrast with the 90° specimen, an initial gap between both strain measurements is observed. The rate of increase, however, is very well captured except towards the end of the simulation. Probe 1 is close to a nodule whose shape is not well captured despite the use of the meshing methodology described in Chapter 2. This nodule is surrounded by a green circle in Figure 4.8 and could have an impact on the local distribution of strain.

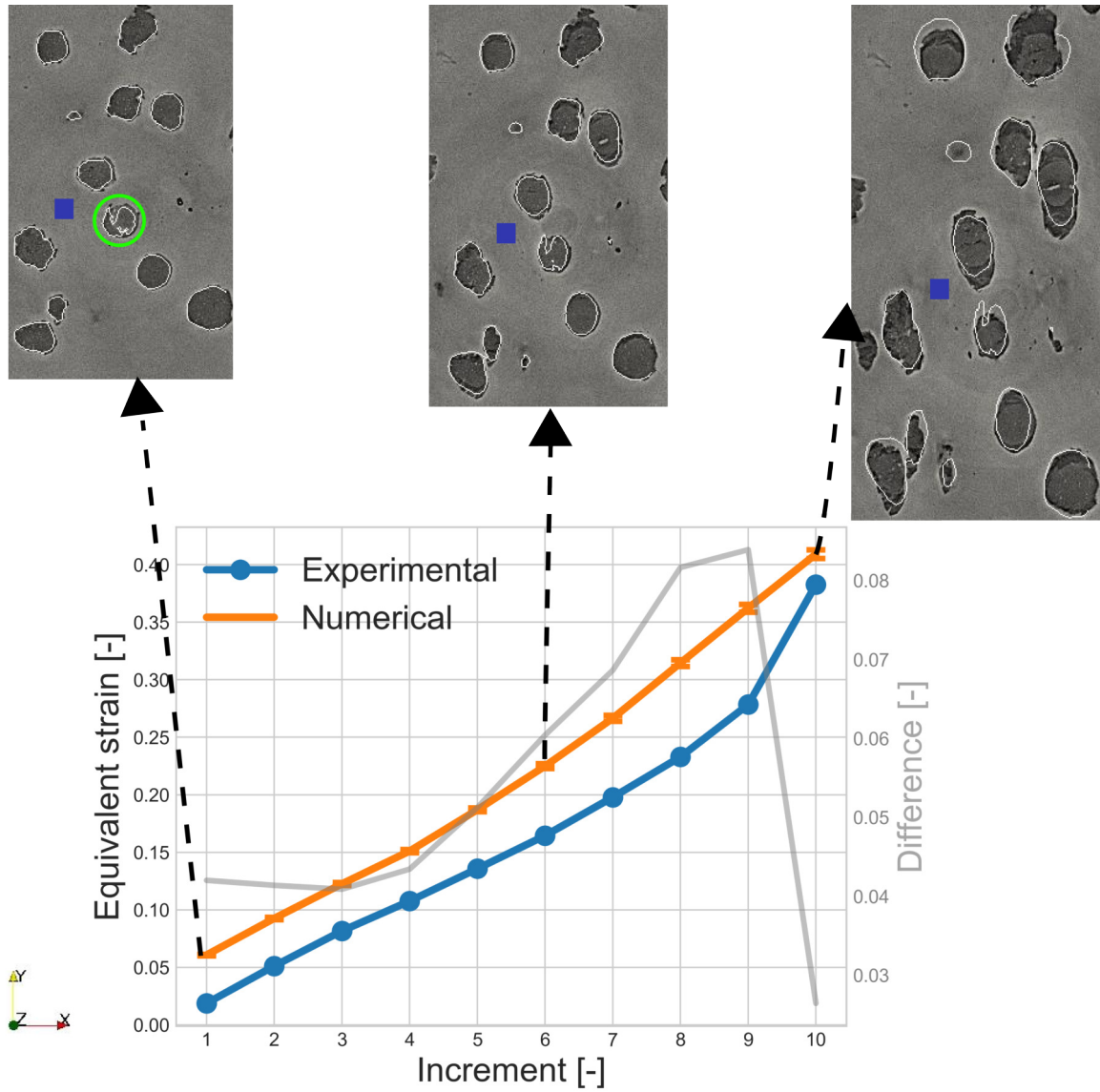


Figure 4.8: Comparison of DVC and FE equivalent strain measures in probe 1 of the 45° specimen. For 3 different increments, a slice of the original image is superimposed with the interface according to the FE simulation. The approximate position of the probe 1 is marked with a blue square. The absolute difference is reported as a gray line.

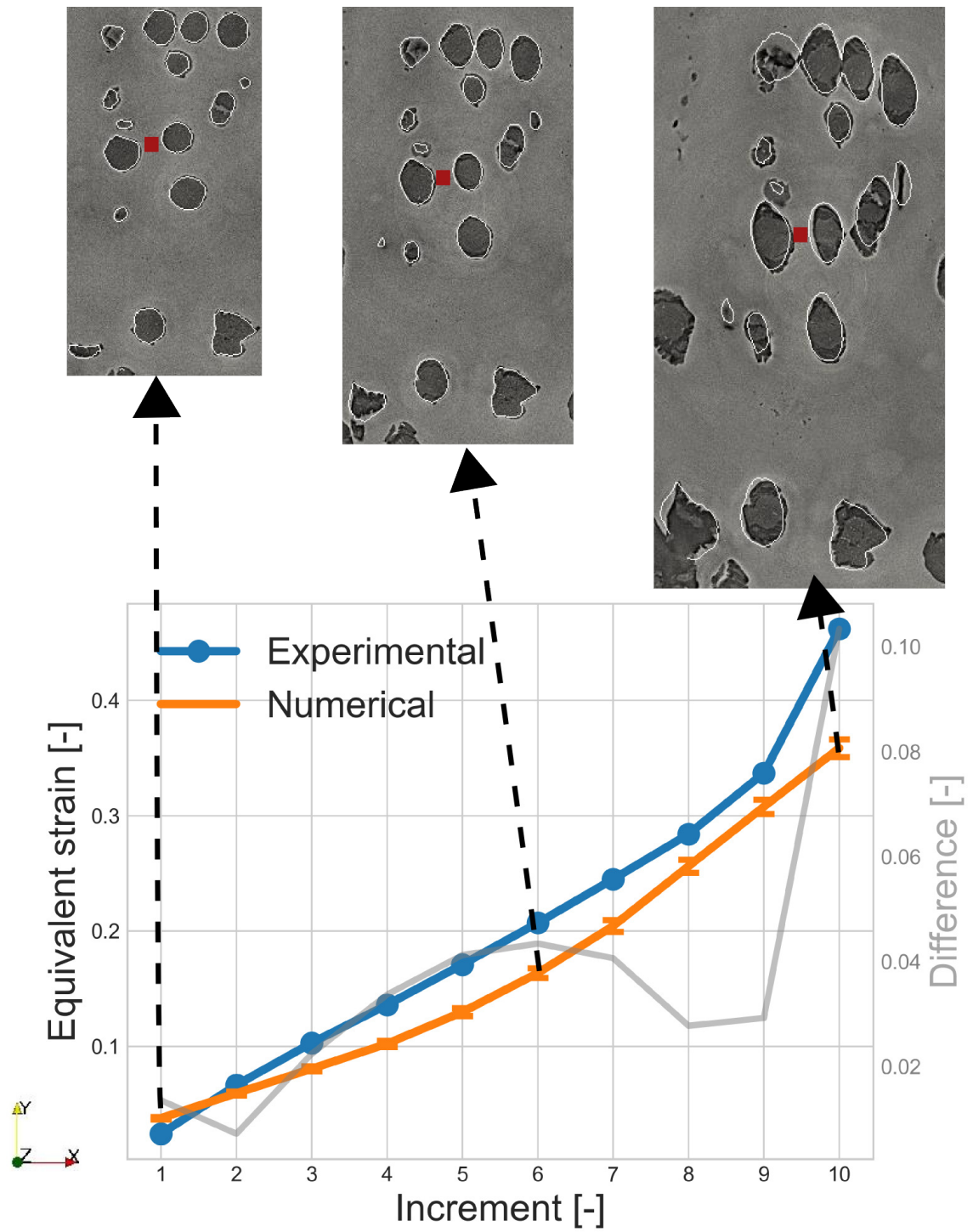


Figure 4.9: Comparison of DVC and FE equivalent strain measures in probe 1 of the 45° specimen. For 3 different increments, a slice of the original image is superimposed with the interface according to the FE simulation. The approximate position of the probe 2 is marked with a red square. The absolute difference is reported as a gray line.

Similarly to the 90° case, in the shown slices (Figures 4.8 and 4.9) of the 45° case, albeit some local differences, an overall good agreement between the predicted position of the interfaces by the FE simulations, and the laminography images, is observed. The differences increase towards the end of the simulation.

The magnitude of the segmentation-related uncertainty is significantly smaller than the difference between the DVC and FE results for the macroscopic equivalent strain of the 45° specimen and the local strain at the two probes. This uncertainty was significant only for the strain at probe 2 for the aforementioned reason (see Section 4.3.2). The influence of the segmentation procedure on the results of the simulations has been previously discussed thoroughly in Chapter 3. The comparison with the DVC results presented in this section while taking into account this uncertainty leads to the conclusion that the differences between the DVC and the FE results are attributable to current limitations in the physical and numerical framework and can be used as hints to improve the current framework.

One possible limitation of the physical modeling is pointed out by the inability of the FE simulations to reproduce the strain increase acceleration towards the end of the simulation for both specimens. This is observed in spite of efforts to calibrate the elasto-plastic material parameters at the microscale via an experimental-computational identification framework with X-ray microtomography [165]. This might point out a deficiency of the employed hardening law: excessive hardening for large strain values. A solution can be the use of hardening laws that saturate for large values of strain such as the Voce hardening law [202]. This is consistent with previous observation via *post mortem* Scanning Electron Microscopy (SEM) fractography of a smaller void population that is not visible in the laminography images due to their small size with respect to the laminography spatial resolution (2.19 μm voxel size). These smaller voids are neither modeled explicitly in the FE mesh nor considered implicitly in the behavior law. Accounting for the softening induced by the smaller void population is a perspective of this work. This could be done for example through the use of a coupled damage model in the matrix.

Despite the differences in local strain measures between DVC measurements and FE predictions in the 45° case, the results are considered satisfactory. Very good agreement was obtained for the macroscopic strain of both specimens and for the pre-coalescence local strains of the local probes of the 90° specimen. The local strain values in the probes of the 45° specimen were not predicted accurately, but their rate of increase was well reproduced. The FE strain predictions are thus considered satisfactory and can now be used for the study of void coalescence.

4.4 Strain field evolution

The strain results provided by the FE simulations were validated via comparison with DVC strain measurements in Section 4.3 and their limitations as well as future aspects to be improved were discussed. After this validation, the FE results can be analyzed with confidence in a study of void coalescence. To initiate this study, the evolution of the strain field in given slices of the domain is presented in this section.

Figure 4.10 presents the evolution of the strain field for the 90° specimen in the slice that contains probe 1 superimposed with the corresponding slice of the laminography images. The approximate location of the probe is indicated by a blue square for the first increment. Although considerable void growth is evidenced, no coalescence instances are observed. Intense strain bands are developed between neighboring voids. The strain bands can span multiple voids. The intervoid ligament that contains probe 1 is larger than those ligaments that typically present strong strain concentration bands. This intervoid ligament presents a strain band in zigzag pattern and a round and more intense strain concentration zone in a corner of this zigzag pattern. A green line indicates the position of the zigzag pattern in Figure 4.10c.

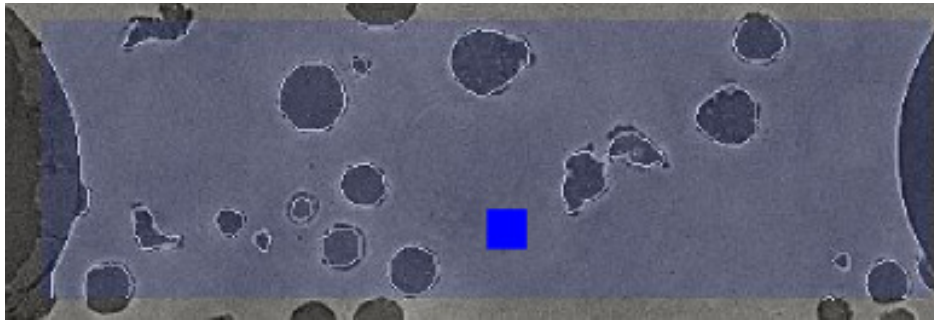
The strain field evolution in the slice containing probe 2 of the 90° specimen is described in Figure 4.11. In this slice, intense strain bands can be observed between neighboring voids that are very close to each other as early as at increment 5 (Figure 4.11b). Coalescence by internal necking is observed in some of these strain bands at increment 11 (Figure 4.11c) including the position of probe 2.

The evolution of the strain field of the 45° in the slice containing probe 1 is presented in Figure 4.12. Only one instance of coalescence by internal necking is observed in a particularly small intervoid ligament. The strain band that covers the location of probe 1 is straight and diffuse.

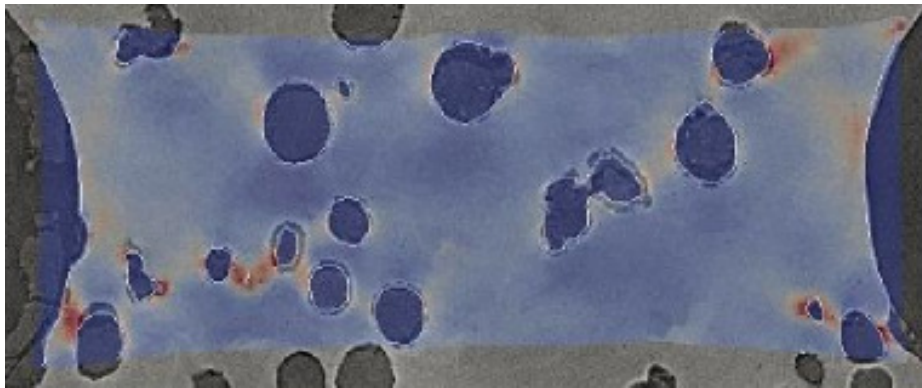
Figure 4.13 describes how the strain field evolves in the slice of the 45° specimen that contains probe 2. Increment 6 (Figure 4.13b) exhibits a few intense strain concentration bands that result in coalescence at increment 11 (Figure 4.13c). Intense concentration strain bands are observed at increment 11. The intervoid ligament where probe 2 is located does not present a distinct strain concentration band.

4.4.1 Discussion

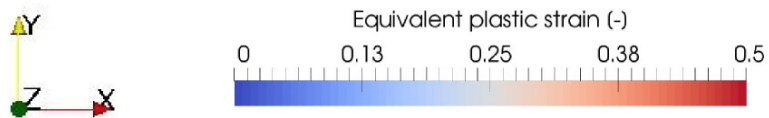
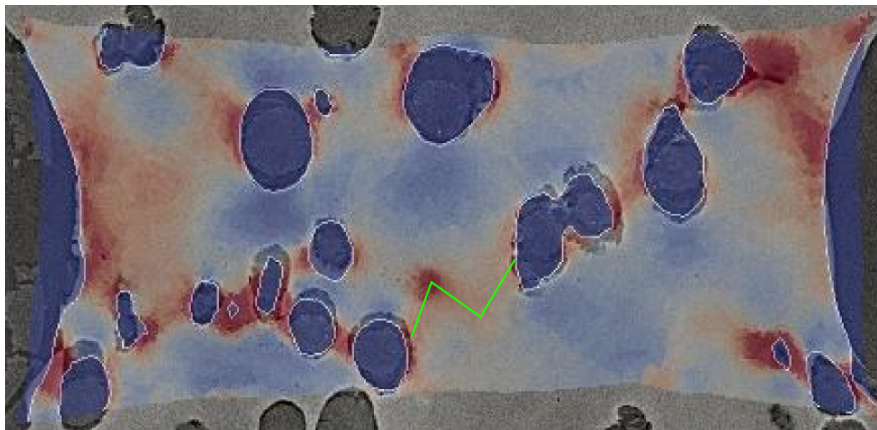
The positions of the probes were chosen in the work Buljac et al. [123] to study, via DVC measurements, void coalescence through two different mechanisms: void sheet coalescence (probe 1 of both specimens) and internal necking (probe 2 of both specimens). The authors of this study found the equivalent strain to be a promising local indicator of coalescence and a



(a)

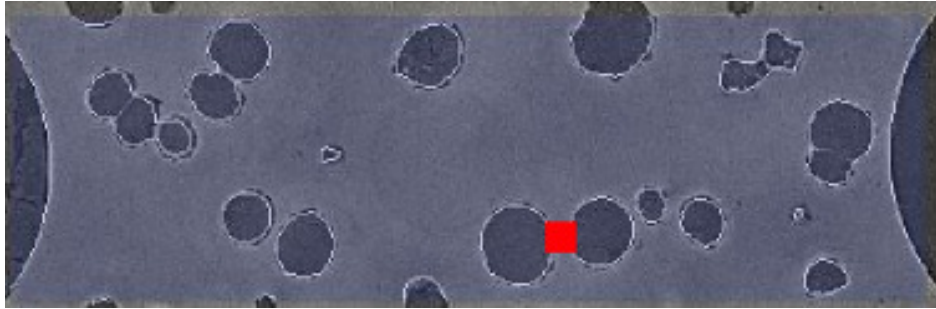


(b)

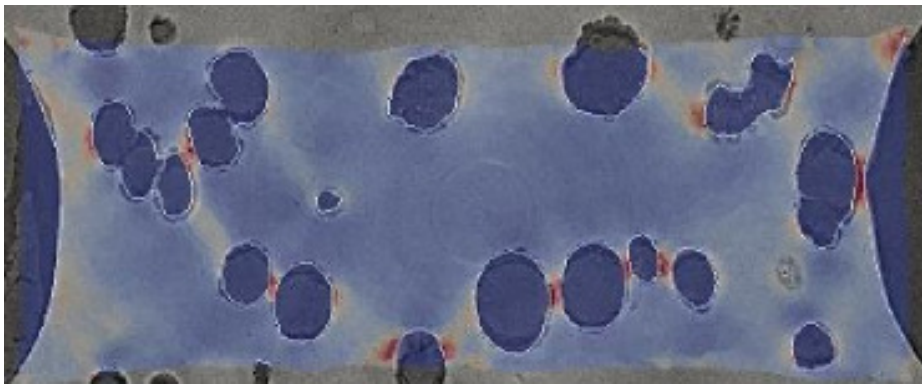


(c)

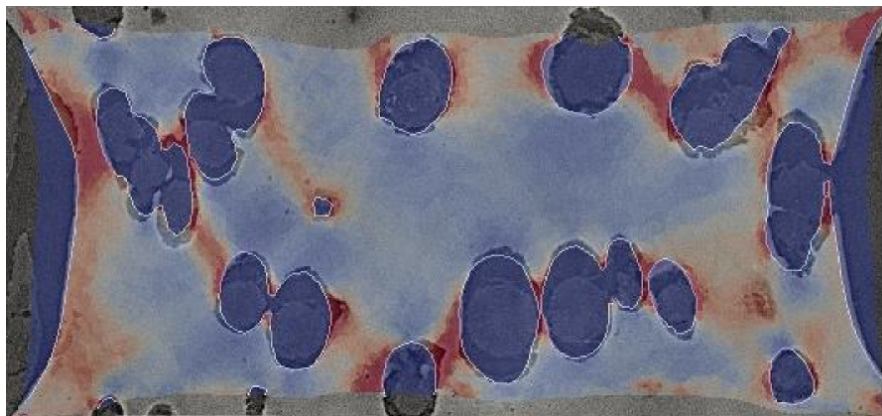
Figure 4.10: Strain distribution in the slice of the computational domain that contains the center of probe 1 for the 90° specimen at increments (a) 1, (b) 10, and (c) 19. The approximate position of probe 1 is indicated by a blue square for increment 1.



(a)



(b)



(c)

Figure 4.11: Strain distribution in the slice of the computational domain that contains the center of probe 2 for the 90° specimen at increments (a) 1, (b) 5, and (c) 11. The approximate position of probe 2 is indicated by a red square for increment 1.

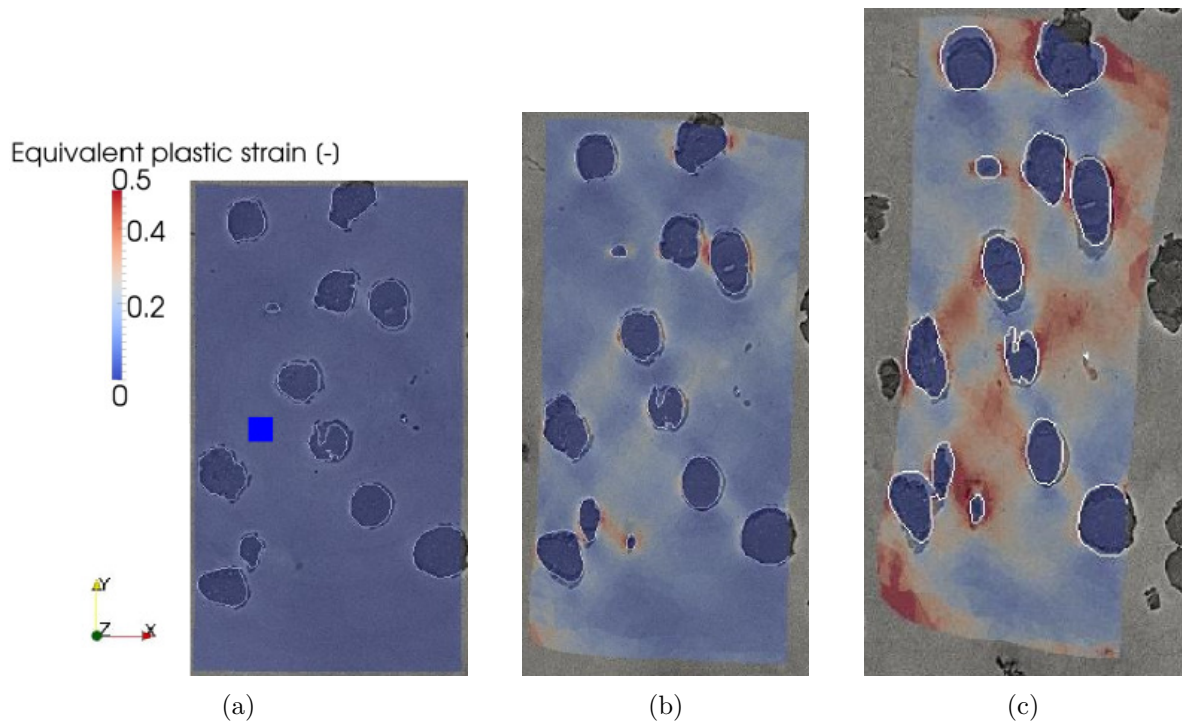


Figure 4.12: Strain distribution in the slice of the computational domain that contains the center of probe 1 for the 45° specimen at increments (a) 1, (b) 6, and (c) 11. The approximate position of probe 1 is indicated by a blue square for increment 1.

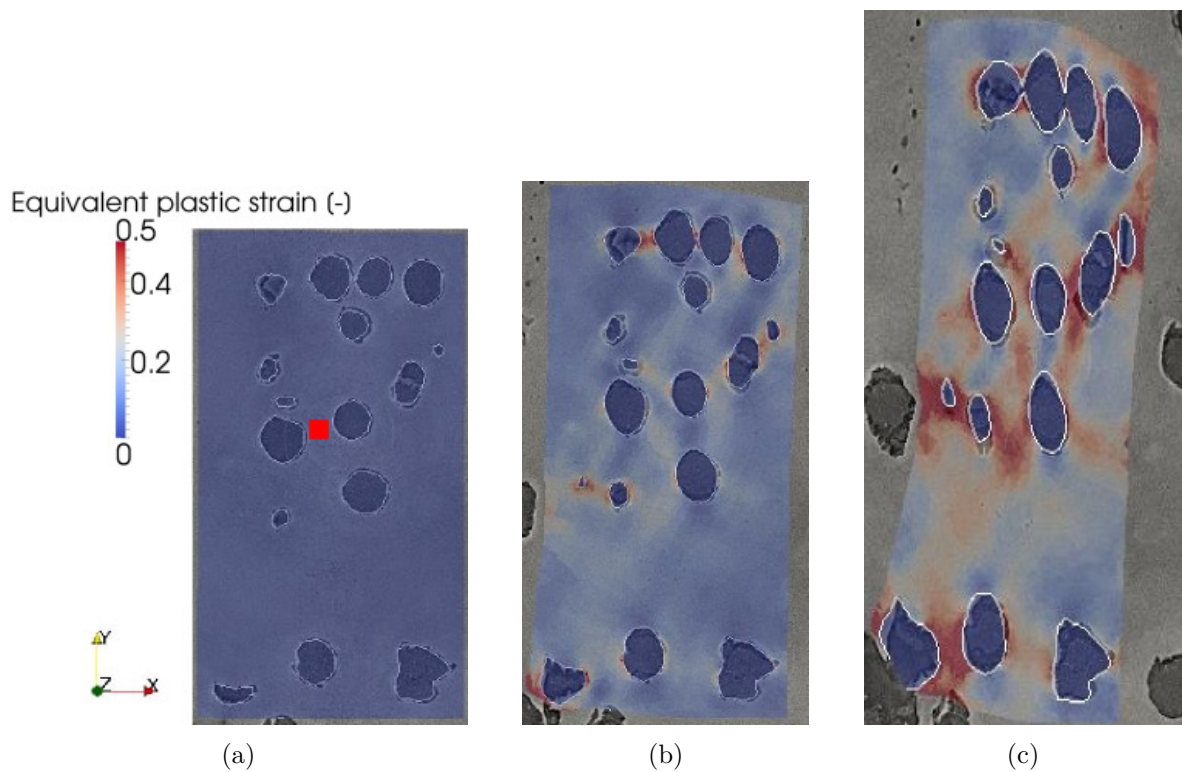


Figure 4.13: Strain distribution in the slice of the computational domain that contains the center of probe 2 for the 45° specimen at increments (a) 1, (b) 6, and (c) 11. The approximate position of probe 1 is indicated by a blue square for increment 1.

strain threshold value of approximately 40% for the void sheet mechanism and of 45% for the internal necking mechanism, was observed and discussed. However, if the observed instance of coalescence is taken into account for probe 2 of the 90° specimen, which corresponds to increment 11 in Figure 4.6, the observed pre-coalescence strain value corresponds to 20%.

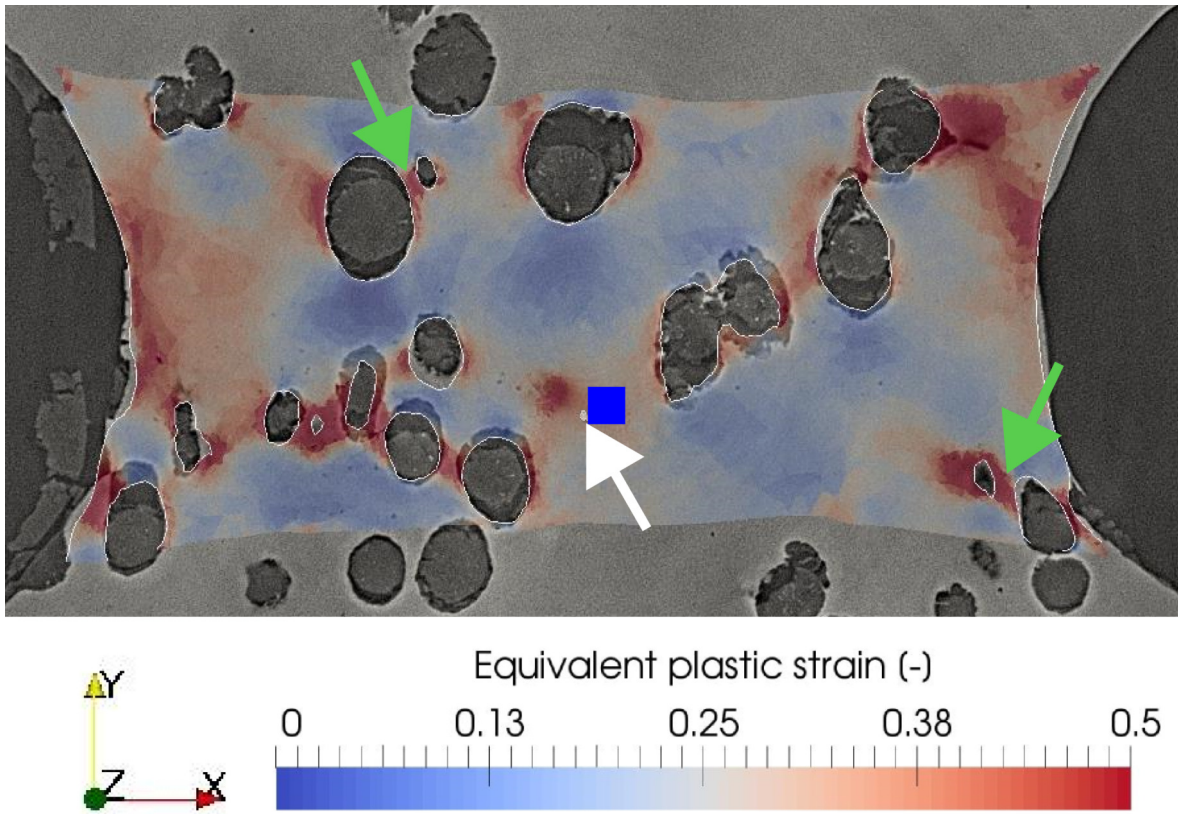
In the present chapter, the notion of the equivalent plastic strain as a local indicator of void coalescence is revisited with the results of the FE simulations that provide an improved spatial resolution with respect to the DVC measurements. If the equivalent strain is a sufficient and accurate coalescence indicator, coalescence should be observed wherever the threshold is exceeded. To test this idea pre-coalescence strain fields will be compared with the post-coalescence laminography image in the slices where the probes lie.

Figure 4.14 shows the pre-coalescence strain field in the slice where probe 1 is located at increment 19 (Figure 4.14a) and the corresponding slice post-coalescence at increment 20 (Figure 4.14b). The slice exhibits a crack that crosses most of the specimen section. The position of the crack follows the strain localization pattern, the less intense part of which corresponds precisely to the ligament that contains probe 1. Two instances of highly strain intervoid ligaments that do not present coalescence are observed and are reported with green arrows in Figure 4.14a.

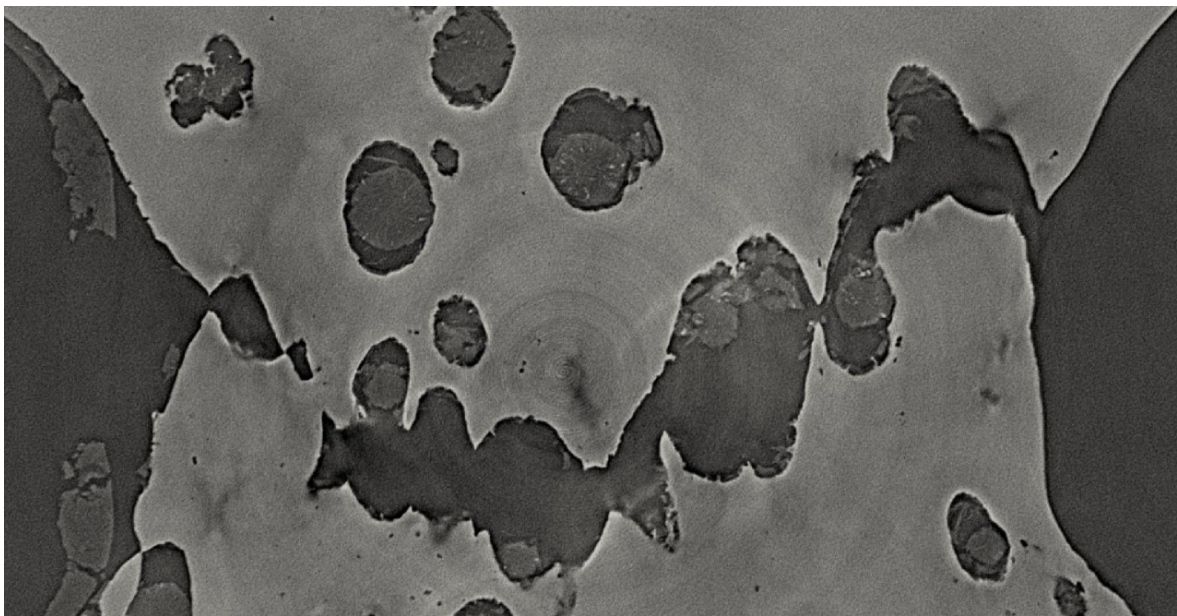
The ligament that contains probe 1 presents the previously described strain band in zigzag pattern which could be an indicator of interactions with microstructural heterogeneities in depth direction. In fact, white contours (shown by a white arrow in Figure 4.14a) to the left of the blue square confirm the presence of a void in approximately the same position of the probe hidden in depth direction. Three-dimensional interactions such as this one could be at the origin of apparent void-sheet instances that are in fact a combination of two internal necking instances in a three voids cluster. This possibility is studied in Chapter 5. This does not rule out the presence of pure void-sheet instances as the examination of fracture surfaces has provided hints of the presence of this mechanism in this specimen [123]. However, the confirmed presence of the third void hidden in the ligament in depth direction cannot be neglected in this particular instance.

The pre-coalescence strain field for the 90° specimen at increment 10 (Figure 4.15a) and the corresponding post-coalescence slice at increment 11 (Figure 4.15b) are presented in Figure 4.15 for the slice corresponding to probe 2. Six intervoid ligaments present concentration bands with high strain values, two of which do not present coalescence in the following increment.

The strain field prior to coalescence and the corresponding post-coalescence configuration for the 45° specimen are presented for the slice corresponding to probe 1 in Figure 4.16 and to probe 2 in Figure 4.17. Figure 4.16b evidences a crack at approximately 45° with respect to the loading (vertical) direction. The crack position does not correspond to the most strained

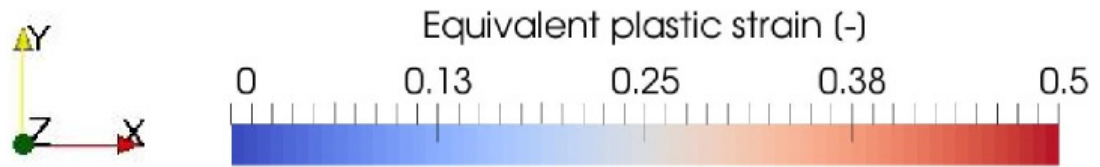
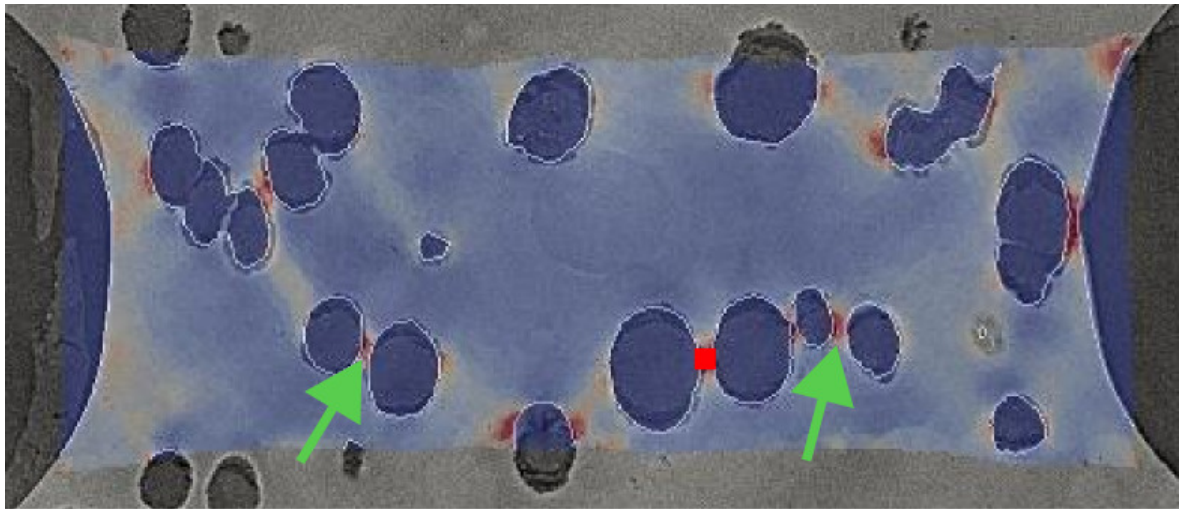


(a)

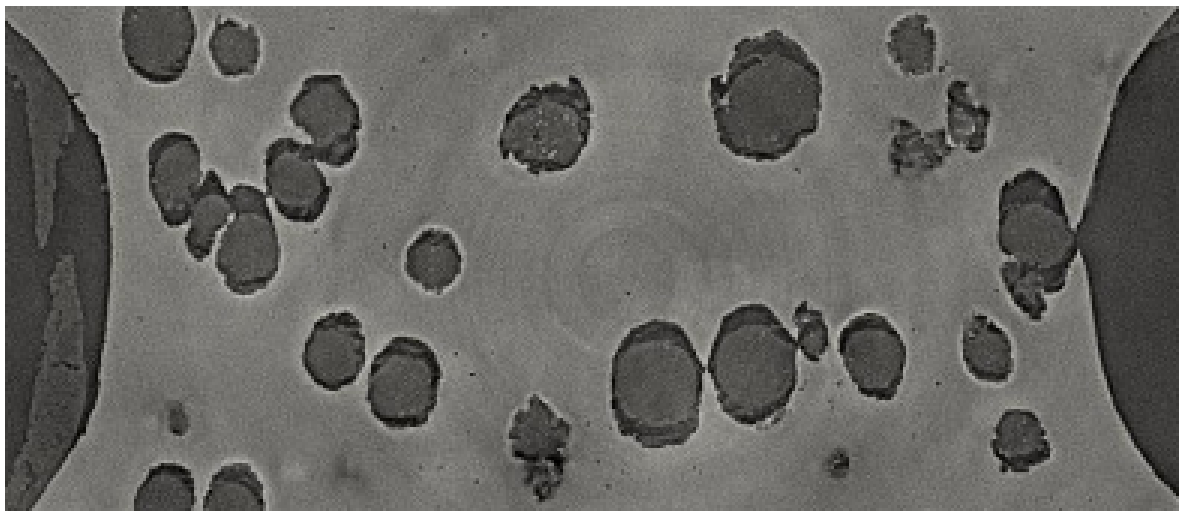


(b)

Figure 4.14: Slice containing probe 1 of the 90° specimen (a) before (increment 19) and (b) after coalescence (increment 20). For increment 19, the strain field predicted by the FE simulation is superimposed with the microstructure and the approximate position of probe 1 is indicated by a blue square.



(a)



(b)

Figure 4.15: Slice containing probe 2 of the 90° specimen (a) before (increment 10) and (b) after coalescence (increment 11). For increment 10, the strain field predicted by the FE simulation is superimposed with the microstructure and the approximate position of probe 2 is indicated by a red square.

parts of the domain and it crosses a ligament that did not present a strain concentration band. A highly strain ligament that does not undergo coalescence is observed in this slice (marked with a green arrow). Similarly, in the slice corresponding to probe 2 (Figure 4.17b), the observed crack crosses ligaments that gave no indication of coalescence based on the strain levels, while two highly strained ligaments do not present coalescence.

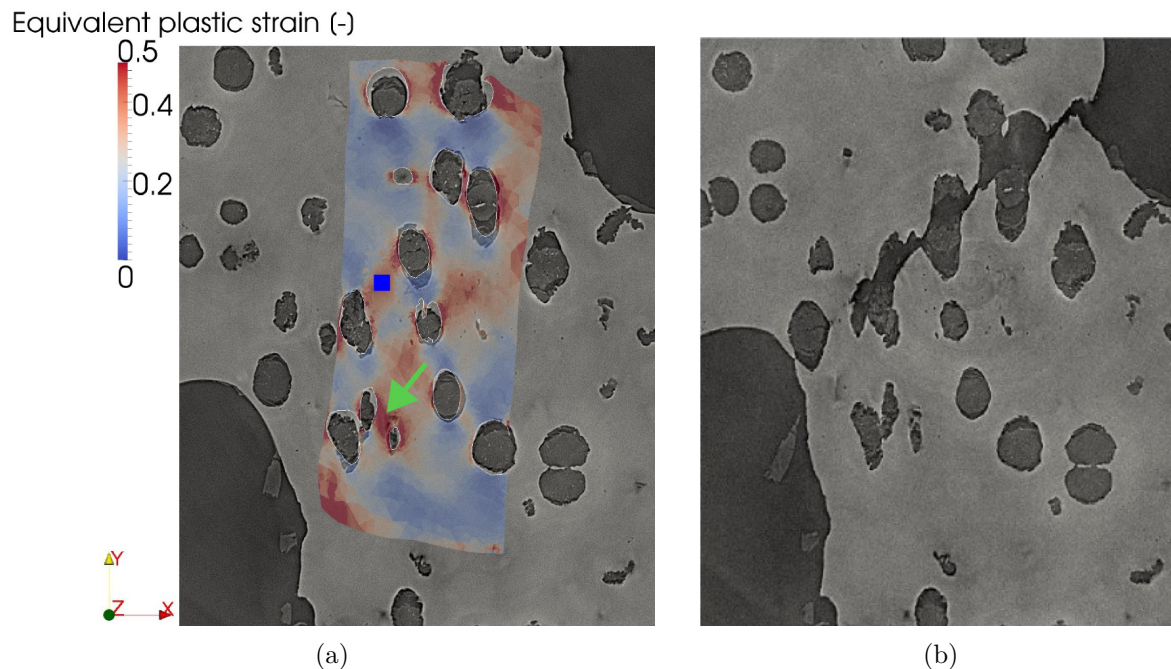


Figure 4.16: Slice containing probe 1 of the 45° specimen (a) before (increment 10) and (b) after coalescence (increment 11). For increment 10, the strain field predicted by the FE simulation is superimposed with the microstructure and the approximate position of probe 1 is indicated by a blue square.

Although the equivalent strain can be a reliable indicator of coalescence, such as in the slice containing probe 1 of the 90° specimen (Figure 4.14), the observation of these slices shows that highly strained instances that do not experience coalescence immediately after attaining high levels of strain, are not uncommon. This suggests that the equivalent strain alone is not an appropriate indicator of coalescence. For this reason, Chapter 6 presents a more extensive quantitative analysis that includes, in addition to the equivalent strain, stress measures and topological information such as initial intervoid distance.

Time discretization could be an intervening factor. Between two consecutive increments, the unobserved microstructural evolution could induce changes in the strain distribution. This could explain why some apparently less strained ligaments seem to undergo coalescence before apparently more strained ligaments. Additional scans would be necessary to improve the temporal discretization and confirm this.

Using cubic probes of the size of a DVC element in the FE simulation was useful for validation purposes, but a more appropriate probe shape and size could be used to take advantage of the spatial resolution of the FE simulations. Section 4.5 discusses this aspect.

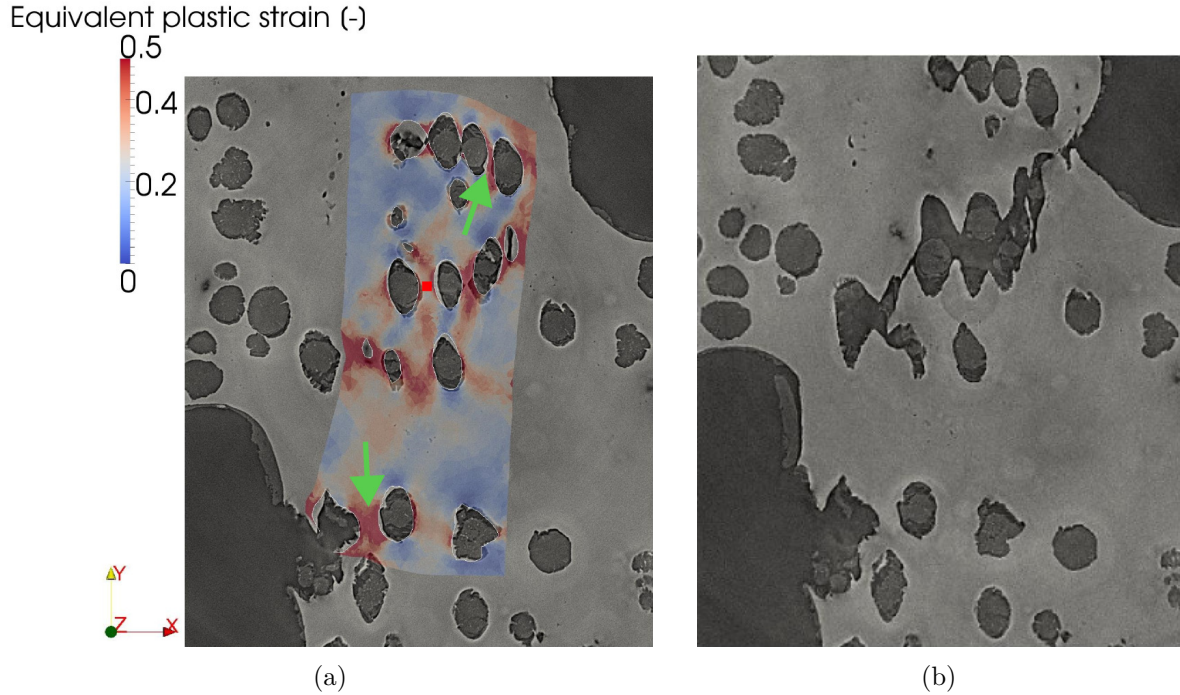


Figure 4.17: Slice containing probe 2 of the 45° specimen (a) before (increment 10) and (b) after coalescence (increment 11). For increment 10, the strain field predicted by the FE simulation is superimposed with the microstructure and the approximate position of probe 2 is indicated by a red square.

4.5 Effect of probe size on FE strain measures

The local strain measures that were presented in Sections 4.3 and 4.4 were calculated in cubic probes with the size of a DVC element in order to establish a direct comparison. Since the FE simulations allow for more local strain measures, the effect of the probe size is studied in this section. First, a mesh sensitivity analysis is carried out to verify that the results remain adequately mesh-independent when smaller probe sizes are employed 4.5.1. Then the effect of the probe size on local strain measures is assessed 4.5.2. The edge of the cubic probe will be scaled with a factor f . When $f = 1$, the probe size corresponds to the size of the DVC element.

4.5.1 Mesh sensitivity analysis

A local mesh refinement was carried out around the probes to reduce mesh dependence and to correctly reproduce the desired cubic shape. This mesh refinement is depicted in Figure 4.18. To achieve this, in the refined volume, the isotropic metric \mathbf{M} was not calculated with Equation (2.29). Instead, it was affected with the following value:

$$\mathbf{M}_{\text{refined volume}} = \text{diag} \left(\frac{1}{(f_m h_{min})^2} \right), \quad (4.1)$$

where f_m is a coefficient that will be varied to produce different levels of local refinement. For the sake of brevity, the analysis is presented only for the 90° specimen. In this analysis, the probe size corresponds to an edge scaling factor f of 0.25. This means that the volume of the probe size corresponds to $\frac{1}{64th}$ the volume of a DVC element.

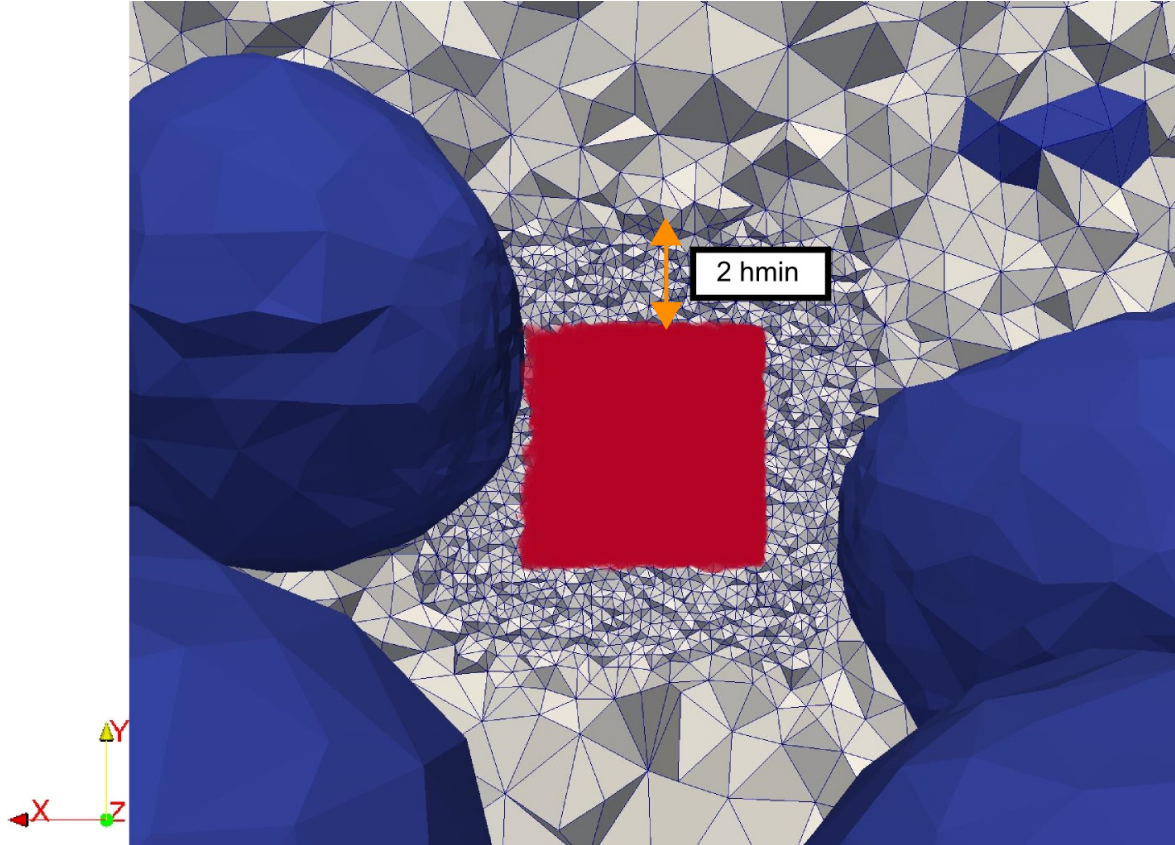


Figure 4.18: Probe 2 of the 45° specimen is shown in red with the local mesh refinement around it for a slice of the domain. The voids are shown in blue.

The employed values of f_m are 1, 0.5 and 0.25. Figure 4.19 and Figure 4.20 present the mesh sensitivity results for probe 1 and probe 2, respectively. The maximum absolute difference between the three data sets are also presented. The equivalent strain in probe 1 is not sensitive to the variations of f_m in the chosen range, and a maximum strain difference of 0.02 is registered at the end of the simulation. The equivalent strain in probe 2 is more sensitive. A maximum strain difference of 0.175 is obtained at the end of the simulation. The strain difference between the results with $f_m = 0.5$ and $f_m = 0.25$ is barely 0.03. A value of $f_m = 0.5$ is hence considered to produce mesh-independent results and will be used in the remainder of the study. The drop of strain in the final increment for probe 2 is caused by increased numerical diffusion of the probe volume due to an insufficiently fine mesh in the case with $f_m = 1$.

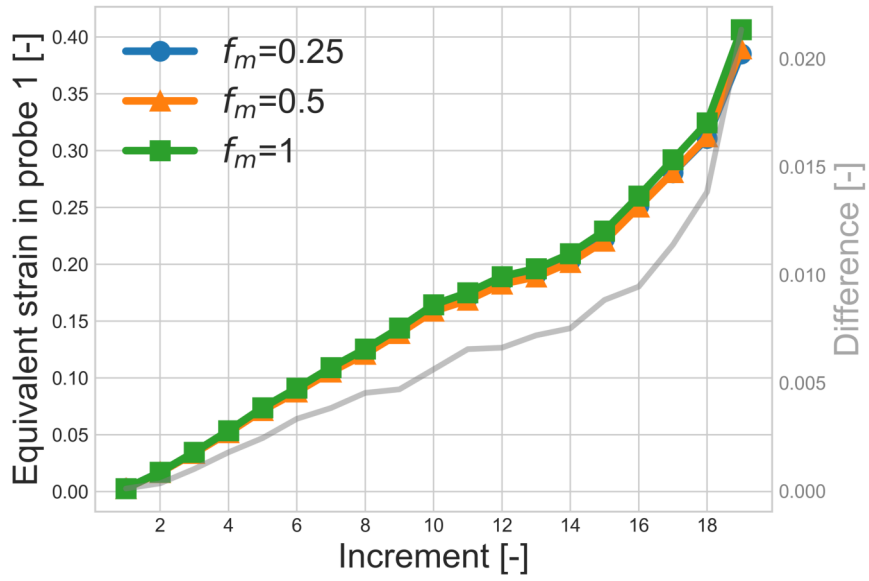


Figure 4.19: Mesh sensitivity of the equivalent strain in probe 1 of the 90° specimen. The absolute difference is reported as a gray line.

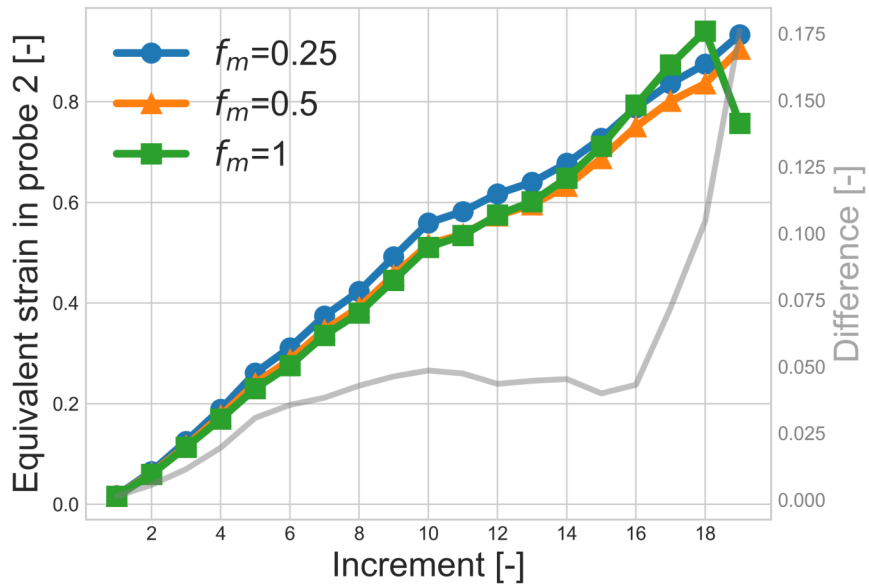


Figure 4.20: Mesh sensitivity of the equivalent strain in probe 2 of the 90° specimen. The absolute difference is reported as a gray line.

4.5.2 Probe size sensitivity analysis

The sensitivity of the local strain measures to the probe size is assessed in this section. The reported strain measurements correspond to a volume-average of the equivalent strain in the probe volume. Thus, if significant strain gradients are present, the strain measures are sensitive to the probe volume size. Three different values of the edge scaling factor f are employed. The used values are 1, 0.5 and 0.25. In order to have at least two different probe sizes that can be entirely accommodated in the intervoid ligament of probe 2, for this probe only, the values of f used are 1, 0.4 and 0.25. An additional strain measure is provided for each of the probes. This strain measure corresponds to the most local strain measure possible with the resolution of the FE mesh, i.e., to the strain in the element that contains the coordinates of the center of the probe, and will be referred to as point probe.

Figure 4.21 and Figure 4.22 provide three-dimensional views of the different employed probe sizes for the 90° and 45° specimens, respectively. In the case of probe 2 of the 90° specimen, only the probe sizes corresponding to $f = 0.4$ and $f = 0.25$ are shown in order to provide a clearer visualization. The probe size corresponding to $f = 1$ of this probe was shown in Figure 4.1a.

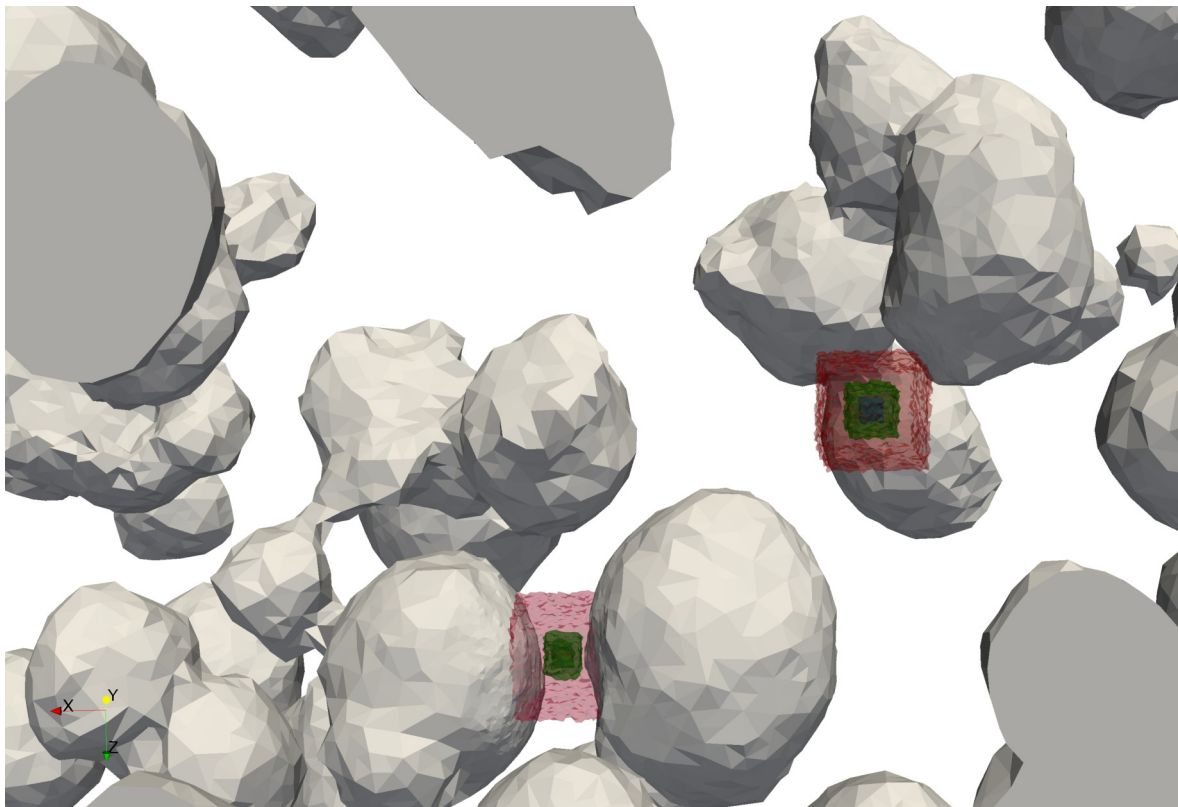


Figure 4.21: Three-dimensional view of the microstructure of the 90° specimen with the used probe sizes.

The sensitivity of the equivalent strain in probe 1 of the 90° specimen with respect to the probe size is shown in Figure 4.23. Very little variation is observed across the four

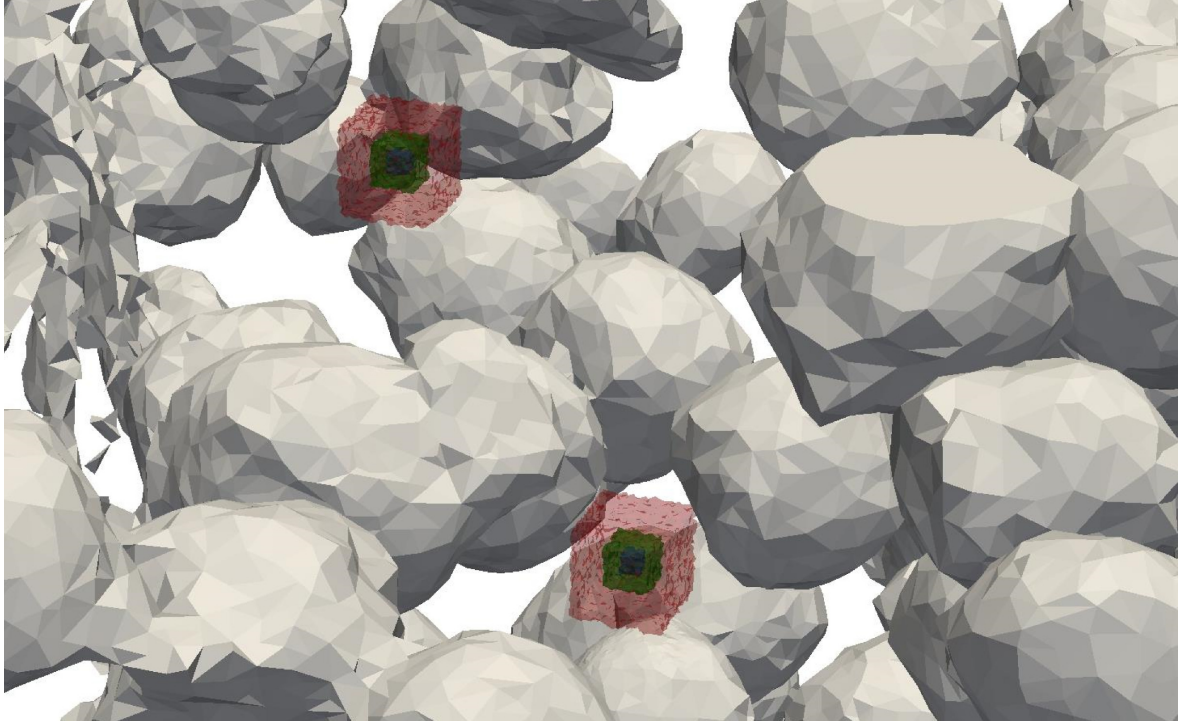


Figure 4.22: Three-dimensional view of the microstructure of the 45° specimen with the used probe sizes.

probe sizes. A maximum strain difference of 0.03 is obtained at the end of the simulation. This is consistent with the observed strain fields (Figure 4.10). The probe is located in a diffuse zigzag strain pattern without sharp gradients and, for this reason, the local measure of equivalent strain is not very sensitive to probe size.

Figure 4.24 presents the sensitivity of the equivalent strain of probe 2 of the 90° specimen with respect to the probe size. The probe size corresponding to $f = 1$ predicts strain values that are considerably lower than those predicted by the rest of the probe sizes. When $f = 1$, the probe is not small enough to fit in the intervoid ligament and the presence of the void phase in the probe volume alters the resulting averaged strain. The remaining three probe sizes correspond to probes that fit in the intervoid ligament and present very similar results up to increment 14. In the subsequent increments, the prediction of the point probe starts to diverge from the predictions of the $f = 0.40$ and $f = 0.25$ probes and at the end of the simulation, the former is lower than the latter with a strain difference of approximately 0.1. This difference results from the sharp gradients to which the probe is submitted after flowing out of the intervoid ligament, which are illustrated in Figure 4.25. Coalescence occurs at increment 11 for this ligament. The strain values for probes with $f = 0.40$ are significantly larger than those reported by Buljac et al. [123]. The results are satisfactory in the sense that the FE simulations can provide a sensible strain measurements from the beginning of the simulation and up to coalescence even in very narrow intervoid ligaments.

The sensitivity to probe size of the strain measures associated to probes 1 and 2 of the

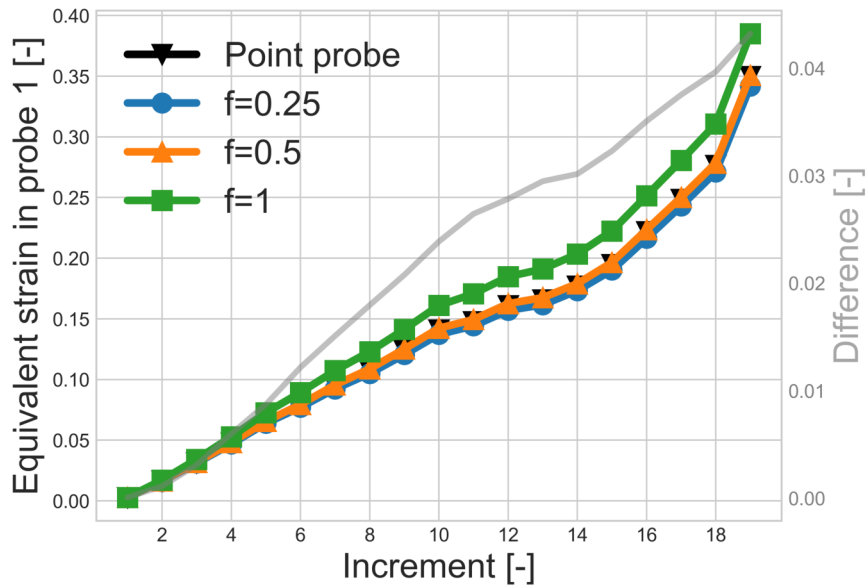


Figure 4.23: Probe size sensitivity of the equivalent strain in probe 1 of the 90° specimen. The absolute difference is reported as a gray line.

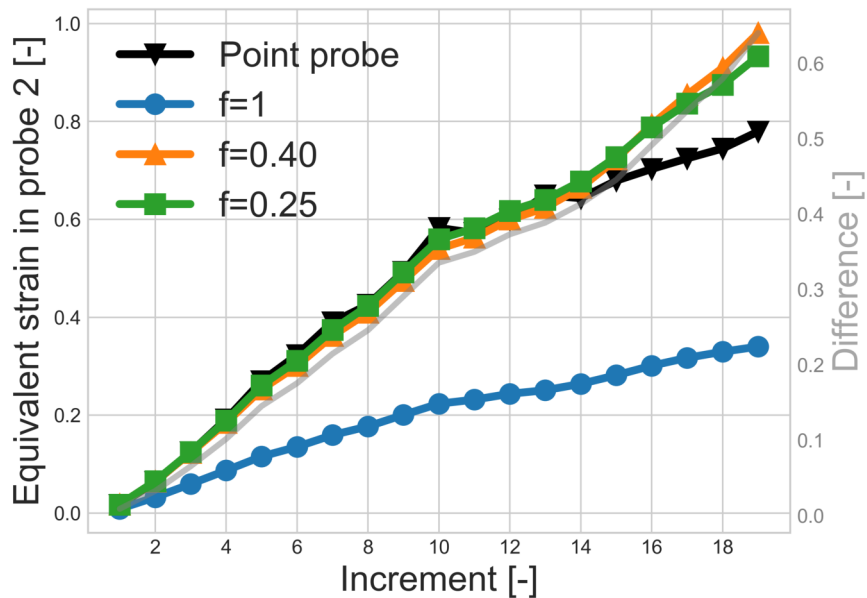


Figure 4.24: Probe size sensitivity of the equivalent strain in probe 2 of the 90° specimen. The absolute difference is reported as a gray line.

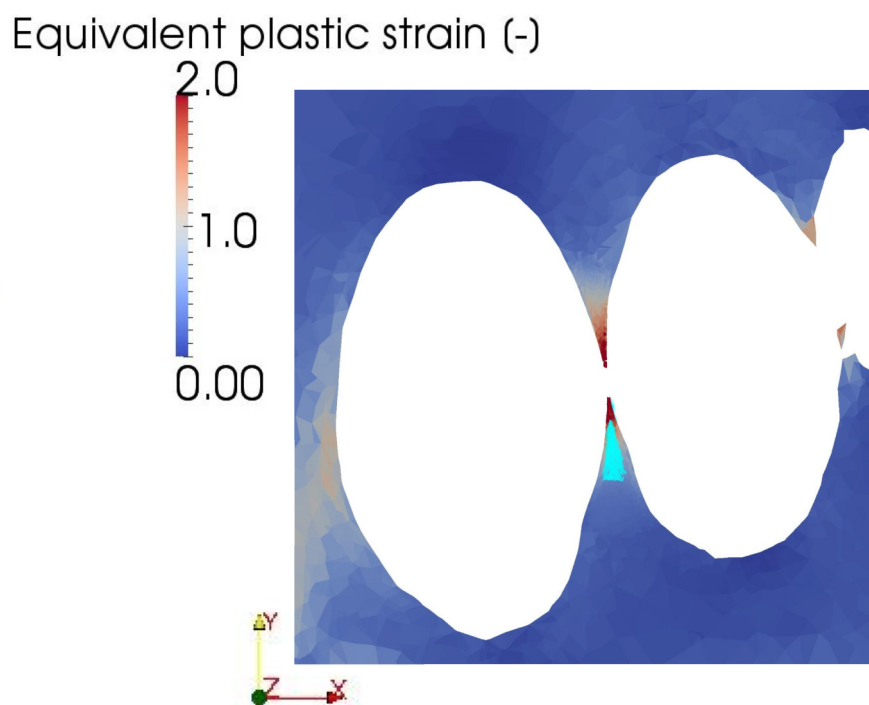


Figure 4.25: Strain gradient in the neighborhood of probe 2 of the 90° specimen at increment 19. Probe 2 with $f = 0.40$ is shown in light blue.

45° specimen are presented in Figures 4.26 and 4.27 respectively. For probe 1, the four strain measures are similar with a final maximum strain difference of 0.025. When the probe size decreases (from $f = 1$ to $f = 0.25$), the strain increases monotonically. When the probe size further decreases, however, the strain measure of the point probe is between those corresponding to $f = 0.25$ and $f = 0.5$. For probe 2, a maximum strain difference of 0.0275 is obtained and although the results of probe sizes associated to 0.5 and below are considerably close during the whole simulation, a non monotonic behavior is again observed with respect to probe size.

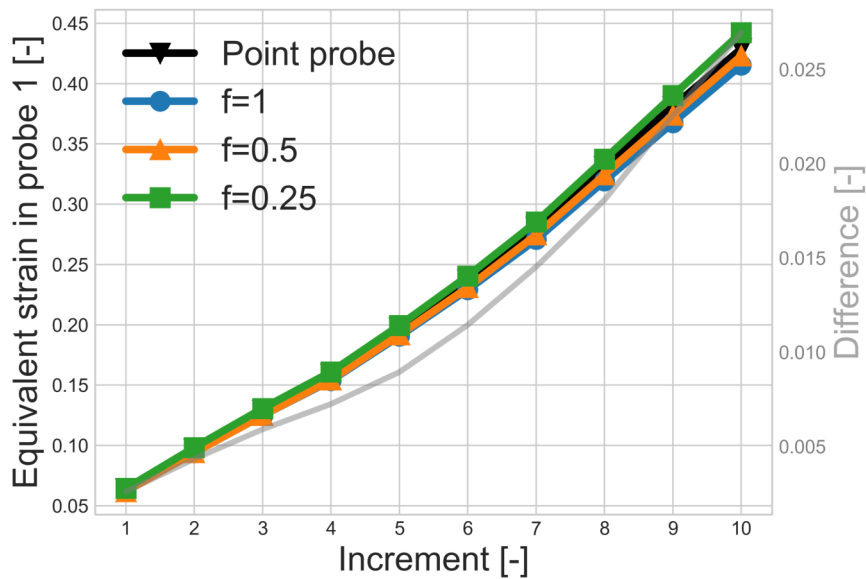


Figure 4.26: Probe size sensitivity of the equivalent strain in probe 1 of the 45° specimen. The absolute difference is reported as a gray line.

To explore the non monotonic behavior found for the strain in probes 1 and 2 of the 45° specimen, the distribution of the equivalent strain in a slice containing probe 2 of the 45° is depicted in Figure 4.28 for increments 1, 4 and 8. The probes corresponding to $f = 1$, $f = 0.5$ and $f = 0.25$ are also shown. The heterogeneity of the strain field in the intervoid ligament explains the non monotonic behavior. For example, part of the largest probe is very close to the void-matrix interface, which corresponds to the most strained zones. This can increase the strain measure in the probe beyond the strain registered in the smaller probes. This also illustrates how the strain measures in the probes depend on its size, shape and orientation. This dependency is avoided with the use of the point probe. For this reason, the point probe strain is considered a less ambiguous and more local strain measure. Chapter 6 contains a discussion on an appropriate strain measure for a coalescence criterion.

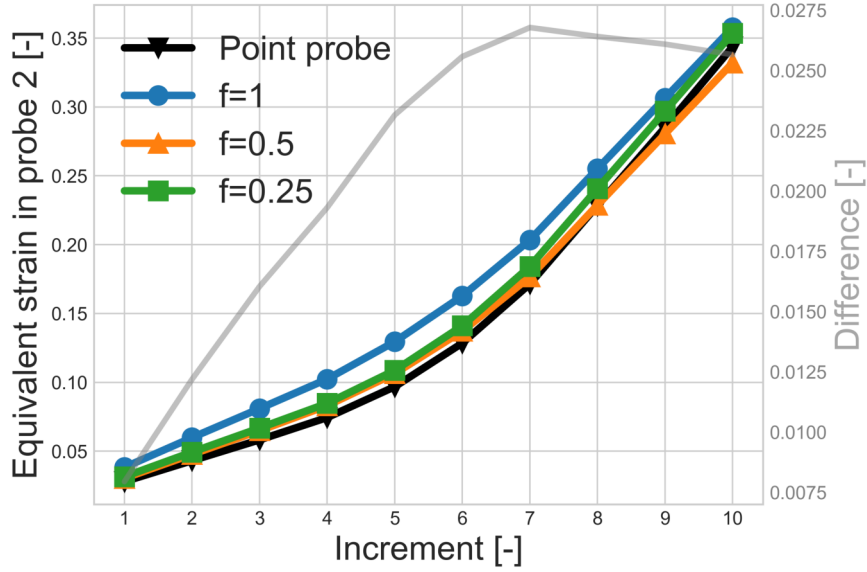


Figure 4.27: Probe size sensitivity of the equivalent strain in probe 2 of the 45° specimen. The absolute difference is reported as a gray line.

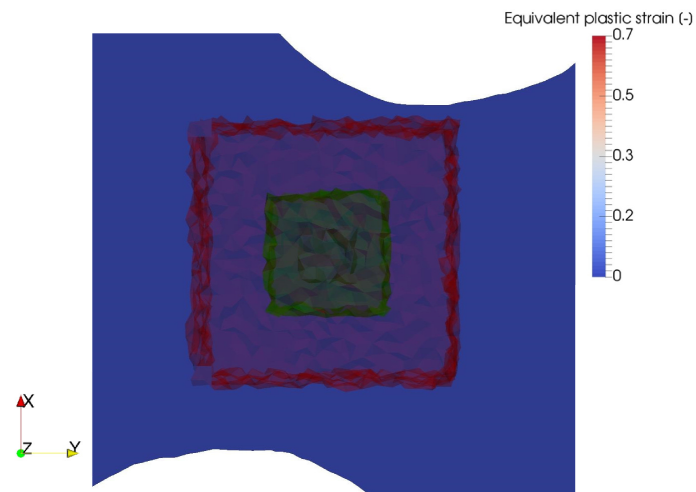
4.6 Conclusions

In this chapter, a detailed comparison of DVC and FE strain measures was carried out. A macroscopic and two local measures were considered for two different specimens and image segmentation-related uncertainties were taken into account.

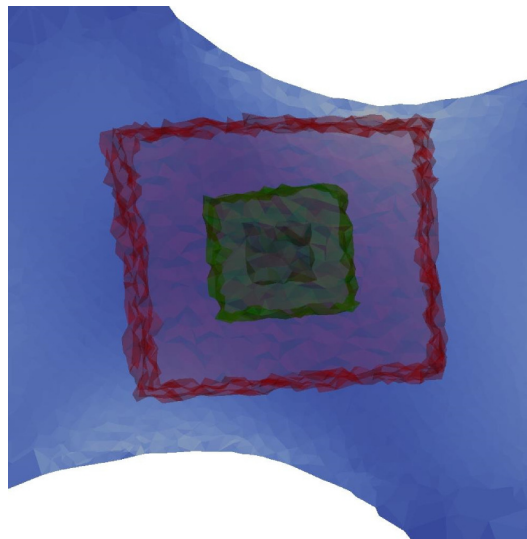
A very good agreement was observed for the macroscopic equivalent strain of both specimens as well as for the pre-coalescence local strains of the 90° specimen. The rate of increase of the strain was well predicted for the local measures of the 45° specimen, but the strain values showed larger discrepancies. The FE strain measures are overall considered satisfactory and suitable to be used in the study of void coalescence.

The comparison between DVC measurements and FE predictions revealed that the image segmentation-related uncertainties are negligible with respect to the differences between the strain measures. This implies that the obtained differences can be used to identify limitations of the physical and numerical framework.

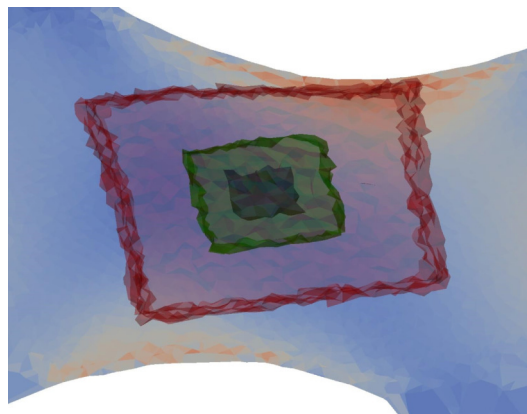
When the specimen approaches final fracture, an acceleration of the rate of increase of strain was observed in the DVC results. The FE simulations failed to capture this acceleration. This is thought to be a deficiency of the hardening law for very large strain values since it does not saturate. This can be improved in future work by using a hardening law with saturation for large strain values or a behavior law for porous plasticity or a coupled damage model such as the Lemaitre model [22]. To do so, a new parameter identification procedure at the microscale would be necessary.



(a)



(b)



(c)

Figure 4.28: Distribution of the equivalent strain in a slice containing probe 2 of the 45° specimen for increments (a) 1, (b) 4 and (c) 8. The three used probe sizes are shown.

To assess the suitability of the equivalent strain as a coalescence indicator, the strain field evolution was described in detail for different slices of the three-dimensional simulations. The pre-coalescence strain fields were compared with the corresponding post-coalescence slices of the laminography images. The pre-coalescence equivalent strain proved to be a reliable coalescence indicator in several instances, but a non negligible number of highly strained instances that do not undergo coalescence were observed.

The results presented in this chapter call into question the possibility of using the pre-coalescence strain as a local coalescence criterion. The DVC analyses are less suitable for this than the FE simulations because of their limited spatial resolution. The improved local precision of the FE simulations highlights the importance of the combined SRCL-DVC-FE approach. The FE simulations also open up the possibility of introducing the stress state in the analysis. A more extensive quantitative analysis considering topological information as well as strain and stress measures is presented in Chapter 6.

A sensitivity analysis of the local strain measures with respect to the probe size was carried out. The strain measures were most sensitive in small intervoid ligaments. A point probe of the size of a FE element provides the most local information without dependence on probe size, shape and spatial orientation. The punctual information will be used in Chapter 6 in a more complete study of void coalescence. Before that, however, a numerical study of void coalescence in a three voids cluster is presented in Chapter 5 as an effort to clarify the observed coalescence mechanisms.

Résumé en français

Dans ce chapitre, une comparaison détaillée des mesures de déformation DVC et FE (éléments finis) a été réalisée. Une mesure macroscopique et deux mesures locales ont été analysées pour deux échantillons différents et les incertitudes liées à la segmentation d'images ont été prises en compte.

Un très bon accord a été observé pour la déformation équivalente macroscopique des deux échantillons ainsi que pour les déformations locales de pré-coalescence de l'échantillon à 90°. Le taux de croissance de la déformation a été bien prédit pour les mesures locales de l'échantillon à 45°, mais les valeurs de la déformation ont montré des écarts plus importants. Les mesures de la déformation FE sont globalement considérées comme satisfaisantes et appropriées pour être utilisées dans l'étude de la coalescence des pores.

La comparaison entre les mesures DVC et les prédictions FE a révélé que les incertitudes liées à la segmentation d'images sont négligeables par rapport aux différences entre les mesures de déformation. Cela implique que les différences obtenues peuvent être utilisées pour identifier les limites du cadre physique et numérique.

Lorsque l'échantillon approche de la rupture finale, une accélération de la vitesse de déformation a été observée dans les résultats de la DVC. Les simulations FE n'ont pas réussi à capturer cette accélération. Ceci est considéré comme une déficience de la loi d'écroutissement pour des très grandes valeurs de déformation, car cette loi ne sature pas. Cela peut être amélioré dans des travaux futurs en utilisant une loi d'écroutissement avec saturation pour des valeurs de déformations importantes, une loi de comportement pour la plasticité poreuse ou un modèle d'endommagement couplé tel que le modèle de Lemaitre [22]. Pour ce faire, une nouvelle procédure d'identification des paramètres à l'échelle microscopique serait nécessaire.

Pour évaluer la pertinence de la déformation équivalente en tant qu'indicateur de coalescence, l'évolution du champ de déformation a été décrite en détail pour différentes tranches des simulations tridimensionnelles. Les champs de déformation de pré-coalescence ont été comparés aux tranches post-coalescence correspondantes des images de laminographie. La déformation équivalente de pré-coalescence s'est révélée être un indicateur de coalescence fiable dans plusieurs cas, mais un nombre non négligeable d'instances très sollicitées ne subissant pas de coalescence ont été observées. Les résultats présentés dans ce chapitre remettent en question la possibilité d'utiliser la déformation de pré-coalescence comme critère de coalescence locale. Les analyses DVC s'y prêtent moins bien que les simulations FE en raison de leur résolution spatiale limitée. La précision locale améliorée des simulations FE souligne l'importance de l'approche combinée SRCL-DVC-FE. Les simulations FE ouvrent également la possibilité d'introduire l'état de contrainte dans l'analyse. Une analyse quantitative plus approfondie prenant en compte des informations topologiques ainsi que des mesures de déformation et de contrainte est présentée dans le chapitre 6.

Une analyse de sensibilité des mesures de déformation locales par rapport à la taille du capteur a été réalisée. Les mesures de la déformation étaient les plus sensibles dans les petits ligaments inter-cavités. Un capteur de la taille d'un élément FE fournit les informations les plus locales sans dépendre de la taille, de la forme et de l'orientation spatiale de la sonde. Les informations ponctuelles seront utilisées dans le chapitre 6 dans une étude plus complète de la coalescence des pores. Avant cela, cependant, une étude numérique de la coalescence des pores dans un groupe de trois pores est présentée dans le 5 dans le but de clarifier les mécanismes de coalescence observés.

Chapter 5

Void growth and coalescence in a three-dimensional non-periodic void cluster

Contents

5.1	Introduction	116
5.2	Methodology	118
5.2.1	Methodology for the study of void and/or inclusion clusters	118
5.2.2	Parametric study	119
5.3	Results	121
5.3.1	Results for the case with $d_1 = 1$ and $d_2 = 1$	121
5.3.2	Effect of d_2	124
5.3.3	Effect of d_1	129
5.3.4	Global results and discussion	132
5.3.5	Effect of hardening	134
5.4	Conclusions	135

5.1 Introduction

Void coalescence is usually categorized into three different mechanisms [57, 62]. The first and most common mechanism is coalescence by internal necking of the intervoid ligament. In the second mechanism, two voids seemingly wide apart, are suddenly united by a narrow void sheet. This is referred to as void-sheet mechanism. The third and less common mechanism is known as necklace coalescence or coalescence in columns, in which voids link up along their length.

Void-sheet coalescence was observed by Cox and Low [203] in an AISI 4350 alloy (see Figure 5.1). The authors identified these void sheets as planar features formed by small voids, and oriented at 45° with respect to the tensile axis. The orientation of this feature coincides with the direction of maximum shear. This void-sheet mechanism can have a negative impact on the ductility of the material [203, 204].

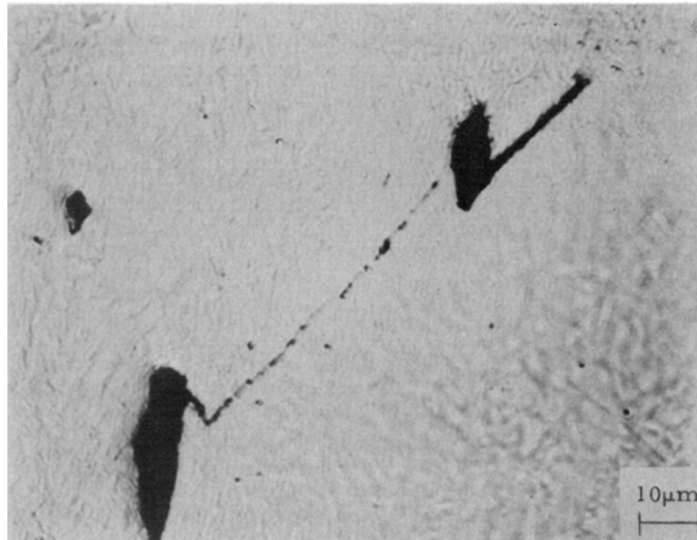
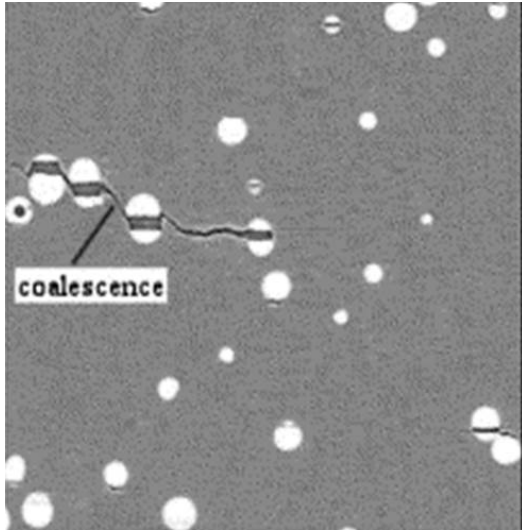


Figure 5.1: Instance of void-sheet mechanism observed by Cox and Low [203] in an AISI 4350 alloy.

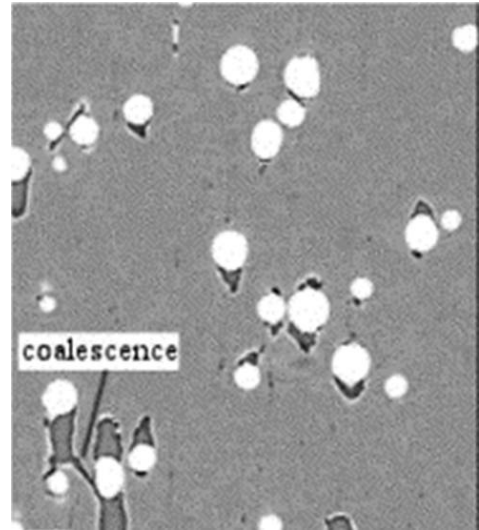
Recent efforts have employed three-dimensional imaging techniques, such as X-ray tomography or Synchrotron radiation computed tomography (SRCT), to study and improve the understanding of ductile damage mechanisms [143–145, 205].

Babout et al [206] studied damage in model metallic materials via X-ray tomography by carrying out in situ tensile tests in two different aluminum matrices reinforced with spherical hard ceramic particles. The authors observed coalescence (Figure 5.2) in the highest strained regions between voids at approximately 45° from the tensile direction.

In the analysis of SRCL images of nodular graphite cast iron, various instances of apparent void-sheet coalescence have been observed [123]. Two examples of these instances are presented in Figure 5.3. The tensile direction corresponds to the vertical direction. Two



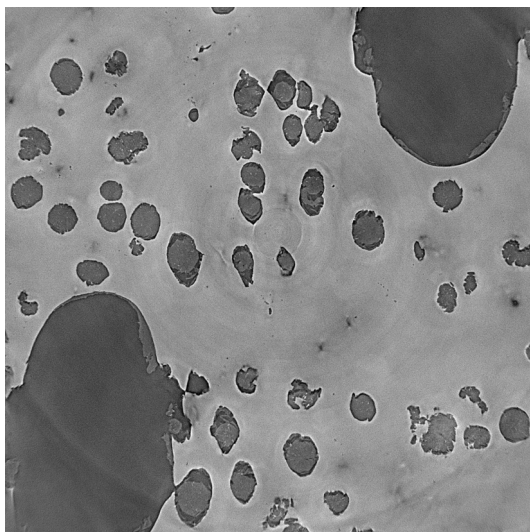
(a) Hard matrix



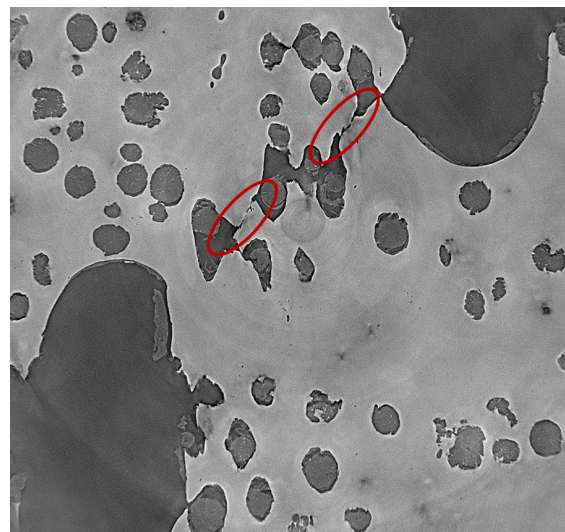
(b) Soft matrix

Figure 5.2: Coalescence instances observed by Babout et al. [206]. Figures adapted from [206].

coalescence instances are indicated in red in Figure 5.3b. As noted in Chapter 4, even though the two-dimensional slices suggest the occurrence of the void-sheet mechanism, the three-dimensional images hint at a possible intervention of voids located close to the observed coalescence; the work presented in this chapter aims at investigating numerically the possible intervention of neighboring voids on such coalescence modes.



(a) Before coalescence



(b) After coalescence

Figure 5.3: Apparent void-sheet instance observed in a two-dimensional slice of a laminography scan of nodular cast iron [9, 10].

This chapter constitutes a parenthesis in terms of methodology. Instead of the SRCL-DVC-FE framework, a simpler *ad-hoc* numerical methodology is proposed to investigate three-dimensional effects on the apparent void-sheet mechanisms. A three-dimensional non-periodic

cluster of three voids is investigated in a parametric study. Since a classical unit-cell approach is not suitable for this task, a methodology for the study of three-dimensional non-periodic clusters of voids and/or particles is proposed. In section 5.2, the proposed methodology and the parametric study are described. Results are presented and discussed in Section 5.3, and conclusions are drawn in Section 5.4.

5.2 Methodology

5.2.1 Methodology for the study of void and/or inclusion clusters

Motivation

The use of three-dimensional imaging in conjunction with FE modeling brings about opportunities to study ductile damage in more realistic situations. This increase in realism implies an increase in complexity and microstructural parameters are observed rather than controlled. For example, in a typical unit-cell, the intervoid distance is constant and imposed with the cell geometry; in a FE analysis of an immersed microstructure, an intervoid distance distribution is obtained when the image is immersed. To verify an hypothesis or investigate a specific effect without necessarily recurring to periodic arrangements and idealized shapes, it might be desirable 1. to control a given microstructural variable or 2. to study a certain isolated configuration or clusters of voids and/or particles. This is the main motivation for the methodology proposed in this work.

Description

A methodology for the study of void and/or inclusion clusters, is proposed here as a complement to FE analysis of realistic microstructures. It has the following defining characteristics:

- dedicated to the study of void and/or inclusion non-periodic clusters.
- Possibility of using microstructural features of non-idealized shapes.
- Reference to a far-field stress.
- The calculations can be controlled with a given stress state in terms of stress triaxiality ratio and Lode parameter.
- Possibility of imposing arbitrary non-proportional loadings.

- Possibility of obtaining detailed information of the studied configuration such as the individual void volume evolution or the evolution of the minimum intervoid distance between two voids. (See Section 5.3 for an example).

A domain with an embedded microstructural configuration is modeled. The size of the domain is considerably larger than the embedded configuration to assure negligible interaction with the boundaries. The microstructural configuration analyzed in this study is depicted in Figure 5.4a.

The cubic domain is depicted in Figure 5.4b and the boundary conditions are schematized. Three symmetry planes are used (red arrows in Figure 5.4b). The vertical velocity is imposed on the top plane (green arrow in Figure 5.4b), and is calculated to impose a given vertical logarithmic strain. The horizontal velocities corresponding to the perpendicular directions of the two remaining faces (blue arrows in Figure 5.4b) are imposed. In order to obtain a desired stress state in the domain, these horizontal velocities are iteratively calculated during the simulations via an optimization algorithm. A simplex algorithm [207] implemented in the open-source nonlinear-optimization library NLOpt [208] and coupled with CimLib [156], was used. The stress state is imposed in terms of stress triaxiality ratio T and normalized Lode angle $\bar{\theta}$. For all the simulations presented here, constant values of $T = 1$ and $\bar{\theta} = 0.34$ were used; a high triaxiality value was chosen to promote void growth, and value of the normalized Lode angle is similar to those found locally in the vicinity of void-sheet like instances in micromechanical FE simulations with immersed microstructures and realistic boundary conditions such as those documented in the work of Shakoor et al. [10].

The described methodology differentiates itself from unit-cell studies such as, for example, the works of Tvergaard [43] or Khan and Bhasin [45], by its focus on a isolated non-periodic void cluster. Although the applied boundary conditions result in periodicity, the relative size of the void cluster with respect to the domain ensures that the interaction with the boundaries is inconsequential.

5.2.2 Parametric study

This parametric study has two objectives. The first one is to provide a general description of the behavior of a three voids cluster during the stages of growth and coalescence. The second objective is to assess if such a configuration can be related to the observed instances of void-sheet coalescence (See section 5.1). In this study, the term coalescence refers to actual void impingement and not to the plastic localization stage that precedes it. A pair of voids is herein said to undergo coalescence when the intervoid distance reaches zero.

Since the parametric study is computationally demanding, the matrix is initially considered elasto-perfectly plastic (Young's modulus $E = 210000\text{MPa}$, Poisson's ratio $\nu = 0.3$ and

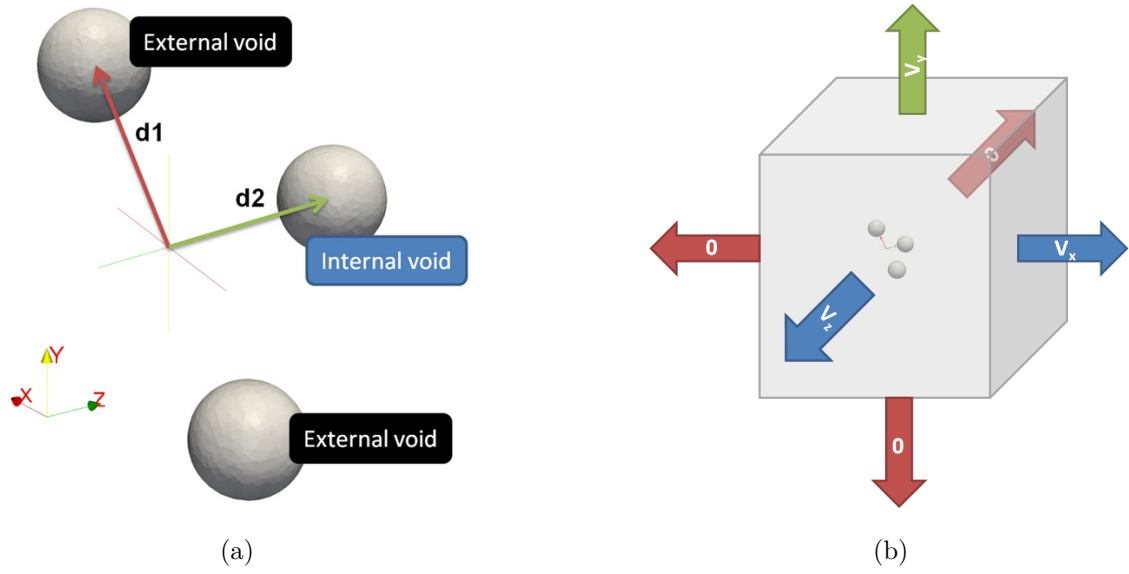


Figure 5.4: (a) Scheme of initial configurations of the three voids and (b) scheme of computational domain.

yield stress $\sigma_y = 290\text{MPa}$) and the void phase is modeled as a compressible Newtonian fluid (viscosity $\eta = 2.1\text{MPa s}^{-1}$)

Studied configuration

The three voids cluster is depicted in Figure 5.4a. It is constituted by three voids with a radius $R = 50\mu\text{m}$: two of them will be referred to as external voids and the third one will be referred to as the internal void. The line that connects the centers of the two external voids forms 45° with the main loading direction (the vertical direction). The vertical position (y-direction) of the center of the internal void is located exactly at mid-height of the domain and hence between the two external voids. The internal void is shifted in the thickness direction (z-direction) by a given distance.

Parameters

To construct different initial configurations, the relative positions of the voids in the three voids cluster were described with two parameters, which are depicted in Figure 5.4a along with a scheme of a given initial configuration. The two adimensional parameters are: d_1 the distance between the center of the domain and the center of the external voids divided by R , and d_2 , the distance between the center of the domain and the center of the internal void divided by R .

The explored parametric space is summarized in Table 5.1; the accomplished simulations

Table 5.1: Explored parametric space.

$d_1 \backslash d_2$ [-]	1	1.75	2.5	3.25	4
1	⊗	⊗	⊗	⊗	⊗
1.75	⊗	⊗	⊗		⊗
2.5	⊗	⊗		⊗	⊗
3.25		⊗	⊗		⊗

are indicated by a cross. A total of 16 simulations were carried out. The range between 1 and 3.25 was used for d_1 , and the range between 1 and 4 was used for d_2 .

5.3 Results

Results for a single simulation with $d_1 = 1$ and $d_2 = 1$ are first discussed in Section 5.3.1. Subsequently, the results of the parametric study are presented in Sections 5.3.2, 5.3.3 and 5.3.4.

5.3.1 Results for the case with $d_1 = 1$ and $d_2 = 1$

The results for the case with $d_1 = 1$ and $d_2 = 1$, indicated in red in Table 5.1, are now discussed. A plastic localization band, shown in Figure 5.5 at 0.7% of imposed macroscopic equivalent strain, is formed between the two external voids. The internal void presents a heterogeneous growth acceleration. The preferred growth direction points towards the position of the acceleration band between the external voids. These accelerated void growth eventually leads to coalescence by internal necking between the internal void and the external voids.

Figure 5.6a shows a three-dimensional view of the voids after coalescence at 0.13% of macroscopic equivalent strain. The shape of the internal void significantly deviates from a spheroidal shape; the void develops a high curvature zone that extends towards the strain localization band between the external voids. This deviation puts in evidence the heterogeneous acceleration of void growth due to the interaction with the external voids.

Figure 5.6b presents a two-dimensional cut of the same simulation also after coalescence at 0.13% of macroscopic equivalent strain. In this depiction of the void arrangement, the

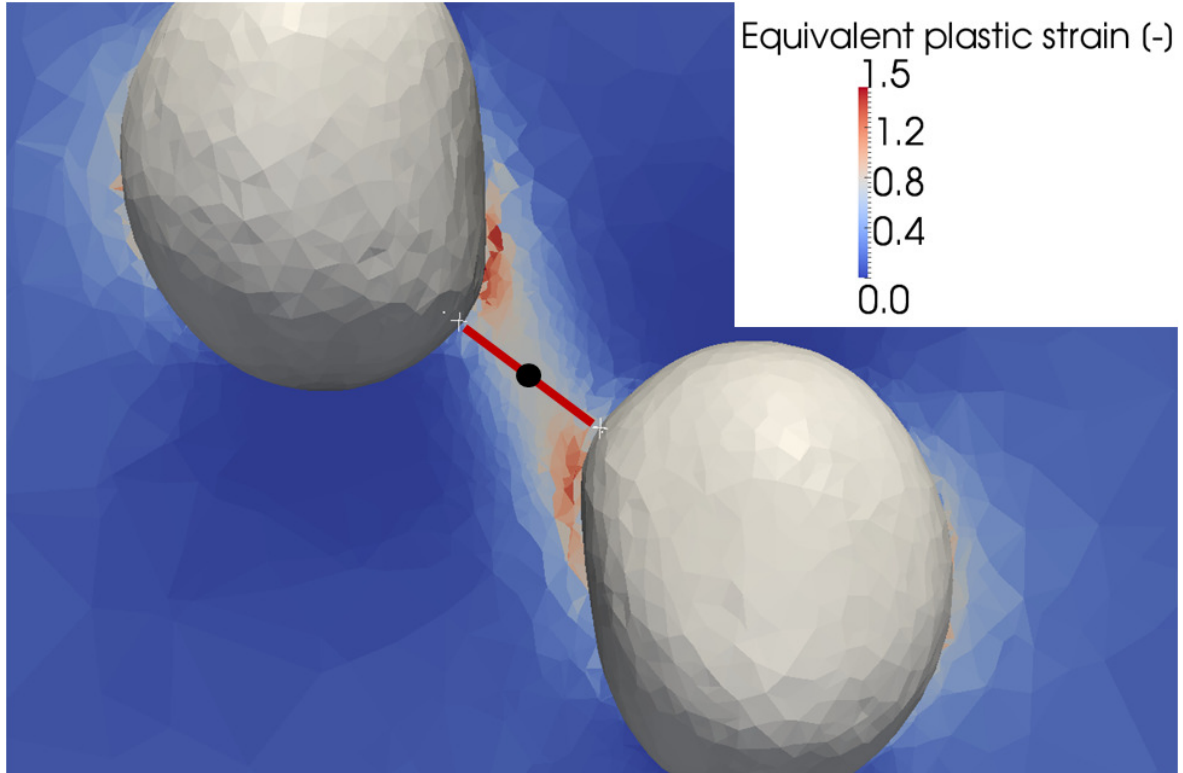
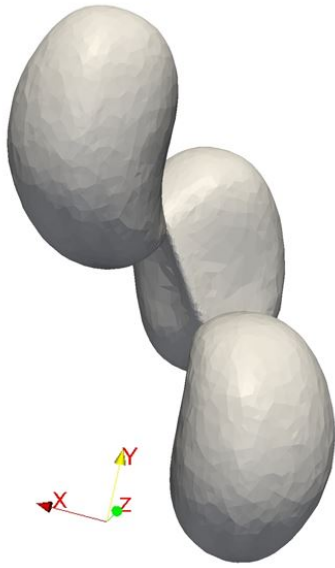


Figure 5.5: Strain localization band in a plane containing the external voids at 0.7% of imposed macroscopic equivalent strain. The minimum intervoid distance is indicated by a red line and its middle point by a black dot.

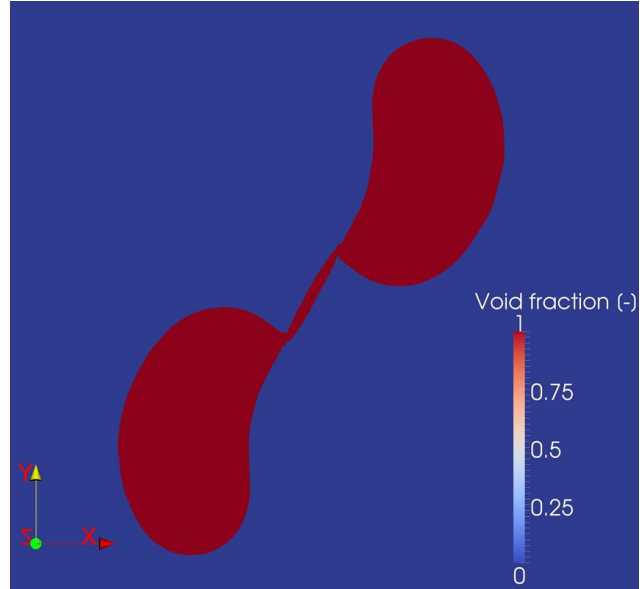
bulk of the internal void cannot be seen. Instead, a narrow void band between the external voids is visible. This narrow region is the part of the internal void that coincides with the shown cross-section. If only this image of the void arrangement is available and the presence of a third void is ignored, it might be interpreted as an instance of void-sheet coalescence. This supports the hypothesis that three-dimensional interactions between voids can produce coalescence of multiple voids that highly resemble the void-sheet mechanism if observed from a two-dimensional perspective.

This coalescence mechanism between 3 voids will be described by considering three observables: the normalized void volume of each void (Figure 5.7), the minimum intervoid distance for each pair of voids (Figure 5.8), and the equivalent plastic strain at the middle point of the shortest path between each pair of voids (Figure 5.9). The minimum intervoid distance and the middle point of the shortest path are schematized in Figure 5.5 for a pair of voids with a red line and a black dot, respectively.

In Figure 5.7, the normalized void volume is presented for each void as a function of the imposed macroscopic equivalent strain ε_{yy} ; the end of the curves corresponds to the value of ε_{yy} at the moment of coalescence. The behavior of the two external voids is identical since there is no asymmetry to differentiate them. The internal void, however, presents an accelerated void growth that, at coalescence, represents an additional 10% volume increase



(a) Three-dimensional view



(b) Two-dimensional view

Figure 5.6: Configuration of voids after coalescence at 0.13% of macroscopic equivalent strain for $d_1 = 1$ and $d_2 = 1$.

with respect to the external voids. Since all the voids are subject to the same macroscopic stress state, it is the local differences of stress state, i.e., the interaction with the external voids, that induce this accelerated void growth and promote the formation of the observed high curvature zone (Figure 5.6a). This high curvature region will, in turn, modify the stress state ahead of the resulting notch-like feature and further accelerate void growth.

Since the behavior of the two external voids is identical, only two pairs of voids are considered in the following: the external-external pair and one of the two internal-external pairs. Figure 5.8 presents the evolution up to coalescence of the minimum intervoid distance for these two pairs of voids. As the domain is deformed, both curves decrease monotonically and almost linearly with nearly identical rates of decrease. The internal-external pairs experience coalescence when their minimum intervoid distance approaches zero.

Figure 5.9 exhibits the evolution of the plastic strain at the middle point of the shortest path between voids. At the middle point of the external-external pair, the equivalent strain evolves linearly with a slope of approximately 7.8, i.e., even if no exponential trend is observed, this local strain increases a lot more rapidly than the strain imposed on the domain. The equivalent strain at the middle point of the internal-external pair increases exponentially. This is consistent with the observed final configuration since it is the internal-external pair that undergoes coalescence by internal necking. Coalescence occurs at a macroscopic equivalent strain of 0.11.

The analysis of the case with $d_1 = 1$ and $d_2 = 1$ provided evidence of the heterogeneous void growth that results from the interaction between the three voids in the cluster. The

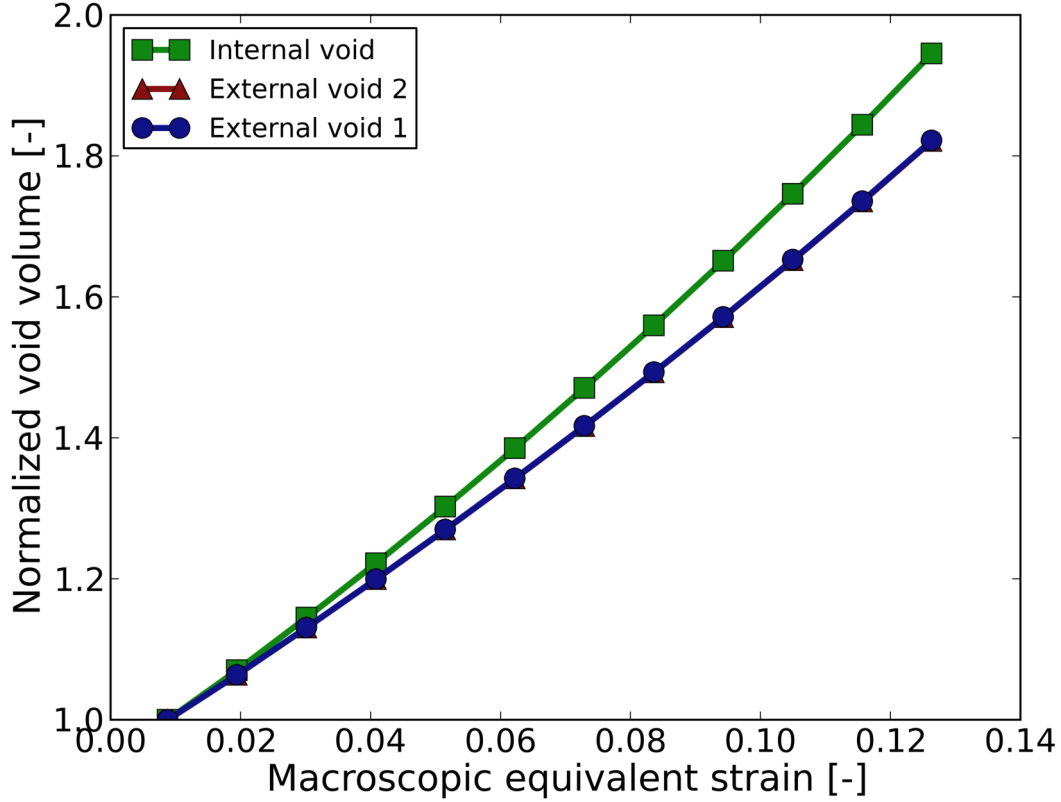


Figure 5.7: Normalized void volume for $d_1 = 1$ and $d_2 = 1$.

coalescence of the cluster was described through three observables: the normalized void growth, the minimum intervoid distance and the equivalent strain at the middle point of the shortest path between each pair of voids. Sections 5.3.2 and 5.3.3 investigate further the described coalescence mechanism by exploring how these three observables evolve when the relative positions of the voids in the cluster change.

5.3.2 Effect of d_2

The effect of d_2 is examined in this subsection, i.e., the position of the external voids is fixed ($d_1 = 1$), and the effect of changing the position of the internal void is examined. This corresponds to exploring the design space in the sense indicated in blue in Table 5.1. The evolution of void volume, intervoid distance and local plastic strain as functions of the macroscopic equivalent strain, change with increasing d_2 . These evolutions are described in Figures 5.10, 5.11 and 5.12, respectively. Figure 5.13 presents three-dimensional views of the voids just after coalescence.

As described in section 5.3.1, the case with $d_2 = 1$ (Figure 5.10a) presents a linear evolution in terms of void volume. When d_2 increases, the void volume evolution changes

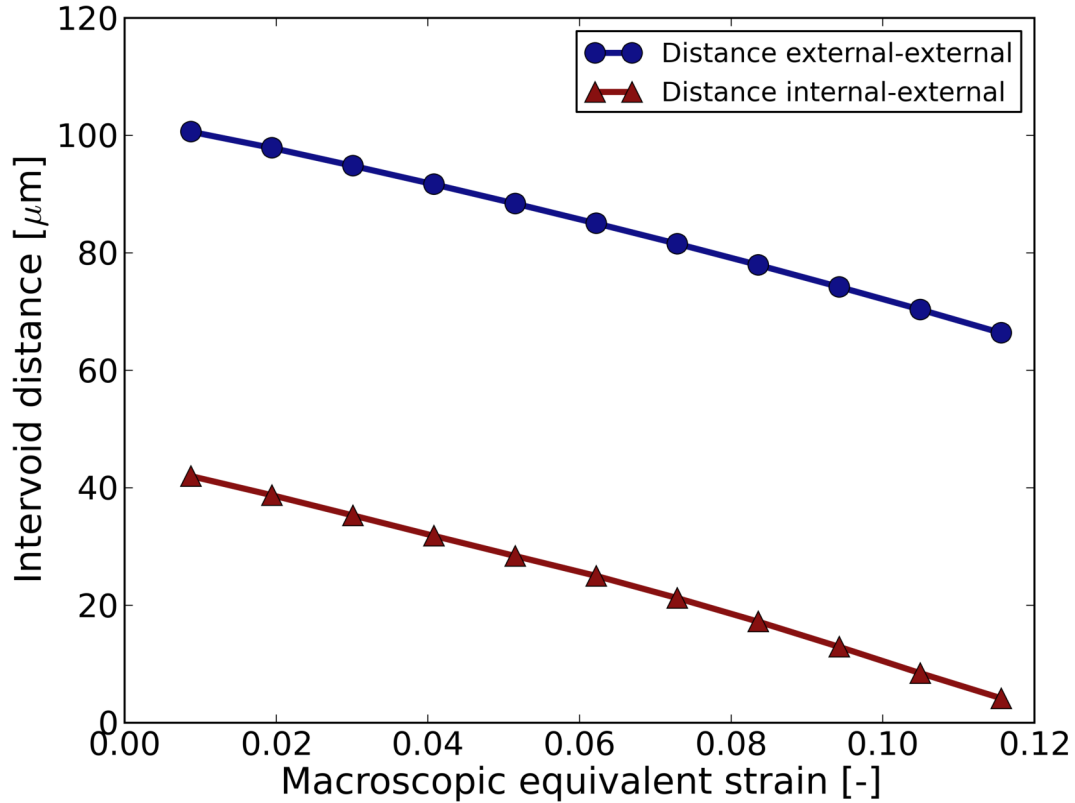


Figure 5.8: Minimum intervoid distance for $d_1 = 1$ and $d_2 = 1$.

and presents an exponential behavior. The $d_2 = 1$ case (Figure 5.10a) presents a normalized void growth of about 1.95 for the internal void at coalescence, and it increases up to 7.8 for the case with $d_2 = 4$ (Figure 5.10d).

Even when d_2 is 4 times d_1 , the internal void presents more void growth than the external voids. Since all voids are subject to the same macroscopic stress state, this shows that amount of void growth undergone by a given void can be a complex function of its position in a given void cluster.

The evolution of the relationship intervoid distance-macroscopic equivalent strain is depicted in Figure 5.11. In the same manner as for the normalized void volume, the linear behavior of the intervoid distance observed for $d_2 = 1$ disappears when d_2 increases.

For the cases with $d_2 = 1$ (Figure 5.11a) and $d_2 = 1.75$ (Figure 5.11b), the internal-external pair of voids are closer in the initial configuration and coalesces first. Also for the case $d_2 = 3.25$ (Figure 5.11c), coalescence of the internal-external pair is observed first even if the initial intervoid distance of this pair represents approximately 140% of the intervoid distance of the external-external pair. For the case $d_2 = 4$ (Figure 5.11d), the initial intervoid distance of the internal-external pair is 160% that of the external-external pair, and a simultaneous

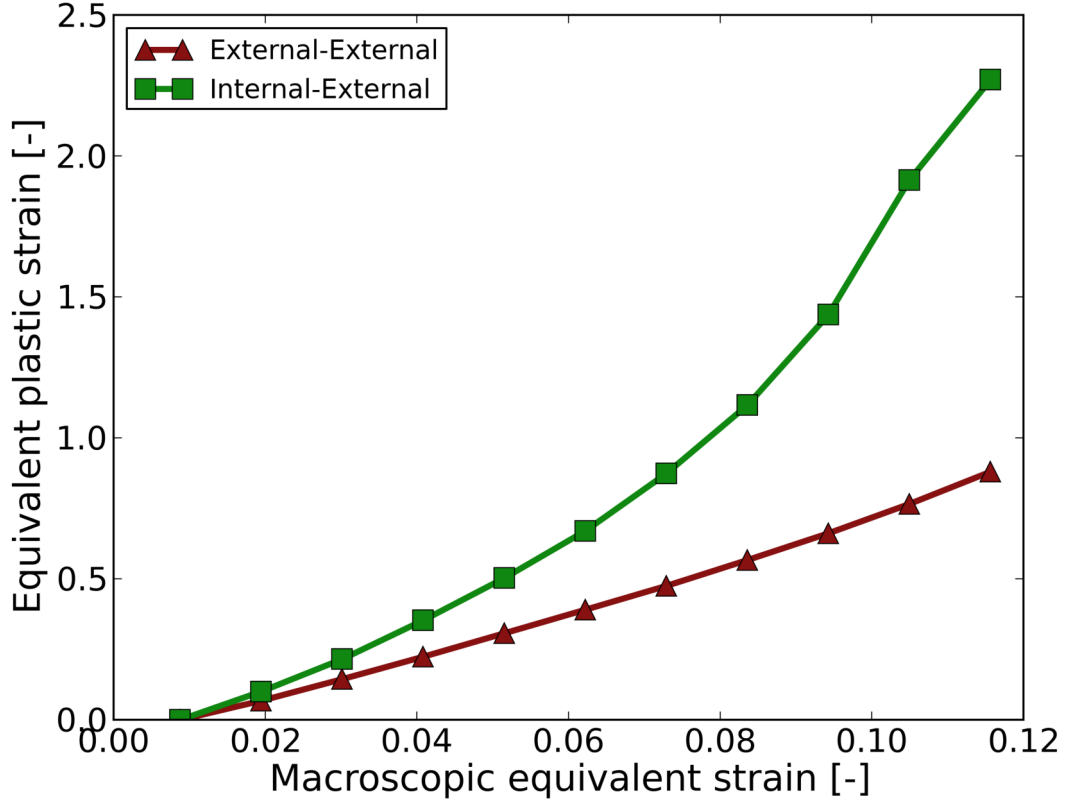


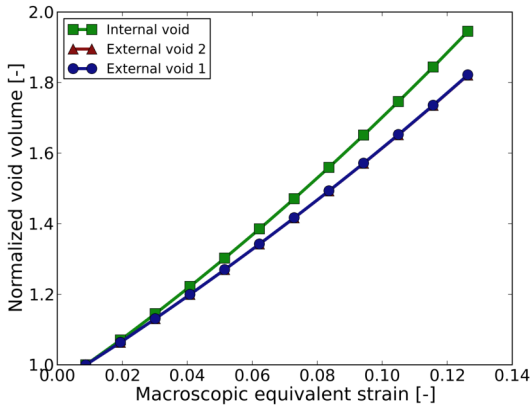
Figure 5.9: Equivalent plastic strain at middle point of shortest path between voids for $d_1 = 1$ and $d_2 = 1$.

coalescence between the 3 voids is observed (Figure 5.13d).

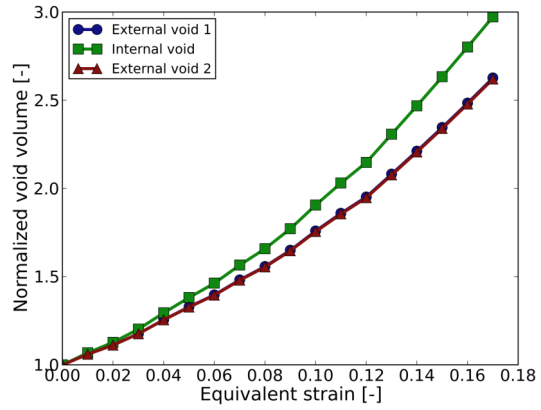
Figure 5.12 presents the evolution the equivalent plastic strain at the middle point of the shortest path between each pair of voids, for four different values of d_2 . The last value of the macroscopic equivalent strain of each pair of curves represents the value for which coalescence was observed; it increases monotonically with d_2 , and goes from 0.11 (Figure 5.12a) to 0.39 (Figure 5.12d). Irrespectively of the value of the macroscopic equivalent strain, the local strain just before coalescence is in the range of 2.5-3.0

The plastic strain in the middle of the internal-external pair behaves exponentially for all four cases. For the the external-external pair, it goes from a linear behavior to an exponential behavior as d_2 increases, and it is practically superimposed with that of the internal-external pair when d_2 reaches a value of 4.

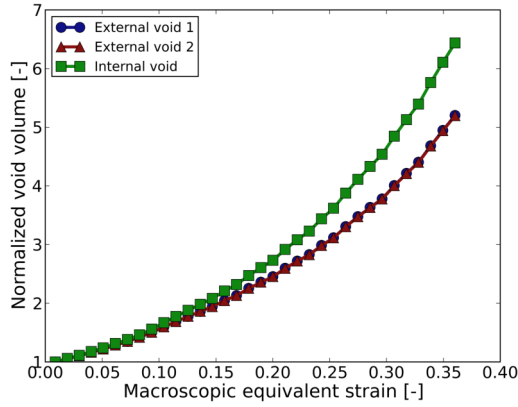
Figure 5.13 presents three-dimensional views of the configuration of the voids just after coalescence for the four cases described in this section. The perspective in each image was adjusted to try to capture well the resulting arrangement. The notch-like feature resulting from the formation of the high curvature region is present in all four cases even if the void shapes vary considerably between the different configurations. For d_2 inferior to 4, the co-



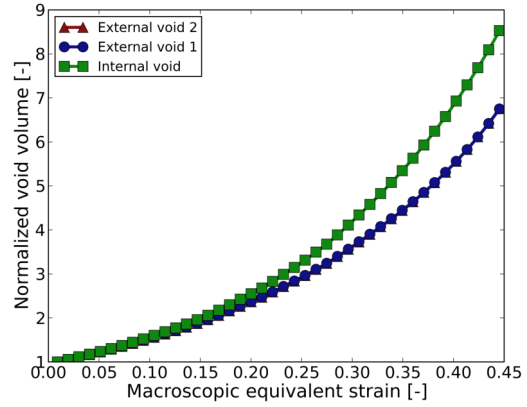
(a) $d_2 = 1$



(b) $d_2 = 1.75$



(c) $d_2 = 3.25$



(d) $d_2 = 4$

Figure 5.10: Effect of d_2 on the normalized void volume for a fixed value of $d_1 = 1$.

alescence by internal necking is observed between the internal-external pairs. For $d_2 = 4$ simultaneous coalescence between the three voids is obtained.

Effect of the internal void on void growth

In this section, the effect of the presence of the internal void on void growth is studied. Figure 5.14 presents the normalized void volume of the external voids for different values of d_2 and a fixed value of $d_1 = 1$. As the internal void moves away from the void cluster, the external void grows more slowly and the domain deforms further before coalescence. In the limit case, the internal void is so far away from the cluster that there is no more influence of this void on the growth of the external voids. This case was modeled by simulating only the two external voids in absence of the internal void and is also represented in Figure 5.14. In this case, coalescence occurs later and the void growth rate is lower.

Figure 5.14 also presents the prediction of the Rice-Tracey model [11] along with a simu-

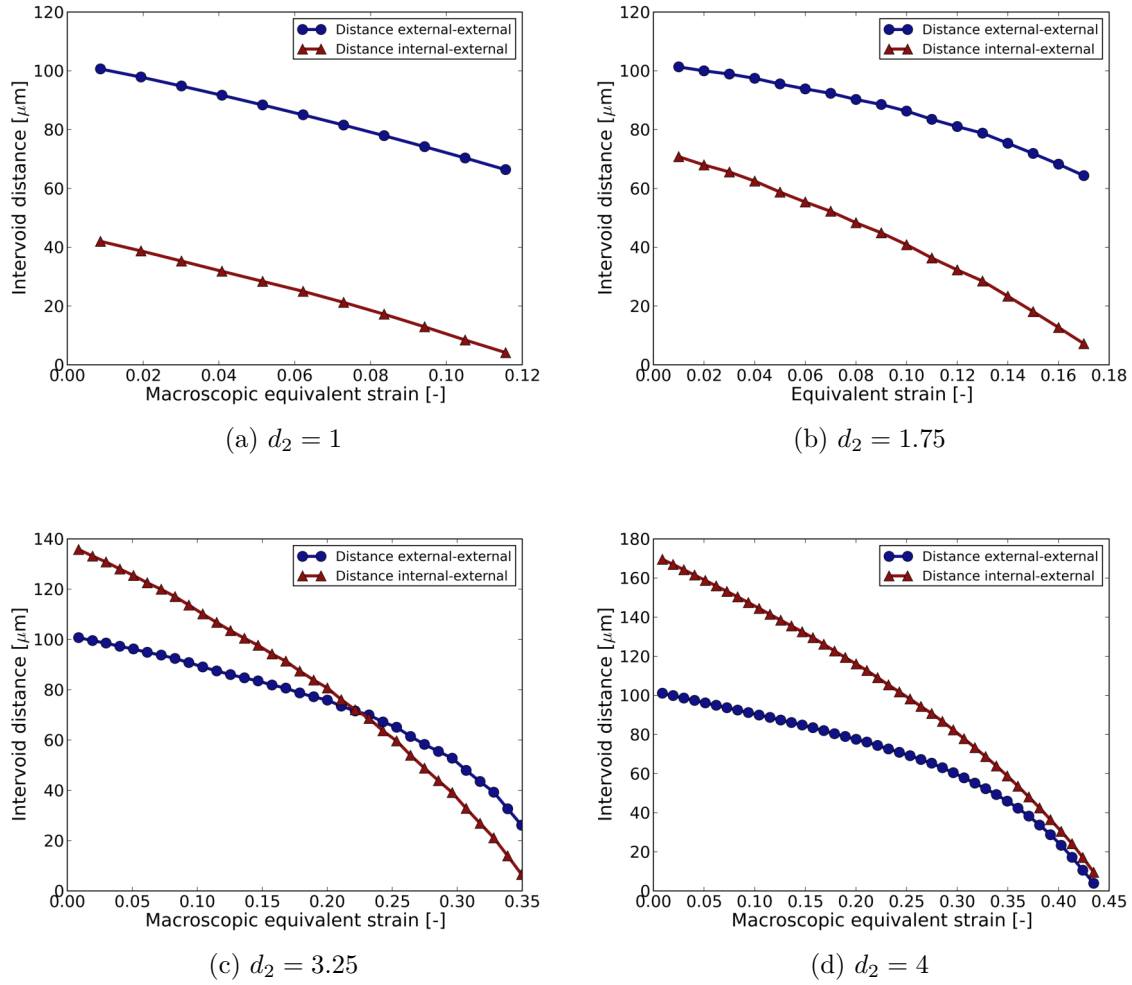


Figure 5.11: Effect of d_2 on the minimum intervoid distance for a fixed value of $d_1 = 1$.

lation with a single void under the same conditions. The single void simulation is reasonably close to the Rice-Tracey prediction. The slight underestimation produced by the Rice-Tracey model is consistent with the analysis provided by Huang [209] on dilatation rates of spherical voids. The presence of a second void (simulation with no internal void) accelerates void growth and thus the result deviates from the Rice-Tracey prediction. When a third void is introduced (the rest of the simulations presented in Figure 5.15), the results deviate even further from the Rice-Tracey model even for large values of d_2 . Given that all the simulations were carried out under the same stress triaxiality ratio, these results illustrate the importance of considering the interactions between voids in heterogeneous arrangements.

Figure 5.15 depicts the final configuration after coalescence of the void cluster in the presence of the internal void (Figure 5.15a) and in the absence of the internal void (5.15b). When the internal void is present, coalescence between the internal void and the external voids occurs very early (imposed equivalent strain of 0.11). In the absence of the internal void, coalescence between the external voids occurs much later (imposed equivalent strain of 0.46), i.e., four times later than in the presence of the internal void. The appearance of

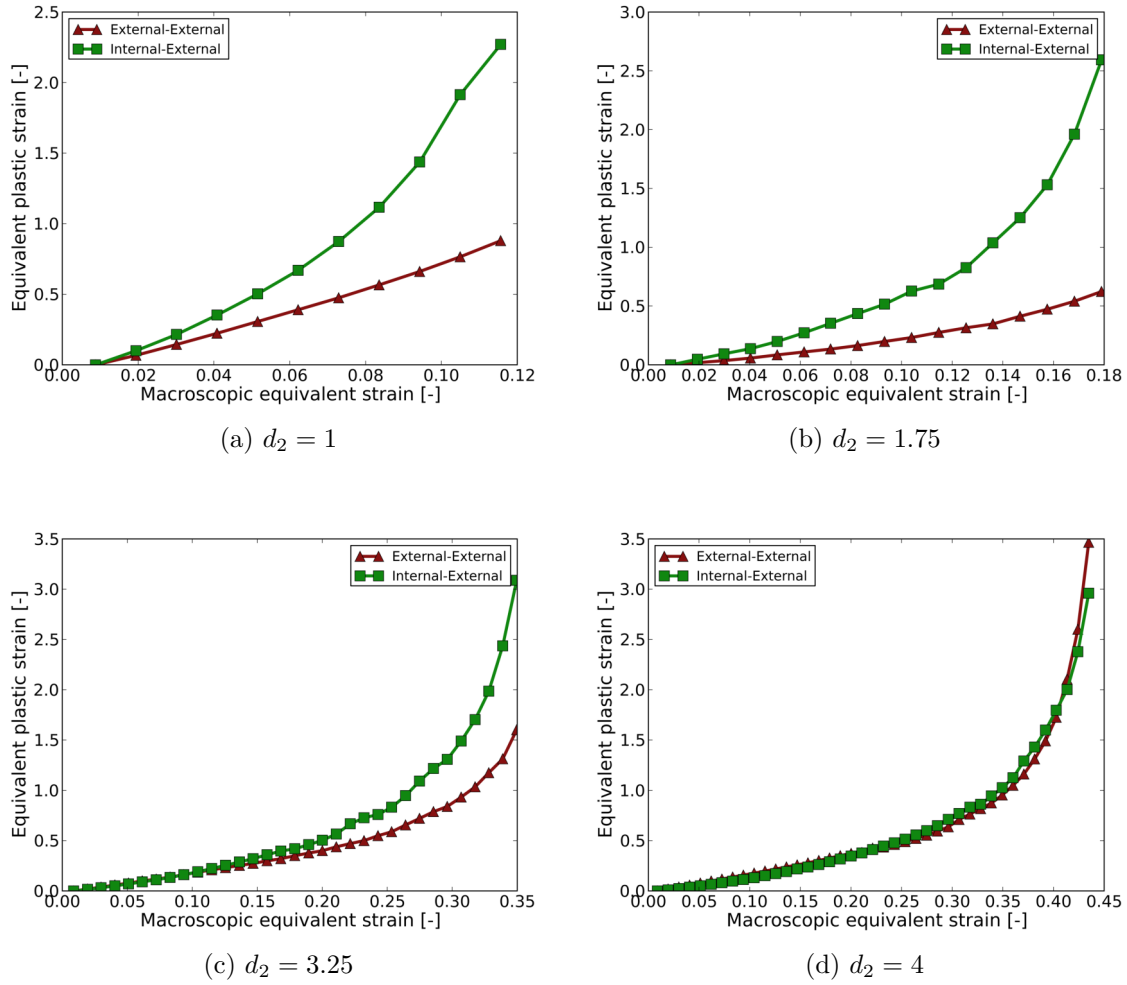


Figure 5.12: Effect of d_2 on the equivalent plastic strain at middle point of shortest path between voids for a fixed value of $d_1 = 1$.

the coalesced voids in Figure 5.15b resembles the experimental observations of Weck and Wilkinson [199] in metallic sheets with laser drilled holes when the holes were oriented at 45 deg with respect to the loading direction; the voids first undergo considerable volume change by mainly elongating in the loading direction, and then present coalescence far from their equator.

5.3.3 Effect of d_1

This section describes how the evolution of normalized void volume, minimum intervoid distance and plastic strain in the middle point between the shortest path between voids, changes with d_1 for a fixed value of d_2 of 1.75; the position of the internal void will be fixed and the external voids will change their position (sense indicated in green in Table 5.1). Four cases are examined. The fourth case ($d_1 = 3.25$), does not present coalescence up to the end of the simulation which corresponds to a final macroscopic equivalent strain of 0.5.

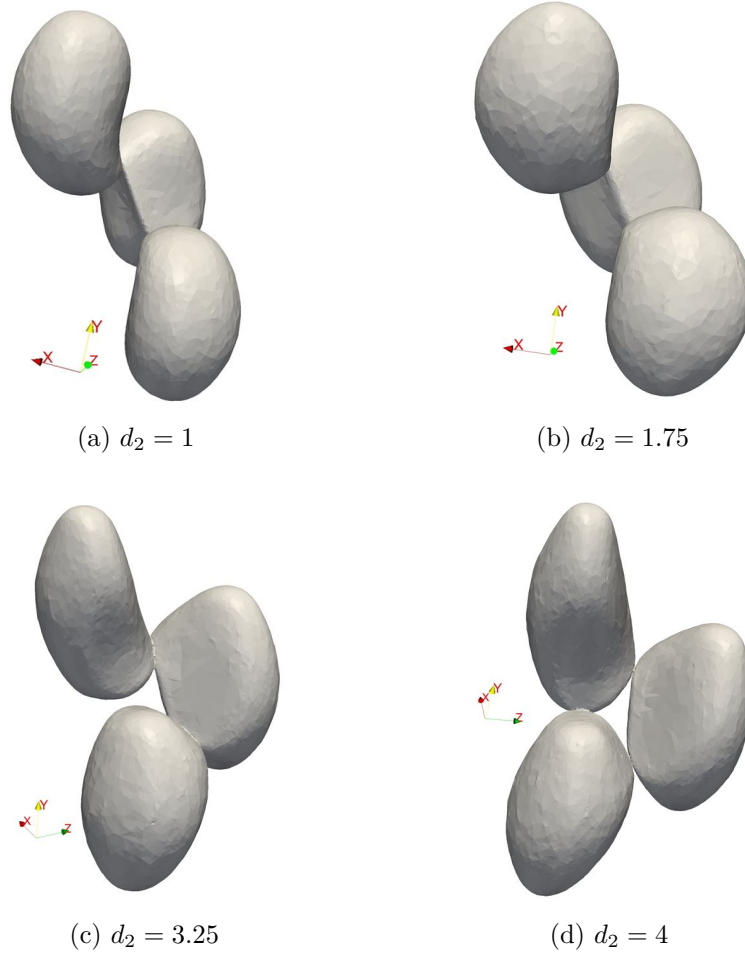


Figure 5.13: Final configuration of voids after coalescence for $d_1 = 1$ and different values of d_2 .

The way how the evolution of void volume changes with d_1 , is depicted in Figure 5.16. In all cases an exponential increase is observed, and the increase of the internal void volume is superior to that of the external voids. The difference of normalized void growth between the internal and external voids increases with d_1 and goes from 0.3 when $d_1 = 1$ (Figure 5.16a) to 0.95 when $d_1 = 2.5$ (Figure 5.16c).

Figure 5.17 demonstrates the effect of d_1 on the evolution of the minimum intervoid distance. In these four cases, the initial intervoid distance in the external-external pair is greater than that of the internal-external pair. The internal-external pair presents a higher rate of decrease. The curves change in a similar manner when d_1 is increased: an accelerated decrease of the intervoid distance is observed for lower values of d_1 , and it decreases more linearly as d_2 increases.

The effect of d_1 on the evolution of the equivalent plastic strain at the middle point of the shortest paths between voids, is illustrated in Figure 5.18. For both pairs, the evolution of the equivalent strain is exponential for low values of d_1 and transitions towards linearity when d_1 increases. The value of the macroscopic equivalent strain at coalescence increases

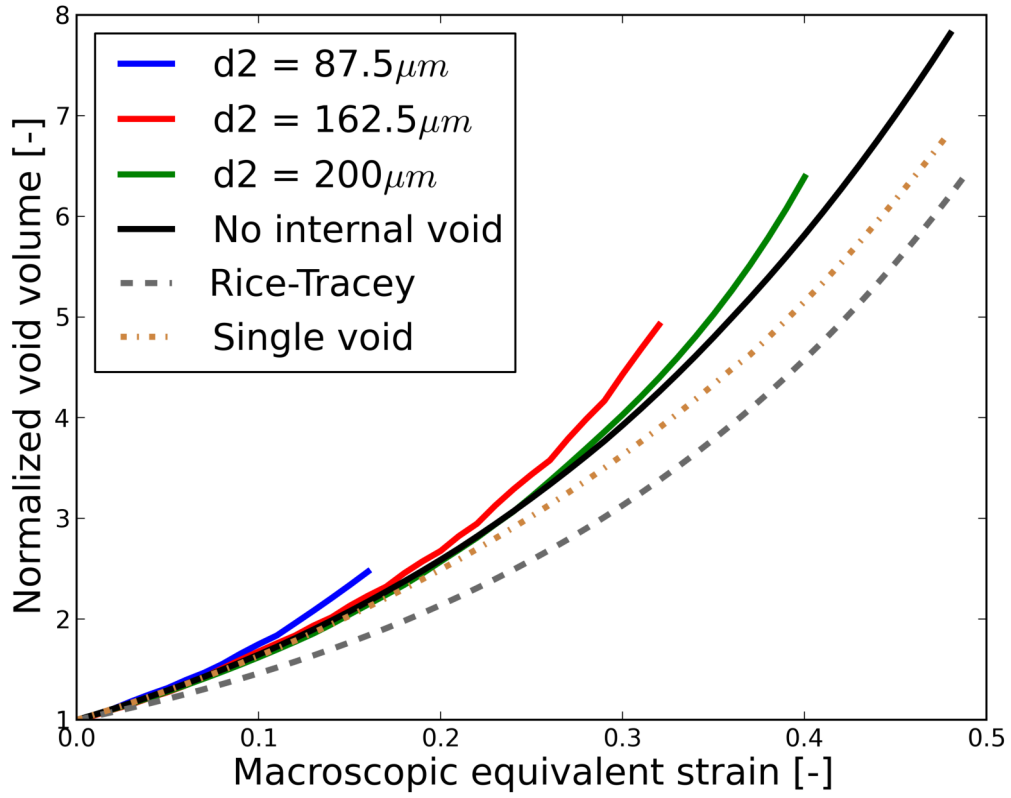


Figure 5.14: Effect of the internal void on the growth of the external void.

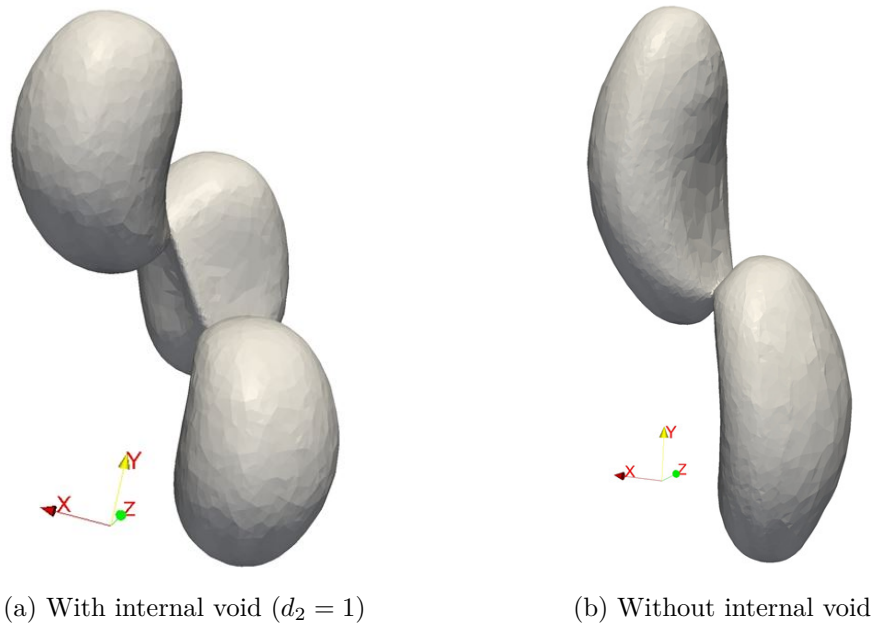


Figure 5.15: Final configuration of voids after coalescence.

monotonically with increasing d_1 . The cases with $d_1 = 1$ and $d_1 = 1.75$ present, like the cases in section 5.3.2, a value of equivalent strain at coalescence in the middle of the internal-

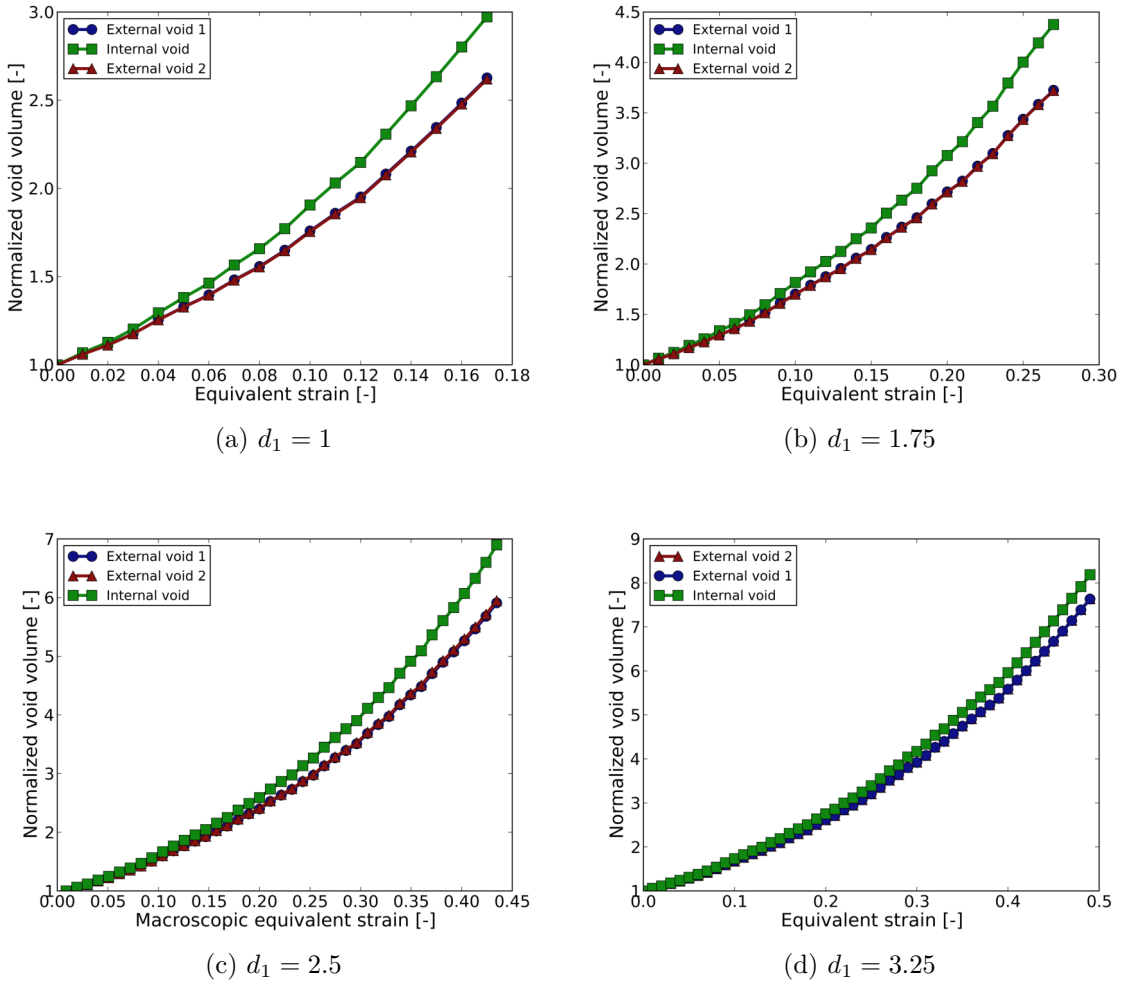


Figure 5.16: Effect of d_1 on the normalized void volume for a fixed value of $d_2 = 1.75$.

external in the range between 2.5 and 3.0. The case with $d_1 = 2.5$ presents a higher value with 3.8, and case with $d_1 = 3.25$ presents no coalescence and a smaller value of plastic strain of 1.7.

5.3.4 Global results and discussion

In Figure 5.19, a response surface is depicted. This response surface presents the macroscopic equivalent strain at coalescence as a function of d_1 and d_2 . Accomplished simulations are indicated as a blue dot. The white zones indicate that coalescence was not observed up to the end of the simulation, i.e., up to 0.5 of macroscopic equivalent strain. Coalescence was observed for a wide range of strains: from 0.1 up to 0.5.

The parametric space could be explored more assiduously if the presented coalescence mechanisms is to be described more in detail. In particular, the transitions between the parameter combinations that exhibit coalescence and those that don't should be further

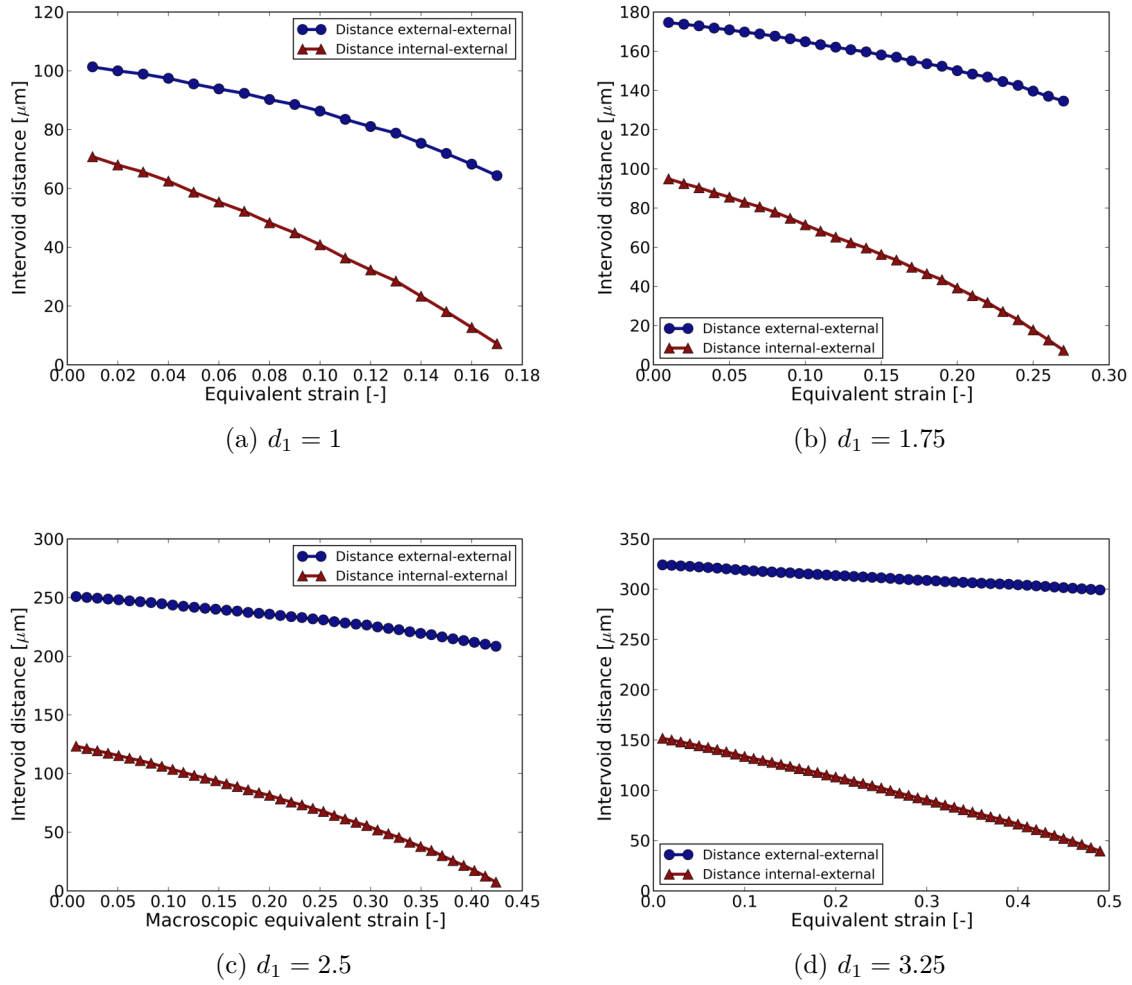


Figure 5.17: Effect of d_1 on the minimum intervoid distance for a fixed value of $d_2 = 1.75$.

explored if quantitative information is to be used. However, the objective of the parametric study was to show that the coalescence mechanisms between three voids can be observed for many different initial configurations. Figure 5.19 demonstrates that this mechanism is obtained for a wide range of values of d_1 and d_2 given that the domain is sufficiently deformed.

The acceleration increase of the local equivalent strain with respect to the far-field strain has already been reported in the work of Bandstra and Koss [48] for a Gurson material model; the authors observed a more complex localization behavior. The use of an elastic-perfectly plastic material in this work highlighted the interaction of the voids while neglecting the effect of secondary voids, which was desirable to study the hypothesis that three dimensional interactions could lead to apparent void-sheet coalescence instances.

As seen in sections 5.3.2 and 5.3.3, most of the observed coalescence instances in the parametric study present a local strain before coalescence in the range of 0.25-0.3. The evolution of the intervoid distance provides a very natural threshold for coalescence by internal necking: coalescence occurs when the minimum intervoid distance for a pair of voids reaches

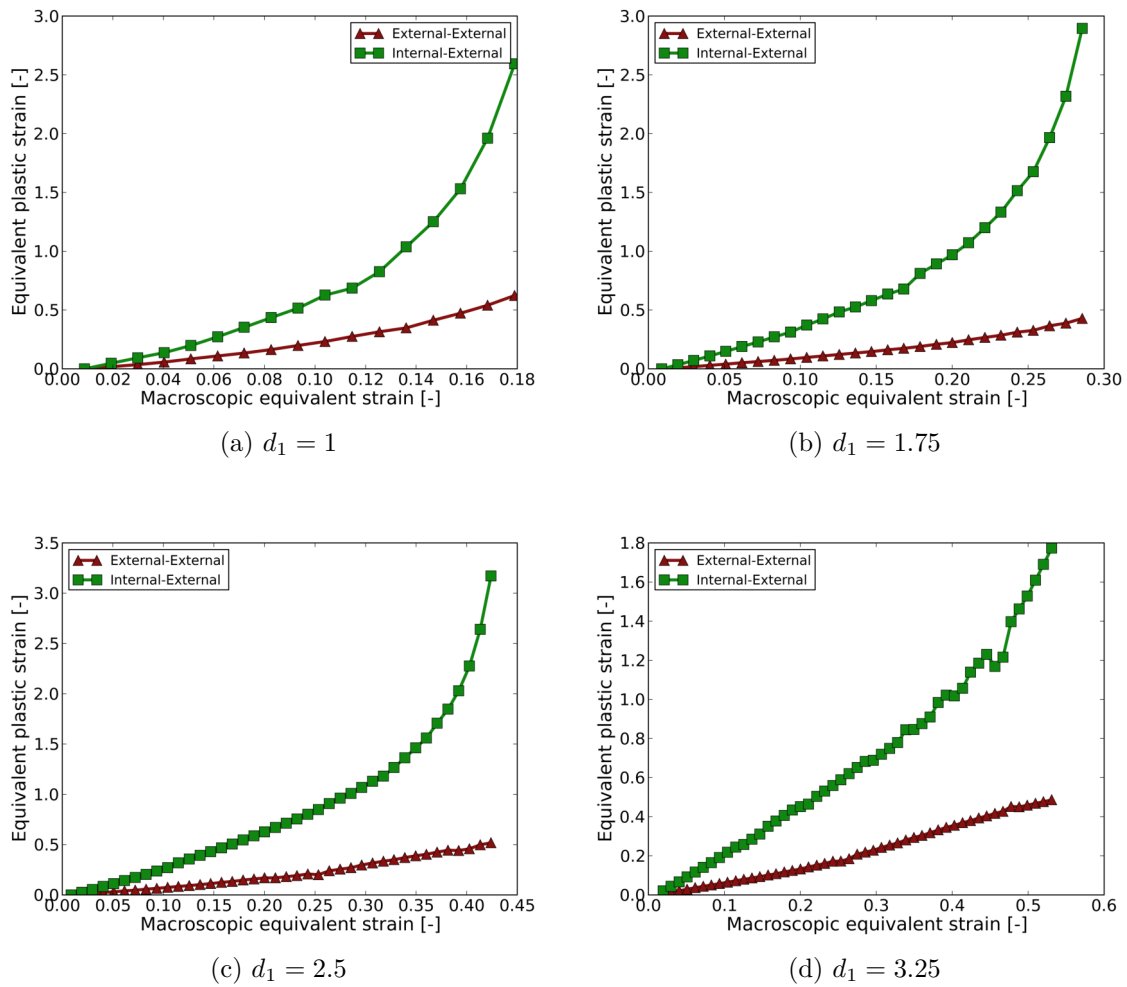


Figure 5.18: Effect of d_1 on the equivalent plastic strain at middle point of shortest path between voids for a fixed value of $d_2 = 1.75$.

zero. The simple trends observed for this variable in the results of the simulations, are promising in the sense that they could be described with simple evolution laws. This idea is explored in Chapter 6.

5.3.5 Effect of hardening

The initial parametric study presented in this chapter used an elasto-perfectly plastic material to decrease the computational burden. This allowed to confirm that a three-voids cluster can coalesce in such a way that resembles the void-sheet mechanism when a two-dimensional slice is observed. This mechanical behavior, however, is not representative of the studied nodular cast iron. In order to assess the influence of hardening on this coalescence mechanism, the parametric study was extended considering hardening. The Ludwik hardening law was used:

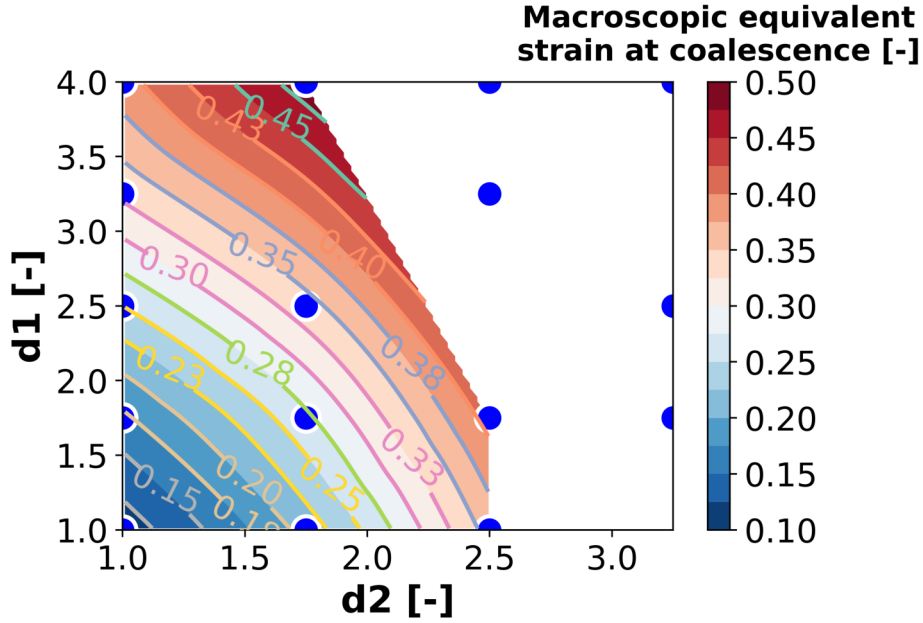


Figure 5.19: Equivalent strain of the domain at coalescence as a function of d_1 and d_2 . The blue dots indicate the accomplished simulations.

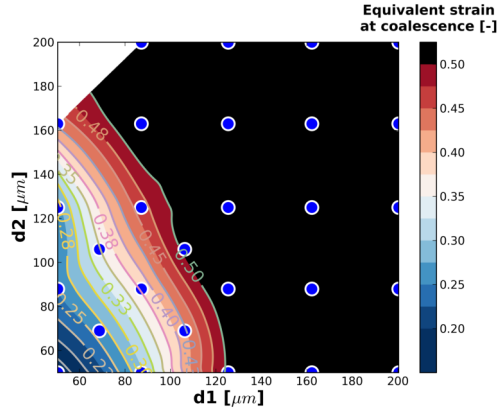
$$\sigma_{eq} = \sigma_y + K\varepsilon_{pl}^n. \quad (5.1)$$

A total of 85 additional FE simulations were carried out for three different levels of hardening corresponding to $K = 95.5$ MPa, $K = 191$ MPa and $K = 382$ MPa and a constant value of $n = 0.35$. A two dimensional response surface for each value of K is provided in Figure 5.20. The blue dots indicate accomplished FE simulations. The white zones denote lack of information and the black zones denote parameters for which coalescence was not observed. As hardening increases, the black zone extends in the parametric space, i.e., coalescence is observed less frequently. When hardening is present, the hardened zones become more difficult to deform, which promotes a more diffuse and uniform deformation distribution. The observed coalescence mechanism between the three voids is still present even for $K = 382$ MPa and is illustrated for $d_1 = 1$ and $d_2 = 1$ in Figure 5.21.

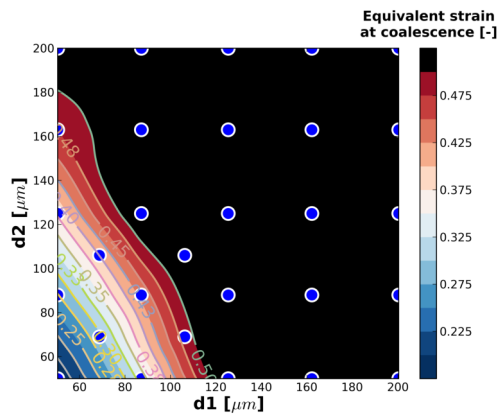
5.4 Conclusions

A methodology for the study of three-dimensional non-periodic clusters of voids and/or particles was proposed as a complementary approach in the study of the micromechanisms of ductile damage.

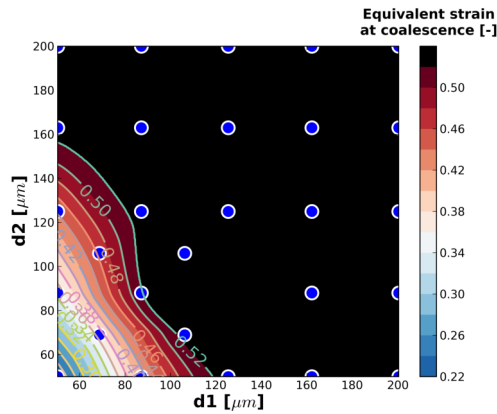
The proposed methodology was put in use to assess if the interaction with neighboring voids could play a role in apparent void-sheet instances observed in different materials. The



(a) $K = 95.5$ MPa



(b) $K = 191$ MPa



(c) $K = 382$ MPa

Figure 5.20: (a) Original slice at mid-thickness of the 90° specimen, and (b) after applying the 3D-mean filter.

FE simulations of a cluster with three voids show that accelerated and non-homogeneous void growth is promoted in the vicinity of the plastic localization band; a high curvature region that grows towards the localization band is formed. The coalescence mechanism between the voids corresponds to internal necking.

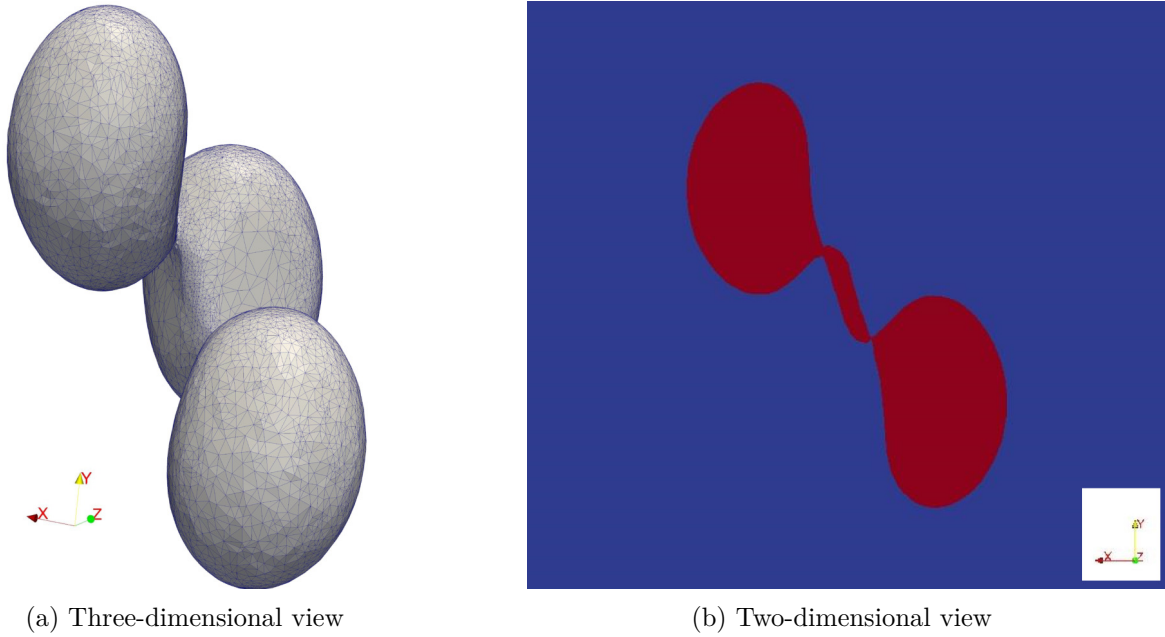


Figure 5.21: Configuration of voids after coalescence for simulation with hardening and for $d_1 = 1$ and $d_2 = 1$.

If a two-dimensional cut of the voids after coalescence is made, the resulting image considerably resembles the experimental observations. This supports the hypothesis that three dimensional interactions can play a role in the apparent void sheet instances. More generally, these results point at the importance of considering three-dimensional and non-periodic phenomena in the study of ductile damage at the microscale.

The predictions of the Rice-Tracey void growth model were compared with simulations with one, two, and three voids. When one void is considered, the results of the simulation are close to the Rice-Tracey prediction. When two or three voids are simulated, the Rice-Tracey model deviates significantly from the numerical results. This highlights the importance of considering the effect of intervoid interactions in non-simplified configurations.

The results of the parametric study provided a detailed description of the void growth and coalescence of the studied three voids cluster and the effect of the initial configuration on the coalescence was studied. It was observed that under an identical far-field stress, the growth undergone by a void depends on its relative position in the cluster. Further work is necessary to better understand the complex interactions between voids in realistic clusters.

The described coalescence mechanism was observed in the absence and in the presence of strain hardening. The latter represents more realistically the mechanical behavior of nodular cast iron. This shows that three-dimensional effects can indeed be at the origin of the previously observed void-sheet instances. Analysis of the fracture surfaces have, however, given evidence of the intervention of a secondary population of voids in the coalescence mechanisms [123]. This suggests that in nodular cast iron, coalescence occurs by void impingement

in some instances by pure internal necking and in some instances with internal necking with the intervention of secondary voids.

Results from the parametric study suggest that the equivalent plastic strain at the middle point of the shortest path between voids or the evolution of the minimum intervoid distance, might be appropriate coalescence indicators. Chapter 6 explores this further.

Résumé en français

Dans ce chapitre, une méthodologie pour l'étude des groupes tridimensionnels non périodiques de pores et/ou de particules a été proposée comme approche complémentaire dans l'étude des micromécanismes d'endommagement ductile. La méthodologie proposée a été utilisée pour évaluer si l'interaction avec les pores voisins pouvait jouer un rôle dans les occurrences apparentes du mécanisme « void-sheet » observées dans différents matériaux.

Les simulations FE d'un groupe de trois pores montrent que la croissance accélérée et non homogène des pores est favorisée dans le voisinage de la bande de localisation plastique ; une région à forte courbure qui se développe vers la bande de localisation est formée. Le mécanisme de coalescence entre les pores correspond à la striction interne.

Si une visualisation bidimensionnelle des pores après la coalescence est réalisée, l'image résultante ressemble considérablement aux observations expérimentales. Cela confirme l'hypothèse voulant que des interactions tridimensionnelles puissent jouer un rôle dans les instances du mécanisme « void-sheet » apparent. Plus généralement, ces résultats soulignent l'importance de prendre en compte les phénomènes tridimensionnels et non périodiques dans l'étude de l'endommagement ductile à l'échelle microscopique.

Les prédictions du modèle de croissance de pores de Rice-Tracey ont été comparées à des simulations avec un, deux et trois pores. Lorsqu'un seul pore est considéré, les résultats de la simulation sont proches de la prédiction de Rice-Tracey. Lorsque deux ou trois pores sont pris en compte, le modèle de Rice-Tracey s'écarte considérablement des résultats numériques. Cela souligne l'importance de prendre en compte l'effet des interactions entre pores dans des configurations non simplifiées.

Les résultats de l'étude paramétrique ont fourni une description détaillée de la croissance et de la coalescence des pores dans le groupe de trois pores étudié et l'effet de la configuration initiale sur la coalescence a été analysé. Il a été observé que sous un champ de déformation lointain identique, la croissance subie par un pore dépend de sa position relative dans le groupe. Des travaux supplémentaires sont nécessaires pour mieux comprendre les interactions complexes entre les pores dans une porosité réaliste.

Le mécanisme de coalescence décrit a été observé en l'absence et en présence d'un écroutissage. Ce dernier représente de manière plus réaliste le comportement mécanique de la fonte à graphite sphéroïdal. Cela montre que les effets tridimensionnels peuvent en effet être à l'origine des occurrences précédemment observées du mécanisme « void-sheet ». L'analyse de la surface de rupture a toutefois mis en évidence l'intervention d'une population secondaire de pores dans les mécanismes de coalescence [123]. Ceci suggère que dans la fonte nodulaire, la coalescence se produit par striction interne pure dans certains cas ; et, dans d'autres cas, par striction interne avec intervention de pores secondaires.

Les résultats de l'étude paramétrique suggèrent que la déformation plastique équivalente au milieu du plus court chemin entre pores ou l'évolution de la distance minimale entre pores pourrait constituer un indicateur de coalescence approprié au sein de la porosité globale du matériau. Le chapitre 6 explore cela plus avant.

Chapter 6

Towards a micromechanical coalescence model in nodular cast iron

Contents

6.1	Introduction	141
6.2	Results and analysis	142
6.2.1	Comparison with laminography images	142
6.2.2	Strain evolution in the intervoid ligament	144
6.2.3	Precoalescence strain as coalescence criterion	148
6.2.4	Precoalescence strain in the stress space	149
6.2.5	Uncoupled damage parameters as coalescence indicators	152
6.2.6	Intervoid distance as coalescence criterion	154
6.2.7	A simple probabilistic approach	161
6.3	Discussion	166
6.4	Conclusions and perspectives	167

6.1 Introduction

In general, void coalescence can occur by three different mechanisms: coalescence by internal necking, void-sheeting, and coalescence in columns (necklace mode) [62]. In Chapter 3, the uncertainty related to image segmentation in the SRCL-DVC-FE framework was estimated. Chapter 4 validated the FE strain measurements by comparison with DVC. The results of Chapter 5 suggest that only internal necking, with or without the intervention of secondary voids, is present in the mechanical the studied nodular cast iron specimens. This chapter constitutes a study of void coalescence by internal necking in nodular cast iron.

At the macroscale, when using porous plasticity behavior laws such as the Gurson model [27], coalescence criteria based on critical porosity [13, 210], critical stress values [133], or average inter-cavities distance [210] have been employed.

A micromechanical model for void coalescence was proposed by Thomason [61]. The critical stress value that signals the onset of coalescence in this model depends on void spacing and aspect ratio. The Thomason model has seen different extensions and improvements. Localization in planes not perpendicular to the principal loading direction was accounted for in the extension by Scheyvaerts et al. [211]. Other works have focused on accounting for a second population of voids [212].

Efforts to advance coalescence modeling have relied heavily on unit-cell calculations [133, 213, 214]. This imposes periodicity in the studied microstructure.

The term coalescence is often used to describe the transition from diffuse plastic deformation to a localized phase of plastic deformation during which the material outside of the localization band undergoes unloading [63]. Although this terminology is useful in unit-cell studies, these two distinct phases are harder to recognize in the simulation of complex and heterogeneous non-periodic microstructures. For this reason, in this work, the term coalescence is used to describe actual void impingement.

This chapter documents recent efforts towards establishing a micromechanical coalescence criterion by means of the SRCL-DVC-FE framework. The accuracy of the FE simulations is discussed in light of a comparison with the laminography images in Section 6.2.1. Then, the feasibility of using the pre-coalescence strain in the intervoid ligament as a coalescence indicator, is assessed in Section 6.2.3. An attempt to describe the pre-coalescence strain as a function of the stress state is presented in Section 6.2.4. The suitability of three different damage criteria as coalescence indicators is assessed in Section 6.2.5. A coalescence criterion based on the evolution of the intervoid distance is proposed in Section 6.2.6 and a probabilistic approach is proposed in Section 6.2.7. A discussion of the results is presented in Section 6.3 and Section 6.4 summarizes the conclusions and perspectives of this chapter.

6.2 Results and analysis

The analysis in this chapter is restricted to the 90° specimen. A simple automatic coalescence detection algorithm was implemented in the FE framework. It is a fully three-dimensional methodology to avoid misinterpretations based on two-dimensional slices. Its use allowed 18 potential coalescing void pairs to be identified among the 7626 possible void pairs corresponding to the 124 voids present in the computational domain. Figure 6.1 displays the position of the intervoid ligaments connecting the 18 void pairs. Out of these 18 void pairs, 12 of them are retained for the rest of the study and the remaining 6 are used for validation purposes.

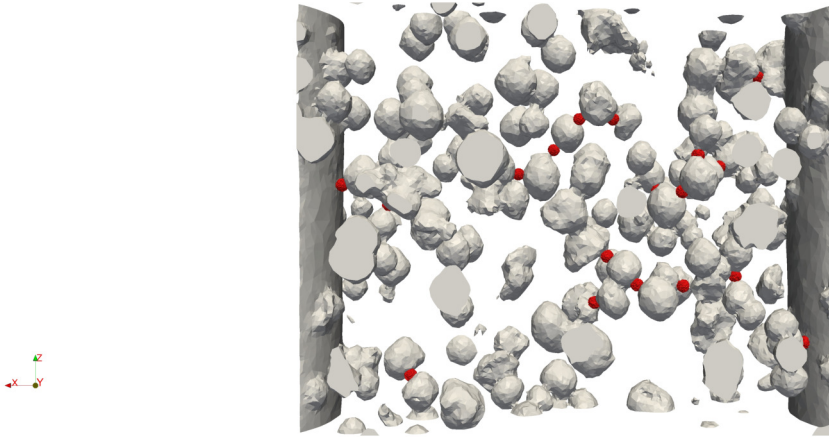


Figure 6.1: Three-dimensional view of the simulated microstructure. The voids are shown in gray and the positions of the 18 chosen intervoid ligaments are displayed in red.

The 12 retained void pairs will be analyzed in this work to evaluate the feasibility of establishing a micromechanical void coalescence criterion in nodular cast iron.

A thorough mesh verification procedure has been carried out in Chapter 3. Local mesh refinement is employed in selected intervoid ligaments to provide strain measurements that are mesh-independent [215]. This is illustrated in Figure 6.2 for a pair of voids. In the gray volume, a mesh size of $h_{min}/4$ is imposed.

6.2.1 Comparison with laminography images

In chapter 4, a detailed comparison of strain measurements obtained from DVC and the current FE simulations was carried out at two different probe volumes. The conclusion from this study was that the FE simulations provided accurate strain values, but had the tendency to underestimate the strain acceleration during the last two increments. Based on this previous study, the FE strain measurements are considered here as accurate and reliable.

To evaluate the capacity of the FE simulations of predicting the correct instant of coa-

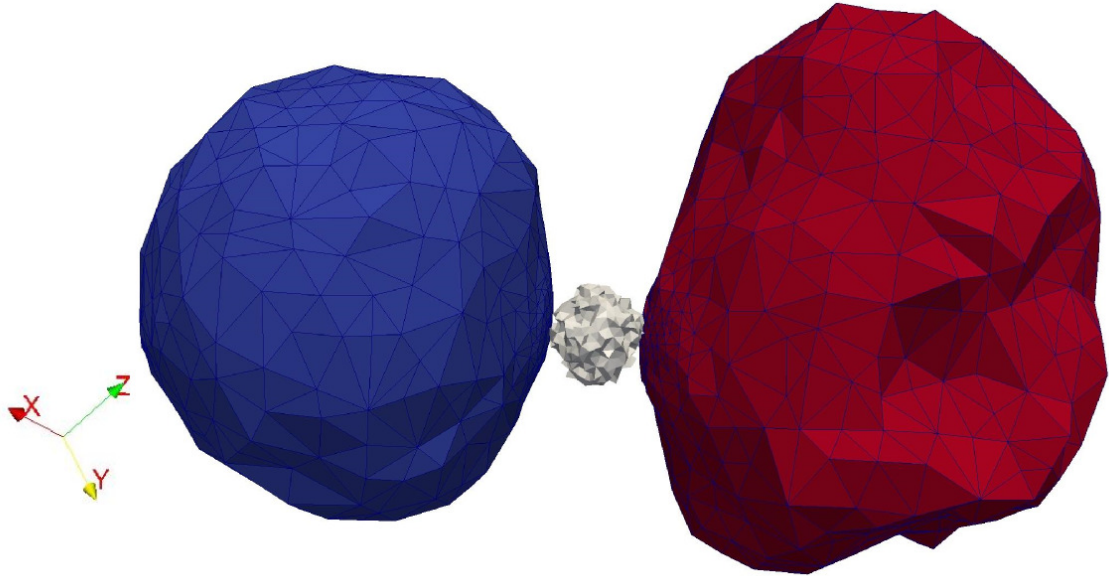


Figure 6.2: Local mesh refinement in the intervoid ligament of a pair of voids (blue and red volumes). The gray volume indicates the zone affected by the local refinement.

lescence, a complementary comparison is presented in this section. Determining the instant of coalescence of a void pair in the FE simulations is straightforward with the use of the coalescence detection algorithm. With this information, the effort required to determine the instant of coalescence according to the laminography images of the in-situ test, is reduced since a good approximation of the position of the void pair is provided by the FE simulation. The instant of coalescence according to the laminography images was determined by careful examination of these three-dimensional images.

The comparison of the instant of coalescence is expressed in Figure 6.3 in terms of the volume-averaged strain in the computational domain or macroscopic equivalent strain. In 3 of the 12 void pairs, coalescence is observed at the same macroscopic strain in the FE simulation and the laminography images. For only 1 of the 12 void pairs the FE simulation predicts coalescence earlier than observed in the laminography images. For the remaining 8 void pairs, coalescence in the laminography images is observed earlier than predicted by the FE simulation with corresponding macroscopic strain differences ranging from approximately 0.01 to 0.06.

The fact that the FE simulations predict coalescence later than observed in the laminography images is consistent with the simulations' tendency to underestimate the strain acceleration rate towards the end of the simulation. This could be a consequence of the use of a hardening law with no saturation since it's use neglects the effect of a second population of voids in the matrix [123] despite calibration of the matrix's mechanical properties at the microscale [165]. This is to be improved in future work, but doing so demands considerable calibration efforts at the microscale. Nevertheless, the results of the FE simulations are considered satisfactory given that they provide accurate measurements of strain [215] and

gray level residuals similar to those provided by DVC [9]. Efforts towards establishing a coalescence criterion at the microscale are documented in the following sections.

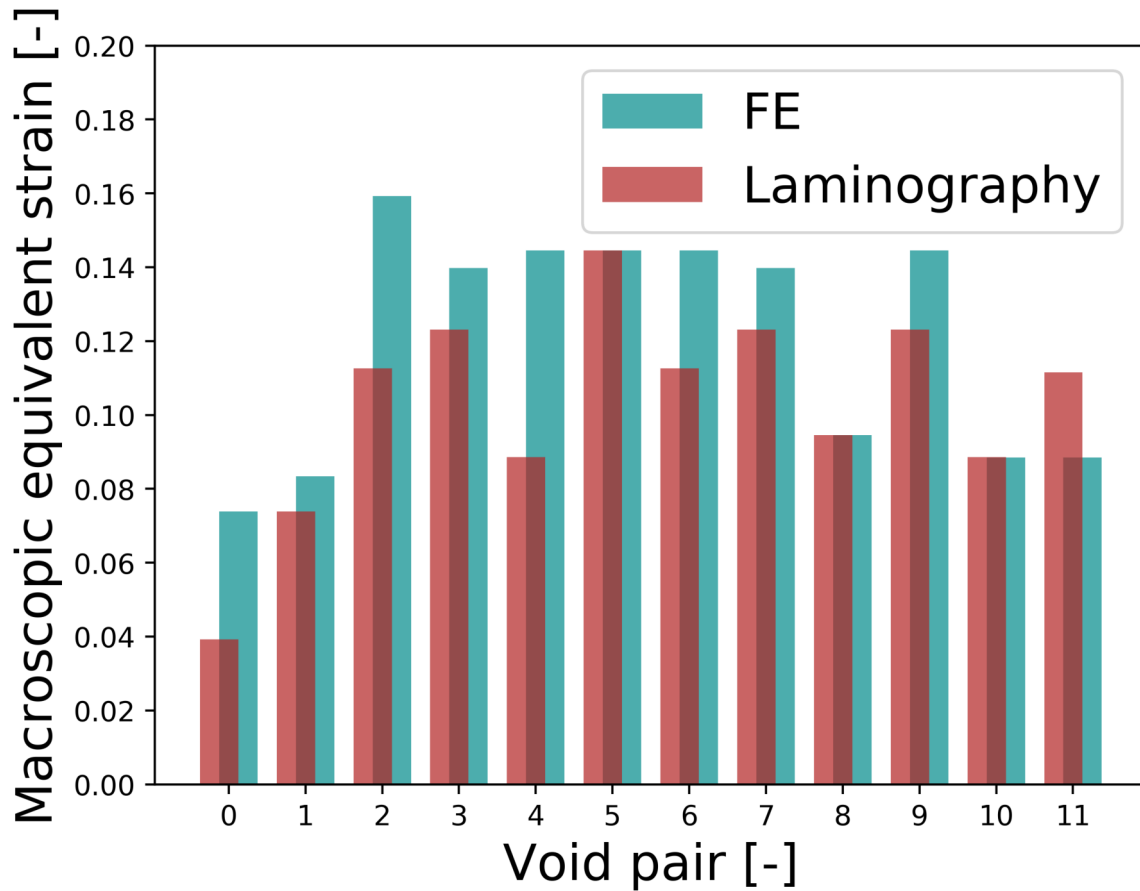


Figure 6.3: Equivalent macroscopic strain at the moment of coalescence for 12 different void pairs according to laminography images and the FE simulations.

6.2.2 Strain evolution in the intervoid ligament

In this section, the evolution of the plastic equivalent strain in the intervoid ligament of the 12 voids is assessed. More specifically, the shortest path between each void pair was identified and the evolution of the local punctual strain in this path was obtained from the FE simulation for each of the void pairs at each increment. The voids will be referred to with an index in the range from 0 to 11.

Figure 6.4 shows the strain in a cutting plane that contains the shortest path between the voids of pair 9 at increment 8. The localization band does not coincide perfectly with the direction of the shortest path. Examination of the strain field for the other void pairs confirms this observation. In general, the shortest path between voids forms a certain angle with the corresponding strain localization band in the intervoid ligament.

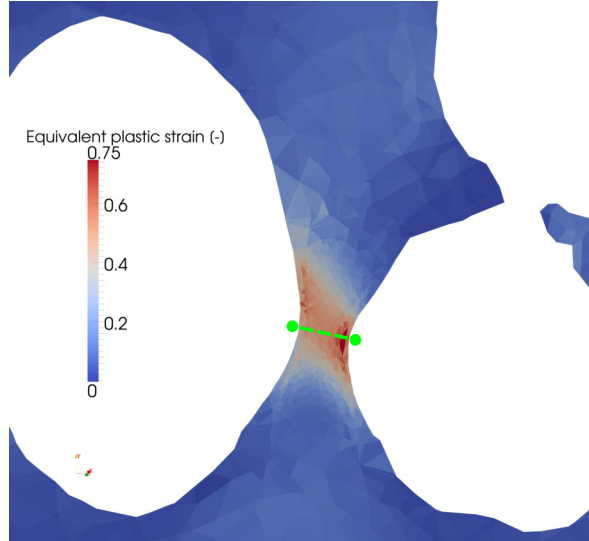


Figure 6.4: Strain concentration band in the intervoid ligament of pair 9 at increment 8 in a cutting plane. The shortest path between the voids is signaled with a green dashed line.

The evolution of the equivalent plastic strain along the shortest path between voids is shown in Figure 6.5 for void pair 6. The strain evolution for the 12 void pairs is presented in the appendices. The length of the shortest path or minimum intervoid distance evolves during the simulation. For this reason, to facilitate the understanding of the strain profiles, the strain is presented as a function of a normalized distance along the shortest path between voids. In this normalized intervoid distance, the value 0 represents the interface of the first void of the pair, and 1 the interface of the second void of the pair.

The strain profiles are shaped differently, with different symmetry levels. In general, however, a constant strain value could be a reasonable approximation at a given increment. Observation of the strain band in Figure 6.4 suggests that the strain level in the middle of the shortest path between voids could be used as a strain level representative of the concentration band in the intervoid ligament. This measurement of the equivalent plastic strain in the middle of the shortest path between voids is hence chosen as a first approximation of a representative strain measurement for a void pair for the remainder of the study. This allows the analysis to be greatly simplified.

The strain profiles also suggest a nonlinear evolution of the strain levels during the simulation. This idea is explored further in Section 6.2.4.

The initial and postcoalescence configurations of the void pairs 6-8 are shown in Figures 6.6, and for the rest of the void pairs in the appendices. In the postcoalescence configurations, a red arrow points at the location where coalescence occurred.

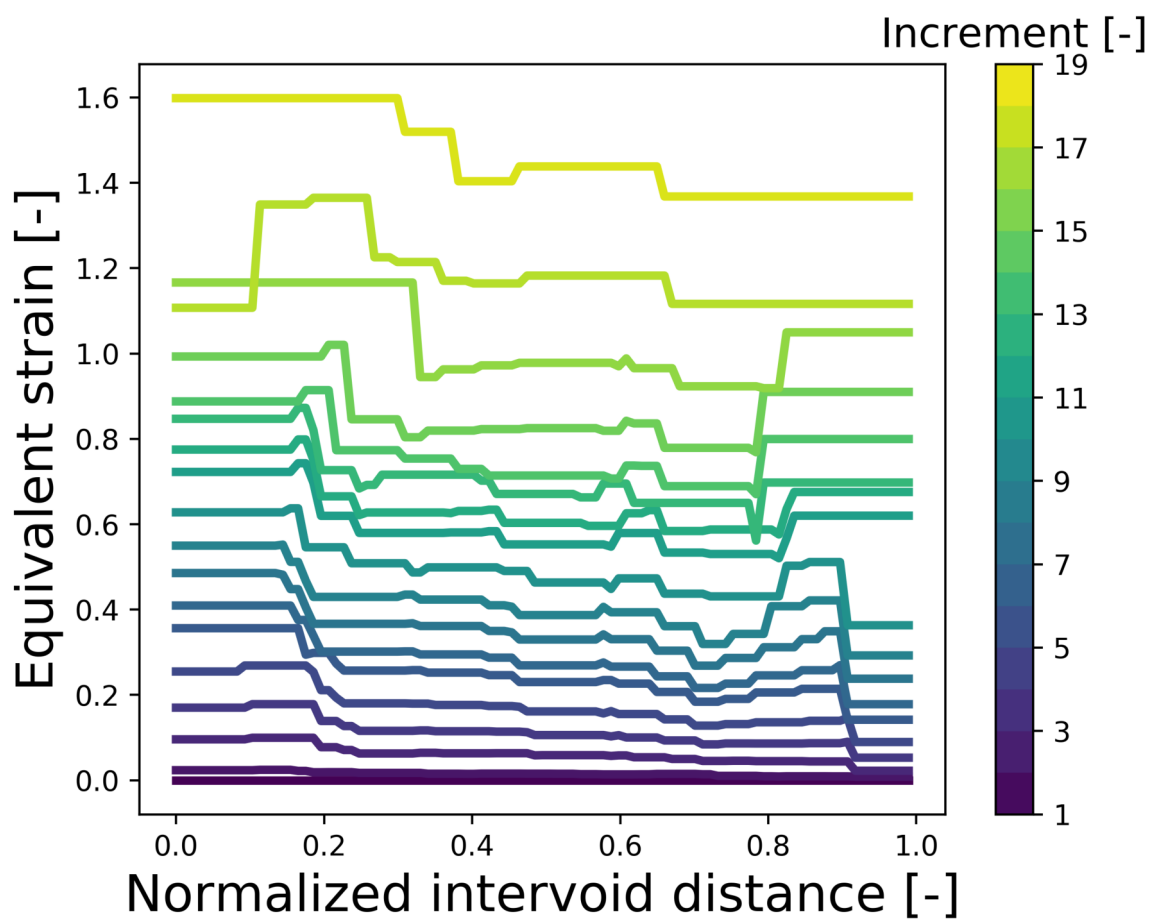
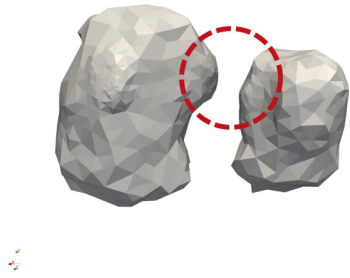
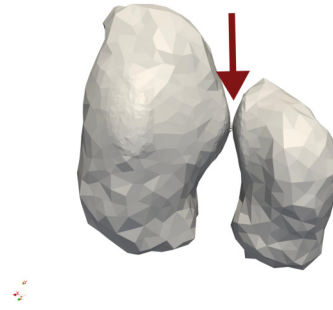


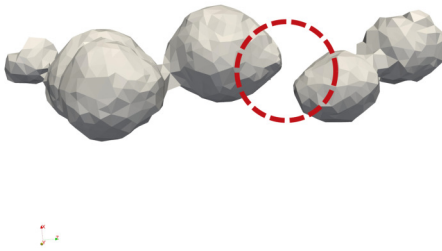
Figure 6.5: Strain profiles in the shortest path between two voids obtained from the FE simulation for the void pair 8.



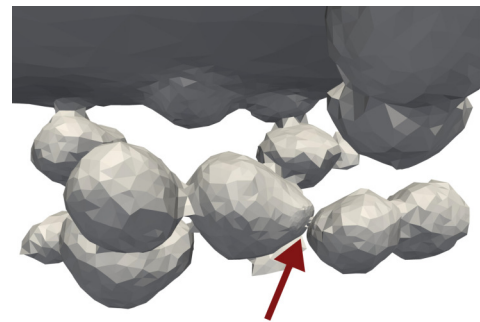
(a) Pair 6 - Initial



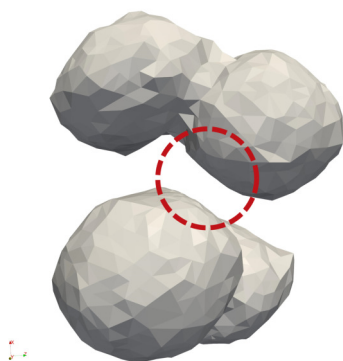
(b) Pair 6 - Postcoalescence



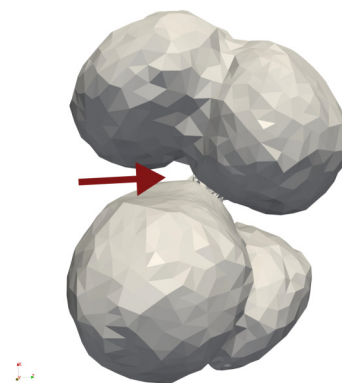
(c) Pair 7 - Initial



(d) Pair 7 - Postcoalescence



(e) Pair 8 - Initial



(f) Pair 8 - Postcoalescence

Figure 6.6: Three-dimensional views of the void pairs in their initial (left column) and postcoalescence (right column) postcoalescence configurations for void pairs 6-8.

6.2.3 Precoalescence strain as coalescence criterion

Local values of equivalent strain at the microscale have been proposed as possible coalescence indicators for the internal necking mechanism [123, 199]. Mixed and inconclusive evidence for the suitability of the strain as coalescence indicator was found in Chapter 4. Possible reasons for the inconclusiveness of the analysis were the limited amount of analyzed information and probable misinterpretation of results due to the examination of two-dimensional slices in a complex three-dimensional simulation. To improve on this study, instead of the original 2 probe volumes, the strain value at 12 different intervoid ligaments is analyzed here and no use of two-dimensional slices is made.

In this section, the suitability of the precoalescence equivalent strain as coalescence criterion is assessed. Figure 6.7 presents the evolution of the equivalent plastic strain in the intervoid ligament for the 12 analyzed void pairs as a function of the macroscopic equivalent strain. An apparent exponential trend is observed for all of the void pairs with different degrees of increase rate. The registered precoalescence strain values are in the range from 1.40 to 1.96.

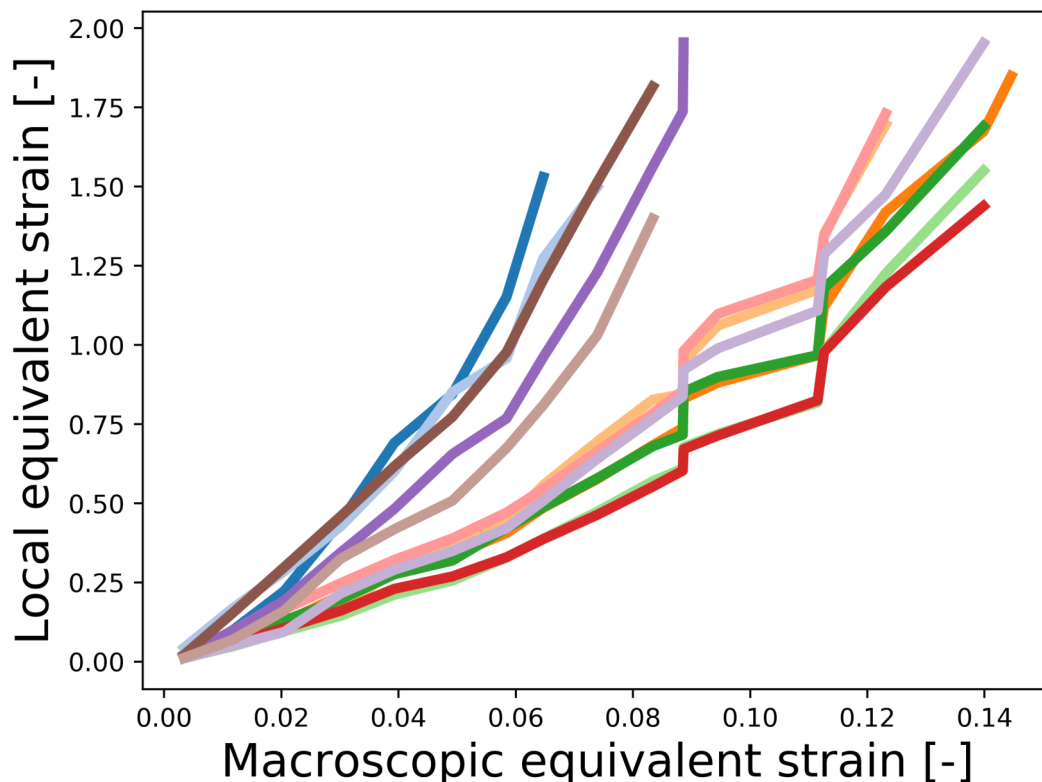


Figure 6.7: Strain evolution in the intervoid ligament for 12 void pairs.

In order to quantify how efficiently the precoalescence strain value can predict coalescence, a Probit analysis [216] is carried out. This is a regression analysis applied to binary data. In

the present case, the binary variable is the occurrence or absence of coalescence and the independent variables is the local equivalent strain. Expressed in terms of coalescence probability, this corresponds to 100% or 0% of coalescence probability, respectively. Figure 6.8 presents the obtained pre-coalescence strain values as red dots (100% of coalescence probability). To carry out the Probit analysis, data associated to absence of coalescence is needed. This data is obtained from the local strain in the previous increment to the pre-coalescence increment for each void pair, and is presented in blue in Figure 6.8 (0% coalescence probability).

An ideal coalescence indicator would present no overlap between the ranges corresponding to the data points with 100% and 0% of coalescence probability. This is not the case, an overlap is observed. The probit analysis consists in fitting the probit function, the inverse cumulative distribution function of the normal distribution, to the binary data. The resulting curve is shown in Figure 6.8 as a dashed black line. Based on this analysis, a strain threshold could be established by choosing the strain value corresponding to 50% coalescence probability. Simple inspection of Figure 6.8 shows, however, that using this value as a coalescence criterion would result in multiple mistaken predictions of coalescence. To quantify this, McFadden's pseudo-R-squared [217] can be employed. A pseudo-R-squared value of 0.35 was obtained, which is not satisfactory.

Since the local equivalent strain alone did not perform well as a coalescence indicator, the stress state is incorporated in the analysis in the next section.

6.2.4 Pre-coalescence strain in the stress space

In the previous section, it was found that the pre-coalescence strain values varied in a range from 1.40 to 1.96 for the 12 analyzed void pairs. Since the stress field is heterogeneous, the different intervoid ligaments are subject to different stress states. Perhaps incorporating the stress state in the analysis will reveal a relation between the pre-coalescence strain and the stress state that will explain the observed variability of pre-coalescence strain values. This idea is explored in this section.

Figures 6.9a and 6.9b present the evolution of the stress triaxiality ratio T and the Lode parameter L , respectively, in the middle of the shortest path between voids for the 12 analyzed void pairs. The definitions of the stress triaxiality ratio and of the Lode parameter are recalled for clarity:

$$T = \frac{\sigma_1 + \sigma_2 + \sigma_3}{3\sigma_{eq}}, \quad (6.1)$$

$$L = \frac{2\sigma_2 - \sigma_1 - \sigma_3}{\sigma_1 - \sigma_3}, \quad (6.2)$$

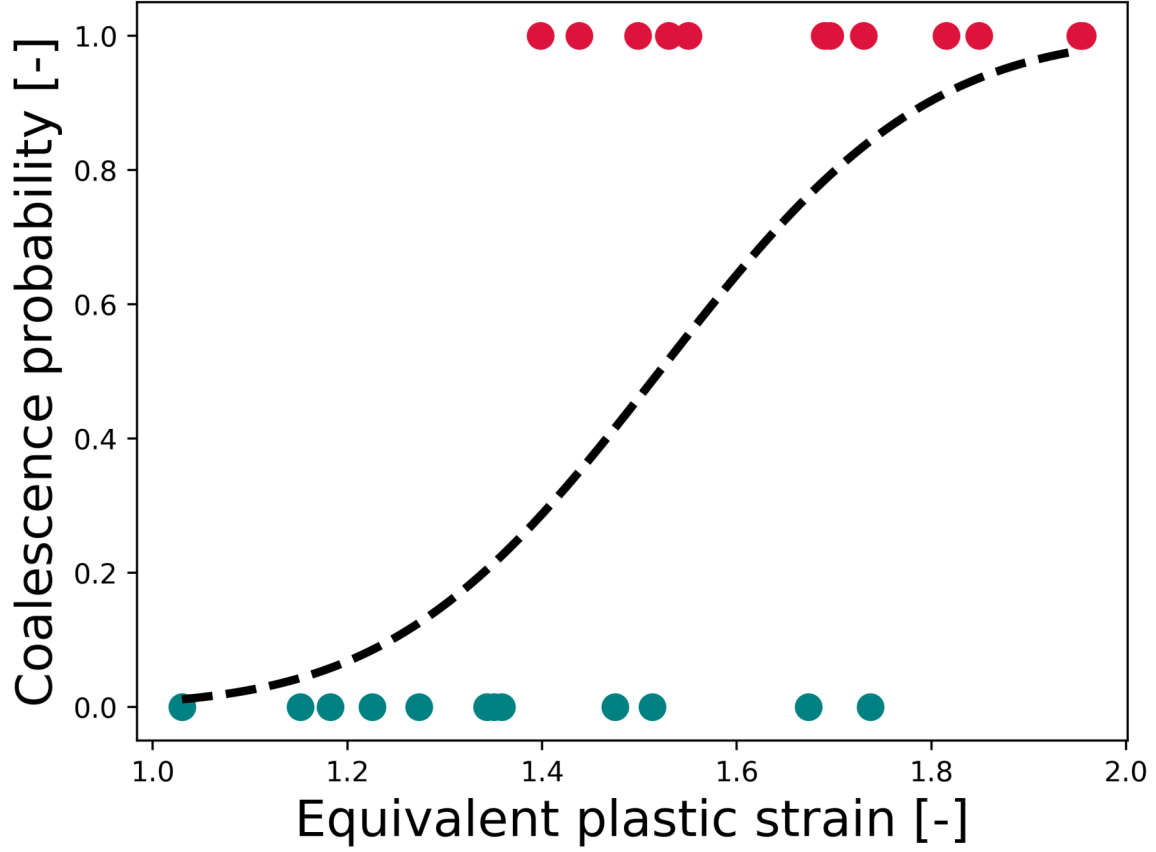


Figure 6.8: Probit regression for the equivalent strain in the intervoid ligament.

where σ_i is the i^{th} principal stress and $\sigma_1 > \sigma_2 > \sigma_3$, and σ_{eq} is the von Mises equivalent stress.

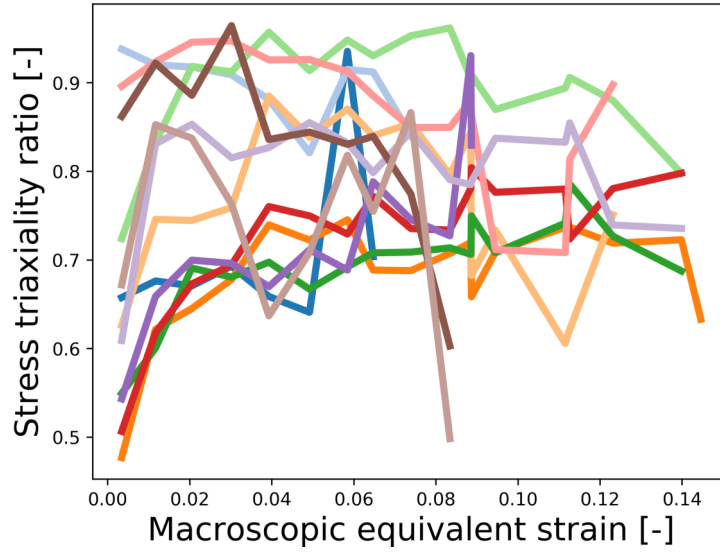
Strain-averaged measures of T and L were calculated up to coalescence as follows:

$$T_{average} = \frac{\sum_i T_i \Delta \varepsilon_i}{\sum_i \Delta \varepsilon_i}, \quad (6.3)$$

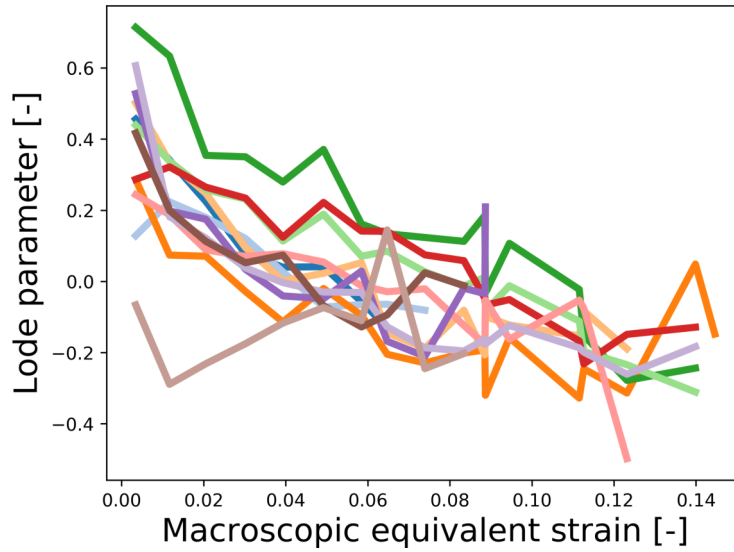
$$L_{average} = \frac{\sum_i L_i \Delta \varepsilon_i}{\sum_i \Delta \varepsilon_i}, \quad (6.4)$$

where $\Delta \varepsilon$ is the increment of equivalent strain.

Figure 6.10a presents the pre-coalescence strain values as a function of the average stress triaxiality ratio for the 12 studied void pairs. Pearson's correlation coefficient was calculated and a value of -0.13 was obtained. Similarly, Figure 6.10b shows the pre-coalescence strain



(a) Stress triaxiality ratio



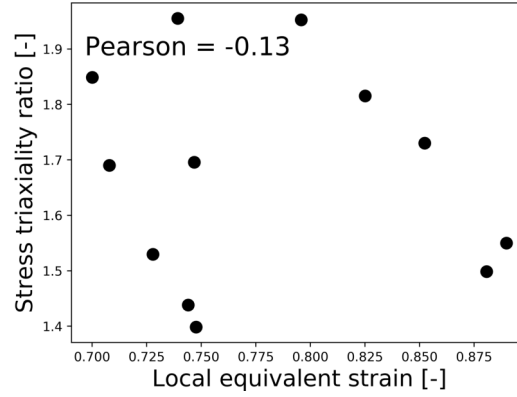
(b) Lode parameter

Figure 6.9: Evolution of the (a) stress triaxiality ratio and of the (b) Lode parameter in the intervoid ligaments.

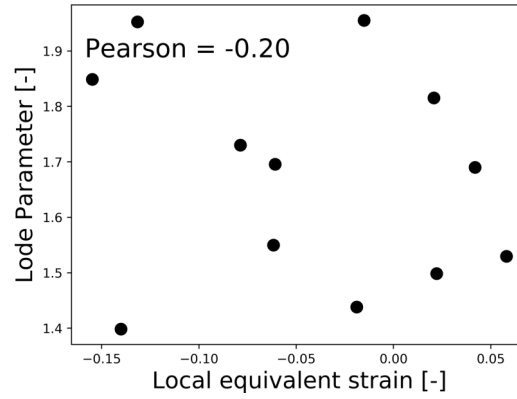
as a function of the average Lode parameter. The associated value for Pearson's coefficient is -0.20. Indeed, Figures 6.10a and 6.10b do not suggest a clear trend. To further verify this, the precoalescence strain is presented in Figure 6.11 as a function of both, average Lode parameter and triaxiality. The resulting response surface clearly illustrates the absence of a relation between the precoalescence strain and the stress state.

This approach is thus considered unfruitful and another approach based on damage indi-

cators is explored in the next session.



(a)



(b)

Figure 6.10: Precoalescence strain in the interviod ligament as a function of the (a) stress triaxiality ratio and of the (b) Lode parameter.

6.2.5 Uncoupled damage parameters as coalescence indicators

In this section, the possibility of using uncoupled damage parameters as coalescence indicators, is explored. To do this, three different criteria are considered. The general form of a damage parameter D is as follows:

$$D = \int_0^{\bar{\epsilon}} f(\boldsymbol{\sigma}) d\bar{\epsilon}, \quad (6.5)$$

where $f(\boldsymbol{\sigma})$ is a function of a stress state, and $\bar{\epsilon}$ is the equivalent strain.

The first considered damage indicator is the Cockcroft-Latham [14] damage indicator. It has an associated stress state function f_{CL} with the following expression:

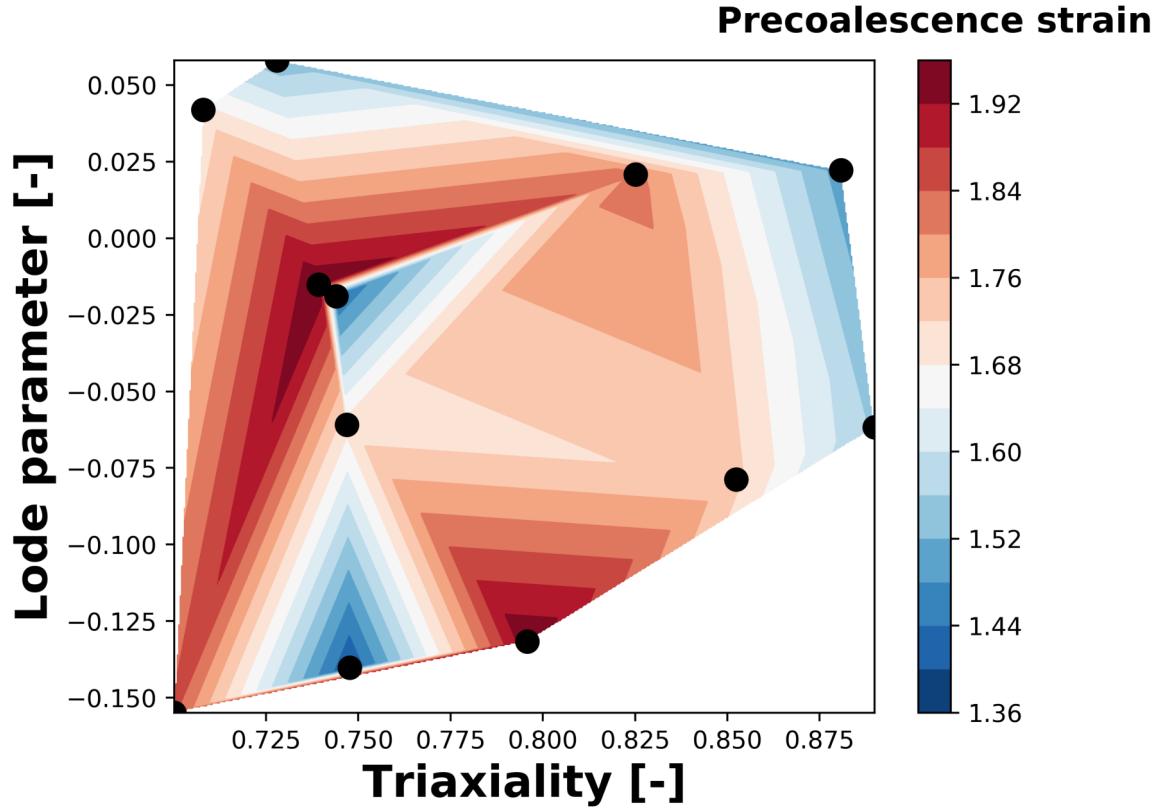


Figure 6.11: Precoalescence strain in the intervoid ligament as a function of the stress triaxiality ratio and the Lode parameter

$$f_{CL}(\boldsymbol{\sigma}) = \max(\sigma_1, 0). \quad (6.6)$$

The Rice-Tracey damage indicator [11] is the second considered damage indicator and has the following associated stress state function f_{RT} :

$$f_{RT}(\boldsymbol{\sigma}) = \exp\left(\frac{3}{2}T\right). \quad (6.7)$$

The third and final considered damage parameter is the Lou damage parameter [18], which has the following stress state function f_{Lou} :

$$f_{Lou}(\boldsymbol{\sigma}) = \left(\frac{2}{\sqrt{L^2 + 3}}\right)^{C_1} \left(\frac{\max(1 + 3T, 0)}{2}\right)^{C_2}, \quad (6.8)$$

where C_1 and C_2 are coefficients to be identified, but that will both be considered equal to unity in this work.

Figures 6.12a, 6.12b and 6.12c present the evolution of the damage parameters for the 12 void pairs. The pre-coalescence values of the Cockcroft-Latham damage parameter exhibit a high variability. This impedes the definition of a threshold value beyond which coalescence is considered to occur. The Rice-Tracey and Lou damage parameters present a smaller spread in the pre-coalescence values.

To quantify these observations, a Probit analysis is performed for each of the damage parameters and the resulting curves are depicted in Figures 6.13a, 6.13b and 6.13c. For the Cockcroft-Latham parameter (Figure 6.13a), the ranges of the data points with 100% coalescence probability and those with 0% coalescence probability, overlap almost entirely. The corresponding overlaps for the Rice-Tracey and Lou damage parameters are considerably smaller.

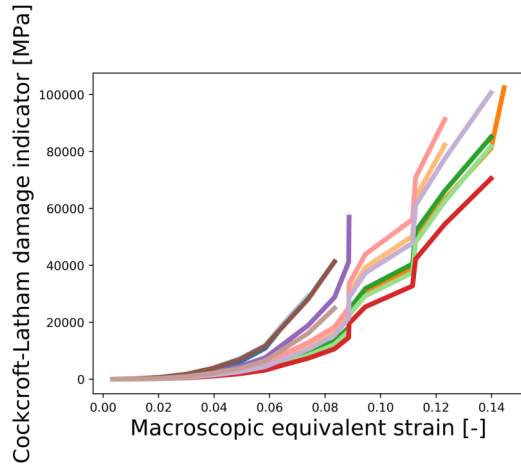
The fitting accuracy for the Probit regression is summarized in Table 6.1 for the three damage parameters as well as for the pre-coalescence strain Probit regression presented in Section 6.2.3. The poorest fitting accuracy is exhibited by the Cockcroft-Latham criterion with a pseudo-R-squared value of 0.06. The Rice-Tracey criterion, based on the stress triaxiality ratio, represents a considerable improvement over the Cockcroft-Latham criterion, with a pseudo-R-squared of 0.29. The inclusion of the Lode parameter in the analysis through the Lou damage parameter improves slightly the fitting accuracy by reaching a pseudo-R-squared value of 0.35. The latter is, however, only marginally superior to the plastic equivalent strain as coalescence criterion, which presented a pseudo-R-squared of 0.35. The use of a failure criterion does not seem to improve the coalescence prediction capability compared to a strain-based approach.

Table 6.1: Fitting accuracy for Probit regression of three different damage indicators and of the plastic equivalent strain

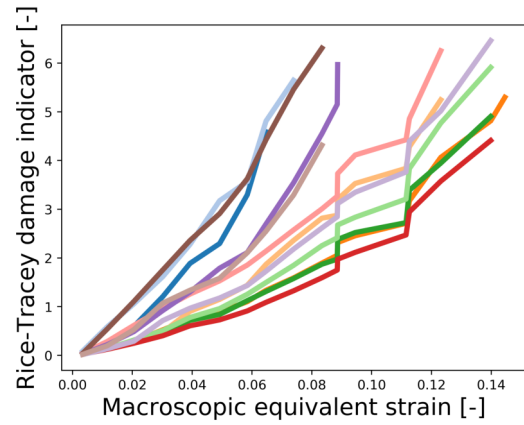
Criteria	Pseudo R^2 [-]
Plastic equivalent strain	0.35
Cockcroft-Latham	0.06
Rice-Tracey	0.29
Lou	0.35

6.2.6 Intervoid distance as coalescence criterion

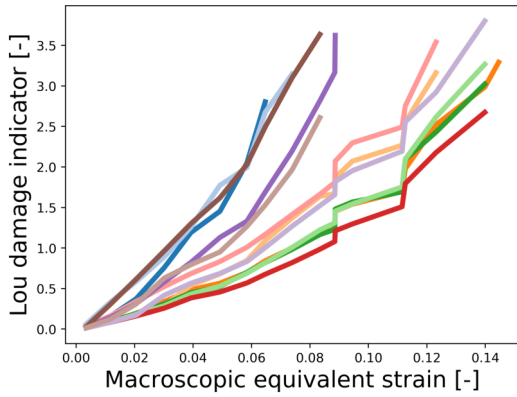
In this section, the possibility of a coalescence criterion based on the evolution of the intervoid distance is studied. The basic idea is that the moment of coalescence can be known if the evolution of the intervoid distance can be predicted. The first step towards examining such a model is then examining the evolution of the intervoid distance. This differs with the work of Fansi [210], who proposed a critical value for fracture in three different dual phase steels based on in-situ measurement via X-ray tomography of inter-cavity distance carried



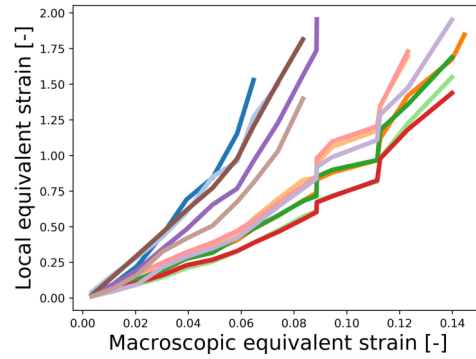
(a) Cockcroft-Latham



(b) Rice-Tracey



(c) Lou



(d) Strain

Figure 6.12: Evolution of the (a) Cockcroft-Latham, (b) Rice-Tracey, and (c) Lou damage indicators and of the (d) local equivalent strain in the intervold ligaments.

out by Landron et al. [218].

Figure 6.14 presents the evolution of the intervold distance for the 12 void pairs as a function of the macroscopic strain. Very linear trends with varying slopes, are observed. Linear regression was carried out for each of the curves. The minimum obtained coefficient of determination R^2 was 0.98 and the average R^2 was 0.99. Similarly linear trends have been reported by Landron et al. [219] for the average inter-cavity distance in three different dual phase steels.

The simplicity of a linear trend is an attractive feature for a distance-based coalescence criterion. Since the initial intervold distance is known, it would be enough to predict the slope of the curve to determine the moment of coalescence. The problem translates into predicting the slope m .

When the evolution of the equivalent strain in the intervold ligament was examined (Fig-

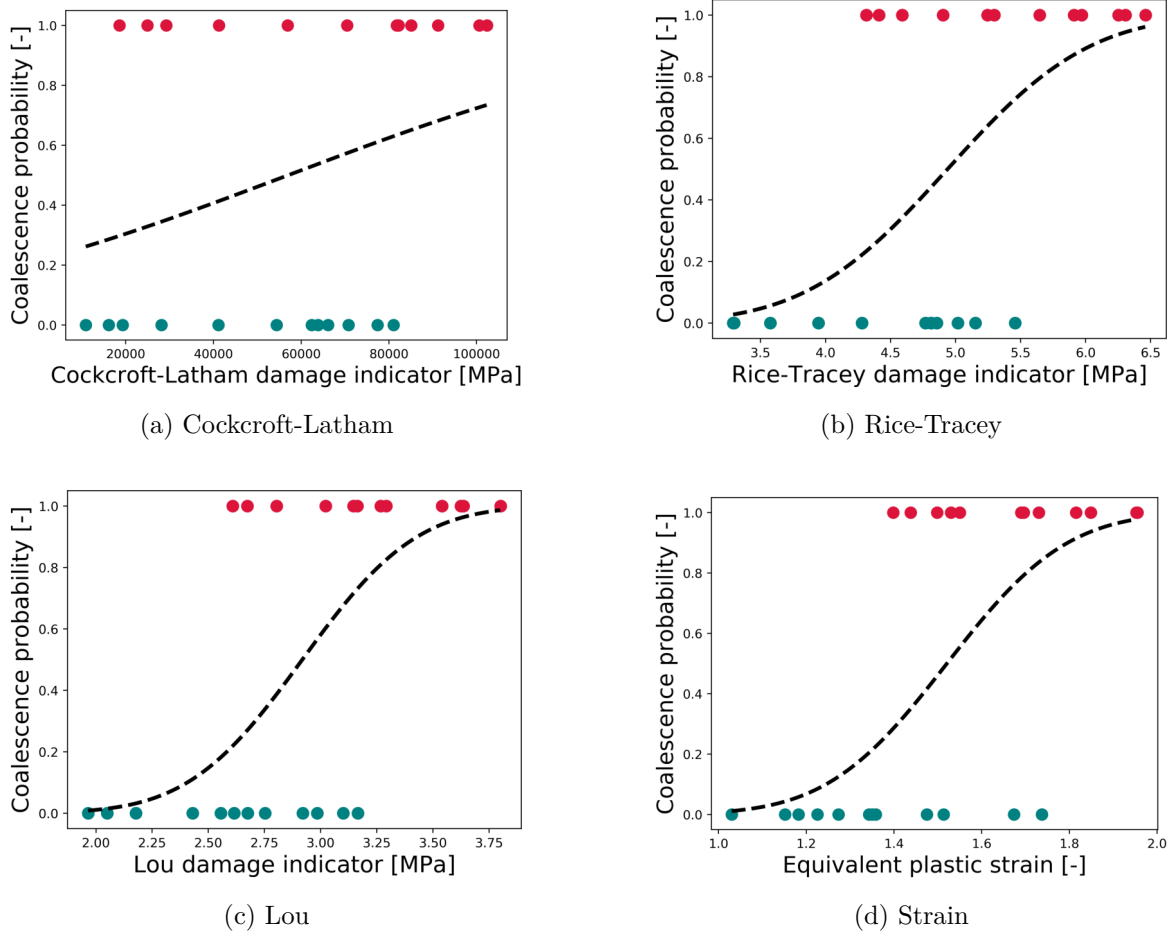


Figure 6.13: Probit regression for the (a) Cockcroft-Latham, (b) Rice-Tracey, and (c) Lou damage indicator and (d) local equivalent strain in the intervoid ligament.

ure 6.7), an exponential trend was observed with different increase rates. To test if the distance slopes are correlated with the strain increase rate in the intervoid ligaments, regression with an exponential function with the following form, is carried out:

$$\varepsilon_{local} = -1 + \exp(b_{acc}\varepsilon_{macro}), \quad (6.9)$$

where ε_{local} is the equivalent plastic strain in the ligament, ε_{macro} the macroscopic equivalent strain and b_{acc} is a fitting constant that represents the increase rate of the local strain. The minimum and maximum obtained R^2 are 0.95 and 0.98 respectively.

Correlation between the distance slope and three variables will be assessed. These variables are the b_{acc} coefficient, the initial intervoid distance d_0 and the initial angle α formed between the loading direction and the shortest path between two voids. The distance slope does not present a clear trend with respect to any of these three variables. The Pearson correlation coefficient was calculated and -0.65, -0.48 and -0.09 was obtained for b_{acc} , d_0 and α respectively.

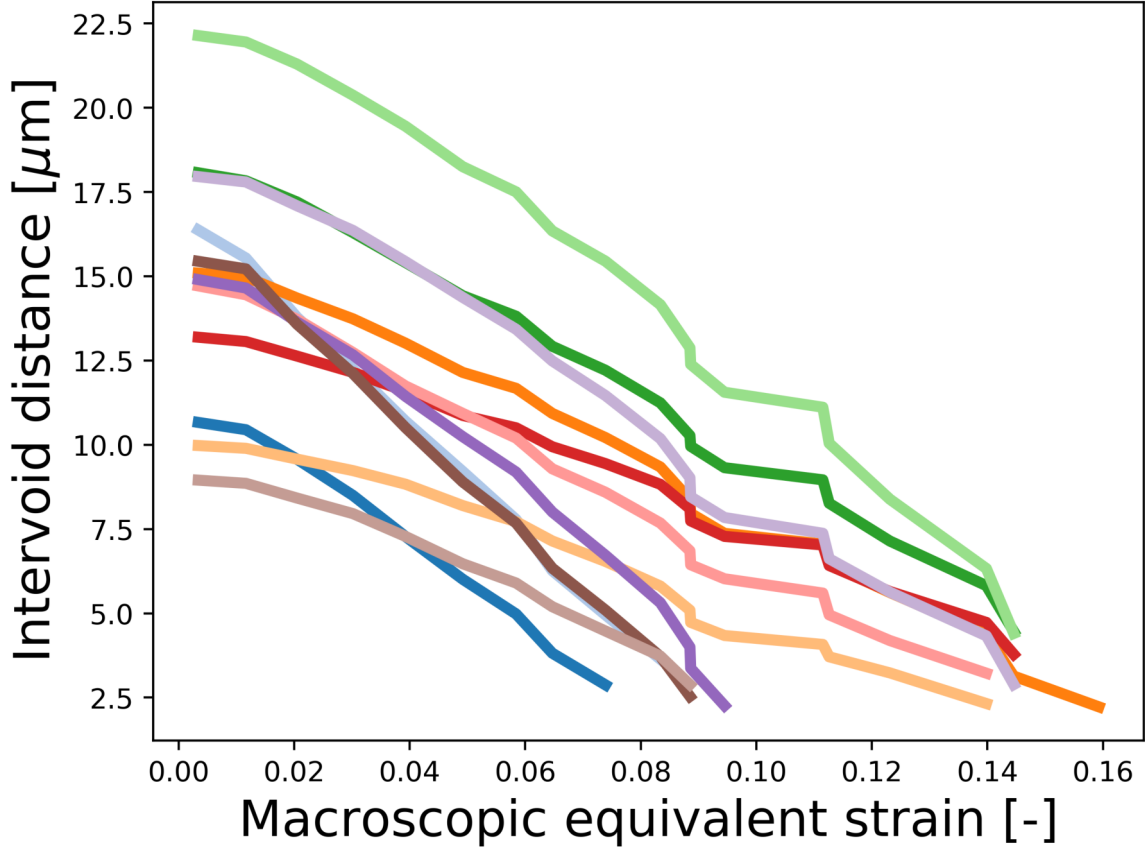


Figure 6.14: Evolution of the minimum intervoid distance.

Since the three considered variables do not explain the variability of the distance slope, a combination of these variables will be employed in linear multivariate regression. A first model to predict the distance slope is proposed with the following expression:

$$m = A + B d_0 + C b_{acc} + D \alpha, \quad (6.10)$$

where A , B , C , and D are fitting parameters. Since α presented a low correlation coefficient, a second and simpler model that considers only the initial intervoid distance and the strain increase rate, is proposed:

$$m = A + B d_0 + C b_{acc}. \quad (6.11)$$

The resulting coefficients for both model are summarized in Table 6.2 along with the R^2 values. Both models obtained a R^2 equal to 0.97, which is very satisfactory. Since including α in the model does not improve the explained variance, the simpler model is preferred. This suggests that the distance slope can be accurately predicted by taking into account the initial intervoid distance and the strain increase rate. This is illustrated in Figure 6.15 with

a response surface based on linear interpolation. In this response surface, the distance slope contours exhibit a linear relation with respect to d_0 and b_{acc} .

Table 6.2: Parameters and coefficient of determination for two models to predict the slope of the evolution of the intervoid distance

	A [μm]	B [-]	C [μm]	D [μm]	R ² [-]
Model 1	90.00	-7.20	-11.52	0.13	0.97
Model 2	98.00	-7.10	-11.27	-	0.97

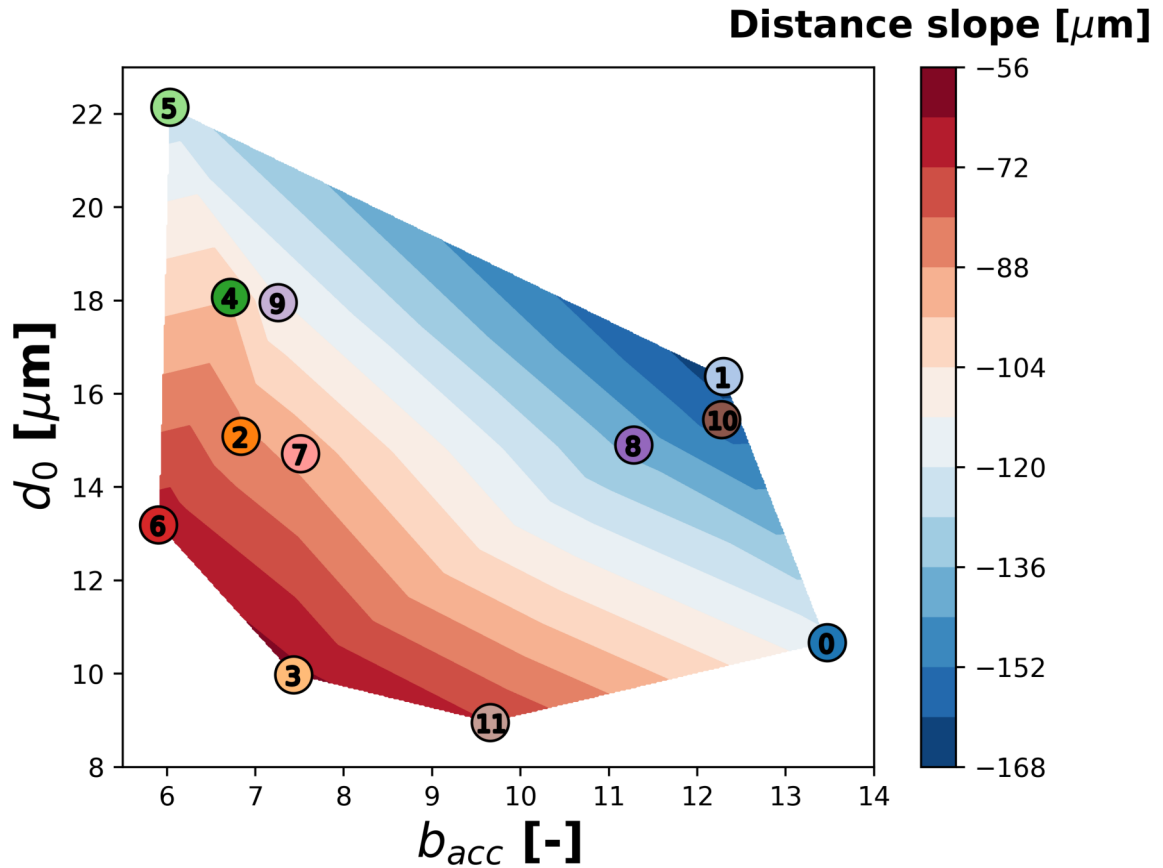


Figure 6.15: Slope of the intervoid distance as a function of the initial intervoid distance and of the coefficient of the exponential law.

It has been established that the model can accurately predict the slope of the training data. The objective, however, is to describe the distance evolution. To verify how well the intervoid distance is predicted, the original distance data obtained from the FE simulation is compared with the distance calculated using the initial intervoid distance and the slope calculated by the model. This comparison is depicted in Figure 6.16 where the FE data is presented as continuous lines and the model predictions as dashed lines. The quality of the prediction is quantified by means of the determination coefficient. The minimum and average R^2 obtained values are 0.66 and 0.88, respectively, which is satisfactory.

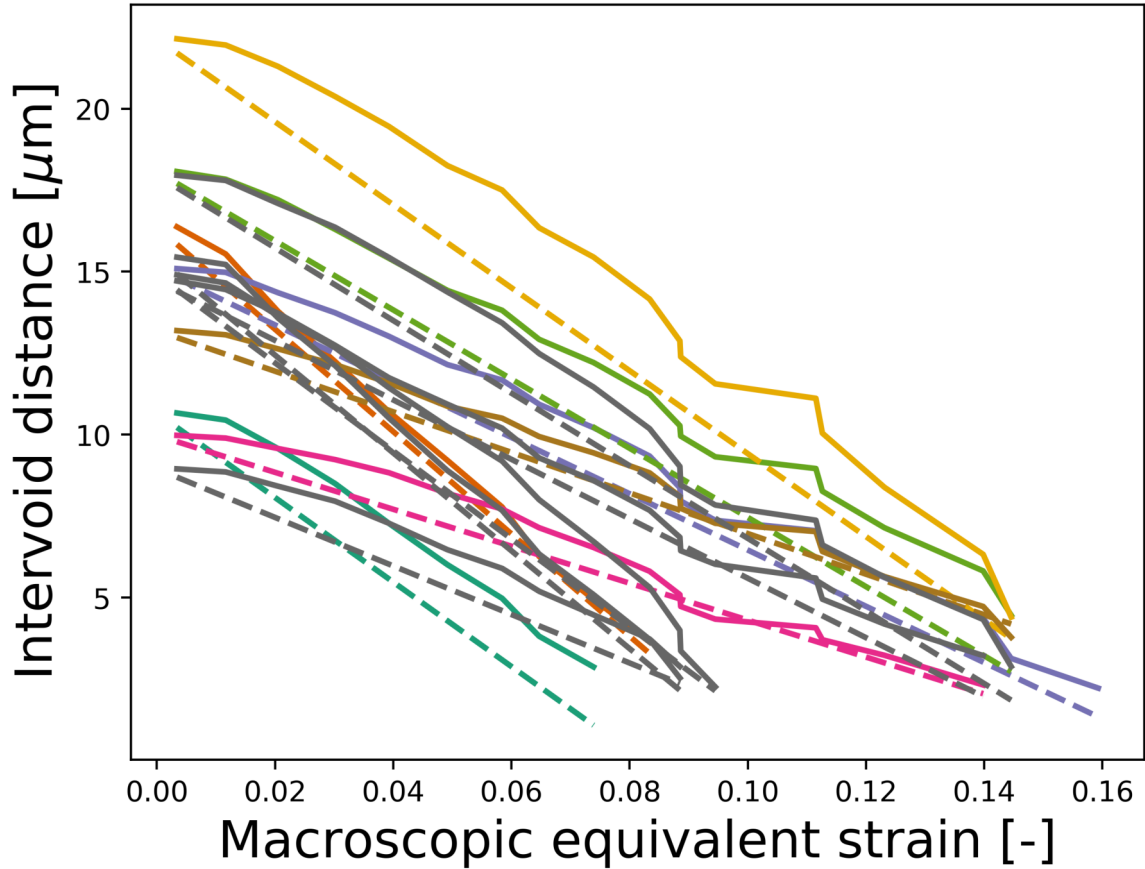


Figure 6.16: Comparison between predicted intervoid distance and intervoid distance according to the FE simulation for 12 void pairs.

Model validation

From the original 18 void pairs, the data of 6 void pairs have not been used. It will be used in this section to validate the model. The distance and strain evolution of these 6 validation void pairs are displayed in Figures 6.17 and 6.18, respectively. The former is the variable to be predicted by the model and the latter, along with the initial intervoid distance, is the input for the model. As in Section 6.2.6, regression with an exponential function for the strain evolution is carried out.

The distance slope of the 6 validation void pairs are calculated with the previously trained model. The distance evolution is calculated with the predicted slope. The predicted and FE distance evolutions are compared in Figure 6.19. The coefficient of determination R^2 is used to quantify the quality of the predictions. The minimum and average obtained R^2 values are 0.68 and 0.80. These values are comparable to those obtained for the training data and the model predictions are considered satisfactory.

The model was calibrated and validated with data from the FE simulations. This implies that the model is affected by the physical and numerical models that need to be improved. As

it was established in Section 6.2.1, the FE simulations provide accurate strain measurements, but underestimate the strain increase rate at the simulation and, consequently, predict coalescence later than observed in the laminography images. After improving the constitutive modeling in the FE simulations, the model should be recalibrated and adjusted to possible changes in the kinetics.

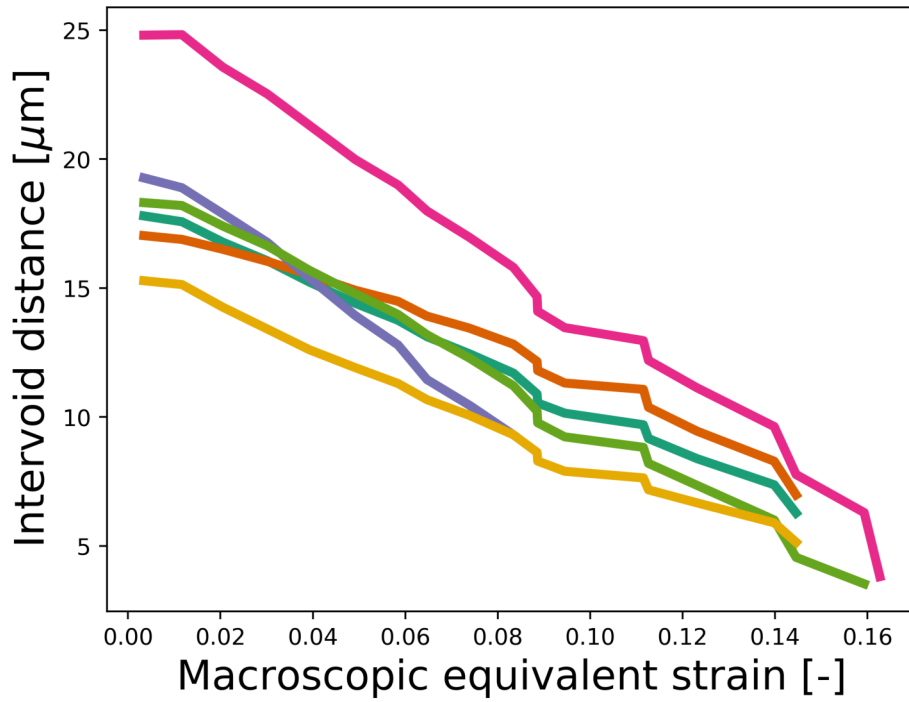


Figure 6.17: Distance evolution for six additional void pairs for validation purposes.

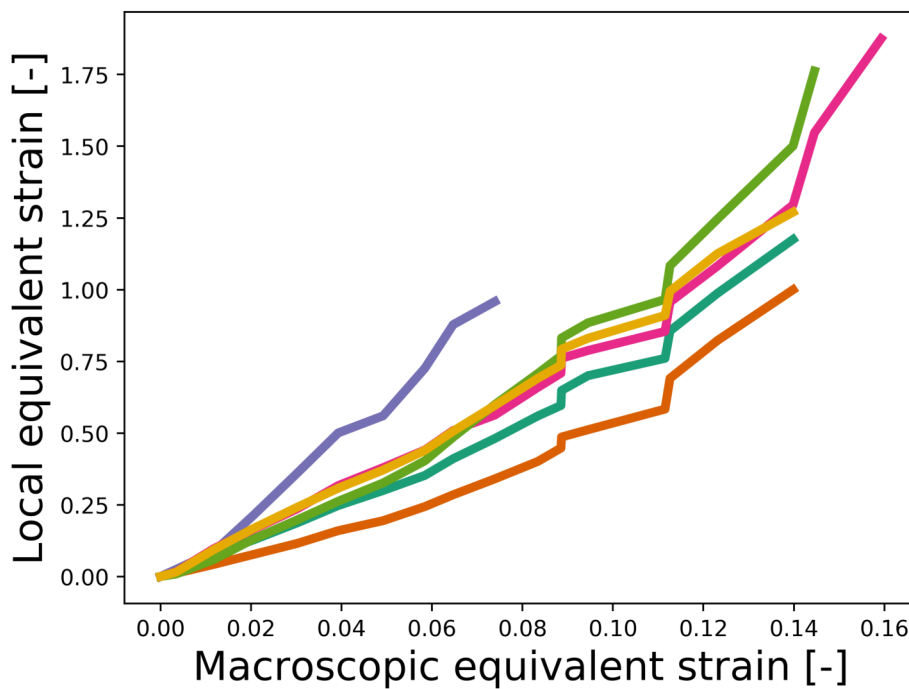


Figure 6.18: Local strain evolution for six additional void pairs for validation purposes.

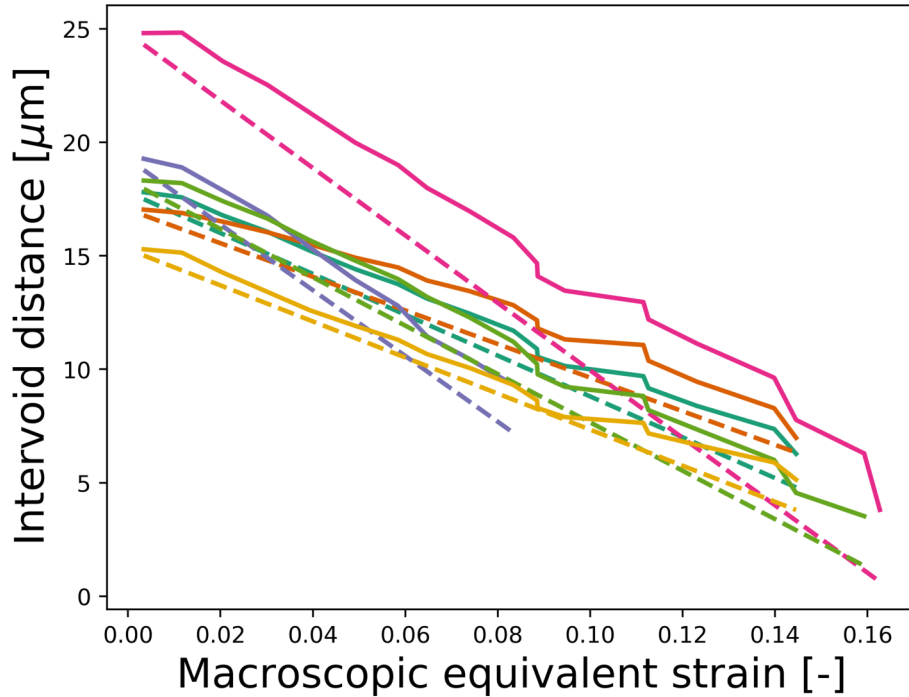


Figure 6.19: Comparison between predicted intervoid distance (dashed lines) and intervoid distance according to the FE simulation (solid lines) for 6 void pairs for model validation.

6.2.7 A simple probabilistic approach

This section presents a probabilistic approach based on the empirical coalescence probability. The empirical coalescence probability might be expressed in terms of global or local observables.

In terms of macroscopic strain

In this section, a probabilistic model is proposed in order to bridge the observations at the microscale with macroscopic models. This probabilistic model expresses, for a given value of the macroscopic equivalent strain, the probability of observing void coalescence for that same value or smaller values of the equivalent strain. The macroscopic equivalent strain is chosen as independent variable as it can be obtained either from DVC or FE calculations and represents a clear macroscopic reference.

The required input for the model is simply the number of coalesced void pairs and the corresponding macroscopic equivalent strain at the moment of coalescence. This requires the identification of each coalescence event in the laminographic images. Identification of coalescence by simple inspection would be very time consuming and extremely complicated given the quantity of voids present in the domain. An alternative would be to use an automatic void tracking algorithm directly on the laminography images such as the one implemented by

Lecarme et al. [220]. Similar capabilities were introduced in the CimLib library [156] during this work. These developments allow tracking the evolution of each individual void and identifying when it undergoes coalescence. For simplicity, these capabilities of the CimLib library are used and the information obtained during the FE simulations is followed by inspection of the laminography images to confirm the coalescence events.

Once the input information is available, the empirical probability of coalescence can be calculated straightforwardly. To obtain a model that provides the coalescence probability as a function of the macroscopic equivalent strain, a cumulative Weibull distribution is then fitted to the empirical probability. The expression for a cumulative Weibull distribution is the following:

$$P(x) = 1 - \exp\left(-\ln(2)\left(\frac{x}{k}\right)^\lambda\right), \quad (6.12)$$

where P represents the probability of coalescence occurring for a value less than or equal to x , the independent variable. k is the shape parameter of the distribution and represents its median. λ is the scale parameter of the distribution and controls its spread.

The empirical probability and the fitted Weibull distribution as a function of the macroscopic equivalent strain, are presented in Figure 6.20. The fitted Weibull distribution presents a value of 4.66 for λ , a value of 0.1 for k , and a determination coefficient R^2 of 0.98. Although it would be desirable to do this analysis with more data, the Weibull distribution describes very well the available data.

On the integration of the probabilistic approach in the GTN model

Based on previous observations, Chu and Needleman [30] expressed the rate of change of the void fraction due to nucleation $\dot{f}_{nucleation}$ as a function of the equivalent plastic strain $\bar{\varepsilon}^{Pl}$. After acknowledging the fact that this relationship depends on the topology of the microstructure, these authors proposed the idealization that the nucleation strain follows a normal distribution around a mean equivalent nucleation strain $\bar{\varepsilon}_N$:

$$\dot{f}_{nucleation} = \frac{\psi}{S\sqrt{2\pi}} e^{-1/2\left(\frac{\bar{\varepsilon}^{Pl} - \bar{\varepsilon}_N}{S}\right)^2} \bar{\varepsilon}^{Pl}, \quad (6.13)$$

where S is the standard deviation and ψ is the coefficient used to link the nucleated void volume and the void fraction. ψ has later been denoted as f_N and represents the total void volume fraction that can be nucleated.

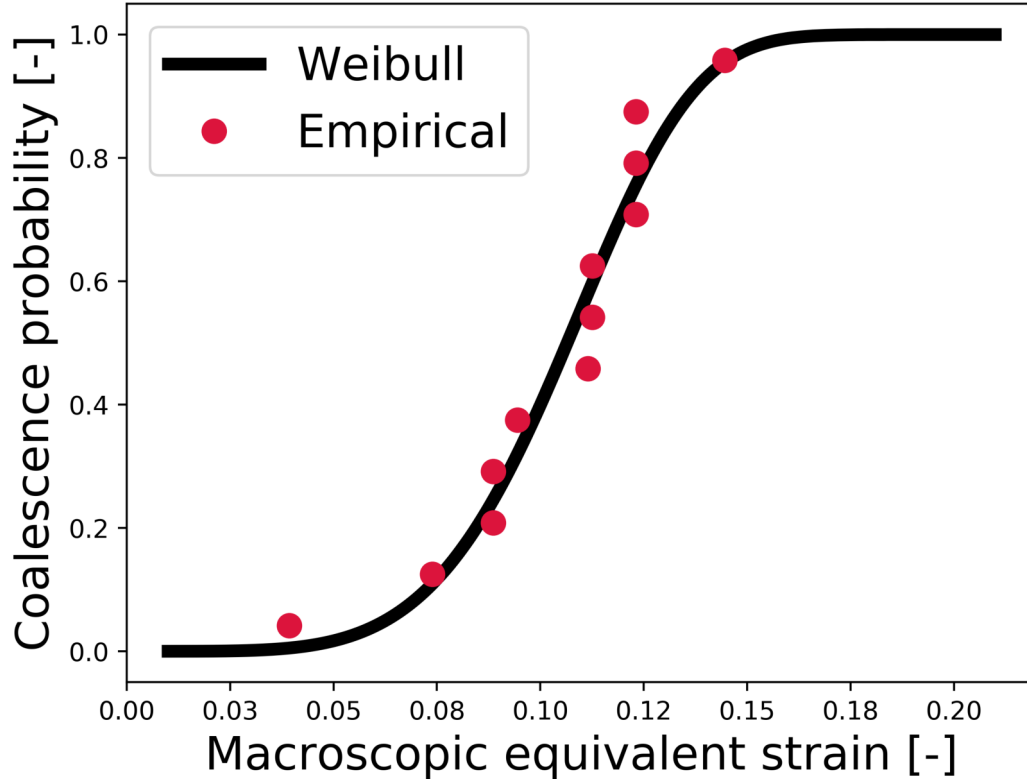


Figure 6.20: Empirical coalescence probability in terms of the macroscopic strain and corresponding fit cumulative Weibull distribution.

Coalescence criteria have been expressed in terms of a critical stress, such as in the Thomason model [221] or in terms of the void fraction, such as in the modifications proposed by Tvergaard and Needleman [29] to the original Gurson model [27]. The satisfactory description of the coalescence probability with a Weibull distribution depicted in Figure 6.20 suggests that a coalescence criterion based on the macroscopic equivalent strain could be appropriate.

Void coalescence is preceded by a locally accelerated void growth and void growth is driven by plastic deformation. In this sense, it is natural for the coalescence probability to be expressed in terms of strain. In a similar way to the approach of Chu and Needleman [30] for void nucleation, the coalescence probability could be related to a coalescence-induced rate of increase of the void fraction as follows:

$$\dot{f}_{coalescence} = \psi_{coalescence} \frac{\partial P(\varepsilon)}{\partial \varepsilon} \dot{\varepsilon}^{Pl}, \quad (6.14)$$

where $\psi_{coalescence}$ is a coefficient used to link the coalescence-induced void growth and the void fraction, and $\frac{\partial P}{\partial \varepsilon}$ can be expressed as:

$$\frac{\partial P\left(\bar{\varepsilon}^{Pl}\right)}{\partial \varepsilon} = \ln(2) \frac{\lambda}{k} \left(\frac{\bar{\varepsilon}^{Pl}}{k}\right)^{\lambda-1} \exp\left(-\ln(2) \left(\frac{\bar{\varepsilon}^{Pl}}{k}\right)^{\lambda}\right). \quad (6.15)$$

Since k and λ were already determined, the only parameter to be calibrated is $\psi_{coalescence}$. λ controls the spread of the distribution, which means that the size of the macroscopic strain range between the first and last occurrence of coalescence is proportional to λ , and k represents the median coalescence strain of the distribution. k and λ were determined by least squares minimization of the Weibull distribution with respect to the empiric macroscopic coalescence values. Although $\psi_{coalescence}$ is linked to the total amount of void fraction due to coalescence and could be calibrated based on micromechanical simulations, it is not straightforward to separate its contribution from the total void growth. An alternative would be its calibration at the macroscale.

The total growth rate of the void volume fraction could then be expressed as:

$$\dot{f}_{total} = \dot{f}_{nucleation} + \dot{f}_{growth} + \dot{f}_{coalescence}. \quad (6.16)$$

An equivalent approach was proposed by Tvergaard in 1982 [222], but has remained largely unused while the popularity of the coalescence treatment in the GTN model has increased (see Section 2.1.1). The probabilistic approach is here preferred because it does not artificially shrink the yield surface with a sudden change in the slope of the void fraction. A second argument in favor of the probabilistic approach is that the results presented in this Section constitute micromechanical evidence supporting it and are summarized by the satisfactory goodness of fit. It is, however, to be tested in macroscopic applications.

Local probabilistic model

In this section, two alternatives of a local probabilistic model are presented. The first one is based on the local pre-coalescence strain and the second one on the local Lou damage indicator. In both cases, input from the FE micromechanical simulations was necessary. Consequently, the application of these models is not the macroscopic scale. Instead, they could be useful for local approaches that do not seek to model ductile damage in full detail.

The obtained empirical coalescence probabilities as well as the corresponding fitted Weibull distribution are presented in Figure 6.21 for the local strain-based model and in Figure 6.22 for the model based on the local Lou damage indicator. Both models presented a coefficient of determination of 0.99.

This approach is complementary to the approach presented in Section 6.2.7 and could be

useful to include coalescence in micromechanical simulations with a simplified representation of the microstructure, such as in the work of De Geus [223].

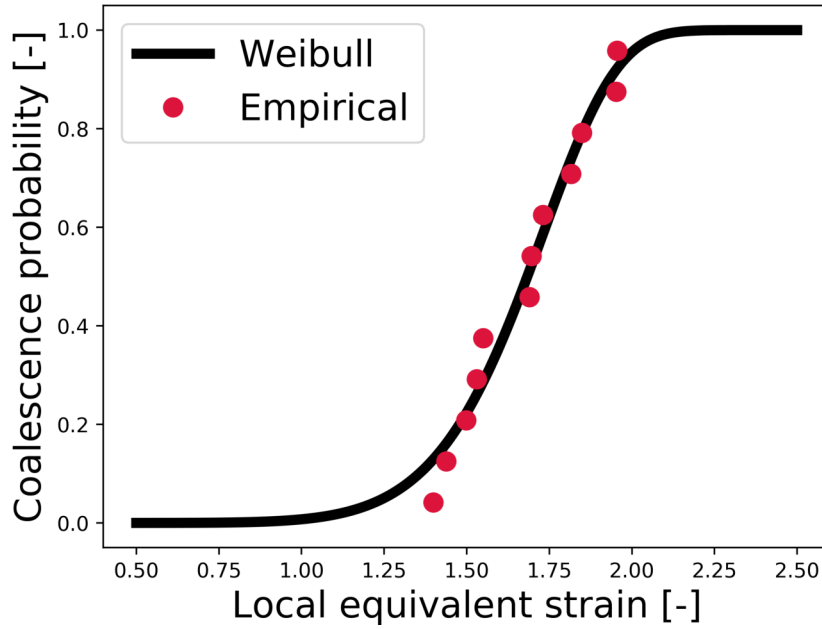


Figure 6.21: Empirical coalescence probability in terms of the local strains and corresponding fit cumulative Weibull distribution.

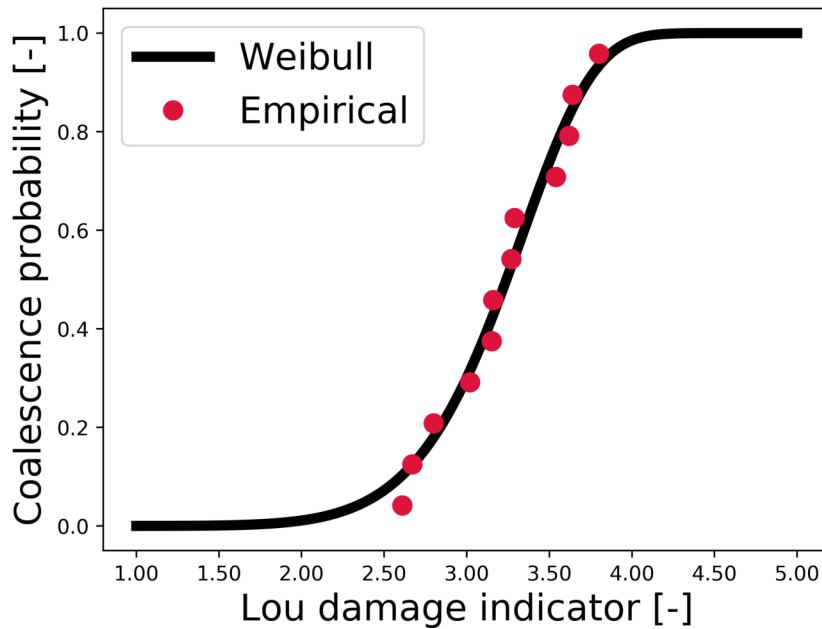


Figure 6.22: Empirical coalescence probability in terms of the local Lou damage indicator and corresponding fit cumulative Weibull distribution.

6.3 Discussion

Different approaches for the prediction of void coalescence were tested in Section 6.2. The most satisfactory approach was the use of the intervoid distance evolution as coalescence criterion (Section 6.2.6). The assessed physical mechanism is void coalescence by internal necking. Since the phenomenon responsible for this mechanism is void growth driven by plastic deformation, a measure of the strain constitutes, along with the initial intervoid distance, a natural necessary input for the prediction of the intervoid distance.

With the proposed intervoid distance model, given the initial geometry and a measure of the increase rate of the strain in the intervoid ligament, the evolution of the intervoid distance can be determined as a function of the macroscopic equivalent strain. The instance of coalescence is achieved when the intervoid distance reaches zero.

For the calibration of the model, the initial topology and kinematic information at the microscale are necessary. The former can be obtained via a three-dimensional imaging technique such as tomography. The latter requires either DVC with high spatial resolution or micromechanical simulations. The DVC-SRCL-FE methodology is well suited for this task, but the suitability of other more widely available techniques could be tested.

The need for kinematic information at the microscale is a difficulty in the calibration of the model. If a correlation could be found between the local increase rate of the strain and topological information, only the initial topological information would be necessary.

The validity of the model is naturally restricted to the material and conditions for which it was proposed and for which it has been tested. Its applicability for other materials and loading conditions is to be verified. The accuracy and shortcomings of the current framework were discussed in Section 6.2.1. When the current shortcomings are addressed, with improved constitutive modeling, for example, the formulation of the model should be revisited. Nevertheless, finding such a simple relationship in a heterogenous micromechanical simulation of an immersed microstructure, is a promising result.

The evolution of the intervoid distances exhibits an important variability. To illustrate this, the average of the slopes and the corresponding relative error for each of the slopes were calculated. An average error of 25.77% and a maximum error of 26.22% were obtained. This level of error is not negligible, but might be sufficient for obtaining approximate information without the need of microscopic kinematic information.

The variability exhibited by the evolution of the local strain values and by the intervoid distance illustrates the importance of considering realistic microstructures instead of idealized ones. The topology of the microstructure is probably at the origin of an important part of this variability. An implication of these results is that care must be taken when considering

periodic arrangements of microstructural features for homogenization. Results based on periodic configurations are attractive since they are simpler to obtain and analyze, but are not able to capture the variability that stems from a realistic and complex topology.

The final objective of such a model is to be used at the macroscale. The transition to the macroscale is still not straightforward. Possible applications in FE² schemes would be envisaged when topological information of the microstructure is available.

On the other hand, the probabilistic approach provides a straightforward link with the macroscopic scale. To be calibrated, it requires detailed information at the microscale, namely, the identification of the coalescence events in a given microstructure and the corresponding macroscopic strain. The resulting fit for a cumulative distribution function can be integrated in a GTN-like model with the additional calibration of one parameter.

6.4 Conclusions and perspectives

A micromechanical study of void coalescence by internal necking with an experimental-numerical framework was carried out. In this framework, FE simulations with immersed microstructures and realistic boundary conditions, were conducted.

The accuracy of the FE simulations in the context of void coalescence was discussed based on previous work and a new comparison with laminography images. The FE strain measurements were found satisfactorily accurate except at the end of the simulation when the acceleration of the strain increase is not well captured. The predicted moment of coalescence is earlier than observed experimentally. This is to be improved with better constitutive modeling. The required calibration at the microscale of a more appropriate hardening law or accounting for damage in the matrix is a perspective of this work. Nevertheless, the current framework was considered appropriate and accurate enough to assess the feasibility of establishing a coalescence criterion at the microscale.

12 void pairs were identified and confirmed to undergo coalescence during the FE simulation. 6 other void pairs were chosen for validation of a possible coalescence criterion.

The evolution of the equivalent plastic strain in the shortest path between voids was described for 12 different void pairs. Based on these results, the strain at the middle of point of the shortest path between voids, was considered as a value representative of the strain levels in the ligament. This value was used in the remainder of the work.

Five different approaches were tested in an attempt to establish a coalescence criterion. The first three were unfruitful. These were using the pre-coalescence strain as coalescence criterion, establishing a relationship between the pre-coalescence strain and the stress space,

and using uncoupled damage criteria as coalescence indicators.

An internal necking coalescence criterion was proposed based on the evolution of the minimum intervoid distance between two voids. The initial intervoid distance and the increase rate of the local strain are the input by this model. Once calibrated, the model can predict the evolution of the intervoid distance as a function of the macroscopic equivalent strain. Coalescence is achieved once this distance reaches zero. This model was satisfactorily validated with data from 6 void pairs.

A probabilistic approach based on the empirical coalescence probability was proposed. Three different variations were presented for which the coalescence probability was expressed in terms of the macroscopic equivalent strain, the local equivalent strain or the local Lou damage parameter. The former provides a straightforward connection with the macroscale and the way in which it can be integrated in a GTN-like behavior law was described. The two latter provide an alternative for less detailed calculations at the microscale.

A perspective of this work for the intervoid distance model is to substitute the kinematic data required as input for purely topological information. This would eliminate the need for kinematic information after calibration of the model and the model could be applied based on information from a laminography image of the initial state. This requires understanding and quantifying how the local topology intervenes in the rate of increase of the strain in the intervoid ligament.

Another perspective is to integrate the probabilistic approach in a porous plasticity constitutive model such as the GTN model. Its integration is straightforward, but requires validation. A single parameter would need to be calibrated to link the increase of the void fraction due to coalescence.

Finally, the intervoid distance model and the probabilistic approach could be coupled together. The output of the former, i.e., the moment at which coalescence occurs for each void pair, is the input of the latter. This would mean that the coalescence law in a GTN-like model could eventually be calibrated based on the information of a single tomographic image with only one additional parameter to be calibrated at the macroscale. A perspective of this work is to test the feasibility of this approach. If this is successful, it could also be extended to other loading conditions and materials.

Résumé en français

Une étude micromécanique de la coalescence des pores par striction interne dans un cadre expérimental et numérique a été réalisée. Dans ce cadre, des simulations FE avec des microstructures immergées et des conditions limites réalistes ont été réalisées.

La précision des simulations FE dans le contexte de la coalescence des pores a été discutée sur la base de travaux antérieurs et d'une nouvelle comparaison avec des images de lamino-graphie. Les mesures de déformation FE ont été jugées suffisamment précises, sauf à la fin de la simulation, lorsque l'accélération de la déformation n'est pas bien reproduite. Le moment de coalescence prédit par FE est précoce par rapport aux observations expérimentales. Cela pourra être amélioré avec une meilleure modélisation du comportement de la matrice. La calibration à l'échelle microscopique d'une loi d'écroutissage plus appropriée ou la prise en compte de l'endommagement dans la matrice est une perspective de ce travail. Néanmoins, le cadre actuel a été jugé approprié et suffisamment précis pour évaluer la possibilité d'établir un critère de coalescence à l'échelle microscopique.

Douze paires de pores ont été identifiées et ont confirmé la coalescence au cours de la simulation FE. Six autres paires de vides ont été choisies pour la validation d'un possible critère de coalescence.

L'évolution de la déformation plastique équivalente dans le plus court chemin entre pores a été décrite pour 12 paires de pores différentes. Sur la base de ces résultats, la déformation au milieu du plus court chemin entre pores a été considérée comme une valeur représentative des niveaux de la déformation dans le ligament. Cette valeur a été utilisée dans le reste du travail.

Cinq approches différentes ont été testées pour tenter d'établir un critère de coalescence. Les trois premières se sont révélées infructueuses. Celles-ci utilisaient la déformation de pré-coalescence comme critère de coalescence, établissaient une relation entre la déformation de pré-coalescence et l'espace de contrainte et utilisaient des critères de rupture non couplés comme indicateurs de coalescence. Un critère de coalescence interne de striction a été proposé sur la base de l'évolution de la distance minimale entre pores. La distance initiale entre les pores et le taux d'augmentation de la déformation locale sont les entrées de ce modèle. Une fois calibré, le modèle peut prédire l'évolution de la distance entre pores en fonction de la déformation équivalente macroscopique. La coalescence est atteinte lorsque cette distance atteint zéro. Ce modèle a été validé de manière satisfaisante avec les données de 6 paires de pores non utilisées durant la phase de calibration.

Une approche probabiliste basée sur la probabilité empirique de coalescence a été proposée. Trois variations différentes ont été présentées pour lesquelles la probabilité de coalescence a été exprimée en termes de déformation équivalente macroscopique, de déformation équivalente locale ou du paramètre d'endommagement local de Lou. La première offre un lien direct avec l'échelle macroscopique et la manière dont elle peut être intégrée dans une loi de comportement de type GTN a été décrite. Les deux dernières offrent une alternative aux calculs à l'échelle microscopique.

Une perspective de ce travail pour le modèle de distance entre pores consiste à sub-

stituer les données cinématiques requises en tant qu'entrée par des informations purement topologiques. Cela éliminerait le besoin d'informations cinématiques après la calibration du modèle et le modèle pourrait être appliqué sur la base d'informations provenant d'une image de laminographie de l'état initial de la microstructure. Cela nécessite de comprendre et de quantifier comment la topologie locale intervient dans le taux d'augmentation de la déformation dans le ligament inter-cavités.

Une autre perspective consiste à intégrer l'approche probabiliste dans un modèle constitutif de plasticité poreuse tel que le modèle GTN. Son intégration est simple mais nécessite une validation. Un seul paramètre devrait être calibré pour lier l'augmentation de la fraction de vide due à la coalescence.

Enfin, le modèle de distance entre pores et l'approche probabiliste pourraient être couplés. La sortie du première modèle, c'est-à-dire le moment auquel la coalescence se produit pour chaque paire de pores, serait ainsi l'entrée du second modèle. Cela signifierait que la loi de coalescence dans un modèle de type GTN pourrait éventuellement être calibrée sur la base des informations d'une seule image tomographique avec un seul paramètre supplémentaire à calibrer à l'échelle macroscopique. Une perspective de ce travail est de tester la faisabilité de cette approche. Si cela fonctionne, cette approche pourrait également être étendu à d'autres conditions de chargement et d'autres matériaux.

Chapter 7

Conclusions and perspectives

7.1 Conclusions

In this work, the SRCL-DVC-FE methodology developed within the COMINSIDE project was employed in a micromechanical study of ductile damage of nodular cast iron based on FE simulations with immersed microstructures and realistic boundary conditions. Several improvements were developed in this work in order to enhance the automatic analysis of void nucleation, growth and coalescence.

Simulations with immersed microstructures require image segmentation, i.e., deciding to which physical phase each voxel belongs to. The effect of image segmentation on the final mechanical observables of the FE simulations was assessed in the SRCL-DVC-FE framework through comparison of three different segmentation methods for two different specimens. The three methods included a manual thresholding, an automatic thresholding algorithm and a machine learning algorithm.

Global and local observables were considered in the comparison of the segmentation methods. The global observables were macroscopic equivalent strain and stress, and void volume fraction. The local observables were local equivalent strain in two probe volumes for each specimen located in different intervoid ligaments. The most sensitive observables were the local strain values and the void volume fraction. The void volume fraction was more sensitive for the 90° specimen than for the 45° specimen. The sensitivity of the local strain measures increased when they were closer to the void-matrix interface.

An uncertainty associated to image immersion was calculated in the comparative study of the image segmentation methods. This uncertainty was taken into account in a detailed comparison between DVC and FE strain measurements. It was revealed that the segmentation-related uncertainties are negligible with respect to the differences between the DVC and FE

measurements. This implies that the segmentation procedure was satisfactory and that the analysis of these differences can be used to identify limitations of the physical and numerical framework.

In the comparison between DVC and FE measures, a very good agreement was observed for the macroscopic equivalent strain of both specimens. The local strain measures presented very good agreement for the 90° specimen. For the 45° specimen, the local strain values showed larger discrepancies, but their rate of increase was well predicted.

The rate of increase of the strain was observed to increase towards the end of the tests in the DVC results. This acceleration was not well captured by the FE simulations. This shortcoming is thought to be due mainly to the fact that the second population of voids that has been confirmed in the matrix is not taken into account in the numerical simulations. Improving the constitutive modeling by either explicitly taking damage into account or by using a hardening law that saturates for large values of strain is a perspective of this study. The FE strain predictions are, however, considered satisfactory.

In an effort to contribute to the understanding of the coalescence mechanisms in nodular cast iron and previously observed instances of the void-sheet mechanism, a numerical study was carried out. The objective was to verify the hypothesis that three-dimensional effects could play a role in the observed void-sheet instances. In order to reach this goal, an *ad-hoc* methodology was proposed. In this methodology, three-dimensional clusters were simulated with a clear reference to a far-field stress and without recurring to periodicity of the microstructure.

A three-voids cluster was studied with the proposed methodology. It was found that the three voids can coalesce in such a way that, if a given two-dimensional slice of the domain is observed, an apparent void-sheet is present. This highlights the importance of three-dimensional and non-periodic models for the study of ductile damage. Based on these results and previous observations of fracture surface, it is considered that only coalescence by internal necking, with or without intervention of secondary voids, occurs in the studied specimens. Nodular cast iron is a material with a particularly high void volume fraction. This favors the occurrence of this mode of coalescence. Other engineering materials with smaller void volume fractions are less likely to exhibit this phenomenon.

Since the FE strain measurements were validated and the coalescence mechanisms clarified, a more extensive study of coalescence with the SRCL-DVC-FE framework was carried out. In this study, it was found out that the FE simulations tend to predict coalescence earlier than observed in the laminography images. A finer temporal discretization could provide further elements to understand these differences as well. This would require additional in-situ laminography results. Not taking into account damage in the matrix and modeling the nodules as voids are two factors that could influence these differences. The simulations

are however considered accurate enough to assess the possibility of establishing a coalescence criterion at the microscale.

Different approaches were tested in order to establish a coalescence criterion in 12 different intervoid ligaments. Two different approaches presented promising results. The first proposed approach consists in predicting the moment of coalescence based on the evolution of the intervoid distance as a function of the macroscopic equivalent strain. The input of this model are the initial intervoid distance and the increase rate of the local strain. The model was calibrated with data from the 12 studied intervoid ligaments and validated with data from 6 additional ligaments. The model predictions were considered satisfactory.

The second proposed approach is probabilistic. Two variants were proposed. In the first variant, the empiric coalescence probability is expressed in terms of the macroscopic equivalent strain and a Weibull distribution is fitted. A way to integrate this model into a porous plasticity behavior law was detailed. This requires fitting only one parameter at the macroscale and would avoid the use of the effective porosity that is commonly used. The second variant is very similar in nature, but formulated in terms of the local pre-coalescence strain. The local variant can be used in numerical calculations at the microscale that do not seek to reproduce in detail the topological changes associated to ductile damage.

An important characteristic of the two proposed approaches for coalescence is that they were formulated based on simulations of immersed microstructures under realistic boundary conditions that were conducted up to very large strain values. No simplifying hypothesis with respect to the topology of the microstructure were used. Finding these simple relationships in complex microstructures under heterogeneous boundary conditions is a major result of this work.

7.2 Perspectives

Two shortcomings of the current physical framework were identified. The first one is that the acceleration of the strain increase rate observed in DVC, is not captured by the FE simulations. The second one is that the FE simulations predict coalescence earlier than observed in the laminography images. This could be improved by considering the influence of the secondary population of voids with a porous plasticity behavior law. Parameter identification at the microscale remains, however, a time-consuming task. A satisfying compromise could be given by a hardening law with saturation since it presents a smaller number of parameters to identify. The improvement of the constitutive modeling is a clear and important perspective of this work.

Another major perspective is to use the data resulting from the FE simulations for calibration of a porous plasticity behavior law such as the GTN. The SRCL-DVC-FE framework

is a promising alternative for the calibration of macroscopic behavior laws. Classic calibration of porous plasticity behavior laws at the macroscale is difficult due to the number of parameters that need to be identified. The output resulting from the SRCL-DVC-FE simulations include the evolution of internal variables such as equivalent plastic strain and void fraction, and could be used to calibrate porous plasticity models.

Another possibility of contributing to modeling at the macroscale is through new void nucleation, growth and coalescence criteria. The capability of the proposed intervoid distance coalescence model to be used at the macroscale is still unclear. It would be incorporated in FE² schemes. A more attractive alternative would be to find a way to substitute the required kinematic input by purely topological information. If this is achieved, initial statistics of the microstructure could be enough to calibrate the model. This requires more work. Finding a way to correlate the global loss of load-bearing capacity with the topological changes at the microscale would open new possibilities to propose macroscopic behavior laws inspired on the micromechanisms of ductile damage.

A clear perspective is testing the probabilistic model for coalescence that was proposed. Its integration in the GTN model was detailed and the modifications it would require are not significant. This would allow its validation at the macroscale and to test its merits with respect to the classic coalescence treatment in the GTN model.

The two proposed approaches to void coalescence could work in a complementary manner. This requires additional work. The intervoid distance model can provide the necessary input for the probabilistic approach. The two approaches could then be coupled. This implies that the probabilistic approach could be indirectly calibrated based on tomographic information of the initial configuration only.

Extending the study to other loading conditions is an important perspective. This is a necessary condition so that more universal micro or macroscopic models can be proposed with the SRCL-DVC-FE framework.

The methodology proposed in Chapter 5 for the study of three-dimensional and non-periodic microstructures can be an useful tool to test different loading conditions a priori. It could then help decide which are interesting enough to study via the SRCL-DVC-FE framework since SRCL is time-consuming and costly.

The hypothesis of considering the graphite nodules as voids is to be abandoned if other loading conditions such as compression or shear are considered. This would require a robust contact detection methodology to be implemented in the numerical framework.

There is clear interest of applying this framework to other materials. Some early steps have already been taken. An initial study of void nucleation mechanisms has been carried out for steel-ceramic composites and for aluminum alloys. The former constitutes an example of

a direct industrial application and the latter the opportunity of calibrating nucleation models at the microscale. In the future, such numerical techniques could also be applied to study the fracture mechanisms of multiphase metallic materials.

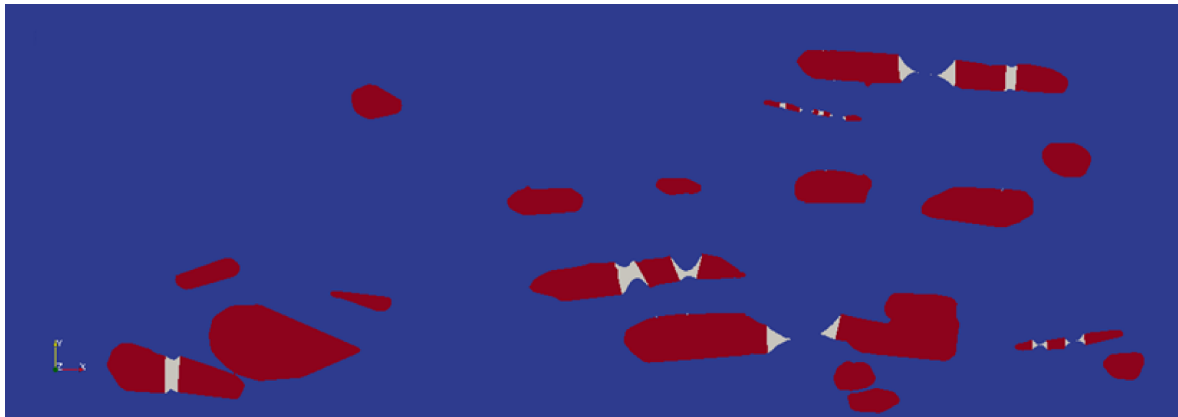


Figure 7.1: Two-dimensional simulation of a steel-ceramic composite under compression to study its nucleation mechanisms. The matrix is shown in blue, the particles in red and the nucleated voids in white.

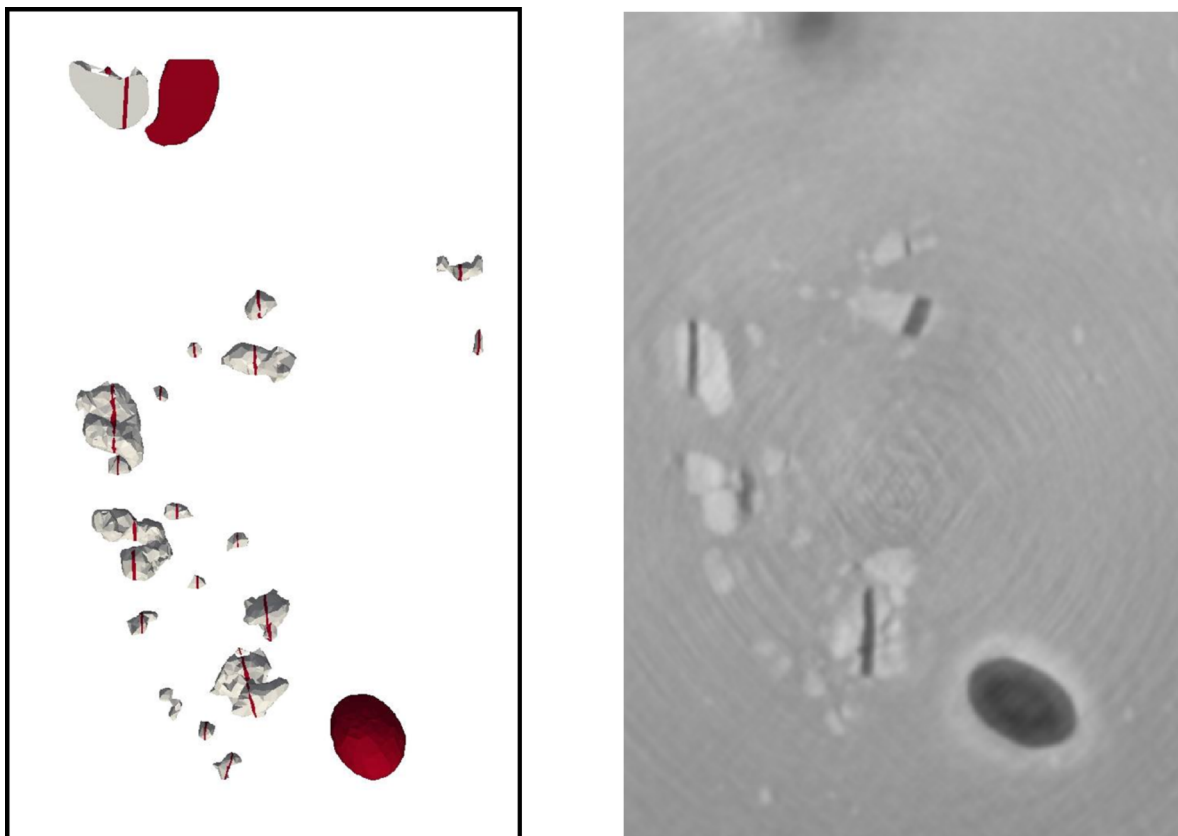


Figure 7.2: Three-dimensional simulation of an aluminum alloy with the SRCL-DVC-FE framework (left) and slice of the laminography image (right). The voids are shown in red and the particles in gray and exhibit fracture. Good quantitative agreement is observed.

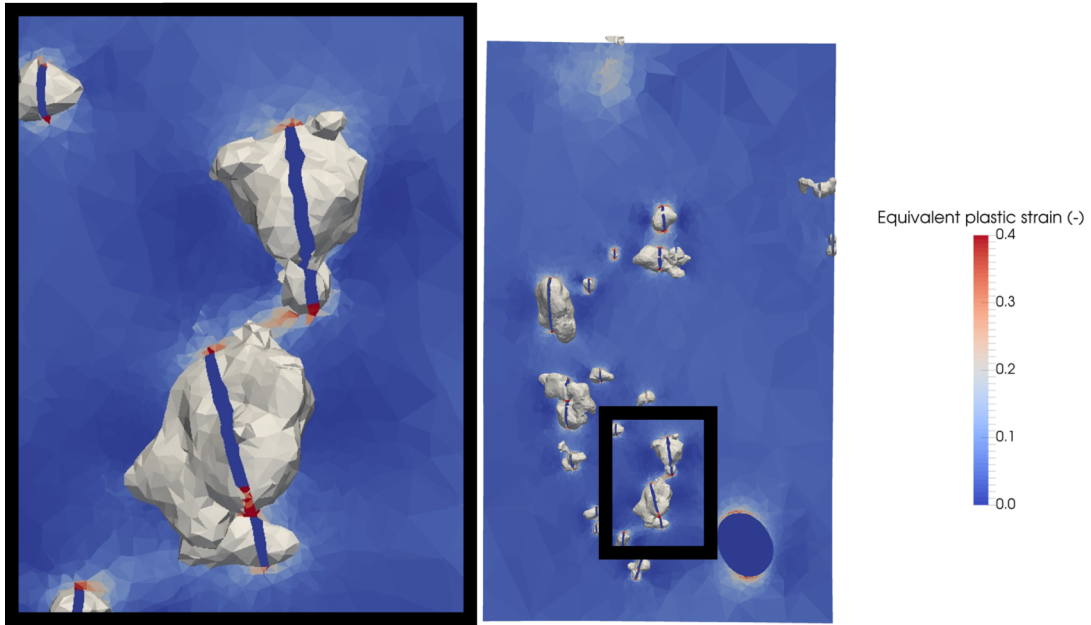


Figure 7.3: Three-dimensional simulation of an aluminum alloy with the SRCL-DVC-FE framework. The strain field is shown and the black rectangle indicates a zoomed area.

Acknowledgements

This work was performed within the COMINSIDE project funded by the French Agence Nationale de la Recherche (ANR-14-CE07-0034-02 grant).

Appendix A

Strain profiles

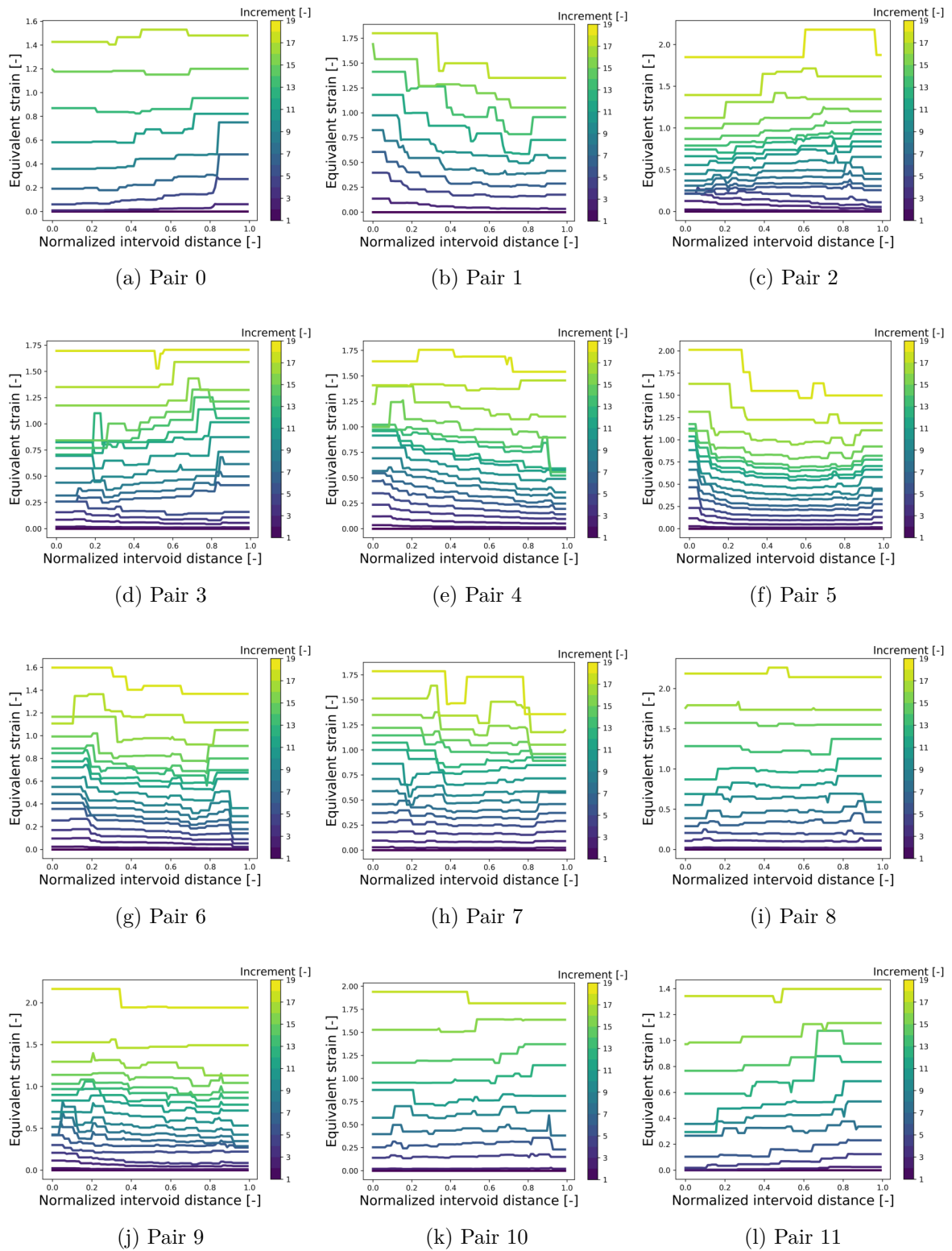
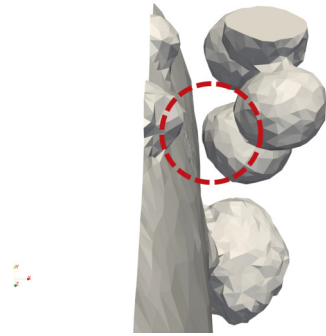


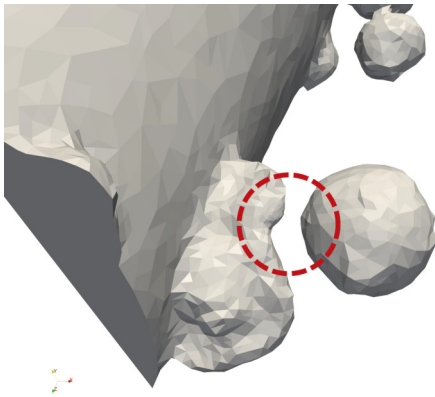
Figure A.1: Strain profiles in the shortest path between two voids obtained from the FE simulation for 12 void pairs.



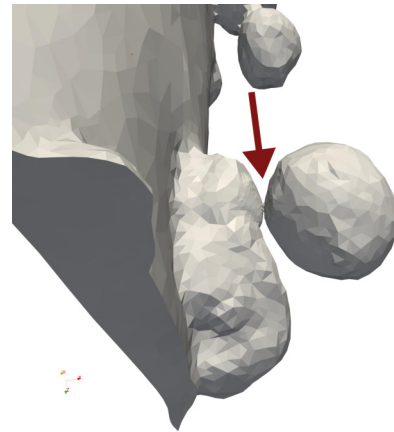
(a) Pair 0 - Initial



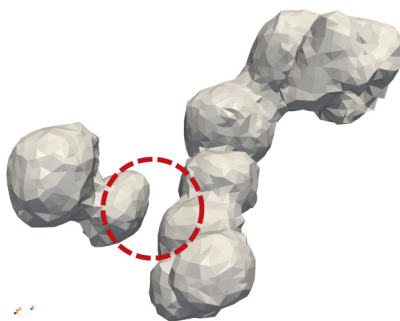
(b) Pair 0 - Postcoalescence



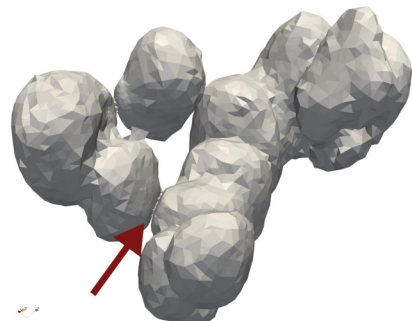
(c) Pair 1 - Initial



(d) Pair 1 - Postcoalescence

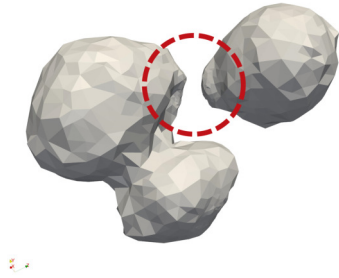


(e) Pair 2 - Initial

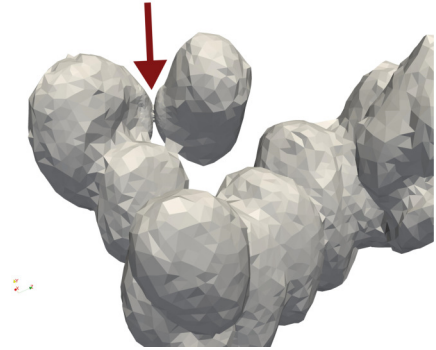


(f) Pair 2 - Postcoalescence

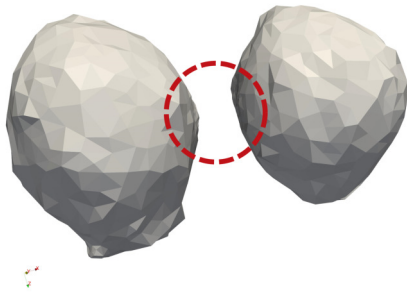
Figure A.2: Three-dimensional views of the void pairs in their initial (left column) and postcoalescence (right column) configurations for void pairs 0-2.



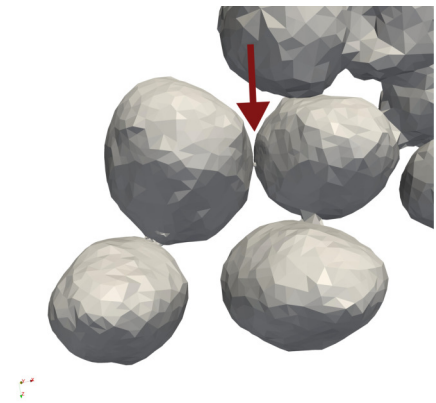
(a) Pair 3 - Initial



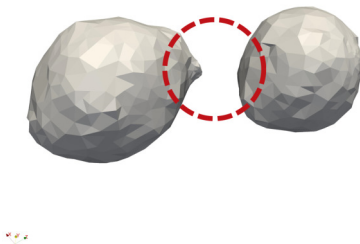
(b) Pair 3 - Postcoalescence



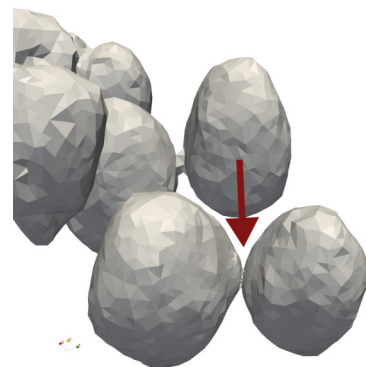
(c) Pair 4 - Initial



(d) Pair 4 - Postcoalescence

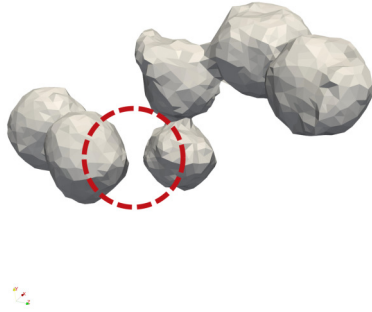


(e) Pair 5 - Initial

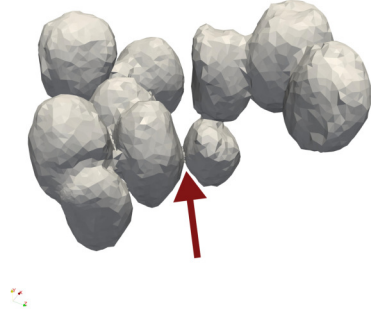


(f) Pair 5 - Postcoalescence

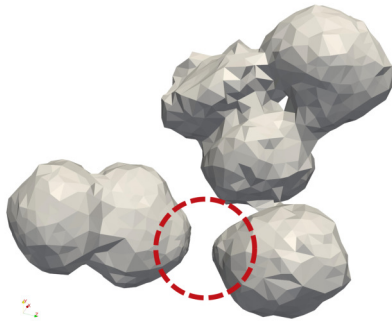
Figure A.3: Three-dimensional views of the void pairs in their initial (left column) and postcoalescence (right column) configurations for void pairs 3-5.



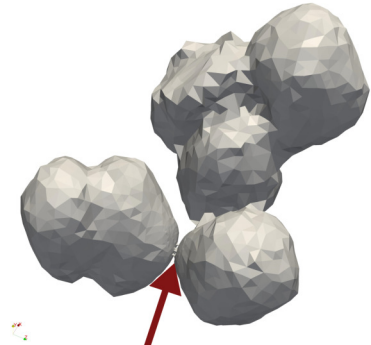
(a) Pair 9 - Initial



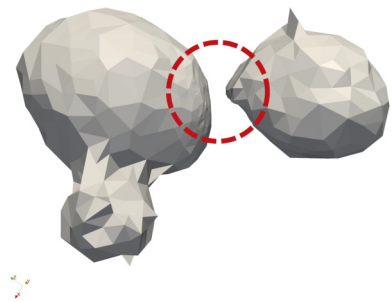
(b) Pair 9 - Postcoalescence



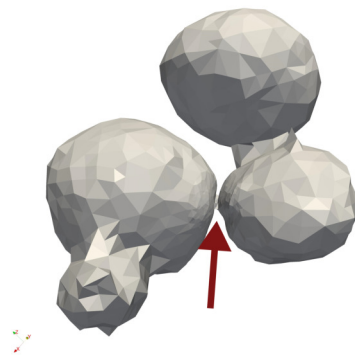
(c) Pair 10 - Initial



(d) Pair 10 - Postcoalescence



(e) Pair 11 - Initial



(f) Pair 11 - Postcoalescence

Figure A.4: Three-dimensional views of the void pairs in their initial (left column) and postcoalescence (right column) configurations for void pairs 9-11.

Bibliography

- [1] I. Westermann, K. O. Pedersen, T. Furu, T. Børvik, and O. S. Hopperstad, “Effects of particles and solutes on strength, work-hardening and ductile fracture of aluminium alloys,” *Mechanics of Materials*, vol. 79, pp. 58–72, 2014. (Cited on page 7.)
- [2] T. F. Morgeneyer, J. Besson, H. Proudhon, M. Starink, and I. Sinclair, “Experimental and numerical analysis of toughness anisotropy in aa2139 al-alloy sheet,” *Acta Materialia*, vol. 57, no. 13, pp. 3902–3915, 2009. (Cited on page 7.)
- [3] T. F. Morgeneyer, L. Helfen, I. Sinclair, H. Proudhon, F. Xu, and T. Baumbach, “Ductile crack initiation and propagation assessed via in situ synchrotron radiation-computed laminography,” *Scripta Materialia*, vol. 65, no. 11, pp. 1010–1013, 2011. (Cited on pages 7, 8, and 31.)
- [4] T.-S. Cao, C. Bobadilla, P. Montmitonnet, and P.-O. Bouchard, “A comparative study of three ductile damage approaches for fracture prediction in cold forming processes,” *Journal of Materials Processing Technology*, vol. 216, pp. 385–404, 2015. (Cited on pages 8 and 14.)
- [5] J. Papasidero, V. Doquet, and D. Mohr, “Ductile fracture of aluminum 2024-t351 under proportional and non-proportional multi-axial loading: Bao-wierzbicki results revisited,” *International Journal of Solids and Structures*, vol. 69, pp. 459–474, 2015. (Cited on page 8.)
- [6] M. Shakoof, M. Bernacki, and P.-O. Bouchard, “Ductile fracture of a metal matrix composite studied using 3d numerical modeling of void nucleation and coalescence,” *Engineering Fracture Mechanics*, vol. 189, pp. 110–132, 2017. (Cited on pages 9 and 29.)
- [7] P. Matic and A. B. Geltmacher, “A cellular automaton-based technique for modeling mesoscale damage evolution,” *Computational materials science*, vol. 20, no. 1, pp. 120–141, 2001. (Cited on page 9.)
- [8] T. De Geus, M. Cottura, B. Appolaire, R. Peerlings, and M. Geers, “Fracture initiation in multi-phase materials: A systematic three-dimensional approach using a fft-based solver,” *Mechanics of Materials*, vol. 97, pp. 199–211, 2016. (Cited on page 9.)

- [9] A. Buljac, M. Shakoor, J. Neggers, M. Bernacki, P.-O. Bouchard, L. Helfen, T. F. Morgeneyer, and F. Hild, “Numerical validation framework for micromechanical simulations based on synchrotron 3D imaging,” *Computational Mechanics*, vol. 59, no. 3, pp. 419–441, 2017. (Cited on pages 9, 19, 39, 46, 66, 117, and 144.)
- [10] M. Shakoor, A. Buljac, J. Neggers, F. Hild, T. F. Morgeneyer, L. Helfen, M. Bernacki, and P.-O. Bouchard, “On the choice of boundary conditions for micromechanical simulations based on 3D imaging,” *International Journal of Solids and Structures*, vol. 112, pp. 83–96, 2017. (Cited on pages 9, 19, 40, 41, 46, 117, and 119.)
- [11] J. R. Rice and D. M. Tracey, “On the ductile enlargement of voids in triaxial stress fields,” *Journal of the Mechanics and Physics of Solids*, vol. 17, no. 3, pp. 201–217, 1969. (Cited on pages 15, 127, and 153.)
- [12] Y. Bai and T. Wierzbicki, “A new model of metal plasticity and fracture with pressure and lode dependence,” *International journal of plasticity*, vol. 24, no. 6, pp. 1071–1096, 2008. (Cited on page 15.)
- [13] F. A. McClintock, “A criterion for ductile fracture by the growth of holes,” *Journal of applied mechanics*, vol. 35, no. 2, pp. 363–371, 1968. (Cited on pages 15 and 141.)
- [14] M. Cockcroft and D. Latham, “Ductility and the workability of metals,” *J Inst Metals*, vol. 96, no. 1, pp. 33–39, 1968. (Cited on pages 15 and 152.)
- [15] M. Wilkins, R. Streit, and J. Reaugh, “Cumulative-strain-damage model of ductile fracture: simulation and prediction of engineering fracture tests,” tech. rep., Lawrence Livermore National Lab., CA (USA); Science Applications, Inc., San Leandro, CA (USA), 1980. (Cited on page 15.)
- [16] G. R. Johnson and W. H. Cook, “Fracture characteristics of three metals subjected to various strains, strain rates, temperatures and pressures,” *Engineering fracture mechanics*, vol. 21, no. 1, pp. 31–48, 1985. (Cited on page 15.)
- [17] Y. Bai and T. Wierzbicki, “Application of extended mohr–coulomb criterion to ductile fracture,” *International Journal of Fracture*, vol. 161, no. 1, p. 1, 2010. (Cited on page 15.)
- [18] Y. Lou, H. Huh, S. Lim, and K. Pack, “New ductile fracture criterion for prediction of fracture forming limit diagrams of sheet metals,” *International Journal of Solids and Structures*, vol. 49, no. 25, pp. 3605–3615, 2012. (Cited on pages 15 and 153.)
- [19] L. M. Kachanov, “On creep rupture time,” *Izv. Acad. Nauk SSSR, Otd. Techn. Nauk*, vol. 8, pp. 26–31, 1958. (Cited on page 15.)
- [20] G. Rousselier, “Finite deformation constitutive relations including ductile fracture damage,” *Three-dimensional constitutive relations and ductile fracture.(A 83-18477 06-39) Amsterdam, North-Holland Publishing Co., 1981,, pp. 331–355, 1981. (Cited on page 15.)*

- [21] G. Rousselier, “Ductile fracture models and their potential in local approach of fracture,” *Nuclear engineering and design*, vol. 105, no. 1, pp. 97–111, 1987. (Cited on page 15.)
- [22] J. Lemaitre, “A continuous damage mechanics model for ductile fracture,” *Journal of engineering materials and technology*, vol. 107, no. 1, pp. 83–89, 1985. (Cited on pages 15, 16, 111, and 114.)
- [23] J. Lemaitre and R. Desmorat, *Engineering damage mechanics: ductile, creep, fatigue and brittle failures*. Springer Science & Business Media, 2005. (Cited on page 16.)
- [24] J. Lemaitre, R. Desmorat, and M. Sauzay, “Anisotropic damage law of evolution,” *European Journal of Mechanics-A/Solids*, vol. 19, no. 2, pp. 187–208, 2000. (Cited on page 16.)
- [25] P.-O. Bouchard, L. Bourgeon, S. Fayolle, and K. Mocellin, “An enhanced lemaître model formulation for materials processing damage computation,” *International Journal of Material Forming*, vol. 4, no. 3, pp. 299–315, 2011. (Cited on page 16.)
- [26] T.-S. Cao, J.-M. Gachet, P. Montmitonnet, and P.-O. Bouchard, “A lode-dependent enhanced lemaître model for ductile fracture prediction at low stress triaxiality,” *Engineering Fracture Mechanics*, vol. 124, pp. 80–96, 2014. (Cited on page 16.)
- [27] A. L. Gurson, “Continuum theory of ductile rupture by void nucleation and growth: Part I—yield criteria and flow rules for porous ductile media,” *Journal of engineering materials and technology*, vol. 99, no. 1, pp. 2–15, 1977. (Cited on pages 16, 141, and 163.)
- [28] V. Tvergaard, “Influence of voids on shear band instabilities under plane strain conditions,” *International Journal of Fracture*, vol. 17, no. 4, pp. 389–407, 1981. (Cited on pages 16 and 18.)
- [29] V. Tvergaard and A. Needleman, “Analysis of the cup-cone fracture in a round tensile bar,” *Acta metallurgica*, vol. 32, no. 1, pp. 157–169, 1984. (Cited on pages 17, 19, and 163.)
- [30] C. Chu and A. Needleman, “Void nucleation effects in biaxially stretched sheets,” *Journal of engineering materials and technology*, vol. 102, no. 3, pp. 249–256, 1980. (Cited on pages 17, 162, and 163.)
- [31] T.-S. Cao, P. Montmitonnet, and P.-O. Bouchard, “A detailed description of the gurson–tvergaard–needleman model within a mixed velocity–pressure finite element formulation,” *International Journal for Numerical Methods in Engineering*, vol. 96, no. 9, pp. 561–583, 2013. (Cited on page 18.)
- [32] M. Gologanu, J.-B. Leblond, and J. Devaux, “Approximate models for ductile metals containing non-spherical voids—case of axisymmetric prolate ellipsoidal cavities,”

- Journal of the Mechanics and Physics of Solids*, vol. 41, no. 11, pp. 1723–1754, 1993. (Cited on page 18.)
- [33] K. Nahshon and J. Hutchinson, “Modification of the gurson model for shear failure,” *European Journal of Mechanics-A/Solids*, vol. 27, no. 1, pp. 1–17, 2008. (Cited on page 18.)
- [34] J. Wen, Y. Huang, K. Hwang, C. Liu, and M. Li, “The modified gurson model accounting for the void size effect,” *International Journal of Plasticity*, vol. 21, no. 2, pp. 381–395, 2005. (Cited on page 18.)
- [35] A. A. Benzerga and J. Besson, “Plastic potentials for anisotropic porous solids,” *European Journal of Mechanics-A/Solids*, vol. 20, no. 3, pp. 397–434, 2001. (Cited on page 18.)
- [36] N. Jacques, S. Mercier, and A. Molinari, “Simulation of the failure of ductile materials under dynamic loading using continuum damage models with micro-inertia,” in *6th European Conference on Computational Mechanics/7th European Conference on Computational Fluid Dynamics (ECCM-ECFD 2018)*, 2018. (Cited on page 18.)
- [37] K. Siruguet and J.-B. Leblond, “Effect of void locking by inclusions upon the plastic behavior of porous ductile solids—i: theoretical modeling and numerical study of void growth,” *International Journal of Plasticity*, vol. 20, no. 2, pp. 225–254, 2004. (Cited on page 18.)
- [38] J. Besson and C. Guillemer-Neel, “An extension of the green and gurson models to kinematic hardening,” *Mechanics of materials*, vol. 35, no. 1-2, pp. 1–18, 2003. (Cited on page 18.)
- [39] A. Needleman, “Void growth in an elastic-plastic medium,” in *Journal of Applied mechanics*, ASME, 1972. (Cited on page 18.)
- [40] C. Thomson, M. Worswick, A. Pilkey, D. Lloyd, and G. Burger, “Modeling void nucleation and growth within periodic clusters of particles,” *Journal of the Mechanics and Physics of Solids*, vol. 47, no. 1, pp. 1–26, 1998. (Cited on page 18.)
- [41] C. Thomson, M. Worswick, A. Pilkey, and D. Lloyd, “Void coalescence within periodic clusters of particles,” *Journal of the Mechanics and Physics of Solids*, vol. 51, no. 1, pp. 127–146, 2003. (Cited on page 18.)
- [42] C. McVeigh, F. Vernerey, W. K. Liu, B. Moran, and G. Olson, “An interactive microvoid shear localization mechanism in high strength steels,” *Journal of the Mechanics and Physics of Solids*, vol. 55, no. 2, pp. 225–244, 2007. (Cited on page 18.)
- [43] V. Tvergaard, “Effect of void cluster on ductile failure evolution,” *Meccanica*, vol. 12, no. 51, pp. 3097–3105, 2016. (Cited on pages 18 and 119.)

- [44] C. Tekoglu, “Void coalescence in ductile solids containing two populations of voids,” *Engineering Fracture Mechanics*, vol. 147, pp. 418–430, 2015. (Cited on page 18.)
- [45] I. Khan and V. Bhasin, “On the role of secondary voids and their distribution in the mechanism of void growth and coalescence in porous plastic solids,” *International Journal of Solids and Structures*, vol. 108, pp. 203–215, 2017. (Cited on pages 18 and 119.)
- [46] N. Ohno and J. Hutchinson, “Plastic flow localization due to non-uniform void distribution,” *Journal of the Mechanics and Physics of Solids*, vol. 32, no. 1, pp. 63–85, 1984. (Cited on page 19.)
- [47] M. Horstemeyer, M. Matalanis, A. Sieber, and M. Botos, “Micromechanical finite element calculations of temperature and void configuration effects on void growth and coalescence,” *international Journal of Plasticity*, vol. 16, no. 7, pp. 979–1015, 2000. (Cited on page 19.)
- [48] J. Bandstra and D. Koss, “Modeling the ductile fracture process of void coalescence by void-sheet formation,” *Materials Science and Engineering: A*, vol. 319, pp. 490–495, 2001. (Cited on pages 19, 84, and 133.)
- [49] J. Bandstra, D. Koss, A. Geltmacher, P. Matic, and R. Everett, “Modeling void coalescence during ductile fracture of a steel,” *Materials Science and Engineering: A*, vol. 366, no. 2, pp. 269–281, 2004. (Cited on page 19.)
- [50] V. Tvergaard and A. Needleman, “Three dimensional microstructural effects on plane strain ductile crack growth,” *International journal of solids and structures*, vol. 43, no. 20, pp. 6165–6179, 2006. (Cited on page 19.)
- [51] J. Bandstra and D. Koss, “On the influence of void clusters on void growth and coalescence during ductile fracture,” *Acta Materialia*, vol. 56, no. 16, pp. 4429–4439, 2008. (Cited on page 19.)
- [52] M. Shakoar, M. Bernacki, and P.-O. Bouchard, “A new body-fitted immersed volume method for the modeling of ductile fracture at the microscale: Analysis of void clusters and stress state effects on coalescence,” *Engineering Fracture Mechanics*, vol. 147, pp. 398–417, 2015. (Cited on pages 19, 26, 27, 36, and 37.)
- [53] X. Sun, K. S. Choi, W. N. Liu, and M. A. Khaleel, “Predicting failure modes and ductility of dual phase steels using plastic strain localization,” *International Journal of Plasticity*, vol. 25, no. 10, pp. 1888–1909, 2009. (Cited on page 19.)
- [54] N. Vanderesse, E. Maire, A. Chabod, and J.-Y. Buffière, “Microtomographic study and finite element analysis of the porosity harmfulness in a cast aluminium alloy,” *International Journal of Fatigue*, vol. 33, no. 12, pp. 1514–1525, 2011. (Cited on pages 19 and 46.)

- [55] S. Youssef, E. Maire, and R. Gaertner, “Finite element modelling of the actual structure of cellular materials determined by x-ray tomography,” *Acta Materialia*, vol. 53, no. 3, pp. 719–730, 2005. (Cited on pages 19 and 46.)
- [56] A. Benzerga, J. Besson, and A. Pineau, “Coalescence-controlled anisotropic ductile fracture,” *Journal of Engineering Materials and Technology*, vol. 121, no. 2, pp. 221–229, 1999. (Cited on page 19.)
- [57] A. Pineau, A. A. Benzerga, and T. Pardoen, “Failure of metals i: Brittle and ductile fracture,” *Acta Materialia*, vol. 107, pp. 424–483, 2016. (Cited on pages 19 and 116.)
- [58] A. Pineau, “Global and local approaches of fracture—transferability of laboratory test results to components,” in *Topics in fracture and fatigue*, pp. 197–234, Springer, 1992. (Cited on page 19.)
- [59] L. Brown and J. Embury, “Initiation and growth of voids at second-phase particles,” in *Proc. Conf. on Microstructure and Design of Alloys, Institute of Metals and Iron and Steel Institute, London. 1973, 1,(33), 164-169*, 1973. (Cited on page 20.)
- [60] P. Thomason, “A theory for ductile fracture by internal necking of cavities,” *J. Inst. Metals*, vol. 96, p. 360, 1968. (Cited on page 20.)
- [61] P. Thomason, “A three-dimensional model for ductile fracture by the growth and coalescence of microvoids,” *Acta Metallurgica*, vol. 33, no. 6, pp. 1087–1095, 1985. (Cited on pages 20 and 141.)
- [62] A. A. Benzerga and J.-B. Leblond, “Ductile fracture by void growth to coalescence,” *Advances in Applied Mechanics*, vol. 44, pp. 169–305, 2010. (Cited on pages 20, 116, and 141.)
- [63] F. Scheyvaerts, T. Pardoen, and P. Onck, “A new model for void coalescence by internal necking,” *International Journal of Damage Mechanics*, vol. 19, no. 1, pp. 95–126, 2010. (Cited on pages 20 and 141.)
- [64] T. Pardoen and J. Hutchinson, “An extended model for void growth and coalescence,” *Journal of the Mechanics and Physics of Solids*, vol. 48, no. 12, pp. 2467–2512, 2000. (Cited on page 20.)
- [65] A. A. Benzerga, “Micromechanics of coalescence in ductile fracture,” *Journal of the Mechanics and Physics of Solids*, vol. 50, no. 6, pp. 1331–1362, 2002. (Cited on page 20.)
- [66] A. Molinari, N. Jacques, S. Mercier, J.-B. Leblond, and A. A. Benzerga, “A micromechanical model for the dynamic behavior of porous media in the void coalescence stage,” *International Journal of Solids and Structures*, vol. 71, pp. 1–18, 2015. (Cited on page 20.)

- [67] M. Torki, A. Benzerga, and J.-B. Leblond, “On void coalescence under combined tension and shear,” *Journal of Applied Mechanics*, vol. 82, no. 7, p. 071005, 2015. (Cited on page 20.)
- [68] C. Tekoglu, J.-B. Leblond, and T. Pardoen, “A criterion for the onset of void coalescence under combined tension and shear,” *Journal of the Mechanics and Physics of Solids*, vol. 60, no. 7, pp. 1363–1381, 2012. (Cited on page 20.)
- [69] M. Shakoor, V. M. Trejo Navas, D. P. Munõz, M. Bernacki, and P.-O. Bouchard, “Computational methods for ductile fracture modeling at the microscale,” *Archives of Computational Methods in Engineering*, pp. 1–40, 2018. (Cited on page 21.)
- [70] J. Wulf, T. Steinkopff, and H. Fischmeister, “Fe-simulation of crack paths in the real microstructure of an al (6061)/sic composite,” *Acta materialia*, vol. 44, no. 5, pp. 1765–1779, 1996. (Cited on page 21.)
- [71] J. Mediavilla, R. Peerlings, and M. Geers, “A robust and consistent remeshing-transfer operator for ductile fracture simulations,” *Computers & structures*, vol. 84, no. 8-9, pp. 604–623, 2006. (Cited on pages 21, 26, and 27.)
- [72] K. Perzyński, A. Wrożyna, R. Kuziak, A. Legwand, and L. Madej, “Development and validation of multi scale failure model for dual phase steels,” *Finite Elements in Analysis and Design*, vol. 124, pp. 7–21, 2017. (Cited on pages 21 and 24.)
- [73] M. Jirásek, “Comparative study on finite elements with embedded discontinuities,” *Computer methods in applied mechanics and engineering*, vol. 188, no. 1-3, pp. 307–330, 2000. (Cited on page 22.)
- [74] J. Oliver, A. E. Huespe, and P. J. Sánchez, “A comparative study on finite elements for capturing strong discontinuities: E-fem vs x-fem,” *Computer methods in applied mechanics and engineering*, vol. 195, no. 37-40, pp. 4732–4752, 2006. (Cited on page 22.)
- [75] T.-P. Fries and T. Belytschko, “The extended/generalized finite element method: an overview of the method and its applications,” *International Journal for Numerical Methods in Engineering*, vol. 84, no. 3, pp. 253–304, 2010. (Cited on page 22.)
- [76] N. Moës, J. Dolbow, and T. Belytschko, “A finite element method for crack growth without remeshing,” *International journal for numerical methods in engineering*, vol. 46, no. 1, pp. 131–150, 1999. (Cited on pages 22 and 23.)
- [77] J. M. Melenk and I. Babuška, “The partition of unity finite element method: basic theory and applications,” *Computer methods in applied mechanics and engineering*, vol. 139, no. 1-4, pp. 289–314, 1996. (Cited on page 22.)
- [78] T. Strouboulis, I. Babuška, and K. Copps, “The design and analysis of the generalized finite element method,” *Computer methods in applied mechanics and engineering*, vol. 181, no. 1-3, pp. 43–69, 2000. (Cited on page 22.)

- [79] T. Belytschko and T. Black, “Elastic crack growth in finite elements with minimal remeshing,” *International journal for numerical methods in engineering*, vol. 45, no. 5, pp. 601–620, 1999. (Cited on pages 22 and 23.)
- [80] C. Daux, N. Moës, J. Dolbow, N. Sukumar, and T. Belytschko, “Arbitrary branched and intersecting cracks with the extended finite element method,” *International journal for numerical methods in engineering*, vol. 48, no. 12, pp. 1741–1760, 2000. (Cited on pages 22 and 23.)
- [81] C. Duarte, O. Hamzeh, T. Liszka, and W. Tworzydło, “A generalized finite element method for the simulation of three-dimensional dynamic crack propagation,” *Computer Methods in Applied Mechanics and Engineering*, vol. 190, no. 15-17, pp. 2227–2262, 2001. (Cited on page 22.)
- [82] S. Osher and J. A. Sethian, “Fronts propagating with curvature-dependent speed: algorithms based on hamilton-jacobi formulations,” *Journal of computational physics*, vol. 79, no. 1, pp. 12–49, 1988. (Cited on page 22.)
- [83] N. Moës, A. Gravouil, and T. Belytschko, “Non-planar 3d crack growth by the extended finite element and level sets—part i: Mechanical model,” *International Journal for Numerical Methods in Engineering*, vol. 53, no. 11, pp. 2549–2568, 2002. (Cited on pages 22 and 23.)
- [84] N. Sukumar, D. L. Chopp, N. Moës, and T. Belytschko, “Modeling holes and inclusions by level sets in the extended finite-element method,” *Computer methods in applied mechanics and engineering*, vol. 190, no. 46-47, pp. 6183–6200, 2001. (Cited on pages 22 and 23.)
- [85] Z. Wang, T. Yu, T. Q. Bui, N. A. Trinh, N. T. H. Luong, N. D. Duc, and D. H. Doan, “Numerical modeling of 3-d inclusions and voids by a novel adaptive xfem,” *Advances in Engineering Software*, vol. 102, pp. 105–122, 2016. (Cited on page 22.)
- [86] N. Sukumar, N. Moës, B. Moran, and T. Belytschko, “Extended finite element method for three-dimensional crack modelling,” *International Journal for Numerical Methods in Engineering*, vol. 48, no. 11, pp. 1549–1570, 2000. (Cited on page 23.)
- [87] S. Loehnert and T. Belytschko, “A multiscale projection method for macro/microcrack simulations,” *International Journal for Numerical Methods in Engineering*, vol. 71, no. 12, pp. 1466–1482, 2007. (Cited on page 23.)
- [88] T. Rabczuk, S. Bordas, and G. Zi, “On three-dimensional modelling of crack growth using partition of unity methods,” *Computers & structures*, vol. 88, no. 23-24, pp. 1391–1411, 2010. (Cited on page 23.)
- [89] P. Laborde, J. Pommier, Y. Renard, and M. Salaün, “High-order extended finite element method for cracked domains,” *International Journal for Numerical Methods in Engineering*, vol. 64, no. 3, pp. 354–381, 2005. (Cited on page 23.)

- [90] N. Sukumar, J. Dolbow, and N. Moës, “Extended finite element method in computational fracture mechanics: a retrospective examination,” *International Journal of Fracture*, vol. 196, no. 1-2, pp. 189–206, 2015. (Cited on page 23.)
- [91] É. Béchet, H. Minnebo, N. Moës, and B. Burgardt, “Improved implementation and robustness study of the x-fem for stress analysis around cracks,” *International Journal for Numerical Methods in Engineering*, vol. 64, no. 8, pp. 1033–1056, 2005. (Cited on page 23.)
- [92] T. Elguedj, A. Gravouil, and A. Combescure, “Appropriate extended functions for x-fem simulation of plastic fracture mechanics,” *Computer Methods in Applied Mechanics and Engineering*, vol. 195, no. 7-8, pp. 501–515, 2006. (Cited on page 23.)
- [93] N. Vajragupta, V. Uthaisangsuk, B. Schmaling, S. Münstermann, A. Hartmaier, and W. Bleck, “A micromechanical damage simulation of dual phase steels using xfem,” *Computational Materials Science*, vol. 54, pp. 271–279, 2012. (Cited on page 24.)
- [94] A. Ramazani, A. Schwedt, A. Aretz, U. Prahl, and W. Bleck, “Characterization and modelling of failure initiation in dp steel,” *Computational materials science*, vol. 75, pp. 35–44, 2013. (Cited on page 24.)
- [95] J. W. Cahn and J. E. Hilliard, “Free energy of a nonuniform system. i. interfacial free energy,” *The Journal of chemical physics*, vol. 28, no. 2, pp. 258–267, 1958. (Cited on page 24.)
- [96] H. Amor, J.-J. Marigo, and C. Maurini, “Regularized formulation of the variational brittle fracture with unilateral contact: Numerical experiments,” *Journal of the Mechanics and Physics of Solids*, vol. 57, no. 8, pp. 1209–1229, 2009. (Cited on page 25.)
- [97] B. Bourdin, G. A. Francfort, and J.-J. Marigo, “Numerical experiments in revisited brittle fracture,” *Journal of the Mechanics and Physics of Solids*, vol. 48, no. 4, pp. 797–826, 2000. (Cited on page 25.)
- [98] C. Miehe, M. Hofacker, and F. Welschinger, “A phase field model for rate-independent crack propagation: Robust algorithmic implementation based on operator splits,” *Computer Methods in Applied Mechanics and Engineering*, vol. 199, no. 45-48, pp. 2765–2778, 2010. (Cited on page 25.)
- [99] M. Ambati, T. Gerasimov, and L. De Lorenzis, “Phase-field modeling of ductile fracture,” *Computational Mechanics*, vol. 55, no. 5, pp. 1017–1040, 2015. (Cited on page 25.)
- [100] M. J. Borden, T. J. Hughes, C. M. Landis, A. Anvari, and I. J. Lee, “A phase-field formulation for fracture in ductile materials: Finite deformation balance law derivation, plastic degradation, and stress triaxiality effects,” *Computer Methods in Applied Mechanics and Engineering*, vol. 312, pp. 130–166, 2016. (Cited on page 25.)

- [101] P. Shanthraj, L. Sharma, B. Svendsen, F. Roters, and D. Raabe, “A phase field model for damage in elasto-viscoplastic materials,” *Computer Methods in Applied Mechanics and Engineering*, vol. 312, pp. 167–185, 2016. (Cited on page 25.)
- [102] T. T. Nguyen, J. Yvonnet, M. Bornert, and C. Chateau, “Initiation and propagation of complex 3d networks of cracks in heterogeneous quasi-brittle materials: Direct comparison between in situ testing-microct experiments and phase field simulations,” *Journal of the Mechanics and Physics of Solids*, vol. 95, pp. 320–350, 2016. (Cited on page 25.)
- [103] T. T. Nguyen, J. Yvonnet, Q.-Z. Zhu, M. Bornert, and C. Chateau, “A phase field method to simulate crack nucleation and propagation in strongly heterogeneous materials from direct imaging of their microstructure,” *Engineering Fracture Mechanics*, vol. 139, pp. 18–39, 2015. (Cited on page 25.)
- [104] T.-T. Nguyen, J. Yvonnet, Q.-Z. Zhu, M. Bornert, and C. Chateau, “A phase-field method for computational modeling of interfacial damage interacting with crack propagation in realistic microstructures obtained by microtomography,” *Computer Methods in Applied Mechanics and Engineering*, vol. 312, pp. 567–595, 2016. (Cited on page 25.)
- [105] C. Gruau and T. Coupez, “3d tetrahedral, unstructured and anisotropic mesh generation with adaptation to natural and multidomain metric,” *Computer Methods in Applied Mechanics and Engineering*, vol. 194, no. 48-49, pp. 4951–4976, 2005. (Cited on page 25.)
- [106] O. C. Zienkiewicz and J. Z. Zhu, “A simple error estimator and adaptive procedure for practical engineering analysis,” *International journal for numerical methods in engineering*, vol. 24, no. 2, pp. 337–357, 1987. (Cited on pages 25 and 26.)
- [107] Z. Zhang and A. Naga, “A new finite element gradient recovery method: superconvergence property,” *SIAM Journal on Scientific Computing*, vol. 26, no. 4, pp. 1192–1213, 2005. (Cited on page 26.)
- [108] R. El Khaoulani and P.-O. Bouchard, “Efficient numerical integration of an elastic-plastic damage law within a mixed velocity-pressure formulation,” *Mathematics and Computers in Simulation*, vol. 94, pp. 145–158, 2013. (Cited on page 26.)
- [109] R. El Khaoulani and P.-O. Bouchard, “An anisotropic mesh adaptation strategy for damage and failure in ductile materials,” *Finite Elements in Analysis and Design*, vol. 59, pp. 1–10, 2012. (Cited on page 26.)
- [110] E. Roux, M. Bernacki, and P.-O. Bouchard, “A level-set and anisotropic adaptive remeshing strategy for the modeling of void growth under large plastic strain,” *Computational Materials Science*, vol. 68, pp. 32–46, 2013. (Cited on pages 26, 27, and 39.)
- [111] E. Roux, M. Shakoov, M. Bernacki, and P.-O. Bouchard, “A new finite element approach for modelling ductile damage void nucleation and growth—analysis of loading path

- effect on damage mechanisms,” *Modelling and Simulation in Materials Science and Engineering*, vol. 22, no. 7, p. 075001, 2014. (Cited on pages 26 and 27.)
- [112] T. Antretter and F. Fischer, “Particle cleavage and ductile crack growth in a two-phase composite on a microscale,” *Computational materials science*, vol. 13, no. 1-3, pp. 1–7, 1998. (Cited on page 26.)
- [113] P.-O. Bouchard, F. Bay, Y. Chastel, and I. Tovená, “Crack propagation modelling using an advanced remeshing technique,” *Computer methods in applied mechanics and engineering*, vol. 189, no. 3, pp. 723–742, 2000. (Cited on page 26.)
- [114] H. Javani, R. H. Peerlings, and M. G. Geers, “Three-dimensional finite element modeling of ductile crack initiation and propagation,” *Advanced Modeling and Simulation in Engineering Sciences*, vol. 3, no. 1, p. 19, 2016. (Cited on pages 27 and 28.)
- [115] S. Feld-Payet, V. Chiaruttini, J. Besson, and F. Feyel, “A new marching ridges algorithm for crack path tracking in regularized media,” *International Journal of Solids and Structures*, vol. 71, pp. 57–69, 2015. (Cited on page 27.)
- [116] P. Areias, J. Reinoso, P. Camanho, and T. Rabczuk, “A constitutive-based element-by-element crack propagation algorithm with local mesh refinement,” *Computational Mechanics*, vol. 56, no. 2, pp. 291–315, 2015. (Cited on page 27.)
- [117] M. Shakoór, P.-O. Bouchard, and M. Bernacki, “An adaptive level-set method with enhanced volume conservation for simulations in multiphase domains,” *International Journal for Numerical Methods in Engineering*, vol. 109, no. 4, pp. 555–576, 2017. (Cited on pages 28, 30, and 36.)
- [118] C. Labrecque and M. Gagne, “Ductile iron: fifty years of continuous development,” *Canadian Metallurgical Quarterly*, vol. 37, no. 5, pp. 343–378, 1998. (Cited on page 28.)
- [119] G. Hütter, L. Zybél, and M. Kuna, “Micromechanisms of fracture in nodular cast iron: From experimental findings towards modeling strategies—a review,” *Engineering Fracture Mechanics*, vol. 144, pp. 118–141, 2015. (Cited on pages 28, 29, and 39.)
- [120] M. Kuna, M. Springmann, K. Mädler, P. Hübner, and G. Pusch, “Fracture mechanics based design of a railway wheel made of austempered ductile iron,” *Engineering Fracture Mechanics*, vol. 72, no. 2, pp. 241–253, 2005. (Cited on page 28.)
- [121] M. Shirani and G. Härkegård, “Fatigue life distribution and size effect in ductile cast iron for wind turbine components,” *Engineering Failure Analysis*, vol. 18, no. 1, pp. 12–24, 2011. (Cited on page 28.)
- [122] M. Endo and K. Yanase, “Effects of small defects, matrix structures and loading conditions on the fatigue strength of ductile cast irons,” *Theoretical and Applied Fracture Mechanics*, vol. 69, pp. 34–43, 2014. (Cited on page 29.)

- [123] A. Buljac, L. Helfen, F. Hild, and T. F. Morgeneyer, “Effect of void arrangement on ductile damage mechanisms in nodular graphite cast iron: In situ 3d measurements,” *Engineering Fracture Mechanics*, vol. 192, pp. 242–261, 2018. (Cited on pages 30, 37, 48, 50, 57, 75, 84, 95, 99, 107, 116, 137, 139, 143, and 148.)
- [124] A. Ghahremaninezhad and K. Ravi-Chandar, “Deformation and failure in nodular cast iron,” *Acta Materialia*, vol. 60, no. 5, pp. 2359–2368, 2012. (Cited on page 30.)
- [125] W. Brocks, S. Hao, and D. Steglich, “Micromechanical modelling of the damage and toughness behaviour of nodular cast iron materials,” *Le Journal de Physique IV*, vol. 6, no. C6, pp. C6–43, 1996. (Cited on page 30.)
- [126] M. Kuna and D. Sun, “Three-dimensional cell model analyses of void growth in ductile materials,” *International Journal of Fracture*, vol. 81, no. 3, pp. 235–258, 1996. (Cited on page 30.)
- [127] M. Dong, C. Prioul, and D. François, “Damage effect on the fracture toughness of nodular cast iron: part i. damage characterization and plastic flow stress modeling,” *Metallurgical and Materials Transactions A*, vol. 28, no. 11, pp. 2245–2254, 1997. (Cited on page 30.)
- [128] K. Zhang, J. Bai, and D. François, “Ductile fracture of materials with high void volume-fraction,” *International Journal of Solids and Structures*, vol. 36, no. 23, pp. 3407–3425, 1999. (Cited on page 30.)
- [129] N. Bonora and A. Ruggiero, “Micromechanical modeling of ductile cast iron incorporating damage. part i: Ferritic ductile cast iron,” *International journal of solids and structures*, vol. 42, no. 5-6, pp. 1401–1424, 2005. (Cited on page 30.)
- [130] L. Collini and G. Nicoletto, “Determination of the relationship between microstructure and constitutive behaviour of nodular cast iron with a unit cell model,” *The Journal of Strain Analysis for Engineering Design*, vol. 40, no. 2, pp. 107–116, 2005. (Cited on page 30.)
- [131] T. Andriollo, J. Thorborg, N. Tiedje, and J. Hattel, “A micro-mechanical analysis of thermo-elastic properties and local residual stresses in ductile iron based on a new anisotropic model for the graphite nodules,” *Modelling and Simulation in Materials Science and Engineering*, vol. 24, no. 5, p. 055012, 2016. (Cited on page 30.)
- [132] T. Andriollo, K. Hellström, M. R. Sonne, J. Thorborg, N. Tiedje, and J. Hattel, “Uncovering the local inelastic interactions during manufacture of ductile cast iron: How the substructure of the graphite particles can induce residual stress concentrations in the matrix,” *Journal of the Mechanics and Physics of Solids*, vol. 111, pp. 333–357, 2018. (Cited on page 30.)

- [133] J. Koplik and A. Needleman, “Void growth and coalescence in porous plastic solids,” *International Journal of Solids and Structures*, vol. 24, no. 8, pp. 835–853, 1988. (Cited on pages 30 and 141.)
- [134] G. Hütter, L. Zybell, and M. Kuna, “Size effects due to secondary voids during ductile crack propagation,” *International Journal of Solids and Structures*, vol. 51, no. 3-4, pp. 839–847, 2014. (Cited on page 30.)
- [135] L. Helfen, T. Baumbach, P. Mikulik, D. Kiel, P. Pernot, P. Cloetens, and J. Baruchel, “High-resolution three-dimensional imaging of flat objects by synchrotron-radiation computed laminography,” *Applied Physics Letters*, vol. 86, no. 7, p. 071915, 2005. (Cited on pages 30, 31, and 32.)
- [136] T. F. Morgeneyer, L. Helfen, H. Mubarak, and F. Hild, “3d digital volume correlation of synchrotron radiation laminography images of ductile crack initiation: an initial feasibility study,” *Experimental Mechanics*, vol. 53, no. 4, pp. 543–556, 2013. (Cited on pages 30, 32, and 33.)
- [137] A. Swinton, “Röntgen ray experiments,” *Nature*, vol. 54, no. 1389, p. 125, 1896. (Cited on page 31.)
- [138] L. Brühl, “Über verwendung von röntgenischen x-strahlen zu paläontologische diagnostischen zwecken,” *Verhandlungen der Berliner physiologischen Gesellschaft. Archiv für Anatomie und Physiologie, Physiologischer, Teil*, pp. 547–550, 1896. (Cited on page 31.)
- [139] V. Cnudde and M. N. Boone, “High-resolution x-ray computed tomography in geosciences: A review of the current technology and applications,” *Earth-Science Reviews*, vol. 123, pp. 1–17, 2013. (Cited on page 31.)
- [140] A. Myagotin, A. Voropaev, L. Helfen, D. Hanschke, and T. Baumbach, “Efficient volume reconstruction for parallel-beam computed laminography by filtered backprojection on multi-core clusters,” *IEEE Transactions on Image Processing*, vol. 22, no. 12, pp. 5348–5361, 2013. (Cited on page 31.)
- [141] T. Ueda, L. Helfen, and T. F. Morgeneyer, “In situ laminography study of three-dimensional individual void shape evolution at crack initiation and comparison with gurson–tvergaard–needleman-type simulations,” *Acta Materialia*, vol. 78, pp. 254–270, 2014. (Cited on page 31.)
- [142] A. Buljac, T. Taillandier-Thomas, T. F. Morgeneyer, L. Helfen, S. Roux, and F. Hild, “Slant strained band development during flat to slant crack transition in aa 2198 t8 sheet: in situ 3d measurements,” *International Journal of Fracture*, vol. 200, no. 1-2, pp. 49–62, 2016. (Cited on pages 31 and 33.)

- [143] J. Gammage, D. Wilkinson, J. Embury, and E. Maire, “Damage studies in heterogeneous aluminium alloys using x-ray tomography,” *Philosophical Magazine*, vol. 85, no. 26-27, pp. 3191–3206, 2005. (Cited on pages 32 and 116.)
- [144] A. Weck, D. Wilkinson, and E. Maire, “Observation of void nucleation, growth and coalescence in a model metal matrix composite using x-ray tomography,” *Materials Science and Engineering: A*, vol. 488, no. 1, pp. 435–445, 2008. (Cited on pages 32 and 116.)
- [145] Y. Shen, T. F. Morgeneyer, J. Garnier, L. Allais, L. Helfen, and J. Crépin, “Three-dimensional quantitative in situ study of crack initiation and propagation in AA6061 aluminum alloy sheets via synchrotron laminography and finite-element simulations,” *Acta Materialia*, vol. 61, no. 7, pp. 2571–2582, 2013. (Cited on pages 32 and 116.)
- [146] T. F. Morgeneyer, T. Taillandier-Thomas, L. Helfen, T. Baumbach, I. Sinclair, S. Roux, and F. Hild, “In situ 3-d observation of early strain localization during failure of thin Al alloy (2198) sheet,” *Acta Materialia*, vol. 69, pp. 78–91, 2014. (Cited on page 32.)
- [147] M. Grédiac and F. Hild, *Full-field measurements and identification in solid mechanics*. John Wiley & Sons, 2012. (Cited on page 32.)
- [148] E. Roux and P.-O. Bouchard, “On the interest of using full field measurements in ductile damage model calibration,” *International Journal of Solids and Structures*, vol. 72, pp. 50–62, 2015. (Cited on page 32.)
- [149] B. Bay, “Methods and applications of digital volume correlation,” *The Journal of Strain Analysis for Engineering Design*, vol. 43, no. 8, pp. 745–760, 2008. (Cited on page 32.)
- [150] A. Buljac, C. Jailin, A. Mendoza, J. Neggers, T. Taillandier-Thomas, A. Bouterf, B. Smaniotto, F. Hild, and S. Roux, “Digital volume correlation: Review of progress and challenges,” *Experimental Mechanics*, vol. 58, no. 5, pp. 661–708, 2018. (Cited on pages 32 and 33.)
- [151] T. Taillandier-Thomas, S. Roux, T. F. Morgeneyer, and F. Hild, “Localized strain field measurement on laminography data with mechanical regularization,” *Nuclear Instruments and Methods in Physics Research Section B: Beam Interactions with Materials and Atoms*, vol. 324, pp. 70–79, 2014. (Cited on page 33.)
- [152] B. K. Bay, T. S. Smith, D. P. Fyhrie, and M. Saad, “Digital volume correlation: three-dimensional strain mapping using X-ray tomography,” *Experimental mechanics*, vol. 39, no. 3, pp. 217–226, 1999. (Cited on page 33.)
- [153] F. Hild and S. Roux, “Comparison of local and global approaches to digital image correlation,” *Experimental Mechanics*, vol. 52, no. 9, pp. 1503–1519, 2012. (Cited on page 33.)

- [154] O. C. Zienkiewicz and R. L. Taylor, *The finite element method for solid and structural mechanics*. Elsevier, 2005. (Cited on page 33.)
- [155] A. Ern and J.-L. Guermond, *Theory and practice of finite elements*, vol. 159. Springer Science & Business Media, 2013. (Cited on page 33.)
- [156] H. Dignonnet, L. Silva, and T. Coupez, “Cimlib: a fully parallel application for numerical simulations based on components assembly,” in *AIP Conference Proceedings*, vol. 908, pp. 269–274, AIP, 2007. (Cited on pages 33, 119, and 162.)
- [157] F. Brezzi, D. Boffi, L. Demkowicz, R. Durán, R. Falk, and M. Fortin, *Mixed finite elements, compatibility conditions, and applications*. Springer, 2008. (Cited on page 36.)
- [158] D. N. Arnold, F. Brezzi, and M. Fortin, “A stable finite element for the stokes equations,” *Calcolo*, vol. 21, no. 4, pp. 337–344, 1984. (Cited on page 36.)
- [159] E. Perchat, *Mini-élément et factorisation incomplètes pour la parallélisation d’un solveur de Stokes 2D: application au forgeage*. PhD thesis, École Nationale Supérieure des Mines de Paris, 2000. (Cited on page 36.)
- [160] R. H. Wagoner and J.-L. Chenot, *Metal forming analysis*. Cambridge University Press, 2001. (Cited on page 36.)
- [161] K. J. Fidkowski and D. L. Darmofal, “A triangular cut-cell adaptive method for high-order discretizations of the compressible navier–stokes equations,” *Journal of Computational Physics*, vol. 225, no. 2, pp. 1653–1672, 2007. (Cited on page 36.)
- [162] T. Coupez, H. Dignonnet, and R. Ducloux, “Parallel meshing and remeshing,” *Applied Mathematical Modelling*, vol. 25, no. 2, pp. 153–175, 2000. (Cited on page 36.)
- [163] D.-L. Quan, T. Toulorge, E. Marchandise, J.-F. Remacle, and G. Bricteux, “Anisotropic mesh adaptation with optimal convergence for finite elements using embedded geometries,” *Computer Methods in Applied Mechanics and Engineering*, vol. 268, pp. 65–81, 2014. (Cited on page 36.)
- [164] M. Shakoor, B. Scholtes, P.-O. Bouchard, and M. Bernacki, “An efficient and parallel level set reinitialization method—application to micromechanics and microstructural evolutions,” *Applied Mathematical Modelling*, vol. 39, no. 23, pp. 7291–7302, 2015. (Cited on page 39.)
- [165] A. Buljac, V. M. Trejo Navas, M. Shakoor, A. Bouterf, J. Neggers, M. Bernacki, P.-O. Bouchard, T. F. Morgeneyer, and F. Hild, “On the calibration of elastoplastic parameters at the microscale via x-ray microtomography and digital volume correlation for the simulation of ductile damage,” *European Journal of Mechanics-A/Solids*, vol. 72, pp. 287–297, 2018. (Cited on pages 39, 41, 46, 94, and 143.)

- [166] Z. Tomičević, J. Kodvanj, and F. Hild, “Characterization of the nonlinear behavior of nodular graphite cast iron via inverse identification. Analysis of uniaxial tests,” *Europ. J. Mech. A/Solids*, vol. 59, pp. 140–154, 2016. (Cited on page 39.)
- [167] D. L. Pham, C. Xu, and J. L. Prince, “Current methods in medical image segmentation,” *Annual review of biomedical engineering*, vol. 2, no. 1, pp. 315–337, 2000. (Cited on page 46.)
- [168] P. Iassonov, T. Gebrenegus, and M. Tuller, “Segmentation of x-ray computed tomography images of porous materials: A crucial step for characterization and quantitative analysis of pore structures,” *Water Resources Research*, vol. 45, no. 9, 2009. (Cited on page 46.)
- [169] M. Sezgin and B. Sankur, “Survey over image thresholding techniques and quantitative performance evaluation,” *Journal of Electronic imaging*, vol. 13, no. 1, pp. 146–166, 2004. (Cited on pages 46 and 48.)
- [170] L. Staniewicz and P. A. Midgley, “Machine learning as a tool for classifying electron tomographic reconstructions,” *Advanced Structural and Chemical Imaging*, vol. 1, no. 1, p. 9, 2015. (Cited on page 46.)
- [171] L.-C. Chen, G. Papandreou, I. Kokkinos, K. Murphy, and A. L. Yuille, “Deeplab: Semantic image segmentation with deep convolutional nets, atrous convolution, and fully connected crfs,” *arXiv preprint arXiv:1606.00915*, 2016. (Cited on page 46.)
- [172] A. Madra, N. El Hajj, and M. Benzeggagh, “X-ray microtomography applications for quantitative and qualitative analysis of porosity in woven glass fiber reinforced thermoplastic,” *Composites Science and Technology*, vol. 95, pp. 50–58, 2014. (Cited on page 46.)
- [173] D. S. Bulgarevich, S. Tsukamoto, T. Kasuya, M. Demura, and M. Watanabe, “Pattern recognition with machine learning on optical microscopy images of typical metallurgical microstructures,” *Scientific reports*, vol. 8, no. 1, p. 2078, 2018. (Cited on page 46.)
- [174] A. Buljac, T. Taillandier-Thomas, L. Helfen, T. F. Morgeneyer, and F. Hild, “Evaluation of measurement uncertainties of digital volume correlation applied to laminography data,” *The Journal of Strain Analysis for Engineering Design*, vol. 53, no. 2, pp. 49–65, 2018. (Cited on pages 46 and 48.)
- [175] L. Helfen, A. Myagotin, A. Rack, P. Pernot, P. Mikulik, M. Di Michiel, and T. Baumbach, “Synchrotron-radiation computed laminography for high-resolution three-dimensional imaging of flat devices,” *physica status solidi (a)*, vol. 204, no. 8, pp. 2760–2765, 2007. (Cited on page 47.)
- [176] J. Schindelin, I. Arganda-Carreras, E. Frise, V. Kaynig, M. Longair, T. Pietzsch, S. Preibisch, C. Rueden, S. Saalfeld, B. Schmid, *et al.*, “Fiji: an open-source plat-

- form for biological-image analysis,” *Nature methods*, vol. 9, no. 7, p. 676, 2012. (Cited on page 47.)
- [177] C. A. Schneider, W. S. Rasband, and K. W. Eliceiri, “Nih image to imagej: 25 years of image analysis,” *Nature methods*, vol. 9, no. 7, p. 671, 2012. (Cited on page 47.)
- [178] R. Adams and L. Bischof, “Seeded region growing,” *IEEE Transactions on pattern analysis and machine intelligence*, vol. 16, no. 6, pp. 641–647, 1994. (Cited on page 48.)
- [179] J. A. Sethian, *Level set methods and fast marching methods: evolving interfaces in computational geometry, fluid mechanics, computer vision, and materials science*, vol. 3. Cambridge university press, 1999. (Cited on page 48.)
- [180] T. Ridler, S. Calvard, *et al.*, “Picture thresholding using an iterative selection method,” *IEEE trans syst Man Cybern*, vol. 8, no. 8, pp. 630–632, 1978. (Cited on page 51.)
- [181] L.-K. Huang and M.-J. J. Wang, “Image thresholding by minimizing the measures of fuzziness,” *Pattern recognition*, vol. 28, no. 1, pp. 41–51, 1995. (Cited on page 51.)
- [182] J. Prewitt and M. L. Mendelsohn, “The analysis of cell images,” *Annals of the New York Academy of Sciences*, vol. 128, no. 1, pp. 1035–1053, 1966. (Cited on page 51.)
- [183] C. Li and P. K.-S. Tam, “An iterative algorithm for minimum cross entropy thresholding,” *Pattern recognition letters*, vol. 19, no. 8, pp. 771–776, 1998. (Cited on page 51.)
- [184] C. H. Li and C. Lee, “Minimum cross entropy thresholding,” *Pattern recognition*, vol. 26, no. 4, pp. 617–625, 1993. (Cited on page 51.)
- [185] J. N. Kapur, P. K. Sahoo, and A. K. Wong, “A new method for gray-level picture thresholding using the entropy of the histogram,” *Computer vision, graphics, and image processing*, vol. 29, no. 3, pp. 273–285, 1985. (Cited on page 51.)
- [186] C. A. Glasbey, “An analysis of histogram-based thresholding algorithms,” *CVGIP: Graphical models and image processing*, vol. 55, no. 6, pp. 532–537, 1993. (Cited on page 51.)
- [187] J. Kittler and J. Illingworth, “Minimum error thresholding,” *Pattern recognition*, vol. 19, no. 1, pp. 41–47, 1986. (Cited on page 51.)
- [188] W.-H. Tsai, “Moment-preserving thresholding: A new approach,” *Computer Vision, Graphics, and Image Processing*, vol. 29, no. 3, pp. 377–393, 1985. (Cited on page 51.)
- [189] N. Otsu, “A threshold selection method from gray-level histograms,” *IEEE transactions on systems, man, and cybernetics*, vol. 9, no. 1, pp. 62–66, 1979. (Cited on page 51.)
- [190] W. Doyle, “Operations useful for similarity-invariant pattern recognition,” *Journal of the ACM (JACM)*, vol. 9, no. 2, pp. 259–267, 1962. (Cited on page 51.)

- [191] A. Rényi, “On measures of entropy and information,” tech. rep., HUNGARIAN ACADEMY OF SCIENCES Budapest Hungary, 1961. (Cited on page 51.)
- [192] A. G. Shanbhag, “Utilization of information measure as a means of image thresholding,” *CVGIP: Graphical Models and Image Processing*, vol. 56, no. 5, pp. 414–419, 1994. (Cited on page 51.)
- [193] G. Zack, W. Rogers, and S. Latt, “Automatic measurement of sister chromatid exchange frequency,” *Journal of Histochemistry & Cytochemistry*, vol. 25, no. 7, pp. 741–753, 1977. (Cited on page 51.)
- [194] J.-C. Yen, F.-J. Chang, and S. Chang, “A new criterion for automatic multilevel thresholding,” *IEEE Transactions on Image Processing*, vol. 4, no. 3, pp. 370–378, 1995. (Cited on page 51.)
- [195] L. Breiman, “Random forests,” *Machine learning*, vol. 45, no. 1, pp. 5–32, 2001. (Cited on page 51.)
- [196] I. Arganda-Carreras, V. Kaynig, C. Rueden, K. W. Eliceiri, J. Schindelin, A. Cardona, and H. Sebastian Seung, “Trainable weka segmentation: a machine learning tool for microscopy pixel classification,” *Bioinformatics*, vol. 33, no. 15, pp. 2424–2426, 2017. (Cited on page 53.)
- [197] K. A. Kasvayee, K. Salomonsson, E. Ghassemali, and A. E. Jarfors, “Microstructural strain distribution in ductile iron; comparison between finite element simulation and digital image correlation measurements,” *Materials Science and Engineering: A*, vol. 655, pp. 27–35, 2016. (Cited on page 84.)
- [198] K. Salomonsson and J. Olofsson, “Analysis of localized plastic strain in heterogeneous cast iron microstructures using 3d finite element simulations,” in *Proceedings of the 4th World Congress on Integrated Computational Materials Engineering (ICME 2017)*, pp. 217–225, Springer, 2017. (Cited on page 84.)
- [199] A. Weck and D. Wilkinson, “Experimental investigation of void coalescence in metallic sheets containing laser drilled holes,” *Acta Materialia*, vol. 56, no. 8, pp. 1774–1784, 2008. (Cited on pages 84, 129, and 148.)
- [200] G. Fischer, J. Nellesen, N. Anar, K. Ehrig, H. Riesemeier, and W. Tillmann, “3d analysis of micro-deformation in vhf-loaded nodular cast iron by μct ,” *Materials Science and Engineering: A*, vol. 577, pp. 202–209, 2013. (Cited on page 84.)
- [201] V. M. Trejo Navas, A. Buljac, F. Hild, T. Morgeneyer, L. Helfe, M. Bernacki, and P.-O. Bouchard, “A comparative study of image segmentation methods for micromechanical simulations of ductile damage,” *Submitted to Computational Materials Science*, 2018. (Cited on page 88.)

- [202] E. Voce, “A practical strain hardening function,” *Metallurgia*, vol. 51, pp. 219–226, 1955. (Cited on page 94.)
- [203] T. Cox and J. R. Low, “An investigation of the plastic fracture of aisi 4340 and 18 nickel-200 grade maraging steels,” *Metallurgical and Materials Transactions B*, vol. 5, no. 6, pp. 1457–1470, 1974. (Cited on page 116.)
- [204] D. Goto, D. Koss, and V. Jablokov, “The influence of tensile stress states on the failure of HY-100 steel,” *Metallurgical and Materials Transactions A*, vol. 30, no. 11, pp. 2835–2842, 1999. (Cited on page 116.)
- [205] E. Maire, S. Zhou, J. Adrien, and M. Dimichiel, “Damage quantification in aluminium alloys using in situ tensile tests in X-ray tomography,” *Engineering Fracture Mechanics*, vol. 78, no. 15, pp. 2679–2690, 2011. (Cited on page 116.)
- [206] L. Babout, E. Maire, and R. Fougères, “Damage initiation in model metallic materials: X-ray tomography and modelling,” *Acta Materialia*, vol. 52, no. 8, pp. 2475–2487, 2004. (Cited on pages 116 and 117.)
- [207] J. A. Nelder and R. Mead, “A simplex method for function minimization,” *The computer journal*, vol. 7, no. 4, pp. 308–313, 1965. (Cited on page 119.)
- [208] S. G. Johnson, “The nlopt nonlinear-optimization package,” 2014. (Cited on page 119.)
- [209] Y. Huang, “Accurate dilatation rates for spherical voids in triaxial stress fields,” *Journal of Applied Mechanics*, vol. 58, p. 1084, 1991. (Cited on page 128.)
- [210] J. Fansi, *Prediction of DP steel fracture by FEM simulations using an advanced Gurson model*. PhD thesis, Ecole nationale supérieure d’arts et métiers-ENSAM; Université de Liège, 2013. (Cited on pages 141 and 154.)
- [211] F. Scheyvaerts, P. Onck, C. Tekoglu, and T. Pardoen, “The growth and coalescence of ellipsoidal voids in plane strain under combined shear and tension,” *Journal of the Mechanics and Physics of Solids*, vol. 59, no. 2, pp. 373–397, 2011. (Cited on page 141.)
- [212] X. Gao and J. Kim, “Modeling of ductile fracture: significance of void coalescence,” *International Journal of Solids and Structures*, vol. 43, no. 20, pp. 6277–6293, 2006. (Cited on page 141.)
- [213] T. Pardoen, F. Scheyvaerts, C. Tekoglu, and L. Lecarme, “Recent progress in micromechanics-based modeling of void coalescence,” in *The SEM Annual Conference. New Mexico, Albuquerque, USA*, 2009. (Cited on page 141.)
- [214] C. Tekoğlu, J. Hutchinson, and T. Pardoen, “On localization and void coalescence as a precursor to ductile fracture,” *Phil. Trans. R. Soc. A*, vol. 373, no. 2038, p. 20140121, 2015. (Cited on page 141.)

- [215] V. M. Trejo Navas, M. Bernacki, and P.-O. Bouchard, “An examination of microscopic precoalescence strain measures in ductile cast iron through mechanical simulations based on 3D imaging,” *In preparation*. (Cited on pages 142 and 143.)
- [216] C. I. Bliss, “The calculation of the dosage-mortality curve,” *Annals of Applied Biology*, vol. 22, no. 1, pp. 134–167. (Cited on page 148.)
- [217] D. McFadden, “Conditional logit analysis of qualitative choice behavior,” *Frontiers in Econometrics*, pp. 105–142, 1974. (Cited on page 149.)
- [218] C. Landron, O. Bouaziz, E. Maire, and J. Adrien, “Characterization and modeling of void nucleation by interface decohesion in dual phase steels,” *Scripta Materialia*, vol. 63, no. 10, pp. 973–976, 2010. (Cited on page 155.)
- [219] C. Landron, E. Maire, O. Bouaziz, J. Adrien, L. Lecarme, and A. Bareggi, “Validation of void growth models using x-ray microtomography characterization of damage in dual phase steels,” *Acta Materialia*, vol. 59, no. 20, pp. 7564–7573, 2011. (Cited on page 155.)
- [220] L. Lecarme, E. Maire, A. K. Kc, C. De Vleeschouwer, L. Jacques, A. Simar, and T. Pardoen, “Heterogenous void growth revealed by in situ 3-d x-ray microtomography using automatic cavity tracking,” *Acta Materialia*, vol. 63, pp. 130–139, 2014. (Cited on page 162.)
- [221] P. Thomason, “A view on ductile-fracture modelling,” *Fatigue & Fracture of Engineering Materials & Structures*, vol. 21, no. 9, pp. 1105–1122, 1998. (Cited on page 163.)
- [222] V. Tvergaard, “Material failure by void coalescence in localized shear bands,” *International journal of solids and structures*, vol. 18, no. 8, pp. 659–672, 1982. (Cited on page 164.)
- [223] T. De Geus, R. Peerlings, and M. Geers, “Microstructural topology effects on the onset of ductile failure in multi-phase materials—a systematic computational approach,” *International Journal of Solids and Structures*, vol. 67, pp. 326–339, 2015. (Cited on page 165.)

Résumé

Ce travail vise à mieux comprendre et modéliser les mécanismes de rupture ductile pour les microstructures hétérogènes. La principale méthodologie du projet repose sur la combinaison de trois techniques : la laminographie *in-situ* par rayonnement synchrotron, la corrélation d'images volumiques (DVC) et la simulation par éléments finis (FE) avec des fonctionnalités avancées de maillage et de remaillage automatique. Ce cadre expérimental-numérique est utilisé pour réaliser des simulations numériques à l'échelle microscopique avec des microstructures immergées et des conditions aux limites réalistes. L'effet de la segmentation d'image sur les observables mécaniques finales est évalué par comparaison de trois méthodologies différentes. Ce travail permet, pour la première fois, d'accéder aux valeurs de déformation locales au début de la coalescence pour des microstructures réelles et des conditions aux limites exactes. Les résultats des simulations sont utilisés pour définir et valider des critères de rupture locaux fonctions des contraintes/déformations ou un critère de coalescence basé sur l'évolution de la distance entre les pores.

Mots Clés

Rupture ductile, endommagement, microstructures hétérogènes, coalescence

Abstract

This work constitutes a micromechanical study of ductile fracture. The main methodology consists of a combination of three techniques: *In-situ* synchrotron radiation computed laminography, digital volume correlation and finite element simulations with advanced meshing and remeshing capabilities. This experimental-numerical framework is employed to carry out numerical simulations at the microscale with immersed microstructures and realistic boundary conditions. The studied material is nodular cast iron, but this methodology has been successfully applied to other materials such as aluminum alloys. Since this is a recent methodology, attention is paid to image immersion as a source of uncertainty. More specifically, the effect of image segmentation on the final mechanical observables, is assessed through comparison of three different segmentation methodologies. The prediction capacity of the numerical simulations is then satisfactorily evaluated through a detailed comparison with experimental measurements. Finally, after evaluating different approaches, the results of the simulations are used to propose and validate a coalescence criterion based on the evolution of the intervoid distance.

Keywords

Ductile fracture, ductile damage, heterogeneous microstructure, void coalescence